Alexander I. Khilko,
Jerald W. Caruthers,
Natalia A. Sidorovskaia

OCEAN ACOUSTIC TOMOGRAPHY

A REVIEW WITH EMPHASIS ON THE RUSSIAN APPROACH

Published on the decision of the Editorial-Board of the IAP RAS

Khil'ko Alexander I., Caruthers Jerald W. and Sidorovskaia Natalia A.

Ocean Acoustic Tomography: A Review with Emphasis on the Russian Approach. Nizhny Novgorod: IAP RAS, 1998. 196 p.

ISBN 5-8048-0001-9

Recent accomplishments in ocean acoustic tomography were presented in this book. In particular, the adiabatic approach in tomographic reconstruction and the methods of diffraction and emission tomography which have been addressed in some details. In final chapter, the major ideas will be summarized to indicate concisely the modern status of tomographic investigations, particularly, as it exists in Russia. This book is intended for the researchers and students engaged in the field of ocean acoustics.

Figures 80, tables 2, citations 162.

Reviewers

Prof. **S. N. Gurbatov**
Dr. **L. S. Dolin**

ISBN 5-8048-0001-9

PREFACE

The purpose of this book is primarily to review and collect under one cover summaries of contributions to the topic of Ocean Acoustic Tomography by Russian researchers. It was a joint effort by the Naval Research Laboratory (NRL) of the United States and the Institute of Applied Physics of the Russian Academy of Sciences (IAP-RAS). The work was jointly supported by the Office of Naval Research (ONR) of the United States and the Russian Foundation for Basic Research (RFBR).

This book is one of a series published by IAP-RAS that deals with various interrelated problems of synthesis and analysis of underwater acoustic signals. These books include: *The Foundation of Acoustical Fields in Oceanic Waveguides*, 1991 (in Russian); *The Foundation of Acoustical Fields in Oceanic Waveguides C Reconstruction of Inhomogeneities*, 1994 (in Russian); *The Foundation of Acoustical Fields in Oceanic Waveguides*, 1995 (in English); *The Foundation of Acoustical Fields in Oceanic Waveguides C Coherence Phenomena*, 1997 (in English); and *The Foundation of Acoustical Fields in Oceanic Waveguides C Reconstruction of Inhomogeneities in Shallow Water*, 1998 (in English).

While the United States has taken one direction in the development of tomographic methods for the study of the World Ocean, the Russians have taken another. The goal here is not only to review Ocean Acoustic Tomography, but also to slant the review with a Russian flavor. This review, however, would not be complete without including selected contribution from the American literature on this topic. An excellent book by the inventors and early developers of Ocean Acoustic Tomography (Walter Munk, Peter Worcester, and Carl Wunsch) already exists that details the contributions of the United States to the subject. The US literature will be cited less frequently than Russian works in this review because the American publications on topics of Ocean Acoustic Tomography are more accessible and better known to the American scientific community.

They also thank all the authors whose works have been include here in altered and condensed form. The present authors, however, take full responsible for any errors that may appear in their alteration of the original works. To those

authors whose works have been used extensively with their permission we owe special thanks. They include: D.I. Abrosimov, E.L. Borodina, L.M. Brekhovskikh, I.B. Burlakova, I.N. Didenkulov, V.N. Fokin, A.G. Nechaev, V.V. Goncharov, A.Yu. Kazarova, B.F. Kur'ianov. The authors and their respective institutes are grateful to ONR for support of this review. V.M. Kurtepov, L.Ya. Lubavin, Yu.V. Petukhov, I.P. Smirnov, A.A. Stromkov, A.I. Vedenev, and V.Yu. Zaitsev. The present authors also regret not mentioning other major contributors they may have overlook in the above credits.

Part I

CLASSICAL TOMOGRAPHIC METHODS

Chapter 1:

INTRODUCTION: CONCEPTS IN ACOUSTIC MODELING AND TOMOGRAPHY

1.1 TOMOGRAPHY AS A PRACTICAL TOOL FOR SOLVING INVERSE PROBLEMS

A process of sensing (or probing) the internal structure of objects by propagating waves through them and analyzing the resulting field is a practical example of solving an *inverse problem.* This process is described mathematically by an integral equation:

$$\iint \psi(\boldsymbol{R},t;\boldsymbol{r},\tau)g(\boldsymbol{r},\tau)d\boldsymbol{r}d\tau = \varphi(\boldsymbol{R},t), \tag{1.1}$$

where $\boldsymbol{r}$, $\boldsymbol{R}$ are position vectors, $g(\boldsymbol{r},\tau)$ is a function of the characteristics of the object under observation, $\varphi(\boldsymbol{R},t)$ corresponds to measured data, and $\psi(\boldsymbol{R},t;\boldsymbol{r},\tau)$ is the kernel of the integral equation. The kernel is determined by the structure of the unperturbed medium and by the measurement scheme. The integral in Eq. (1.1) is constructed from functions that describe properties of the medium along wave propagation paths crossing the inhomogeneity at different angles in a given section (or slice). Thus, measured data on the right-hand side of Eq. (1.1) contain information about medium characteristics. The acoustically observable integral properties, which are described by the function $\varphi(\boldsymbol{R},t)$, can represent travel time or attenuation.

Although the inverse problem has different methods of solution, a procedure introduced in 1917 by Radon [1] has come to be called *"tomographic reconstruction"*, or *"tomography."* Tomography, from the Greek word "tomos", means a layer (or slice). Thus, it implies a process of layer-by-layer reconstruction of the structure by using various types of probing waves. Generally, tomography is based on a principle that determines how to change the parameters of the kernel of the integral equation and how to connect these changes to measured data and properties of the object. The result is a practical solution of the integral equation in terms of a series of measured *projections.* Changes in the kernel of the integral equation determine the methods and algorithms for the measurements of the tomographic projections, or vice versa. Tomographic reconstruction is the restoration of *differential* characteristics of the observed object by mutual processing of all projections. For some cases, the procedure of reconstruction can be reduced to a well-known integral transformation, like the Fourier or Fresnel transformations [2, 3], but more often the transformations are represented on the basis set of *Generalized Functions* [3] or on the basis of *Empirical Orthogonal Functions* (EOF) [4].

Radon's ideas are fundamental principles of the reconstruction of localized characteristics of inhomogeneities from the measured integral characteristics. The successful application of these principles for solving practical problems has been attained only when the development of theory and numerical algorithms [5], and the manufacture of powerful digital computers came together in the early 1970's. This has resulted in a veritable revolution in medical radiology that has allowed the imaging of the internal organs of the human body. Techniques have subsequently been developed for the X-ray and ultrasonic applications [6, 7].

1.2 GOALS OF TOMOGRAPHIC RECONSTRUCTIONS FOR THE OCEANS

Electromagnetic and optical methods for the remote sensing of the ocean environment are well-known. However, these methods are generally limited to sensing phenomena in the oceans' upper layers. Acoustic waves, which interact with the ocean, transport information about the conditions in the ocean volume, particularly, about inhomogeneities and variations in medium parameters. Acoustic waves can be an effective tool for remote investigations of the ocean volume, ocean bottom, as well as the ocean surface, because of their ability to propagate long distances in ocean waveguides. Accordingly, the goal of acoustic remote sensing is a reconstruction of the characteristics of inhomogeneities by measuring the parameters of the received acoustic signals.

Remote sensing by acoustic waves was an essential tool for the investigation of ocean structure even before the introduction of basic tomographic concepts into the ocean study [8-11] (for example, the ubiquitous acoustic depth sounder). The tomographic method for the reconstruction of localized (differential) characteristics of the ocean medium was proposed by Munk and Wunsch in 1979 [12]. They also introduced the term of *"Ocean Acoustic Tomography"* (OAT). OAT has refined ocean sensing and established the distinct methodology for the study of the ocean medium on many scales from the minute to the global.

Acoustic signals propagating along acoustic paths contain integrated information about all inhomogeneities that are distributed along these paths. Each measurement of the acoustic signal gives us only averaged information about all inhomogeneities along the path of propagation [8-10, 13]. On the other hand, the tomographic approach allows for simultaneous measurements of the observation environment with overlapping, but different views. It provides for the reconstruction of inhomogeneities in the volume when the observation system is properly configured and the resulting data are analyzed with the appropriate algorithms. The spatial distributions (images) of the characteristics of inhomogeneities in the observed area can be determined by scanning different properties of the sensing acoustic waves. The reconstruction of the spatially localized (differential) characteristics of media (inhomogeneities in the ocean volume in our case) is a goal of ocean acoustic tomography.

Tomographic methods can be applied to the solution of many practical problems associated with the marine endeavors of mankind: exploitation of marine

resources, including fisheries and minerals; prediction of weather and climatic changes, including the monitoring of the global warming; underwater engineering activity; and marine navigation. The tomographic reconstruction of oceanic inhomogeneities and their temporal variability can help oceanographic research, such as the study of motion of the water masses in flows and eddies, investigations of the characteristics of different types of ocean waves (surface waves, internal waves, Rossby waves), and the study of small-scale phenomena (bubble clouds and fish shoals) [8, 9, 11]. For an important contemporary concern, tomography can contribute in the study of the global warming [12, 14, 15]. Thus, there is a broad area of problems associated with marine commercial activity and oceanographic research that can be solved by the methods of ocean acoustic tomography.

Some of the major factors promoting the creation and development of OAT methods are:

a) Practical applications associated with needs to understand the ocean;
b) Success of the acoustic monitoring of the ocean;
c) Development of techniques for acoustic tomography;
d) Creation of powerful digital computers; and
e) Development of theories and algorithms for modeling acoustic propagation and scattering in the ocean and methods for solving integral equations.

This list is not complete; in fact, we have only sketched the variety of problems that can be resolved by tomographic methods. While the United States has taken one direction in the development of these methods, the Russians have taken another. Our goal here is not only to review ocean acoustic tomography, but also to slant the review with a Russian flavor. This review, however, would not be complete without including the broad American literature on this topic. An excellent book by the inventors of ocean acoustic tomography already exists that details the contributions of the USA to the subject [16]. The US literature will be cited less frequently than Russian works in this review because the American publications on topics of OAT are more accessible and better known to the American scientific community.

In summary, it is important to mention that the monitoring of large ocean regions can be carried out by using OAT and can supplement electromagnetic and optical remote sensing for a more complete description of the ocean. The mathematical and physical bases of the tomographic methods have been developed before its application to the monitoring of the ocean [1, 5, 6, 19-20]. Therefore, ocean acoustic tomography can be considered as an adaptation of those bases to ocean conditions. However, investigations have shown that this generalization has not been easily achieved due to the specific conditions for acoustic signal propagation in ocean waveguides and due to engineering problems associated with measurements in the ocean.

A choice of the particular tomographic approach for the solution of a given ocean observation problem depends on the nature of the inhomogeneity to be investigated and the background ocean conditions in which signals are measured. Moreover, the OAT algorithm, similar to the solution of the inverse problem, is dependent on the ability to model the forward acoustic propagation in the ocean, and

to model the particular types of inhomogeneities and their effects on acoustic propagation. Before discussing OAT in detail, it is useful to mention a few aspects of acoustic modeling and some models describing oceanic inhomogeneities.

1.3 MODELS OF ACOUSTIC WAVE PROPAGATION IN THE OCEAN

The layered waveguide is a simple model for horizontally stratified regions of the ocean. Sound speed changes rapidly with depth in such waveguides, but changes in range are generally relatively weak. An underwater sound channel trapping acoustic signals arises for a special vertical sound speed profile, $c(z)$, for which there is a minimum value of the sound speed at a certain depth.

Acoustic waves in different ocean waveguides propagate in the form of space-time structures which can be observed and described within ray or modal representations [3, 8, 16, 22]. Both representations of acoustic waves can be obtained as solutions to the Helmholtz equation describing the propagation of a linear harmonic wave:

$$\nabla^2 p + k^2 p = 0, \tag{1.2}$$

where ∇^2 is the Laplace operator, $p = p(x,y,z)$ is the sound pressure, $k = \omega / c(x,y,z)$ is the wavenumber, and ω is the angular frequency. Further, $\omega = 2\pi f = 2\pi / T$, where f is the frequency and T is the period of the sound wave.

If the medium is weakly inhomogeneous, i.e., if the magnitude of the sound-speed gradient, $|\nabla c|$, satisfies the condition

$$\frac{\lambda}{c}|\nabla c| \ll 1, \tag{1.3}$$

where λ is the wavelength, the medium is said to satisfy the *adiabatic approximation*. Under the condition of the adiabatic approximation, the solution of Eq. (1.2) can be represented as a ray series:

$$p(\boldsymbol{R}) = \sum_{n=1}^{N} A_n(\boldsymbol{R}) \exp[ik_0 W_n(\boldsymbol{R})], \tag{1.4}$$

where $\boldsymbol{R}$ is the position vector of the point with coordinates (x,y,z), A_n and $k_0 W_n$ are the amplitudes and the phases of rays, $k_0 = \omega / c_0$, and c_0 is the reference sound speed at some fixed point of waveguide (usually at the point where the sound source is located). The values A_n and W_n can be determined from the transport and eikonal equations of the ray acoustics, and the latter is called the *eikonal* [8].

For the case of horizontally layered waveguides, the solution of the Helmholtz equation can be decomposed into a sum of basis functions (modes) by the method of separation of variables. According to the boundary conditions and the radiation conditions at infinity, the solution can be written as the sum of waveguide modes:

$$p(r,z) = \sum_{m=1} c_m \varphi_m(z) H_0^{(1)}(\kappa_m r), \qquad (1.5)$$

where r is the horizontal distance in the two-dimensional cylindrical coordinate system (azimuthal symmetry is assumed), κ_m is the horizontal wavenumber for the mth mode, and the φ_m's are the vertical eigenfunctions for the waveguide modes, $H_0^{(1)}$ is the zero-order Hankel function of the first kind, and the c_m's are the excitation coefficient of waveguide modes [8].

A choice of the ray or modal representations (by Eq. (1.4) or by Eq. (1.5), respectively) in ocean waveguides is determined by efficiency and convenience of their application. The effectiveness of the description of the interaction of sensing acoustic waves with inhomogeneities is important for the solution of the inverse problem and, in particular, for tomographic reconstruction. Thus, the mode approach can be used for calculating acoustic-wave propagation in shallow water. The shallow-water case usually corresponds to the ratio of the water-column depth to the signal wavelength not exceeding ten. On the contrary, the ray approximation is more effective for calculating high-frequency acoustic wave propagation in deep water, especially, for the cases of horizontally inhomogeneous waveguides.

Rays. Initially, tomographic principles were proposed for the reconstruction of relatively smooth sound speed variations in the ocean (cf. Eq. (1.3)). The travel-time delays between ray pulses crossing the observed inhomogeneities at different angles can be measured in this case [12]. Investigations have also shown that the ray approach is effective enough for numerical estimation of phenomena associated with propagation of acoustic waves in the deep ocean, as well as their interaction with inhomogeneities.

Modes. In shallow water the interference among the numerous boundary-reflected paths creates space-time structures which are more readily described by modes. The separated waveguide modes play the role of elementary tomographic projections, and the measured parameter can be the phase of the mode. In the case of the interaction of sensing waveguide modes with smooth inhomogeneities, the modal adiabatic approximation can be used [8, 23].

Thus, for the cases of relatively smooth inhomogeneities, which allow the use of the adiabatic approximation, either ray or modal acoustic-wave descriptions can be applied as convenience dictates. For oceanic inhomogeneities characterized by more sharply defined boundaries, a coupling between modes exists, so that a transfer of acoustic energy among the different modes or rays occurs. In these cases diffraction and scattering models must be used to describe the interaction of the probing waves with these sharply defined inhomogeneities. Different diffraction and scattering models have been developed for the investigation of the efficiency of tomographic methods for reconstruction of this type of oceanic inhomogeneities [22, 24-32].

1.4 TYPES OF OCEANIC INHOMOGENEITIES

Characteristics of oceanic inhomogeneities are determined by various hydrophysical processes in the ocean environment. Very broad limits of the variability of spatial, L, and temporal, T, inhomogeneity scales in the ocean are the results of the complex processes associated with ocean dynamics and different types of inclusions in the ocean. Furthermore, tomographic methods are not limited to the applications in the water column. Inhomogeneities in the bottom and bottom properties are also a subject for tomographic investigations. However, in the following discussion we shall focus mostly on the ocean dynamical processes in the water column.

As measurements and experimental observations have shown, the spatial and temporal scales of oceanic inhomogeneities are bounded by the following values: $10^{-3} \le L \le 10^{6}$ m and $10^{-3} \le T \le 10^{6}$ s. These overall space-time scales of inhomogeneities in the ocean can be further subdivided into micro-scale, meso-scale, synoptic, and gyro-scale inhomogeneities. The subdivisions are related to the basic ocean dynamic processes and can be distinguished by the following approximate classification scheme presented in the literature [9, 10, 13, 24, 33].

Micro-Scale Inhomogeneities. The following inhomogeneities can be classified as micro-scale:

a) micro-scale turbulence:
$10^{-3} \le L \le 10\ m,\ 10^{-3} \le T \le 10^{2}\ s$;
b) vertically layered ocean structures:
$10^{-3} \le L < 10\ m,\ 10^{2} \le T \le 10^{4}\ s$;
c) capillary surface waves:
$10^{-3} \le L \le 10^{-2}\ m,\ 10^{-1} \le T \le 10\ s$;
d) gravity surface waves:
$10^{-1} \le L \le 10^{2}\ m,\ 10^{-1} \le T \le 10^{2}\ s$;
e) short-period internal waves:
$10^{1} \le L \le 10^{3}\ m,\ 10^{2} \le T \le 10^{3}\ s$.

Meso-Scale Inhomogeneities. This class of inhomogeneities includes:

a) long-period internal waves:
$10^{3} \le L \le 10^{4}\ m,\ 10^{3} \le T < 10^{4}\ s$;
b) inertial waves:
$10^{3} \le L \le 10^{5}\ m,\ 10^{4} \le T \le 10^{5}\ s$;
c) tidal flows in shallow water;
d) meso-scale turbulence.

Synoptic Inhomogeneities. Synoptic inhomogeneities are associated with:

a) movements of hydrolenses of cool and warm water;

b) ocean eddies:
$10^4 < L < 10^5\ m,\ 10^5 < T \le 10^6\ s$;
c) the Rossby waves:
$10^4 < L < 10^5\ m,\ 10^5 \le T < 10^6\ s$.

Gyro-Scale Inhomogeneities. Gyro-scale inhomogeneities, related to the ocean circulation and seasonal variability, have very large space-time scales; equivalent, for example, to the scales of oceanic basins.

This classification of inhomogeneities comes from different water motions in the ocean environment, differential heating near the ocean surface, and wind and tidal effects. All these inhomogeneities play a significant role in ocean activity in the layers close to the surface. They can be distributed through and below the major thermocline (a region of strong negative vertical gradient in temperature 100-1000 m below the sea surface). Additionally, there are various inclusions in the ocean environment that also represent inhomogeneities. These can, for example, be particles, bubbles, fish and plankton, fish shoals, clouds of bubbles, ice floes, ships, and engineering constructions. The inclusions can also fit within the micro-scale and meso-scale classification.

On the other hand, all types of inhomogeneities can be distinguished as "weak" or "strong." Weak inhomogeneities cause refraction of sensing waves. Strong inhomogeneities are non-adiabatic and lead to diffraction. Diffraction causes the redistribution of the modal or ray spectrum and creates new modes or rays. Such an additional differentiation is based on the relation between the acoustic wavelength and changes in the inclusion's characteristics (Eq. (1.3)). From this viewpoint, we can speak of smooth (weak, refractive type) or sharp (strong, diffractive) changes of the inhomogeneity properties within the acoustic wavelength. It is easy to understand that this relation determines the peculiarities of sound propagation in the observation region of the ocean. It also determines the sizes of the observation region, the noise level, the sound-source power, and other physical parameters.

1.5 PHYSICAL MODELS OF OCEANIC INHOMOGENEITIES AND ACOUSTIC INTERACTIONS

For the application of tomographic methods to sensing ocean processes, a physical model is generally required as a starting point for the inverting reconstruction technique to obtain the environmental properties. The model usually includes the physical description of the specific inhomogeneity and the acoustic-wave interaction with it. Different physical models, based on the results of experimental observations, are used to describe the characteristics of oceanic inhomogeneities. These models can include deterministic as well as statistical approaches. The following are some examples of the physical models of oceanic inhomogeneities, which are often used for the investigation of OAT system performance. (Here we simply convey the concept, but do not provide a complete list of models. Later more details will be provided when necessary.)

Modeling Ocean Surface Inhomogeneities. Models have been developed to describe the details of the creation of surface waves and scattering of sound by them [8]. It is well-known that the major cause of surface waves is the influence of wind. According to the nature of surface waves, a statistical approach is used to describe their properties. This is generally done by using models describing the surface-wave power spectrum properties. One of the model examples is the Pierson-Moskowitz spectrum [3, 8]. Theories also provide models for forward and backscattering from the surfaces described by power spectrum models [8].

Modeling Internal Waves. The Garret-Munk model is often used for the description of the spectrum of the background field of internal waves [4]. One should generally use a statistical approach to describe the acoustic refraction in the stochastic internal wave field.

Modeling Bottom Inhomogeneities. Various types of inhomogeneities that describe the bottom and its interaction with acoustic waves have been intensively investigated. Despite much effort, a general methodology of the bottom description for the robust application of tomographic methods (especially, diffraction and differential tomography) has not been developed. There is no developed universal model for the description of the seafloor and the acoustic interaction with it at this time. This is due to difficulties associated with the complex structure of the real ocean bottom as well as due to practical problems associated with the application of the techniques. Nevertheless, simple models of the acoustic reflection from the shallow-water bottom, for example, modeled as an elastic half-space [8] or as an isovelocity fluid layer over the elastic half-space [8], have shown a relatively high efficiency for calculation. However, the use of such models sometimes fails to explain measured acoustic data or to extract some useful detailed bottom properties.

Modeling Other Inhomogeneities. Information about models describing other types of oceanic inhomogeneities is practically absent from the literature, apparently, due to shortage of appropriate experimental data. Nevertheless, it is important to mention some examples. The Gaussian spectral model has been applied to describe the structure of the fluctuations of the sound-speed profile in the water column [3]. A polynomial functional form of the spectrum has been used for the description of turbulence pulsations [13, 35]. Finally, ice floes, engineering constructions and other similar inhomogeneities can be considered as elastic or impedance objects causing the diffraction of acoustic waves [19, 24-32].

1.6 AN INTRODUCTION TO RUSSIAN OCEAN ACOUSTIC TOMOGRAPHY

This section discusses the contributions of Russian scientists on specific topics that are related to general ocean acoustic tomography problems.

Investigations that can be identified with OAT began in Russia in 1984 [14, 15, 36]. The first publication on the OAT topic dealt with numerical modeling to

optimize measurement schemes [14]. In Russia before 1984, as in the USA before 1979, much fundamental ocean acoustic tomographic research had been carried although not specifically identified with the term " tomography" [37-40]. Many Russian works from that time were related to the development of methods for noise-source-image reconstruction in layered waveguides. Additionally, the general methods for the solution of the inverse problem had also been developed in Russia before an identifiable beginning of OAT investigations [5, 6]. In particular, methods for regularizing and optimizing the solutions of inverse problems had been proposed [6, 41]. The investigations associated with the traditional idea of OAT as the reconstruction of large-scale smooth perturbations in the sound-speed profile in the ocean were also conducted [8, 36, 37]. Progress and problems of OAT were formulated and analyzed by Goncharov and Kurtepov in 1987 [23].

At the same time efforts were made towards the separation of OAT methods from the viewpoint of using different technique, such as the modal tomographic methods [42, 43], diffraction tomographic methods [2, 19-21, 34, 35, 44-51] and so on. The Doppler tomographic method has been successfully proposed to explore the bottom structure as well as the inhomogeneities at the ocean surface [43, 52]. Ocean acoustic tomography methods using complex pulse signals, synthetic apertures, and noise acoustic sources have been also studied [53-59].

Finally, the design of the hardware to carry out OAT experiments in the real ocean has been accomplished, and appropriate experimental equipment has been built [43, 52-55, 57]. A hallmark in the development was reached during the experiments in the North Atlantic in 1990 [57], where a vertical receiving array and a matched-field procedure were used for the tomographic reconstruction of the two-dimensional spatial distribution of sound-speed perturbations.

Through the mutual understanding of the contributions, that have been and are still to be made by the partner countries science programs to achieve a better understanding of real ocean processes, an effective use of the available resources can be reached through cooperative international programs in the large-scale monitoring of the global ocean by using OAT [17, 54, 57, 60]. This work is dedicated to fostering this better understanding.

Chapter 2:

PRINCIPLES AND METHODS OF OCEAN ACOUSTIC TOMOGRAPHY

2.1 THE GENERAL SCHEME OF OCEAN ACOUSTIC TOMOGRAPHY

In building a general scheme for different ocean acoustic tomographic methods, a broad interpretation of OAT will be used. In this chapter, along with the common methods interpreted as tomographic, such as pulse probing with the use of received pulse travel-time delays and intensity for reconstruction purpose, other acoustic inversion methods known and used before the formal development of the OAT concept will be discussed. Also, several new ideas closely associated with inverse problems, will be introduced. Essentially the only distinction between the term "*Ocean Acoustic Tomography*" and the term "*Acoustical Oceanography*," which is commonly used in the underwater acoustics community today to imply the use of acoustics to study the oceans, is the additional implication that the former is firmly based on the inversion of an integral equation. Here we shall explore the middle ground between acoustical oceanography and the general inverse problem applied to the ocean. From this point of view the terminology and principles for the classification of OAT methods are a little more general than usually assigned to it.

To illustrate the application of tomography to the ocean problems, let us consider the solution of the integral equation (1.1), which was described in the first chapter. Equation (1.1) can be classified as the Fredholm integral equation of the first kind. Depending on the nature of the kernel, $\psi(\boldsymbol{R},t;\boldsymbol{r},\tau)$, the inverse problem can be either well-posed and solvable or ill-posed and non-solvable. In practical situations the objective of OAT is to redefine the problem so that Eq. (1.1) can be solved. The set of measured data, $\varphi(\boldsymbol{R},t)$, associated with the kernel is called the "*tomographic projection*." Tomographic projections can have forms depending on the scheme of tomographic observation and the structure of the ocean waveguide. The various forms have some basic properties. However, they represent the path-integrated characteristics of inhomogeneities. Thus, they describe the observed object on average for the given parameters of measurement scheme (e.g., angles of observation or frequency of insonifying wave).

2.2 SOME FEATURES OF THE SOLUTION OF TOMOGRAPHIC PROBLEMS IN THE OCEAN

A simple tomographic scheme, involving an object producing nonuniform losses for acoustic waves propagating through it, can be formulated as follows. The

observed object, $g(r,\tau)$, is reconstructed by using a set of M projections, which correspond to propagation along a set of ray paths, l_i. Equation (1.1) can be reduced in this case to

$$\int_{l_i} g(x,y)dl = \varphi_i, \quad i = 1,\ldots,M, \tag{2.1}$$

where φ_i is the measured integrated loss for the ray crossing the inhomogeneity, $g(x,y)$, along the ith trajectory. The classical tomographic method for the solution of Eq. (2.1) is the inversion method developed by Radon [1]. However, here another method will be used to illustrate problems that are relevant to OAT. Equation (2.1) can be presented as a system of linear algebraic equations (SLAE) if the observed inhomogeneity can be segmented into N cells along the ith path, where within the jth cell, $g_j = g(x,y)$ can be assumed to be constant. Then equation (2.1) becomes:

$$\sum_{j=1}^{N} D_{ij} g_j = \varphi_i, \quad i = 1,\ldots,M, \tag{2.2}$$

where D_{ij} is the length of the ith trajectory within the jth cell.

Since the solution of an SLAE should be definite and stable, the method of measurement and the system of basic functions must be optimized. *A priori* information about the unperturbed medium, as well as the hypothetical structure of the observed object, can be used to accomplish this optimization. The absence of *a priori* information can lead to ambiguity in the solution. Equation (2.2) usually represents a non-correctly stated problem, so direct inversion of the matrix for the appropriate SLAE is ineffective. To resolve similar problems in OAT, analytical solutions of the integral equation are used. Analytical solutions can be obtained if the conditions of the problem allow for simplifications or by the use of methods of algebraic reconstruction under regularizing algorithms, such as the method of Maximum Entropy [5, 12, 23, 41, 51].

2.3 CLASSIFICATION OF OAT SCHEMES

Different tomographic methods have been proposed for the reconstruction of object structures in ocean waveguides. These methods are distinguished by the characteristics of an unperturbed waveguide and its inhomogeneities and by the acoustic systems and methods employed. Inhomogeneities with different space-time scales can be reconstructed by appropriate tomographic methods using the peculiarities of acoustic-wave propagation in ocean waveguides and wave interaction with observed inhomogeneities.

For the purpose of OAT classification, we re-group oceanic inhomogeneities (cf. section 1.4) into two broader classes: a) large-scale inhomogeneities (synoptic and gyro-scales with characteristic lengths $L \geq 100$ km) and b) small-scale inhomogeneities

(micro- and meso-scales with characteristic lengths $L \leq 100$ km). It is important to mention that oceanic inhomogeneities are usually anisotropic with respect to the horizontal and vertical planes, with the horizontal scales being significantly larger. The gradients of the acoustic property for the large-scale class are generally smaller than those for the small-scale class. To investigate the large-scale inhomogeneities, low frequencies ($f \leq 1$ kHz) are required for the long-range propagation. Higher frequencies ($f \geq 1$ kHz) can be used for the small-scale class since ranges of interest are shorter. In combination, the gradient of ocean property and applicable frequency ranges (see inequality (1.3)) suggest an additional degree of freedom in classifying OAT schemes as discussed below.

Adiabatic Approach for Weak Inhomogeneities. The condition for application of the adiabatic approach can be expressed by the following inequality [24, 31]:

$$D_h \ll L, \tag{2.3}$$

where D_h is the horizontal length of the complete ray cycle or the horizontal scale for the interference pattern of two waveguide modes. Large-scale inhomogeneities satisfy inequality (2.4), and the transformation of energy among rays or waveguide modes during the acoustic-field interaction with the inhomogeneity is negligible for this class, so that the adiabatic approach can be applied.

Diffractive Approach for Strong Inhomogeneities. On the contrary, small-scale inhomogeneities do not satisfy inequality (2.3) and create a significant transformation of energy among modes. They can induce perturbations in the vertical plane as well.

However, the classification into these categories is not fixed. In shallow water, for example, adiabatic techniques can be applied for horizontal cycles, D_h, less than 10 km. In deep water, where $D_h \approx 50$-70 km is possible, diffractive techniques can be used.

The differences between adiabatic and diffractive approaches from the viewpoint of OAT determine the schemes of tomographic observation and the set of measured values. Time delays and losses of acoustic signals are appropriate for adiabatic methods. Complex amplitudes of diffracted and scattered waves are used for diffractive methods.

It is important to note that inhomogeneities of various scales exist simultaneously in the ocean. They can also change randomly in time. Generally, when conditions and scales are quite random in space and time, some particular inhomogeneity is an object of interest and the rest is considered as noise. Often a statistical approach is required to solve this kind of problems.

Statistical Approach for Temporally Random Inhomogeneities. Some oceanic inhomogeneities move or change quickly and randomly. In this case a statistical analysis of the received information is necessary. The effectiveness of the statistical approach depends on the space-time scales of the oceanic inhomogeneities and those

of the observing tomographic system. The use of the statistical approach for tomographic reconstruction does not significantly change the scheme of measurements.

The general problem of tomographic reconstruction in the ocean is the separation of information about observed inhomogeneities from measured data. This problem can be solved by using *a priori* information about the space-time characteristics of the particular inhomogeneities for creating the appropriate reconstruction algorithms [18].

Before discussing different tomographic scheme, we should note that the structure of unperturbed ocean waveguides can also influence the classification of OAT methods significantly. First, the mode or ray basis of tomographic algorithms depends on the nature of the ocean waveguide. Accordingly, the ray and mode approaches can be used to investigate both adiabatic and diffraction OAT methods. Thus, numerous combinations of the classes of methods can be found in the literature, including the *ray adiabatic method* [14, 15, 23], the *mode adiabatic method* [36, 42, 61-64], the *interference adiabatic method* [50, 65], the *differential method* [2, 18, 46-50], the *location methods* [18, 66, 67], the *ray-diffraction methods* [9, 27, 30, 67-73], the *Doppler method* [43, 52, 74, 75], the *Fresnel method* [34, 35, 76-80], and, finally, the *diffraction method with partially coherent insonification* [81, 82]. The last method can be used for reconstruction of both regularly and randomly distributed inhomogeneities in the ocean.

In addition, it is important to distinguish between the two most general groups of OAT methods: *Emission Tomography* and *Transmission Tomography*. There is a third general group which is termed "*Partially Coherent Acoustic Tomography.*" This latter group is somewhat of a hybrid between the first two. These categories will be introduced in the next several sections but covered in greater detail in later chapters.

2.4 TRANSMISSION OCEAN ACOUSTIC TOMOGRAPHY METHODS

The first and most often applied OAT scheme is called the "*Transmission Tomography Method.*" In transmission tomography CW signals are usually used. The received signal amplitude, phase, intensity, travel time, or space-time coherence (for randomly distributed oceanic inhomogeneities), as well as the parameters of complex pulse signals after matched filtering, can be used to extract information about inhomogeneities [48, 50, 66]. Transmission tomography can be either adiabatic or diffractive.

Unlike Eq. (1.1), the integral equation for transmission tomography has an additional term, $\varphi_0(\boldsymbol{R},t)$, which describes the direct illuminating wave in the region of measurement. Then, we arrive at the Fredholm integral equation of the second kind

$$\varphi(\boldsymbol{R},t) = \varphi_0(\boldsymbol{R},t) - \int\int \psi(\boldsymbol{R},t;\boldsymbol{r},\tau) g(\boldsymbol{r},\tau) d\tau\, d\boldsymbol{r}, \tag{2.4}$$

which usually has a stable solution.

It can be shown that the kernel of Eq. (2.4) is dependent on the observed inhomogeneity, $g(r,\tau)$, for refractive as well as boundary types of inhomogeneities. This condition makes the transmission-tomography problem nonlinear. A series of approaches and algorithms are used to linearize Eq. (2.4) for certain conditions [12, 23, 41, 44]. The order of non-linearity is closely associated with the strength of the inhomogeneity. For relatively weak inhomogeneities, which satisfy the Born or Rytov approximations, the problem can be linearized with satisfactory accuracy [41, 44].

When the scattered waves are of the order of the illuminating waves, multi-scattering processes may be important, and Eq. (2.4) remains nonlinear. Different iteration methods have been proposed to solve the nonlinear tomographic problem. One method involves successive Born approximations using prior approximations as the solution of Eq. (2.4) in successive iterations [83]. Another method uses *a priori* information about the unperturbed ocean waveguide, which provides the possibility of reducing the nonlinear problem to the problem with weak inhomogeneities. Thus, to overcome the non-linearity difficulties in the ray-type OAT, an initial model of the ocean with inhomogeneities can be used. An example of this approach is the tomographic reconstruction of ocean eddies [23].

The kernels Eqs. (1.1) and (2.4) are determined by the Green's function of ocean waveguides, by OAT algorithms, and by description of waves in the ocean. Therefore, the Green's function of the unperturbed waveguide is considered as *a priori* information, which can be used for the construction of OAT algorithms. The accuracy of the unperturbed waveguide description determines the tomographic reconstruction efficiency. As was mentioned, the ray or mode approaches are usually used for the description of acoustic waves in ocean waveguides. These approaches are based on the sets of *a priori* hypotheses concerning the ocean waveguide structure in the given observation region. For example, as *Fresnel Tomographic Reconstruction* has shown interference among waveguide modes leads to multiple images of a single, spatially localized inhomogeneity if the free-space Green's function is put into the reconstruction algorithm [35]. Accordingly, *a priori* solution of propagation and scattering problems for ocean waveguides can play a key role in obtaining accurate solutions of problems associated with tomographic reconstruction in the ocean [11, 41, 44, 48].

From a practical point of view, the measurements of tomographic projections can be accomplished by using spatially distributed receiving arrays of hydrophones as well as receiving antennas with synthetic apertures generated by the mixing of the illuminating acoustic sources and/or receiving arrays. Tomographic methods using synthetic apertures are called "*Tomosynthesis*" or "*Dynamic Tomography*" [14].

It is clear that the measurement time in tomographic experiments is limited by the stationary time of observed object or of the intervening medium. This last remark is related to tomographic reconstruction of randomly distributed ocean inhomogeneities, like surface waves, turbulence pulsations, and so on. Appropriate schemes and algorithms have been proposed to solve such problems [46, 52, 59]. The schemes of tomographic measurements for randomly distributed oceanic inhomogeneities are practically the same as for deterministic ones, but the algorithms have some specific features. According to the nature of random inhomogeneities, statistical moments, e.g., coherence function or intensity are exploited in the

reconstruction algorithms. The projection equation for intensity of acoustic signals can be represented in the following form:

$$|\varphi|^2 - |\varphi_0|^2 = \int\int \psi(\boldsymbol{R},t;\boldsymbol{r}_1,\tau_1)\psi^*(\boldsymbol{R},t;\boldsymbol{r}_2,\tau_2)\langle g(\boldsymbol{r}_1,\tau_1)g^*(\boldsymbol{r}_2,\tau_2)\rangle d\tau_1 d\tau_2 d\boldsymbol{r}_1 d\boldsymbol{r}_2, \qquad (2.5)$$

where <..> denotes statistical averaging, and $\tau_2 - \tau_1$ and $\boldsymbol{r}_2 - \boldsymbol{r}_1$ determine temporal and spatial shifting, respectively, for the *Space-Time Correlation Function* (coherence function) calculation. Equation (2.5) follows from the assumptions that the direct and scattering waves are not spatially and temporally correlated (are not coherent), and the Born approach is satisfied. According to Eq. (2.5), in this case tomographic reconstruction reduces to the reconstruction of a power spectrum or coherence function of the inhomogeneity using the measurements of the intensity of scattered waves [48].

This type of OAT usually implies the presence of special acoustic sources for the illumination of observed objects. Information about observed inhomogeneities is contained in acoustic signals interacting with objects, in particular, in measured time delays for adiabatic methods and in complex amplitudes of diffracted waves for diffractive methods. According to the peculiarities of the interaction of acoustic waves with oceanic inhomogeneities, two types of transmission OAT methods can be singled out. They are the subjects of the following two sections.

2.4.1 Methods for the Reconstruction of Synoptic and Gyro-Scale Inhomogeneities

Ray, Mode, and Interferometric Tomographic Methods will be discussed here to continue the classification of OAT methods based in the adiabatic approach for the reconstruction of synoptic and gyro-scale inhomogeneities.

Ray tomographic reconstruction of spatial distributions of the sound speed and ocean currents is based on observing changes in time delays of short acoustic pulses propagating along the ray trajectories. A model of the unperturbed medium has to be specified to provide linearity in the integral equation, Eq. (2.5), connecting the measured time delays with small perturbations of sound speed or current distributions. To solve similar problems using the mode-type method (assuming the modal description of propagation in a waveguide), variations of received signal phase or travel times are used [36, 42]. A two-dimensional cylindrical surface with its normal directed along the ray trajectory in the horizontal plane represents an integration domain in the integral equation for this case. A peculiarity of this approach is a possibility to factoring the kernel of the integral equation, which can be presented as a product of functions for horizontal and vertical coordinates, respectively. Accordingly, the procedure of tomographic reconstruction is also reduced to two steps. First, the horizontal structure is reconstructed. Secondly, the vertical structure for the fixed horizontal plane is restored. It is clear that the mode tomography method is based on modal selection by an array itself or by using a filtration in the time or frequency domains.

The differences between measured characteristics in the mode and ray tomographic methods lead to the differences in the application for solutions of practical problems. The ray method is more convenient for application in the deep ocean, while the mode method can be effectively used in shallow water or subsurface waveguide channels.

The interference structure of the sound field in the ocean in the spatial domain is used by the interferometric OAT method for tomographic reconstruction of variations in sound speed. Perturbations in modal phases are determined by measurements of the perturbations of the interference structures of the acoustic field. Similar to the mode method, the kernel of the integral equation is also factorized for the interferometric method simplifying the reconstruction procedure. The general classification of tomographic methods, based on are the adiabatic approach, is shown in Table 2.1.

TABLE 2.1. ADIABATIC METHODS OF OCEAN ACOUSTIC TOMOGRAPHY

METHOD TYPE	OBJECTS	RECONSTRUCTION	MEASUREMENT
ray	synoptical and gyro-scale inhomogeneities	sound-speed distribution	ray pulse temporal delays
mode			modal pulse temporal delays, mode phases
interferometric			field interference structure

2.4.2 Methods for the Reconstruction of Meso- and Micro-Scales Oceanic Inhomogeneities

Using the classification of oceanic inhomogeneities, discussed in Chapter 1, one can single-out deterministic spatially localized and randomly distributed inhomogeneities of meso- and micro-scales in the ocean. Then, one needs an appropriate description or model that leads to differences in the algorithms for reconstruction and in schemes of tomographic measurements.

The classification of tomographic methods for reconstruction of such oceanic inhomogeneities can be based on different approaches that are used for the solutions of appropriate scattering and diffraction problems [3, 49]. It is usually necessary to separate weak and strong inhomogeneities. A method based on the Born approximation is used for weak inhomogeneities that are characterized by the small scattered field relative to the incident field [8, 31]. The Rytov approximation can be used to solve the tomographic problem for large smooth inhomogeneities [30, 31].

The space-time coherence function for the scattered waves should be used for tomographic reconstruction of space-time distributions of local frequency-angle inhomogeneity spectrum. Differences in the form of the integral equations are determined by the structures of oceanic inhomogeneities. The region forming the scattered signals for smooth meso-scale inhomogeneities is displaced along the path connecting the source of the illuminating waves and the receiving system. The approximate condition, when the refraction of probing waves in the horizontal plane can be neglected, is determined by the inequality $q_s < q_p$, where q_s is the characteristic width of diffracted patterns of the scattered waves in the horizontal plane and q_p is the angular resolution of observation systems. The direct-illuminating waves masks the scattered field in this case. Reduction of this effect is necessary for successive tomographic reconstruction. There are several approaches for resolving this problem. For example, in the *Differential Tomography Method* the excited modal spectrum is strongly displaced relative to the measured modal spectrum [46, 49]. Other techniques involving different methods of space-time filtering are discussed in [74, 75]. It is interesting to note that this problem can also be solved by using natural shadow zones in ocean waveguides, which are the result of the peculiarities of acoustic waves propagation in a stratified ocean [77].

TABLE 2.2. DIFFRACTION METHODS OF OCEAN ACOUSTIC TOMOGRAPHY

METHOD TYPE	OBJECTS	RECONSTRUCTION	MEASUREMENT
ray	internal waves	averaged characteristics	ray pulse time delays
mode	surface inhomogeneities	local spectrum	modal phases
differential	meso-scale inhomogeneities		intensity, modal time delays
location	micro-scale inhomogeneities		intensity, pulse delays
Doppler	surface waves, bottom inhomogeneities	wind speed, heights of inhomogeneities	losses, frequency shift

Refraction of acoustic paths in the horizontal plane can not be neglected for the case of micro-scale oceanic inhomogeneities (when $q_s > q_p$). In this case the separation of the scattered signals from the direct-field background can be accomplished by using the space-time filtering [3, 46, 49, 66]. This reconstruction approach requires strong inhomogeneities and some *a priori* knowledge about them [3, 41, 44]. Similar

problems arise for tomographic reconstruction of the spatially localized objects [70, 75].

For the case of randomly distributed oceanic inhomogeneities, a regular interference structure between the illuminating and scattered waves exists. This fact can be used for tomographic reconstruction [75-80]. The solutions of integral equations for such inhomogeneities are determined by the coefficients of the mode-interaction matrix used for reconstruction of the characteristics of inhomogeneities [75, 76].

Table 2.2 shows the classification scheme for diffraction OAT methods.

2.5 EMISSION OCEAN ACOUSTIC TOMOGRAPHY METHODS

The *Emission Tomography Method* is used for the observation of natural acoustic sources, for example, ocean noise sources [58]. However, man-made, but non-intentional, sources such as ship noise can be considered as sources for emission tomography as well. According to this method, space-time distributions of such acoustic sources in ocean waveguides are reconstructed by using tomographic algorithms to process data measured by spatially distributed receivers or by synthetic aperture receiving systems placed far from the observed objects. Information about acoustic sources is extracted from the space-time coherence functions. As a rule, measurements are carried out for a wide frequency band. Tomographic reconstruction in this case is reduced to the solution of the projection integral equation, Eq. (2.1). Such equations represent non-corrective problems.

Three types of emission tomography can be defined tentatively with respect to distances from the observed sources to the receiving system. Reconstruction of the details of complex radiating noise sources (for example, ships) from near-field measurements is the emission tomographic scheme of the first type [84, 85]. The difficulties associated with this type of tomographic problems concerns dealing with non-propagating acoustic-field components, which are important in the near field of complex acoustic sources. The second type of emission tomography is associated with the reconstruction of the space-time distribution of noise sources for mid-range distances (for example, a distribution of noising ships near ports or a bubble cloud below the sea surface) [86]. Finally, the third type is the reconstruction of low-frequency natural noise sources in the ocean, which determine the noise background in the ocean and put limitations on the tomographic system performance [58].

Emission tomographic methods work without special sound illuminating sources, so the measurement scheme is easier to fulfill. But appropriate algorithms can be more complicated because of the noise nature of the observation objects and the necessity of processing the signals in a wide frequency band.

Usually, emission tomography is associated with the solution of the problems involving reconstruction of spatial distributions of ocean noise sources. The robust processing algorithms used in the technique require measurements of the noise field from two or more spatially distributed receivers to allow for the variation of the observation angles [58, 85, 86]. The common models of ocean noise sources for emission tomography include sources spatially distributed in the horizontal plane and

non-coherent point sources with certain directivity patterns in the vertical plane [87-89]. The properties of the integral equation in this case are determined by the displacement of the noise source and by the number of excited waveguide modes. The kernel of the integral equation can be factored with respect to horizontal and vertical coordinates. In some cases, the two-dimensional distribution of noise sources can be reconstructed, for example, if the source does not have a spatial dependency in its frequency spectrum [58].

2.6 PARTIALLY COHERENT ACOUSTIC TOMOGRAPHIC METHOD

There is an interesting aspect of transmission OAT associated with the application of noise acoustic sources, natural or artificial, in the design of tomographic observation systems [81, 82]. This then introduces a tomographic concept, the *Partially Coherent Tomographic Method*, that is a hybrid of transmission and emission tomographic methods. A statistical description is necessary for the partially coherent (PC) method but, unlike the transmission method, this method can be used without the special illuminating acoustic sources. Investigations on this method are in their initial stages of development, but indications are that the method holds promise for new interesting possibilities for OAT.

Later chapters deal with each of these tomographic methods in more detail. But to close this section, let us emphasis, once more, the very important principle for the classification of tomographic schemes and, associated with them, the methods of OAT. Following this classification, OAT methods dealing with weak ocean inhomogeneities and causing only energy losses and time delays are referred to as adiabatic methods. On the other hand, if strong inhomogeneities are present, new rays or modes are created after the interaction with inhomogeneity, the OAT methods are then called diffraction methods. Both diffraction and adiabatic methods can be based on either ray or mode approaches.

Chapter 3:

ADIABATIC TRANSMISSION TOMOGRAPHY FOR GYRO-SCALE OCEANIC INHOMOGENEITIES

3.1 INFLUENCE OF LARGE-SCALE OCEANIC INHOMOGENEITIES ON SOUND PROPAGATION

Many experiments have proven that low-frequency sound can be registered at many thousands of kilometers from the source because of its very low attenuation. For example, the sound with a frequency of 50 Hz loses only 10 dB for propagation distances of 10,000 km. Furthermore, the presence of the underwater sound channel (USC) provides for a reduced loss from spreading. The Heard Island Feasibility Test, executed by Munk and colleagues in January 1991, demonstrated one more time that large-scale variability of the ocean, like large fronts, currents, and eddies of different scales up to thousands of kilometers, can be investigated with low-frequency acoustic tomographic systems [90, 91]. Figure 3.1 shows the calculated propagation path for

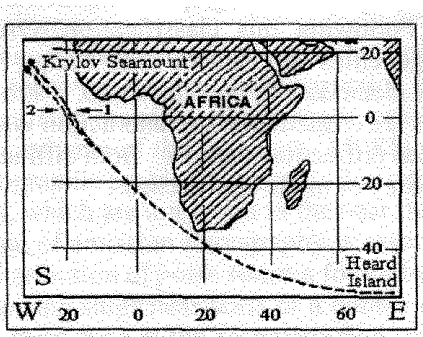

Figure 3.1. Calculated ray paths: 1-Heard Island - Krylov Seamount; 2-Heard Island - the end point of the drift of the Russian Research Vessel *Akademik Nikolai Andreev*. (Adapted from [91].)

sound waves generated in the vicinity of Heard Island in the Indian Ocean and received by a Russian listening station in the Atlantic Ocean located at a distance of approximately 12,500 km [91]. The transmitter at Heard Island was a vertical array of five sound sources with a source level of 220 dB re 1 μPa at 1 m. The propagation time to this station was about 2 hr 20 min. Each acoustic sounding from the source had a frequency of 57 Hz and duration of 1 hour. Figure 3.2 presents the acoustic signal in the time domain (in a 1-Hz band) registered by the station during one hour, in comparison with noise background measured for a silent radiating system. The result of spectral analysis, with a 0.125-Hz resolution, for the signal received by omnidirectional hydrophone at the depth of 800 m is shown in Fig. 3.3. It can be seen

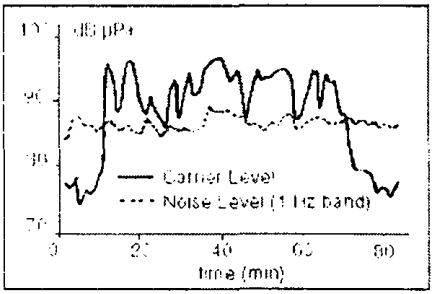

Figure 3.2. Amplitude fluctuations of CW signal. (Adapted from [91]).

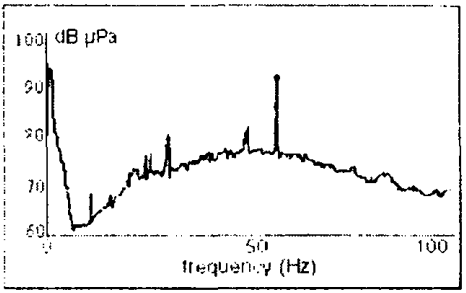

Figure 3.3. Spectrum of received signal with a 0.125-Hz resolution. (Adapted from [91].)

that the transmitted signal at the frequency of 57 Hz exceeds the surrounding noise by approximately 15 dB. (We shall return to the Heard Island experiment later.)

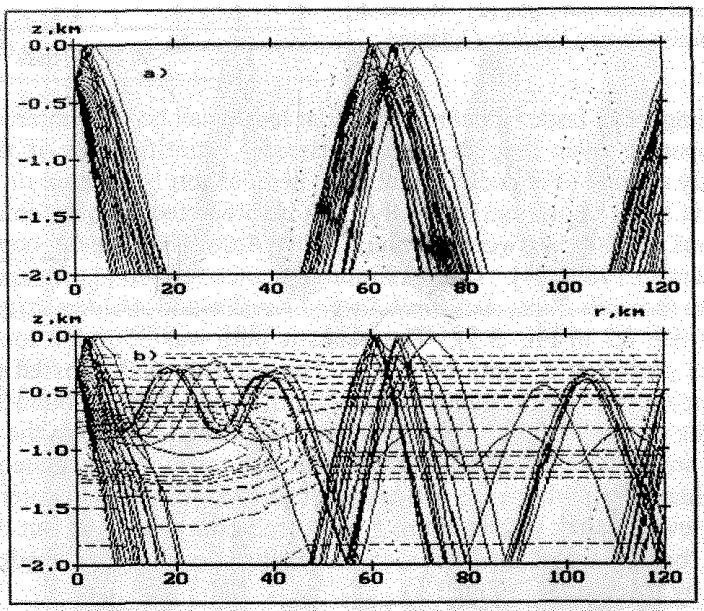

Figure 3.4. Calculated ray paths: (a) without a warm lens; (b) with a warm lens. (Adapted from [93].)

Another very important property of underwater sound propagation is its high sensitivity to even weak inhomogeneities in the water. As an illustration, we consider the influence of the underwater warm lens of Mediterranean Sea water observed southward from the seamount, *Great Meteor,* in the Atlantic Ocean by the Russian research ship *Akademik Nikolay Andreev* [92]. The diameter of the lens was approximately 60 km. The maximum deviation of the sound speed at the center of the lens (at the depth of ~ 1 km) from that of surrounding waters was 16 m/s, i.e., only about one percent. Ray-propagation paths in the water without and with a lens are

about one percent. Ray-propagation paths in the water without and with a lens are presented in Fig. 3.4a and 3.4b, respectively [93]. The source was placed at the periphery of the lens at a depth of 330 m. Sound-speed isolines are also shown in Fig. 3.4b. The lens is in the left part of the figure. We can see that a secondary USC, with its axis at a depth of 600 m, was created by the presence of the lens.

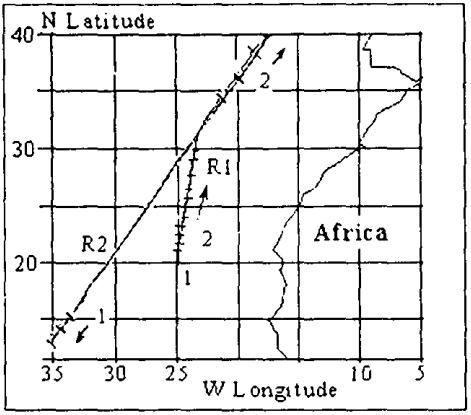

Figure 3.5. Diagram of the positions and courses of the ships on paths R1 and R2: (1)-Research Vessel *Akademik Ioffe*, (2) - Research Vessel *Akademik Sergey Vavilov*. (Adapted from [94].)

An important issue is that many similar lenses can be encountered when sound waves propagate over long distances. Besides, stratification of the ocean can significantly change over such distances. The question is whether or not the sound field retains some regular structure that can be predicted in these conditions. This question was partially answered by the *Canary Basin Experiment*, conducted by the Russian team in 1989 [94]. The maximum distance for sound propagation between two Russian research ships, *Akademik Sergey Vavilov* and *Akademik Ioffe*, was about 3500 km (path R2 in Fig. 3.5). The acoustic path was 3500 km long. A 137-Hz source was placed at a depth of 1 km. The acoustic path crossed a "tongue" of Mediterranean water with higher salinity (and, hence, higher sound speed), which started at the distance of 2800 km. The isolines of sound speed in the vertical plane of path R2 are shown in Fig. 3.6. Path R2 was extremely inhomogeneous, especially in its northern part, where the influence of the Mediterranean waters was strong. Probably, several weak internal lenses were crossed by the path, but their influence could not be registered by the measurements at sparsely placed ship stations (indicated by tick marks in Fig. 3.5).

Many vertical measurements of the sound field were taken along path R1. The result revealed that regular families of rays with high-sound intensity existed along the propagation path. These ray families have also been predicted by numerical simulation. A high-intensity ray tube was formed by the rays leaving the source (at the depth of 325 m) in the angular interval χ=[-9°,-11°]. Ray families for the horizontal distances from 900 km to 1200 km are shown in Fig. 3.7a. The regularity of these rays can be explained by the fact that the cycle lengths, L, of the rays, as a function of their emergence angle from the source, have extrema (i.e., $\delta L/\delta\chi = 0$) in this interval of angles for all distances [94]. It can be shown that the same regular families of rays exist also for path R2. Some of them are shown in Fig. 3.7b. Dotted lines correspond to non-extremal rays.

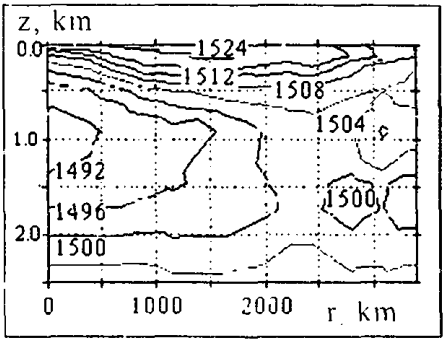

Figure 3.6. Isolines of the sound speed in the vertical plane of path R2. (Adapted from [94].)

The existence of regular predictable structures in the sound field along very long distances, even in a rather inhomogeneous ocean, gives us some hope for solving the inverse problem, i.e., to determine some important parameters of the ocean by measuring parameters of the sound field.

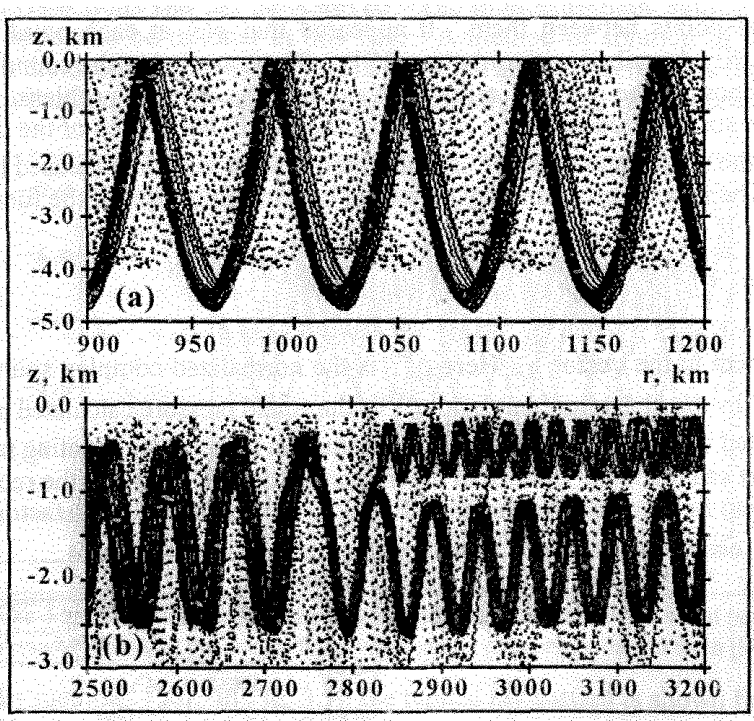

Figure 3.7. Comparison of ray families emitted in the angular interval [-9°,-11°] for: (a) path R1; (b) path R2. (Adapted from [94].)

For simplicity, we consider the two-dimensional problem in the r,z plane. Let us suppose that we have sound-field experimental data of known amplitude and phase at N points in this plane. The inverse problem consists of obtaining the most probable distribution of the sound speed, $c(r,z)$, in this plane by processing the data. The first step in solving this problem is to parameterize the field, $c(r,z)$, i.e., to describe it, most precisely, by a minimal set of parameters, and then to determine these parameters using an appropriate set of experimental acoustic data.

A common procedure to determine the field involves the use of so-called *Empirical Orthogonal Functions* (EOFs). As an example, let us consider EOFs for the *Norwegian Sea Experiment* [4, 57]. The distance between radiating and receiving ships was 105 km. The receiving ship had a 560-m vertical array with 29 hydrophones. The depth of the water column was about 1500 m. A monochromatic signal of 105 Hz was transmitted in the experiment. The vertical profile of the sound speed, $c(z)$, was measured at the source and receiver locations, and also at three additional points between them. It appeared that $c(z)$ at each point, r, can be satisfactorily described with only two EOFs. Thus, analyzing the sound field at all hydrophones of the vertical array and solving the inverse problem, we should determine six amplitudes, $q = \{q_j\}$, $j = 1,...,6$, of the two EOFs at each of the three points between the source and receiver. Linear interpolation may then be used between all points. The inverse problem may be solved by a minimization of the function

$$F(\boldsymbol{q}) = 1 - \left| \sum_{i=1}^{29} p_i^{(E)} p_i^{(T)*} \right|^2 \qquad (3.1)$$

with respect to the vector $\boldsymbol{q}$. Here $p_i^{(E)}$ is the normalized complex sound pressure measured by the ith hydrophone, and $p_i^{(T)}$ is the sound pressure calculated numerically for the fixed vector $\boldsymbol{q}$. The adiabatic approximation (i.e., non-interacting modes) was used in the calculations. Isolines of the measured (dotted lines) and the reconstructed (solid lines) field, $c(r,z)$, are shown in Fig. 3.8. Coincidence is satisfactory.

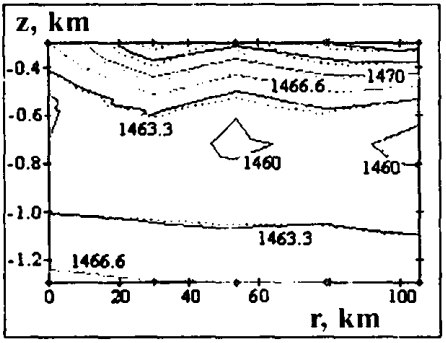

Figure 3.8. Isolines of the experimentally measured (dotted lines) and tomographically reconstructed (solid lines) sound-speed profiles for the Norwegian Sea Experiment. (Adapted from [57].)

The minimization procedure may be also applied to the function

$$F_1(q) = 1 - \left| \sum_{n=1}^{N} a_n^{(E)} a_n^{(T)*} \right|^2 \qquad (3.2)$$

instead of the function in Eq. (3.1). Here $a^{(E)}$ and $a^{(T)}$ are experimental (measured by a vertical array) and calculated (for the given vector q) amplitudes of the nth mode, respectively. Results appear to be practically the same.

3.3 OCEAN ACOUSTIC TOMOGRAPHY ON THE BASIS OF TRAVEL-TIME MEASUREMENTS

The type of experiment described above can be used effectively in the shallow water, when arrivals of sound pulses propagating along rays with different numbers of bottom reflections can not be resolved. The monochromatic source and mode approach appear to be rational in this case. A method of solution of the inverse problem in the deep ocean was suggested by Munk and Wunsch and is based on the ray approximation. This method was originally named the "ocean acoustic

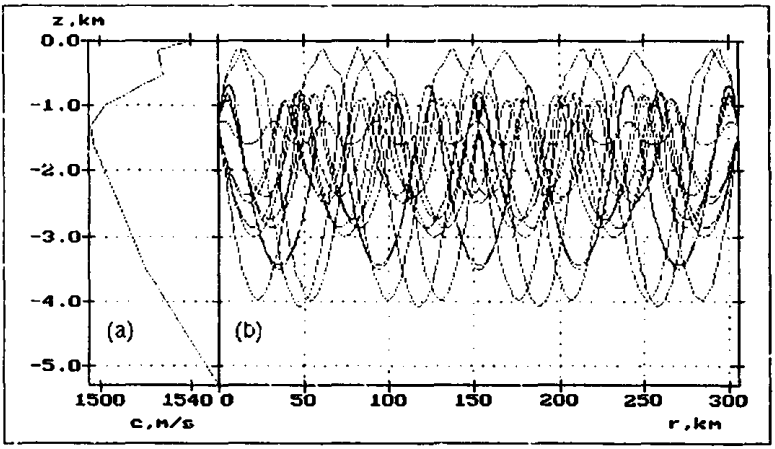

Figure 3.9. Ray propagation paths for the typical deep-water, sound-speed profile. A source is located at the axis of underwater sound channel. (Adapted from [94].)

tomography method" [16]. In Fig. 3.9b the typical ray pattern is shown for a typical deep-ocean, sound-speed profile (Fig. 3.9a) with the source, S, and receiver, R, placed near the axis of the USC. Numerous rays reach the receiver, and the travel times of the sound pulses along the different rays contain the information which we need. Considering the problem in two-dimensions again, the travel time along a particular ray, i, can be written as

$$t_i = \int_{l_i} \frac{dl}{c(r,z)}, \tag{3.3}$$

where l_i is the path taken by the ray.

Let us assume that $c(r,z) = c(z) + \delta c(r,z)$, where $c(z)$ is some known (climatic or measured at the source or receiver location) sound-speed profile, and $\delta c(z)$ determines sound-speed variations. To find $\delta c(r,z)$ using the measured travel times for different rays is a task of tomographic reconstruction. Let δt_i be the variation of t_i due to the variations δc along path l_i. If δc is small enough, we obtain from Eq. (3.3) to good precision:

$$\delta t_i = \int_{l_i} \delta\left(\frac{1}{c}\right) dl + \int_{l_i} \frac{1}{c}\,\delta(dl) = \int_{l_i} \delta\left(\frac{1}{c}\right) dl. \tag{3.4}$$

The second term was dropped since it is equal to zero by Fermat's principle. Hence, each ray gives us, theoretically, one equation for determination of $\delta c(r,z)$. Unfortunately, the arrivals of ray pulses propagating near the USC-axis are not resolvable in time and, therefore, can not be used. In typical mid-Atlantic conditions, using good data processing techniques and rational averaging over time, one needs only 13-16 rays. Each of these rays yields Eq. (3.4) relating δt_i to δc along path l_i.

When we wish to apply the tomographic procedure to a whole ocean region (three-dimensional case), we have to rearrange the measurement scheme. If we have N points where sources and (or) receivers are placed, we have $N(N-1)/2$ ray paths, and the number of equations for determination of the parameters of the medium increases significantly. Of course, the three-dimensional function $\delta c(x,y,z)$, which we seek, must be parameterized in some way. Usually, however, the number of equation appears to be less than the number of parameters describing the medium, so that some kind of *a priori* information about the function, $\delta c(x,y,z)$, should be taken into account for these cases (see the example of numerical modeling discussed below).

Acoustic tomography of ocean currents can also be based on travel-time measurements. In a moving range-independent ocean we have for the propagation time along the ith ray between points A and B

$$t_{iAB}^{\pm} = \int_{l_i^{\pm}} \frac{dl}{c(z) \pm u(z)}, \tag{3.5}$$

for a transmission in the positive(+)/negative(-) r-direction, respectively. A transceiver (source and receiver) is located at both the starting point and end point; $u(z)$ is the flow-velocity component along the ray in the positive r-direction. The integration paths, $l_i^{\pm}$, are along the trajectories of the ith ray and are generally functions of $c(z)$ and $u(z)$. It can be shown that the path geometry is reciprocal to order $u/c \ll 1$, hence $l_i^{+} = l_i^{-} = l_i$. The half sum and difference of reciprocal travel times are defined by

$$s_i = \frac{1}{2}(t_i^{AB} + t_i^{BA}) = \frac{1}{2}(t_i^{+} + t_i^{-}) = \int_{l_i} \frac{c}{c^2 - u^2}\, dl, \tag{3.6}$$

$$d_i = \frac{1}{2}(t_i^{AB} - t_i^{BA}) = \frac{1}{2}(t_i^{+} - t_i^{-}) = -\int_{l_i} \frac{u}{c^2 - u^2}\, dl. \tag{3.7}$$

Usually, c and u are of order 1000 and 0.1 m/s, respectively, so u^2 can be neglected in the denominator. The difference travel time is a small fraction of the one-way travel time. Therefore, c is well determined by one-way travel times in either direction from the ray approximation.

In tomographic algorithms we are often more interested in the travel-time perturbation, δt, from a previous measurement, or from a value inferred for the climatic ocean mean. Linearization of Eq. (3.6) and (3.7) yields

$$s_i = \int_{l_i} \frac{1}{c}\, dl, \quad \delta s_i = -\int_{l_i} \frac{\delta c}{c^2}\, dl, \quad d_i = -\int_{l_i} \frac{u}{c^2}\, dl\,. \tag{3.8}$$

The value δc is of order 10 m/s and is still large compared with u. As before the variations, δc, are well determined by one-way travel time in either direction. However, measurements of u require the use of travel-time difference. We can conclude that by making transmissions in opposite directions along a propagation path, the effects from sound-speed variations and water-flow velocities can be separated.

The first full-scale tomographic experiment was accomplished in 1981 for a two-month period in a 300-km square at 26° N, 70° W in the North Atlantic [95]. The basic design consisted of four sources on the western side of the square and four receivers on the east. A fifth receiver was placed near the northern boundary. All instruments were placed at a nominal depth of 2000 m. The source transmitted a phase-coded, linear-maximal-shift-register sequence on a 224-Hz carrier. During the experiment, three CTDs (conductivity, temperature, depth) and two AXBTs (aircraft-deployed expandable bathythermograph) surveys were carried out. The primary goal of the experiment was to evaluate the effectiveness of purely acoustic measurements in mapping a three-dimensional ocean volume as a function of time. Conventionally obtained environmental data were intended to be used as a reference ocean model, and also to provide a test and measure of the accuracy of the applied tomographic techniques. Unexpectedly, it was found that the environmental data contain information independent of the acoustical observations (and *vice-versa*). Thus, the best possible reconstruction of the three-dimensional ocean can be made by combining all the data — acoustic plus environmental — in the inversion procedure.

The difficulties in the experiment were numerous. To resolve as many arrivals reaching the receiver by different paths as possible, a broadband acoustic signal (with a 5.4-Hz frequency band and 31.25-ms sampling interval) was generated. Travel-time fluctuations caused by the meso-scale ocean variability were masked by other sources of travel-time variance. Mooring motion and clock error were explicitly accounted

for and corrected to a large extent in the inversion procedure. Other travel-time perturbations (for example, fluctuations due to internal waves) are lumped together as random errors. Finally, the signal bandwidth, the sampling rate, the environmental signal-to-noise ratio, and ocean physical effects allowed resolution of ray-multipath arrivals with delay time between two sequential ones longer than 90 ms.

Results of this experiment were rather encouraging, but also highlighted some important problems, which were taken into account in future experiments. The tomographic maps described correctly the main features of meso-scale variability of the ocean. The maps showed that at the beginning of the experiment there was a region of low sound speed (with a 10-m/s sound-speed decrease corresponding to a -2.0 ° C temperature drop) centered within the box. As time passed, this weak eddy moved to the West. The southeast region was initially warmer, replaced by colder water toward the end of the experiment. This was a region of high expected mapping error. Examination of the environmental surveys showed the same features that were seen in the tomography. The tomographic data inversion produced useful spatially averaged profile maps. Although the array configuration was adequate for producing maps of meso-scale features, the poor travel-time resolution (because of the limited bandwidth) caused large errors that prevented going much beyond pattern recognition. Meso-scale variations were mapped with an average accuracy of about 1.5-2 m/s (about 0.3-0.4 ° C).

The *Reciprocal Transmission Experiment* in 1983 [96] overcame the principal shortcoming of the limited bandwidth of the 1981 acoustic sources. Sources with increased bandwidth significantly improved the resolution of rays and the accuracy of the travel-time measurements. This improved accuracy allowed for a more stringent measurement of differential travel time to obtain absolute current velocity (rather than sound speed only). The two-way, reciprocal-sound-transmission method was used to determine the current velocity, $u(z)$. The experiment took place west of Bermuda during August and September.

Acoustic transceivers were placed near the USC-axis (1300 m) with a distance between them of 300 km. They sent and received signals every two hours for 21 days. Travel times along 13 rays in each direction were used for the reconstruction. Ray paths in opposite directions were found to be nearly reciprocal, and effects due to internal waves and mean currents were small. Travel-time sums were inverted to obtain sound speed at two-day intervals, and differential travel times were inverted to obtain absolute current velocity (see Eq. (3.8)). The ocean model for currents consisted of the first three quasi-geostrophic modes with the range dependence given

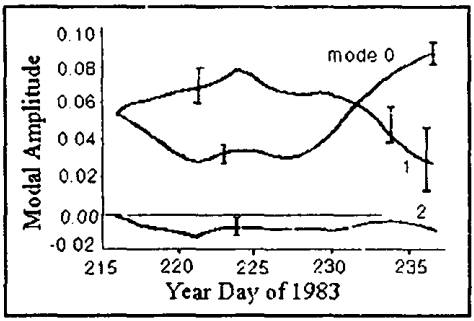

Figure 3.10. Range-averaged current velocity mode amplitudes versus time. Error bars are shown. (Adapted from [94].)

by sines. The three range-averaged mode amplitudes versus time are plotted in Fig. 3.10 with error bars shown. One can see that the second baroclinic mode amplitude does not differ significantly from zero, although it is responsible for the small perturbations in the profiles near the surface. The first baroclinic mode amplitude decreases by a factor of two over the course of the experiment. This variation is associated with the change in separation of the differential travel-time data between the shallow turning rays and the deep turning rays. The error in the first baroclinic-mode amplitude is large because it is determined primarily by the rather uncertain travel times associated with the shallow turning rays. The barotropic mode (mode 0) amplitude increases by a factor of three. The error for the range-averaged barotropic mode is smaller than the error on the first baroclinic mode amplitude because data from all the rays contribute. The results agrees favorably with XBT and AXBT surveys.

It is important to emphasis that reconstruction of ocean currents by solving Eq. (3.8) can be done if ray paths in opposite directions are very nearly reciprocal, i.e., ray tube separation in space is small compared to the scale of medium inhomogeneities. Tomographic reconstruction of flow velocity in powerful currents, where the last condition may not be true, was considered by Godin, et al. [97]. An interesting non-perturbative approach to the problem was discussed there.

The experiments on ocean acoustic tomography, described above, have shown promising perspective for measuring small temperature variations over long distances and for measuring ocean currents in large regions. Appealing applications are possible with the use of a three or more transceiver arrays. With a three-transceiver array, the areal-averaged relative vorticity can be measured [98]. With five or more transceivers, one can directly measure not only the gradients of the relative vorticity but also its Laplacian and thus attempt to balance the potential-vorticity equation [99].

3.4 NUMERICAL SIMULATION IN OCEAN ACOUSTIC TOMOGRAPHY

Numerical simulation for OAT is very useful in many respects, particularly, in the evaluation of:

a) The limits of applicability of linear theory of reconstruction, when terms of order u^2 can be neglected in Eqs. (3.8); and
b) The stability and precision of the reconstruction procedure when some parameters (for example, experimental data used for reconstruction) are known with restricted precision or may fluctuate.

Several numerical techniques for tomographic reconstruction were developed at the Shirshov Institute of Oceanology [100, 101]. A warm eddy observed in the southwestern part of the Sargasso Sea was studied with one of the techniques. The diameter of the eddy was 200 km. The sound speed at its center (at a depth 500 m) was 6 m/s higher than in the surrounding medium. Different positions of the eddy between the sound source and receiver (each at a depth of 1000 m) were considered,

and each time its center was supposed to lie along the path between the source and the receiver, which were 200 km apart. A parameterization of the medium was accomplished by introducing a grid in both the vertical and horizontal directions, with linear interpolation inside each triangular cell. Only two-dimensional situations, when the source and receiver were in the same vertical plane, were been considered. Travel times from the source to the receiver along 14 rays were used as the projections for tomographic reconstruction. The number of unknown parameters in the inversion procedure was greater than the number of equations. Nevertheless, it appeared that, using Tikhonov's regularization method [102] and quite natural *a priori* information, rather satisfactory reconstruction of the medium can be achieved. An rms error of reconstruction was 0.5-0.7 m/s depending on the position of the center of the eddy. Solid lines in Fig. 3.11 are the initial sound-speed isolines, whereas the dotted ones are reconstructed values of the sound speed for the case when the center of the eddy was exactly at the middle between the source and the receiver (the error of reconstruction was minimal in this case). The inversion procedure appeared to be stable when the random error in travel-time measurements did not exceed 15 ms.

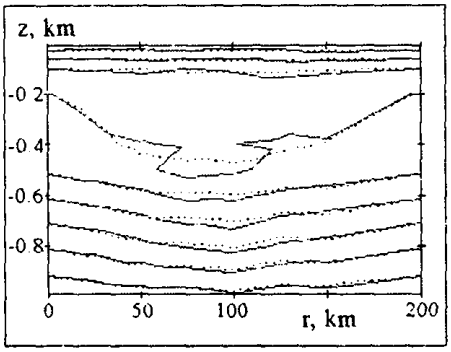

Figure 3.11. The warm eddy reconstruction: solid lines - isolines of the measured sound speed profile; dotted lines - isolines of the reconstructed sound speed profile (Adapted from [100]).

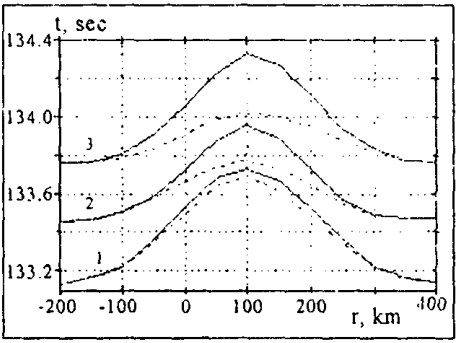

Figure 3.12. Calculated ray travel times versus a location of the Gulf Stream Center: solid lines - exact ray approach; dotted lines - linearized theory (Adapted from [100]).

The linear inversion used in the example fails when the variations, $\delta c(r,z)$, from the mean sound speed, $c(z)$, exceeds approximately 10 m/s. This is a case in the Gulf Stream, for example, where sound-speed fluctuations can be as large as 50 m/s. The dependencies of travel times, t, for three rays on the position of the center of the Gulf Stream ring, at r, lying in the plane connecting the source and the receiver, are shown

in Fig. 3.12. The source and receiver were 200 km apart and the sound speed variation, δc, was equal to 35 m/s. Solid lines corresponds to calculations in accordance with Eq. (3.3). Dotted lines are calculations using the linearized Eq. (3.8) with $u = 0$. We can see that the linearized approach produces errors in travel time up to 50% for some cases. Tomographic reconstruction in such cases becomes much more complex.

3.5 ACOUSTIC MONITORING OF GLOBAL CLIMATE CHANGE

It is well known that increasing the concentration of CO_2, CH, and some other gases in the atmosphere causes a rise in the average global temperature of the Earth. This effect, called the "greenhouse effect," is very important to the future of the mankind. The problem of monitoring the effects of greenhouse gases in the atmosphere at some representative places on Earth has been practically solved. But, for many reasons, calculating the atmospheric temperature trend from these data is rather difficult. A prediction of the trend even from very long series of temperature measurements in the atmosphere is not very reliable due to very the large natural variability of the atmosphere.

It is also known that a significant part of the heat in the atmosphere and solar energy are directly absorbed by the ocean. Thus, direct measurements of the temperature trends in the World Ocean have become an important aspect of the global climate change problem. A significant part of proposed schemes for global climate monitoring includes OAT. The idea of acoustic monitoring of the global climate changes was suggested by Munk and Forbes [103] in 1989. The proposal gives a preference to the analysis of the temperature averaged over long planetary-scale distances in the World Ocean rather than the temperature measurements at some given points. Travel times of acoustic signals are directly related to such an averaged temperature.

The technique, proposed by Munk and Forbes, has two main advantages in comparison with atmospheric measurements. First, the natural "noise" from natural variability of the ocean is much less than that of the atmosphere, due to a larger thermal inertia of the water mass. Second, averaging can be achieved not only in the temporal domain but also in the spatial domain. Existing estimates have shown a warming of the atmosphere by 0.5°C during last 130 years. Appropriate estimates of the warming of the ocean during recent years have indicated that a change in the sound travel time has been typically 0.25 s per year over a 15,000 km distance. Simultaneously, however, meso-scale variability in the ocean causes a one-order higher fluctuations of the travel time. Calculations have also demonstrated that an acoustic experiment of 10-year duration would allow for the establishment of the general temperature trend.

Working Group 96 of the Russian Scientific Committee on Ocean Research has concentrated its efforts on a wide program of ocean acoustic monitoring. The scientific communities of many countries have declared their intentions to participate in this project. Success of the Heard Island Feasibility Experiment [104, 105] was very encouraging in establishing a proposed course of action. The general picture of

acoustic paths from Heard Island to the Indian, Atlantic, and Pacific Oceans are presented in Fig. 3.13. From this illustration one can get an impression about the distances that are present in the problems as they relate to the global monitoring of the ocean.

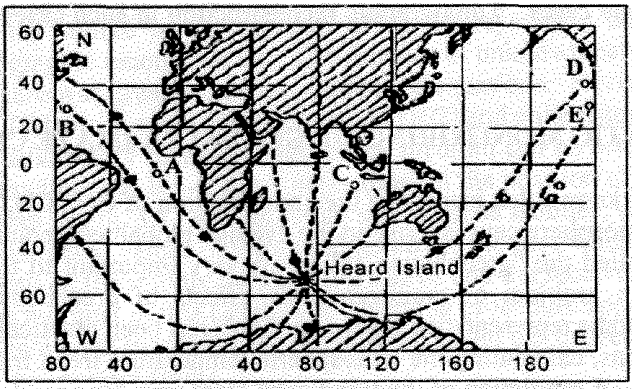

Figure 3.13. Calculated propagation paths from Heard Island to receivers at Ascension (A), Bermuda (B), Christmas (C), Oregon (D), and California (E). (Adapted from [91].)

Some principal problems must be solved before the project can establish a real start. These problems can be separated into three groups. The first group is related to the right choice of sound transmitter and receiver locations. Ideally, one would like to have a system with gyro-scale resolution and meso-scale averaging [104]. Many acoustic paths must be present and analyzed in experiments. Among them, such exotic ones as across the Arctic Ocean (mostly under the ice cover) and from the Russian port at Vladivostok across the Pacific have been discussed.

The second group of the problems requires the development of low-frequency (50-70 Hz) arrays of transmitters and receivers that could operate with high efficiency and 10-years reliability at depths of about 1 km. Such arrays are needed to achieve the necessary acoustic efficiency of the system, as well as to insonify only the near-axis part of the USC. In this case, ocean mammals, inhabiting the upper several hundred meters of the ocean, will not be affected by acoustic signals periodically generated during the many years.

The third important problem is the development of robust algorithms for ray identification (in temporal and angular domains) after their propagation along many thousand-kilometers paths across the rather unstable ocean. The principal intellectual challenge in the algorithm design is the separation of the measured combined greenhouse and ambient-climate effects.

3.6 TOMOGRAPHIC EXPERIMENTS WITH VERTICAL ARRAYS IN THE DEEP OCEAN

The sound field in a layered or nearly layered medium far enough from the source can be represented as a finite sum of propagating normal modes. The modal description is especially convenient for low frequencies when the number of

propagating modes is small. Therefore, measured modal structure at the receiver location will contain the information about the propagation path characteristics and the source location.

To develop tomographic methods, based on the modal approach, experimental measurements of complex modal amplitudes, spanning most of the water column down to the bottom, are needed. Vertical linear arrays are suitable for this purpose. Presently, only a few publications concerning measurements of this sort are available. In particular, such experiments were carried out in shallow water [106, 107] and in the Arctic [108] and Pacific Oceans [109]. One of the main difficulties of these experiments consists of controlling, with high accuracy, the vertical configuration of the array. If this problem is solved, then we arrive at the following linear set of equations for CW signals:

$$p_n^{(E)}(r_n,z_n) = \sum_{m=1}^{M} c_m \varphi_m(z_n)\exp(i\kappa_m r_n), \quad n=1,2,\ldots N, \tag{3.9}$$

where N is a total number of receiving hydrophones, $p_n^{(E)}$ is the experimentally measured signal by the nth hydrophone, the point (r_n,z_n) defines the hydrophone horizontal and vertical coordinates (in the plane of sound propagation), $\varphi_m(z)$ is the vertical eigenfunction of the mth mode, κ_m is the horizontal modal wavenumber, and c_m is the complex excitation coefficient of the mth mode depending on the source location. The solution of this set of equations to extract the ocean parameters has been discussed in detail in Ref. [4].

As mentioned earlier, Norwegian Sea Experiment in 1990 was performed in the using a 560-m vertical receiving array with 29 equally spaced hydrophones [4, 57, 110]. The array was deployed from the ship, and its spatial configuration was monitored by a special acoustic system. The 105-Hz transmitter of the CW-signal was set at a depth of 550 m and at a horizontal distance of 105.5 km from the receiving array. The medium between the source and the receiving array was inhomogeneous. Figure 3.14 represents isolines of sound speed and the bottom bathymetry along the acoustic path.

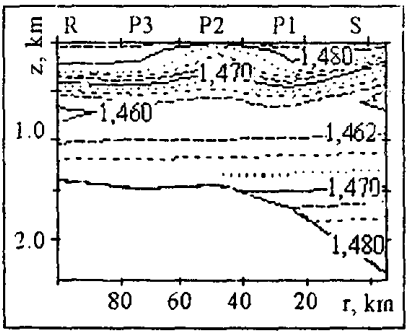

Figure 3.14. Sound-speed isolines and bathymetry for the 1990 Norwegian Sea Experiment. (Adapted from [57].)

Mode amplitudes were calculated according to the procedure described in [108]. Calculated (from the measured data but arbitrarily scaled) modal intensities, $|c_m|^2$, for the first eleven modes (the theoretically predicted number of propagating modes) are shown in Fig. 3.15 by solid vertical lines. The dashed lines correspond to mode intensities theoretically calculated from *Adiabatic Modal Theory* (AMT).

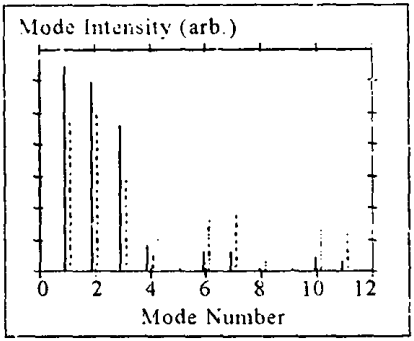

Figure 3.15. The first eleven mode intensities, calculated from measured data (solid lines) and from Adiabatic Modal Theory (dashed lines) for the 1990 Norwegian Sea Experiment. (Adapted from [4].)

For given complex modal amplitudes, c_m, the position of the source emitting the sound wave can be reconstructed numerically. According to AMT, the modes generated by a source at the point (r_s,z_s) give the following pressure field at the receiver location (r,z):

$$p_n^{(AMT)}(r_n,z_n) = \sum_{m=1}^{M} \overline{c_m} u_m(r_n,z_n)\exp\left(i\int_{r_s}^{r_n}\kappa_m dr\right), \quad n=1,2,\ldots N. \tag{3.10}$$

Thus, the angle, α, between two M-dimensional complex vectors, $a=[a_m]$, $a_m = c_m(r_s,z_s)\exp(i\kappa_m r_n)$ and $b=[b_m]$, $b_m = \overline{c_m}(r_s,z_s)\exp\left(\int_{r_s}^{r_n}\kappa_m dr\right)$ depends on the assumed coordinates of the source:

$$C(r_s,z_s)=\cos[\alpha(r_s,z_s)] = \left(\sum_{m=1}^{M} a_m b_m^*\right)\left(\sum_{m=1}^{M}|a_m|^2\right)^{-1/2}\left(\sum_{m=1}^{M}|b_m|^2\right)^{-1/2}. \tag{3.11}$$

The dashed lines in Fig. 3.16 demonstrate the parametric dependence of the function $C(r_s,z_s)$ on the source horizontal location:

$$C_M(r_s) = \underset{z_s}{MAX}|C(r_s,z_s)|. \tag{3.12}$$

One can see that $C_M(r)$ has maximum at $r_s^* = 109$ km, which differs by 3.5 km from the real position of the source. This discrepancy appears to be due to a lack of complete information on the propagation conditions. The sound-speed profiles (SSP) were measured at only five points: the two terminus (R and S) and three additional

points P_1, P_2, P_3 (see Fig. 3.14). Due to drift, these points appeared to have moved about 6 km away from the actual acoustic path. Based on the measured acoustic data, a reconstruction of the SSP along the path can be attempted by using the method called "*Matched Field Tomography*" as a step prior to the source-localization procedure. In the experiment, the appropriate procedures were as follows. Proceeding from five available SSPs, one can calculate the average profile, $\langle c(z)\rangle$. Deviations at five locations in range, $\Delta c_k(z) = c_k(z) - \langle c_k(z)\rangle$, $k = 1,2,\ldots,5$, were approximated by EOFs. Only two of EOFs were found to be necessary to provide a good approximation for all $\Delta c_k(z)$. The SSP between the points R, P_1, P_2, P_3, S were interpolated linearly. Hence, a certain vector, q, with 6 (=2x3) components described completely the sound-speed field along the path. Then, for the given vector, q, the signal at the nth hydrophone was calculated theoretically by AMT. It is important to mention that the quantities $p_n^{(q)}$ cannot generally be considered as linearly dependent on q for practically all possible variations of q. The tomographic procedure consisted of finding the vector q which ensures maximum of the following function:

$$K(q) = \left|\sum_{n=1}^{N} p_n^{(E)} p_n^{(q)*}\right| \left(\sum_{n=1}^{N} |p_n^{(E)}|^2\right)^{-1/2} \left(\sum_{n=1}^{N} |p_n^{(q)}|^2\right)^{-1/2} \qquad (3.13)$$

(cf. Eq. 3.2). The gradient descent method with a starting point of $q = 0$ (corresponding to a layered medium with the average SSP $\langle c(z)\rangle$) can be used to maximize the function $K(q)$.

Deviations of the measured SSP from the average one (dashed lines) and deviations of numerically reconstructed SSP, corresponding to the particular vector q, from the average one (solid lines) are represented in Fig. 3.17 for three points, P_1, P_2, P_3, where environmental measurements were carried out. One can see that the reconstructed profiles are close enough to the measured ones with a deviation of the order of 1 m/s.

A new estimate of the source position was then accomplished by using the parameters of the previously obtained, tomographically reconstructed medium. The result is shown in Fig. 3.16 by the solid line. The new position of the source was

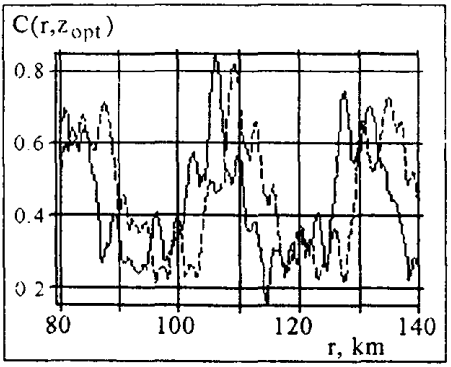

Figure 3.16. Correlation of experimentally measured and numerically calculated acoustic fields at the array as a function of horizontal distance r between the source and the array (the depth of the source is taken to be optimal at each r). Dashed line corresponds to experimentally observed medium and solid line to tomographically corrected one. (Adapted from [57].)

estimated to be 106 km from the receiving array. This estimate deviated by only 0.5 km from the source actual position.

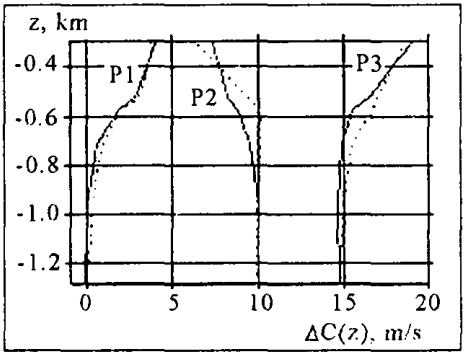

Figure 3.17. Deviations of the measured sound speed profiles from the average ones (dashed lines) and deviations of numerically reconstructed sound speed profiles from the average ones at three horizontal locations. (Adapted from [57].)

3.7 WEAKLY DIVERGENT BUNDLES OF RAYS AND THEIR POSSIBLE USE IN OCEAN ACOUSTIC TOMOGRAPHY

It has been observed in recent experiments on long-range (up to 3500 km) sound propagation over certain paths that the sound field can form very stable shadow and convergence zones. This fact means that the distant sound energy is not inevitably spread over all depths and decays with the distance according to the average decay law [8], but concentrates along some bundles of rays [94, 111]. It was shown that the existence of so-called "*Weakly Divergent Bundles*" (WDBs) of rays is a reason for such concentrations. The conditions for the formation and the propagation of WDBs in a range-dependent ocean have been investigated and published in [112, 113]. Rays within a bundle leave the source with grazing angles, χ, corresponding to extrema of the function $L(\chi)$, the length of a ray cycle with respect to its emergence angle. It appears that the propagation time, $t(\chi)$, along rays in a WDB concentrates near some average value. This is an important characteristic of acoustic propagation for OAT. This property of a WDB follows directly from the following relation [114]:

$$\frac{\partial t}{\partial v} = \frac{1}{v}\frac{\partial L}{\partial v}, \tag{3.14}$$

where $v=c(z_1)=c(z)/\cos\chi(z)$ is the phase velocity in the r-direction for the quasi-plane wave corresponding to a given ray, whereas z_1 is the vertical coordinate at the turning point of this ray. Therefore, functions $t(v)$ and $L(v)$ have extrema at the same v, i.e., for the same angle χ. Hence, propagation times along the different rays in a WDB are also close to each other.

One may anticipate that WDBs can be observed not only in range independent environments, but also under adiabatic conditions (i.e., a slowly changing waveguide). Experiments have shown that WDBs have been observed at great distances (up to

3500 km) even under the conditions of considerable change of the sound channel along the propagation path [94]. An additional confirmation of these results has been obtained also by numerical simulation. It appears that, although the cycle length, $L(\chi;r)$, changes considerably with the distance, some extrema of the function preserve their extremal behavior over a long range. This fact ensures that the ray tube associated with an extremal ray expands comparatively slowly with increasing distance, so the sound intensity remains high along such a tube.

The $z(\chi;r)$-diagram, which specifies the depth, z, at a distance, r, for the ray that leaves the source at the grazing angle, χ, can be used to investigate the average energy parameters of a WDB. For example, if one distributes the total energy of the bundle uniformly over its cross-section for a horizontally stratified medium, one obtains for the squared amplitude (sound intensity) of the bundle:

$$A^2 = \frac{A_0^2 r \cos\chi' \delta\chi'}{\delta z \cos\chi''}, \tag{3.15}$$

where A_0^2 is the sound intensity generated by the same source at a distance, r, in the case of homogeneous medium, χ' and χ'' are grazing angles of the same characteristic ray of the bundle (e.g., with the smallest emergence angle) at the source location and at the distance r, respectively, $\delta\chi'$ is the angular width of the bundle leaving the source, and

$$\delta z = \left| \{z(\chi';r)\} - \{z(\chi'+\delta\chi';r+\left|\frac{\partial r}{\partial \chi'}\right|\sin^2\chi'' d\chi')\} \right|$$

is the depth difference between the bound bundle of rays, which determine the wave front at the receiving point.

The amplitude of a single ray can be described also by Eq. (3.15), if we replace the bundle cross section, $\delta S = 2\pi r \cos\chi'' \cdot \delta z$, by the cross section of an infinitely narrow ray tube $dS = 2\pi r \cos\chi'' \cdot |\partial z/\partial\chi'| d\chi'$. We can introduce the average (over the bundle) derivative $\langle z' \rangle = \Delta Z/\Delta\chi$, where $\Delta Z = \int |z'(\chi;r)| d\chi$ is the sum of quantities $\max\{z(\chi;r)\} - \min\{z(\chi;r)\}$ over all monotonic parts of the $z(\chi;r)$-diagram. The estimated average-squared amplitude of the ray is

$$A_1^2 = \frac{A_0^2 r \cos\chi' \Delta\chi}{\Delta Z \cos\chi''}, \tag{3.16}$$

which is also the sound intensity measured by a directional antenna that resolves the different families of rays in the bundles. (More than one family can be present in the bundle due to the existence of caustics, for example). The ratio A/A_1 is equal approximately to the number of rays of such families.

Let us consider further the previously mentioned Canary Basin Experiment in the context of WDBs (see Figs. 3.5-3.7) [94]. The "tongue" of higher salinity water

caused a formation of a two-channel propagation structure. A WDB (in the angular interval χ=[-2.7°,2.6°]) existing at lesser distances, experienced considerable structural change and split into three bundles with χ's in the intervals: I - [-2.7°,-2°], II - [-1.6°,1.4°], and III - [2°,2.6°]. Bundle II was trapped by a deep, strong channel with its axis at the depth of 1500 m (see Fig. 3.7). This bundle preserved its weak divergency. Bundles I and III, trapped by the upper channel with its axis at 500 m, experienced stronger disturbances. Their energies were smeared over practically the whole channel. This can be seen in Fig. 3.18a, where boundaries $\min\{z(r)\}$ and $\max\{z(r)\}$ are plotted for bundle II (solid lines) and for bundle I (dashed lines). Average ray amplitudes versus distance along the same bundles, calculated from Eq. (3.16), are shown in Fig. 3.18b by the same kind of curves as in Fig. 3.18a.

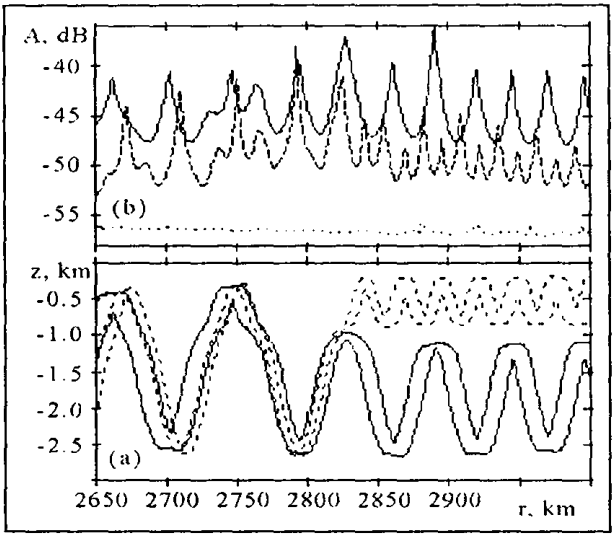

Figure 3.18. (a) - Two WDBs for the experiment in the Canary Basin Experiment; (b) - average ray amplitudes versus distance along the same WDB (see Fig. 3.7).

The amplitudes in bundle II are strongly oscillating because of pulsations in the bundle cross-section. (This, however, is not clearly visible in Fig. 3.18b due to the great difference between horizontal and vertical scales.) Sound amplitudes in this bundle, formed by all other normally divergent rays (dotted line), are 15 dB above the background. Bundle I is more divergent than bundle II. Its ray amplitudes are not higher than 6 dB above the background, so it can not be classified as a WDB.

Horizontal inhomogeneity of the sound channel was strong in a Norwegian Sea Experiment conducted in 1990 [4, 112]. The greatest distance in the experiment was 890 km. The vertical SSP, $c(z)$, at different distances and the bottom bathymetry are presented in Fig. 3.19a. A two-axis channel existed at mid-range. However, even in this strongly range-dependent conditions, some bundles preserve their structures. There are six WDBs corresponding to the following angular intervals: I - [-10°,-7.6°].

II - [-7.6°,-5.9°], III - [-3.2°,-1.7°], IV - [1.7°,3.1°], V - [6.4°,7.9°], and VI - [6.4°,7.9°]. In Fig. 3.19b boundaries of WDB IV, which retains its structure up to the maximum distance, are shown by solid lines. Dashed lines correspond to bundle I, which is formed by rays leaving the source at steeper emergence angles. This bundle is destroyed at distances about $r \approx 630$ km due to the interaction with the bottom.

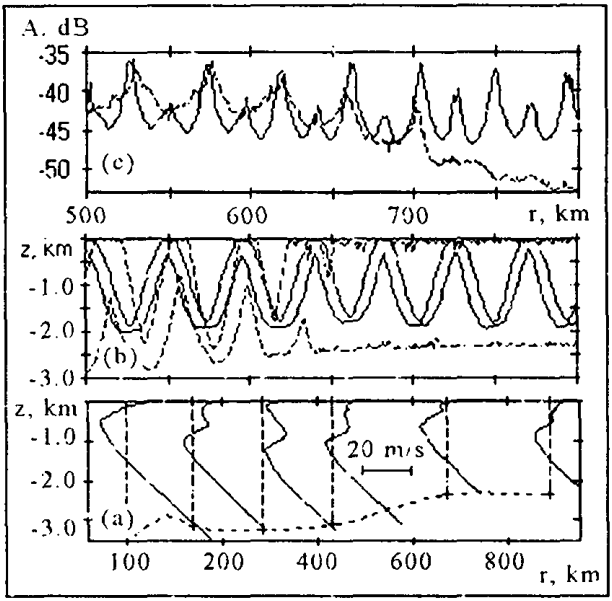

Figure 3.19. The 1990 Norwegian Sea Experiment: (a) - the bathymetry and the sound speed profiles at different distances; (b) - two WDBs; (c) - average ray amplitudes versus distance along the same WDB. (Adapted from [112].)

The average sound amplitudes, A_1, in these bundles are shown in Fig. 3.19c by the same kind of curves. The amplitude in bundle I drops significantly at distances near 630 km and remains close to background level. The amplitude of bundle VI, not shown in Fig. 3.19c, reveals the same behavior. Also not shown in Fig. 3.19c, bundles II and III were considerably affected by horizontal inhomogeneity of the sound speed and were slightly above background. In contrast to this, the amplitude in bundle IV, although strongly oscillating, was considerably higher than background level (by 17 dB at some distances). The average amplitude of bundle V has analogous behavior (also not shown), and only at distances greater than 800 km did it disintegrate due to interaction with the bottom.

In Fig. 3.20a, the normalized amplitude as a function of depth, averaged over 100 m in depth, is plotted on a linear scale as a solid line at a distance of 571 km. The same average amplitude at the distance of 778 km is shown in Fig. 3.20b. Considerable variations in amplitude versus depth indicate that the WDBs play an important role. Dotted lines in the figures represent numerically calculated amplitude

taking into account all rays leaving the source in the angular interval [11°,11°]. The dashed curves correspond to numerical calculations, taking into account only rays forming WDBs — all six at 571 km and four of those not destroyed at 778 km. Behavior of the numerically simulated bundles at 778 km is very similar to that of experimental amplitudes, which means that WDBs play the main role in forming the sound field.

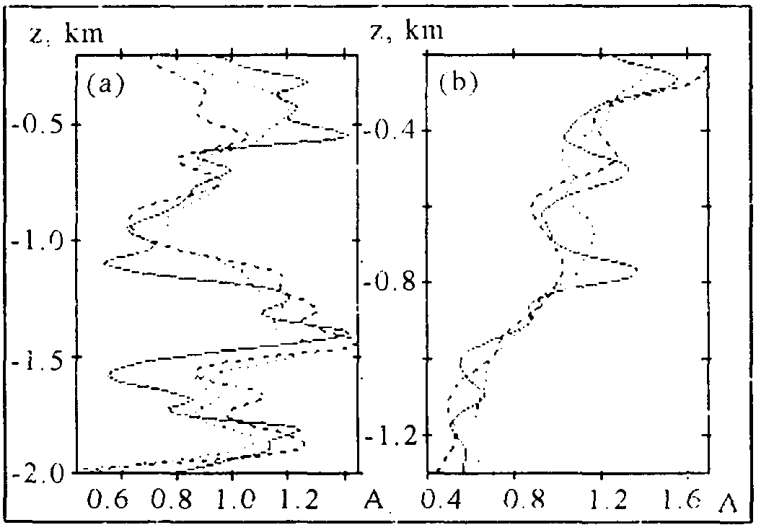

Figure 3.20. The sound field amplitude as a function of depth at a distance of: (a) - 571 km and (b) - 778 km for the 1990 Norwegian Sea Experiment. Solid lines correspond to the experimental data, dotted lines correspond to numerically calculated amplitude, taking into account all rays leaving the source in the angular interval [-11°,11°]; dashed lines correspond to numerically calculated amplitude, taking into account only rays forming the WDB. (Adapted from [112].)

Weakly divergent bundles may have considerable practical importance. They can be used for effective long-range underwater sound communication, for example. In the presence of strongly pronounced inhomogeneities of the sound speed in both horizontal and vertical directions, models using the WDB-approach increase the effectiveness of the matched field method in solving inverse problems. The stability of a WDB in the presence of different kinds of inhomogeneities in the ocean is very important for *Munk-Wunsch Ray Tomography* also. Particularly, bundles can be used as reference rays in "dynamic" tomography, which analyzes differences of arrival times of different rays instead of arrival times itself. For acoustic thermometry of the ocean it is also important to use rays and bundles that are stable under the conditions of strong variability of the ocean.

It should be noted that, when working with WDBs, one must use hydrophone arrays or moving single receivers. A single receiver at a fixed position will be ineffective, because WDBs can change their positions when conditions for sound propagation are changing.

In conclusion, let us discuss the possibility of using WDBs in one of the acoustic paths in the Arctic (the Beaufort Sea - Spitsbergen) proposed for the ATOC

(*Acoustic Thermometry of Ocean Climate*) project [16, 17]. As range-averaged SSPs, $\langle c(z)\rangle$, two typical profiles have been selected: a typical one before the Lomonosov Ridge (solid line in Fig. 3.21a) and one after it (dashed line). Two WDBs are shown in Fig. 3.21b. They leave the source, which is placed at the depth 300 m, in two angular intervals: I - [-7.8°, -7.6°] and II - [7.4°, 7.6°]. Average ray amplitudes versus distance along the same bundles, calculated using Eq.(3.16), are shown in Fig. 3.21c by the same kind of lines as in Fig. 3.21b. Lower turning points of these ray appear to be deeper than the top of the Lomonosov Ridge (at a distance 1950 km in Fig. 3.21b). This fact influences the WDBs in some measurements, but does not disturb their general structure. A standard WDB corresponding to $\chi=0$, not shown in Fig. 3.21, also exists. Such rays have short cycle lengths, and the bundle disintegrates even at moderate distances.

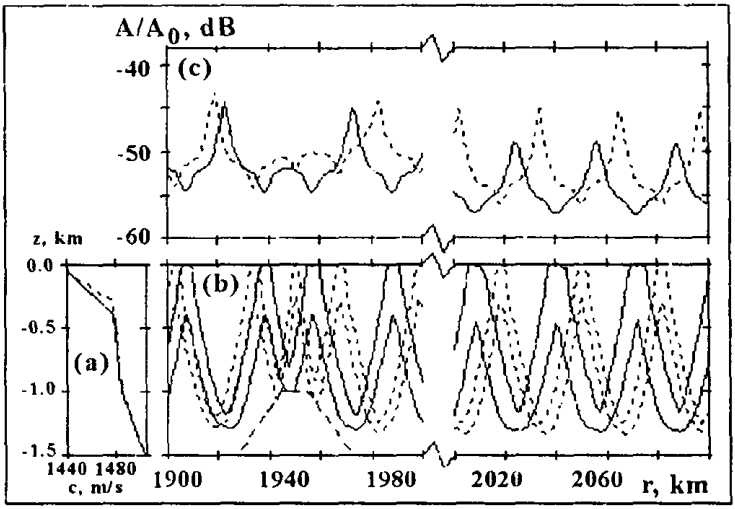

Figure 3.21. (a) Representative sound-speed profiles in the Arctic before the Lomonosov Ridge (solid line) and after the Lomonosov Ridge (dashed line); (b) two WDBs; (c) average ray amplitudes versus distance along the same WDBs. (Adapted from [115].)

The stability of a WDB appears to be very important for detecting small, climatic changes of the average temperature of the Arctic Ocean (ATOC project). To demonstrate this possibility, we have numerically determined the changes of WDB propagation times and amplitudes under the influence of a small increment of temperature $\Delta T(z)$. We assumed a lack of temperature variations at the surface (ice-melting temperature). Maximum variation, $\delta T \equiv \max|\Delta T|$, was introduced for the depth $z=h=30m$. The form of temperature variation is given by, $\Delta T(z)=\delta T\cdot\exp(-|z-h|/H)$ for $z>h$ and $H=5000\,m$. That is, ΔT decreases slowly with increasing depth. Calculations were made for different maximum values from the interval $0\le\delta T\le 0.15°C$. According to the calculations, ray amplitudes in the WDBs at a maximum distance of 2900 km (for all δT) appear to be 10-14 dB higher than the background formed from the rays not

belonging to the WDB. The depth of the central ray in the bundle varies between 300 m and 1300 m, and the vertical cross-section of the bundle changes from 40 m up to 600 m. The pair of the same kind of lines in Fig. 3.22a shows maximum, $t_{max}^{(I,II)}(\delta T)-t_0$, and minimum, $t_{min}^{(I,II)}(\delta T)-t_0$, delay times for both bundles versus δT, where travel time, t_0, corresponds to the slowest ray in the absence of temperature variations ($\Delta T=0$). The intervals, $\Delta t^{(I,II)}(\delta T)=t_{max}^{(I,II)}-t_{min}^{(I,II)}$, show the possible dispersions of the travel times at the distance of 2900 km. The variations of the average amplitudes of these rays are shown in Fig. 3.22b. Small Δt for the bundle in the angular interval [-7.8°, -7.6°] (dotted line) at small δT are due to the additional focusing of the rays reflecting from the front slope of the ridge. The considerable difference in Δt for boundary rays in this bundle for $\delta T > 0.02°C$ is due to the bundle broadening as it reflects from the rear slope of the ridge and from the plateau adjacent to it. This also causes a decrease of approximately 5 dB in sound amplitude in the bundle (Fig. 3.22b).

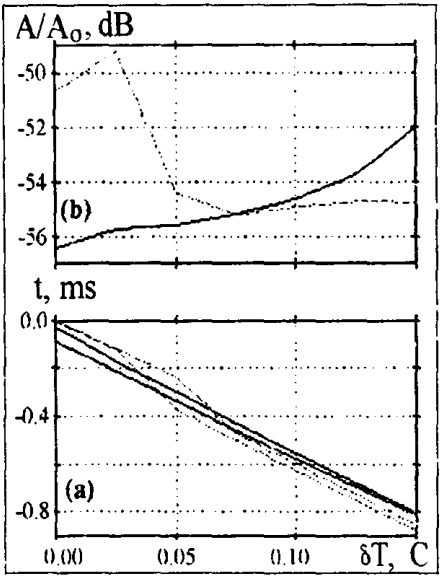

Figure 3.22. The dependencies of parameters of two WDBs (I,II) on temperature variations: (a) the maximum and minimum bundle temporal-delay variations; (b) the average bundle amplitude variations. (Adapted from [115].)

One additional important fact can be learned from Fig. 3.22a. The difference in propagation times of different bundles, as well as for different rays in the same bundle, is considerable (30 ms and more). Therefore, different bundles, and even different rays within them, can be resolved in practice. An approximately linear relation, $\Delta t/t \approx \Delta c/c$, between decreasing of propagation time, Δt, for either bundle and increasing of sound speed, Δc, corresponding to the increase of δT, can be also seen in Fig. 3.22a.

Investigations of the use of WDBs in acoustic tomography and thermometry, especially for the Arctic region, have been presented in [115]. The following problems were considered in that paper:

a) Wave interpretation of WDBs;

b) Frequency dependence of WDBs, including the weakening and disappearance of WDBs with decreasing frequency;
c) Estimation of minimum frequency, for which the effect of WDBs is apparent (about 30 Hz for the Arctic conditions); and
d) Problems of the experimental use of WDBs in OAT and measurements of Arctic Ocean warming.

3.8 INTERFERENCE TOMOGRAPHY ALGORITHMS FOR SYNOPTIC INHOMOGENEITIES AND OCEAN BOTTOM RECONSTRUCTION

An interference algorithm for OAT has been proposed for the reconstruction of the synoptic inhomogeneities of the sound speed by the analysis of perturbations in the inter-mode-phase difference [59]. The inter-mode-phase difference is determined by the measured spatial distribution of the interference structure of the acoustic field. The possibility of solving the phase problem for ocean conditions will be analyzed numerically for synoptic inhomogeneities. Also, an interference method for determining the SSPs, the density, and the attenuation coefficient in the bottom by measuring the sound interference structure and using *a priori* evaluations of the bottom parameters will be discussed.

3.8.1 Interference Tomography for Synoptic Inhomogeneities

Let us consider an irregular underwater waveguide with a SSP that is slowly varying horizontally: $c(r,z)=c_0(z)+\delta c(r,z)$, where $|\delta c|\ll c$. At the point, $(0,z_s)$, we place an harmonic sound source with radiation power P_0. A receiver is located at the point (a,z_r). The SSPs near the source and near the receiver are equal and given by $c_0(z)$. However, due to inhomogeneities, there are SSP variations given by $\delta c(r,z)$ in between. We consider the bottom to be smooth, non-absorbing and homogeneous.

Considering synoptic horizontal scales, we can assume that the characteristic scale of horizontal variations of the SSP is much greater than the mode interference scale, so that the adiabatic approximation can be used to describe the sound field. Numerical estimates have shown that, for synoptic variations of the sound speed, perturbations in the inter-mode-phase difference, ε_{nm}, are small for nearby modes (n and m); that is, $\varepsilon_{nm}=|\delta\Psi_n-\delta\Psi_m|\ll 1$, where $\delta\Psi_n$ is a perturbation of the nth mode phase, associated with the inhomogeneities. In the adiabatic approach, the phase of the nth mode at the receiver location has the form: $\Psi_n(r,\omega)=\int_0^r dr'\,\kappa_n(r',\omega)$. For normal modes, significantly spaced in the modal spectrum, the perturbations in the inter-mode-phase difference may be of the order or even greater than unity.

Assuming that for all mode pairs $\varepsilon_{nm}|\ll 1$, we obtain for the acoustic-field intensity variation associated with synoptic inhomogeneities:

$$\Delta I(a,z_s,z_r) = \tilde{I}(a,z_s,z_r) - I(a,z_s,z_r) \approx$$

$$\approx \frac{P_0}{a}\sum_{n=1}^{N}\sum_{m=1}^{N}\frac{\varphi_n(z_s)\varphi_n(z_r)\varphi_m(z_s)\varphi_m(z_r)\sin((\kappa_n-\kappa_m)a)\varepsilon_{nm}}{\sqrt{\kappa_n\kappa_m}}, \qquad (3.17a)$$

where $\tilde{I}(a,z_s,z_r)$ is the intensity of the acoustic field at the receiver in the presence of inhomogeneities, $I(a,z_s,z_r)$ is the intensity in the receiver without inhomogeneities, φ_n and κ_n are the vertical eigenfunction and horizontal wavenumber of the nth mode in the unperturbed waveguide, N is the number of propagating modes. To formulate directly the basis of interference OAT, we should relate the mode-phase perturbations to the field of inhomogeneities [59]:

$$\delta\Psi_n(r) = -\frac{\omega_0^2}{\kappa_n}\int_0^r dr'\int_0^\infty dz'\varphi_n^2(z')S(r',z'), \qquad (3.17b)$$

where $S(r,z)=\delta c(r,z)/c_0^3(z)$. Thus, Eq. (3.17a) can be inverted with respect to $S(r,z)$ on the basis of well-known algorithms utilizing a regularization method [102].

Calculations have been made for two characteristic types of the ocean underwater waveguides: a deep-sea waveguide with a canonical SSP and a surface duct waveguide with the linear profile of the sound speed. The parameters of the unperturbed waveguide acoustic modes have been calculated by the mode program. In the process of modeling the phase problem, the influence of sea noises has been taken into account. The accuracy of the reconstruction has been estimated by the coefficient η:

$$\eta = \sqrt{\sum_{n,m}|\Delta\varepsilon_{nm}|^2 / \sum_{n,m}|\varepsilon_{nm}|^2}, \qquad (3.18)$$

where $\Delta\varepsilon_{nm}$ is the difference between the true and the reconstructed values of ε_{nm}.

For energetically weak eddies (i.e., $|\varepsilon_{nm}|\ll 1$ for all modal pairs), a satisfactory reconstruction of ε_{nm} (with an accuracy determined by $\eta\leq 0.14$) in the surface duct channel may be achieved by measuring a one-dimensional (horizontal or vertical) interference structure. For a deep-sea channel, the measurement of the two-dimensional interference structure is obligatory. In the case of energetically strong eddies (i.e., δc=15-30 m/s), spatial filtering (to single out large-scale

interference structures for which ($|\varepsilon_{nm}|\ll 1$) should be used. It is necessary to measure the two-dimensional interference structure in both types of channels for a satisfactory reconstruction of ε_{nn}.

Figure 3.23a illustrates the results of solving the phase problem in a deep-sea channel. The calculation was made for a sound-speed variation of $\delta c = 15$ m/s. In this case the optimum reconstruction occurred for the modes with numbers in the interval $42<i<65$. The results for the case of the surface-duct channel are given in Fig. 3.23b. Here the optimum reconstruction was achieved in the interval $54<i<70$. The variation of the noise intensity has shown that a satisfactory reconstruction was observed for the signal-to-noise ratio of the order or greater than 13 dB.

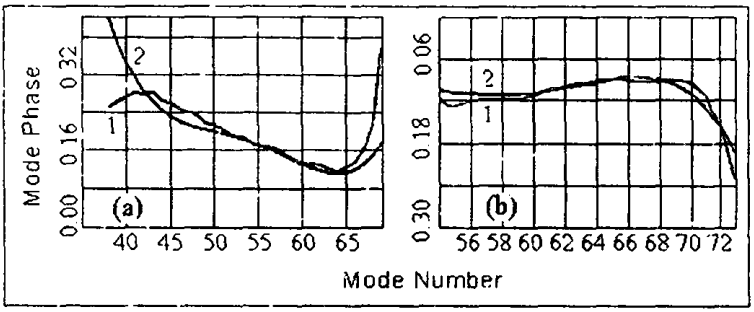

Figure 3.23. Modal-phase perturbation reconstruction for: (a) a typical deep-sea sound channel, (b) a linear sound speed profile with a surface duct. (Adapted from [68])

Thus, by measuring the acoustic-field interference structure, one may determine accurately enough (at least for a certain interval of mode numbers) the inter-mode-phase difference. The inter-mode-phase difference can then be related to synoptic perturbations of the SSP.

3.8.2 Interference Tomography of the Ocean Bottom

Let us consider an ocean waveguide with discontinuities of the sound speed and density at the water-bottom interface, $z=H$. The z-axis is directed downward. Let the SSP be $\tilde{c}=c(z)+\delta c(z)$ and the density be $\tilde{\rho}=\rho(z)+\delta\rho(z)$. Here, $c(z)$ and $\rho(z)$ are *a priori* evaluated sound speed and density. Sound propagation in a medium with attenuation can be described by the following equation for the complex amplitude of sound pressure:

$$\tilde{\rho}\nabla\left(\frac{\nabla\tilde{p}}{\tilde{\rho}}\right)+\frac{\omega^2}{\tilde{c}^2}(1-2i\tilde{\gamma})\tilde{p}=Q\delta^2(\boldsymbol{r}-\boldsymbol{r}_0)\delta(z-z_0), \tag{3.19}$$

where ω is the signal angular frequency, $\tilde{\gamma}=\omega(\lambda+2\mu)/\rho\tilde{c}^2\approx\gamma-\omega(\lambda+2\mu)/\rho c^2$ is generally related to the attenuation coefficient for an isotropic elastic medium described by the Lame constants λ and μ, $Q=\sqrt{8\pi\rho_0 c_0 I^2}$, and P is the source power, ρ_0 and c_0 are the density and sound speed near the source point, $r_0=(0,z_0)$. The magnitude $\tilde{\gamma}\omega/c$ is the attenuation coefficient in a homogeneous medium, which describes dissipative medium parameters, for example, attenuation in the bottom.

A way of applying OAT methods for bottom-parameter reconstruction can be described as follows. The formula, which relates the pressure-field intensity perturbations to the variations of the bottom parameters, is used as a basis for reconstruction of the SSP, density, and attenuation coefficient. An expression for the pressure-field intensity can be written by using the modal description (as was done in the previous section). The average medium parameters in an area under investigation or other *a priori* information can be used as a reference. The modal parameters (e.g., eigenvalues, eigenfunctions) can then be expressed through the bottom parameters by perturbation theory. The formula is then linearized for a short path (the path for which variations of amplitude and phase of modes are small). This linearization simplifies the formula.

Let us consider some results of numerical reconstruction of the sound attenuation coefficient in a homogeneous bottom by measuring the sound intensity for the case of random noise and unknown source power. Without sound-speed and density variations, we can rewrite Eq. (3.17a) as

$$\Delta I(a,z,z_0)=\tilde{I}-I=P\int_H^{\infty}dz'\gamma(z')[K_1(z',a,z,z_0)+K_2(z',a,z,z_0)], \tag{3.20}$$

where

$$K_1(z',a,z,z_0)=\frac{\omega^2}{c^2(z')}\frac{\rho_0}{\rho(z')}\sum_{n=1}^{N}\sum_{k=1}^{N}\frac{q_n(z,z_0)q_k(z,z_0)}{\sqrt{\kappa_n\kappa_k}}\frac{u_n^2(z')}{\kappa_n}\cos[(\kappa_n-\kappa_k)a)],$$

$$K_2(z',a,z,z_0)=-\frac{\omega^2}{c^2(z')}\frac{\rho_0}{\rho(z')}\sum_{n=1}^{N}\sum_{k=1}^{N}\frac{q_n(z,z_0)q_k(z,z_0)}{a\sqrt{\kappa_n\kappa_k}}\sin[(\kappa_n-\kappa_k)a]\times$$

$$\times\left[q_n(z,z_0)\frac{\varphi_n^2(z')}{2\kappa_n^2}-2\sum_{m\neq n}\frac{\varphi_n(z)\varphi_m(z_0)+\varphi_m(z)\varphi_n(z_0)}{\kappa_n^2-\kappa_m^2}\varphi_n(z')\varphi_m(z')\right],$$

$\tilde{I} = |\tilde{p}|^2/2\rho_0 c_0$, $q_n(z,z_0) = \varphi_n(z)\varphi_n(z_0)$, φ_n and κ_n are the nth modal eigenfunction and the horizontal wavenumber in the waveguide with characteristics $c(z)$ and $\rho(z)$, and $\gamma = 0$ $a = |\boldsymbol{r} - \boldsymbol{r}_0|$.

Assuming $\gamma(z) = \gamma = \text{const}$ and taking into account the noise intensity, we can represent Eq. (3.20) as

$$I(a,z,z_0) = \xi(\tilde{I}(a,z,z_0) + I_{ns}) = \gamma_1 Q_1(a,z,z_0) - \gamma_2 Q_2(a,z,z_0), \tag{3.21}$$

where the sound intensity, I, in the reference (no inhomogeneities) waveguide and the coefficients, $Q_i = P_0 \int dz' K_i$, $i = 1,2$, are calculated for the case of a source with fixed power, $P = P_0$, I_{ns} is the noise intensity, $\xi = P_0/P_*$, and P_* is an unknown source power. Instead of the value γ, we have formally substituted the uncorrelated values γ_1 and γ_2. Numerical simulation of the reconstruction of γ was carried out on the basis of Eq. (3.21).

The following model has been used for numerical simulation. The water-column depth is 295 m, the sound speed in the water column is 1483 m/s, the bottom sound speed is 1750 m/s, the source depth is 75 m, and the receiver depth is 55 m. External noise intensity is introduced by random values, I_{ns}, with a uniform distribution in the interval $[0, 2\langle I_{ns}\rangle]$ and dispersion $\langle I_{ns}\rangle^2/3$. Random values of noise intensity are added to the values of $\tilde{I}$ at the measuring points. In the numerical reconstruction we employed an integral-equation-solving program based on Tikhonov's regularizing technique [102]. The horizontal range interval varies from 0.5 to 8 km.

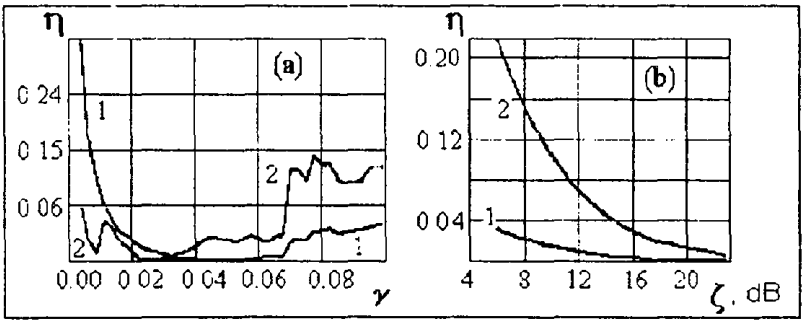

Figure 3.24. Reconstruction error dependence on: (a) - the attenuation coefficient in the bottom half-space, (b) - the signal-to-noise ratio. (Adapted from [68].)

The dependencies of reconstruction error, η ($\eta = |\gamma - \gamma_r|/\gamma$, where γ_r is the reconstructed value), on the attenuation coefficient, γ, and the noise intensity, ζ ($\zeta = 10 \cdot \log(I_m/I_{ns})$), where I_m is the maximum of the sound intensity) are shown in Figs.

3.24a and 3.24b, respectively. Curves 1 and 2 describe the reconstruction of γ_1 and γ_2, respectively. Numerical simulation has shown accurate restoration of the attenuation coefficient for values of the signal-to-noise ratio equal to or larger than 10 dB for the case of unknown source power.

3.9 IDENTIFICATION OF RAY PULSES IN OCEAN ACOUSTIC TOMOGRAPHY WITH A MOVING RECEIVER

The application of the tomographic scheme based on measuring travel-time differences of the different rays has shown that ray-based reconstruction algorithms may be generalized for moving sources and receivers. Some experimental results of the pulse identification testing are discussed in this section.

An experiment was carried out in the western part of the Mediterranean Sea in June - July 1994 [148]. The Russian scientific-research ship, *Akademik Sergey Vavilov,* received acoustic signals from sources of the *International Tomographic Experiment* (THETIS-2) by using two vertical acoustic arrays. The sources radiated periodically coded signals (*m*-sequence [16]) on the carrier frequencies 250 Hz and 400 Hz. The coded sequence of the phase changes contained 511 samples. The digital duration (a duration of the radiated pulse after matched filtering) was equal τ_0=10 ms for 400 Hz and τ_0 =16 ms for 250 Hz. The source depths were z=150 m and z=170 m (near the sound channel axis). The working lengths of the vertical arrays were 127.5 m (with a spacing of 8.5 m) and 64 m (with a spacing of 4 m). The depth range of hydrophones was from 50 m to 180 m.

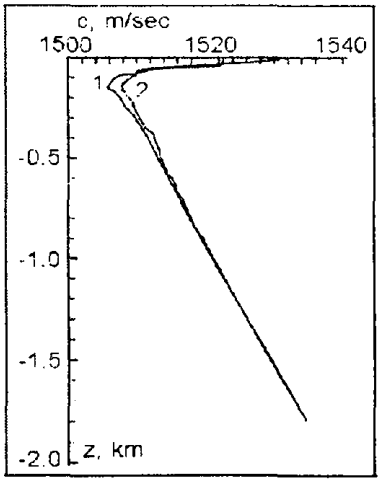

Figure 3.25. Typical sound speed profiles for the THETIS-2 experiment. (Adapted from [148].)

According to the oceanographic data obtained simultaneously with the acoustic measurements, the acoustic waveguide had a surface-duct channel over the entire

region. Typical SSPs are shown in Fig. 3.25. The strong spatial variability of sound speed was observed mostly near the ocean surface. The thickness of the main variability layer was about 150 m. Spatial variations of the sound speed were the greatest near the surface and did not exceed 10 m/s.

From the results simulated by ray and mode programs for the case of short irradiated pulses with the temporal duration, τ, the time structure of the received acoustic signal can be characterized as follows. The group of the separate ray pulses, corresponding to the steepest ray-emergence angles (relative to the horizontal axis), arrives at the receiver first. Later, the group of the pulses corresponding to smaller grazing angles arrives. Relative differences in the travel times between different groups decreases with increasing time, t. From some value $t=t_*$, the pulses corresponding to the different clusters of grazing angles can not be distinguished. One separate group of the ray pulses is usually formed by four rays, which have close emergence angles and close propagation times. The first ray (with minimal delay) in the group leaves the source in the downward direction and arrives at the receiver from below the source horizon, and the last one leaves the source in the upward direction and arrives at the receiver from above the source horizon. In particular, when the receiver is near the axis of the sound channel (and its depth is also close to the source depth), the two middle rays have the same temporal delay, and four rays, forming the separate ray pulse, transform into three. In this case the intensity of the individual pulses, corresponding to small grazing angles, exceeds considerably the pulse intensities of the rest of the groups.

Data processing consisted of matched filtering of the received acoustic signal with subsequent coherent or incoherent averaging of the matched-filter output. Assuming that the ocean sound channel can be modeled as a linear time-invariant system and that the sound propagation can be described by the ray approach, one usually uses matched-filter processing to maximize the signal-to-noise ratio and to optimize estimations of the signal amplitude and time delay in added external Gaussian noise. Matched filtering represents the convolution procedure in the temporal domain [16]. Coherent averaging consists of summing the complex filter outputs. Incoherent averaging consists of summing the intensities of the convolved signals. At the first stage, matched filtering was applied to the acoustic signal received by the center hydrophone. Maximization of the filter response for this hydrophone allowed for estimating the absolute time of radiation and eliminating the Doppler frequency shift. Thus, the random Doppler effect in the frequency domain and variations of the time delays due to irregular drift of the ship could be eliminated at the second stage. The information obtained about frequency and time-delay corrections was then used for processing acoustic data from other hydrophones of the array.

The examples of the incoherently averaged intensity of the convolved signals are shown in Figs. 3.26a and 3.26b (solid lines). Depths of the hydrophones were

about: (a) 160 m and (b) 60 m. The intensity, I, is in dB normalized to some fixed level. The absolute value of the propagation times, t, for the groups of non-differentiated rays was calculated in accordance with the prior estimation of the source-receiver horizontal distance, a= 256.43 km. To identify separate pulses, the dependence of calculated sloping angles of the rays (for the SSP near the source) on time delay, t, are plotted in Figs. 3.26a and 3.26b as circles. The calculation were made for a horizontally inhomogeneous model of the ocean. Variations of the SSP along the propagation paths were determined by linear interpolation of the profiles near the source and receiver (profiles 1 and 2 in Fig. 3.25).

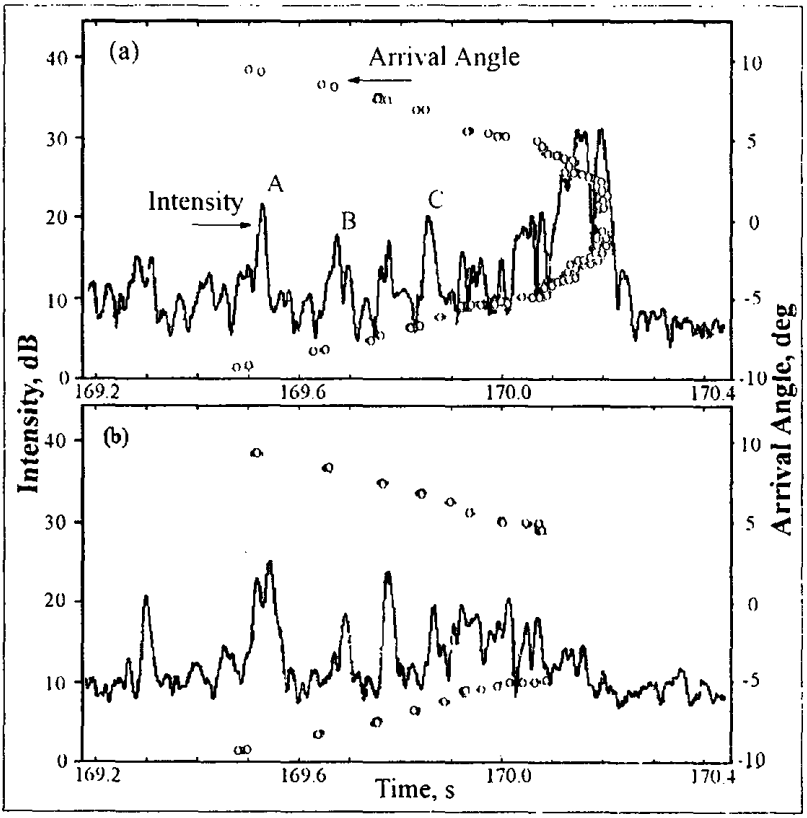

Figure 3.26. Temporal dependence of incoherently averaged intensity of the matched-filter output for the hydrophones at the depths of: (a) - 160 m, (b) - 60 m. Circles correspond to the arrival times of the separate rays with different arrival angles. (Adapted from [148].)

A comparison of the experimental data with the theoretically calculated delays allows identifying the groups of pulses formed by the four rays. The accuracy of the identification can be improved by determining arrival angles of the ray pulses. For this purpose, the dependence of the phase difference of the complex filter outputs

from adjacent hydrophones on time delays can be determined. The dependence of phase difference, $\Delta\psi$, on time delay is shown in Fig. 3.27 for two hydrophones with a vertical spacing of 8.5 m. For the groups B and C, $\Delta\psi$ ($=\psi_2-\psi_1$, where ψ_2 is the signal phase at the hydrophone close to the surface) changes sign from positive (the first ray in the group) to negative (the last ray in the group). For the group of rays, A, the phase difference changes sign from negative to positive, because $|\Delta\psi|>\pi$, but $\Delta\psi$ can be determined only with the accuracy of π. The result shows that the first ray in the group arrives from below the receiver horizon, and the last ray arrives from above the receiver horizon. The fields of the two middle rays in the group interfere with one another, depending on the difference of the phases along the ray trajectories.

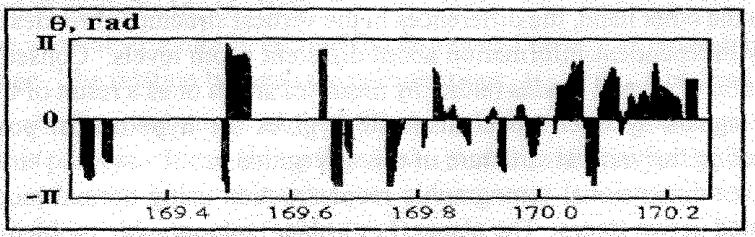

Figure 3.27. Signal-phase difference on two adjacent hydrophones versus arrival time for different groups of rays. (Adapted from [148].)

Measurements have shown that, in the case of a moving receiver, a considerable portion of the ray pulses (corresponding to steep grazing angles) can be identified. The accuracy of the time-delay estimation is proportional to the radiated pulse duration, τ_0.

3.10 A THREE-DIMENSIONAL MODAL APPROACH IN OCEAN ACOUSTIC TOMOGRAPHY

The conventional OAT scheme is based on measurements of the delay times between sound signals propagating along different ray paths in a USC. However, it has been noted (e.g., in [12]) that the ray description of the field at frequencies f=100-1000 Hz is invalid at horizontal distances r>10-30 km from the source in the shallow water. The same is true (at distances r>100-200 km) for narrow-surface-duct waveguides in the deep ocean, which are typical for many regions of the World Ocean. The mode description of the field is the most realistic approach in these cases.

Vertical localization of the acoustic field is much less pronounced for shallow-water waveguides, because of the rapid de-phasing of the modes in such waveguides. Therefore, one cannot measure the parameters of individual levels of a shallow sea, so that the tomography of shallow waters is necessarily two-dimensional (or planar).

For these cases it is inappropriate to attempt a reconstruction of the structure on the basis of the interpretation of tomographic data according to the scheme considered in [12], which essentially exploits the local influence of inhomogeneities intercepted by each ray path of the sound field. Consequently, a different procedure must be applied for the reconstruction in this case. A two-dimensional reconstruction of the structure in a certain region surrounded by a selected configuration of sources and receivers can be implemented by measuring the phase or envelope delay of different propagating modes. A depth-averaged value, weighted in correspondence with the structure of the given mode, is determined for the sound speed in the planar channel. This is the two-dimensional scheme described in [36], where it is proposed to measure the phase of a stable tonal signal in one of the modes identified by the receiving array.

On the other hand, the differences in the vertical structure of modes means that they carry independent information about different depth levels. Consequently, the identification of several modes (either by means of arrays or as a result of the splitting of pulse signals by inter-modal dispersion) gives the hypothetical possibility of reconstructing the vertical structure of the waveguide.

Three-dimensional tomographic reconstruction using normal modes can be implemented in two stages. The planar ((x,y)-plane) tomographic problem should be solved at the first stage. The initial data for the two-dimensional reconstruction can be either the modal-phase perturbations [36] or the modal-pulse delay times by analogy with ray-based tomography. Variations of the characteristics of the nth mode along each transmission path (in fixed planar channel) between the radiating, p, and receiving, q, arrays are given by the following equation for the modal-phase tomography:

$$\delta\Psi_{pq}^{(n)} = \int_{pq} \delta\kappa_n(x,y)dl, \tag{3.22}$$

where $\delta\Psi_{pq}^{(n)}$ is the phase variation of the nth mode between the source, p, and the receiver, q, and $\delta\kappa_n$ is the perturbation of the horizontal wavenumber of the nth mode. For the tomographic scheme, based on time-delay measurements, we have

$$\delta t_{pq}^{(n)} = -\int_{pq} dl \frac{\delta v_n(x,y)}{\delta v_n^2}, \tag{3.23}$$

where $t_{pq}^{(n)}$ is the envelope time delay of the nth mode on the path pq and v_n is the group velocity of the nth mode.

Using the measured set of values of $\delta\Psi_{pq}^{(n)}$ or $\delta t_{pq}^{(n)}$ at the first stage, one can reconstruct the two-dimensional field of the quantities $\delta\kappa_n(x,y)$ or $\delta v_n(x,y)$, respectively.

This reconstruction is usually made by partitioning the investigated region into a certain number of discrete cells and reducing the integral equations, Eqs. (3.22) and (3.23), to an algebraic system of the form [12, 14]:

$$y_i = \sum b_{ij} a_j, \tag{3.24}$$

where y_i is interpreted as $\delta\Psi_{pq}$ for Eq. (3.22) or δt_{pq} for Eq. (3.23), $b_{ij}=R_{ij}$ is the length of the ith path in the jth cell, and a_j is the parameter value in the jth cell ($\delta\kappa_n$ or δv_n), which we would like to reconstruct. The inverse problem, Eq. (3.24), is known to be ill-posed, and its solution must be formulated with the application of appropriate regularization methods [6, 16, 102].

The vertical structure in each of the segregated cells, j, is reconstructed at the second stage. The relation between the perturbations, $\delta\kappa_n$ or δv_n, obtained at the first stage, and small perturbations of the SSP, $\delta c(z)$, in the vertical waveguide plane is used for this purpose. It can be readily shown that this relation for $\delta\kappa_n$ has the form

$$\delta\kappa_n = (\omega^2/2\kappa_n)\int dz\, S(z)\varphi_n^2, \tag{3.25}$$

where $S(z)=\delta[c^{-2}(z)]$ is an unknown inhomogeneity, φ_n is the vertical eigenfunction of the nth normal mode, and φ_n satisfies the normalization condition $\int_0^\infty \varphi_n^2(z)dz=1$. For the perturbations of the group velocity we arrive at:

$$\delta v_n/v_n = \int dz\, S(z)\theta_n(z), \tag{3.26}$$

where $\theta_n(z)=\sum_m A_{nm}\varphi_n(z)\varphi_m(z)$, $c_n=\omega/\kappa_n$ is the phase velocity of the nth mode, and $A_{nn}=c_n(z v_n - c_n)$ or $A_{nm}(n\neq m)=[4\omega^2 c_n v_n/(\kappa_m^2-\kappa_n^2)]\int dz[\varphi_n(z)\varphi_m(z)/c^2(z)]$. The problem of the reconstruction of $S(z)$ from Eq. (3.25) or (3.26) is also ill-posed. First of all, the systems of functions, $\{u_n\}$ and $\{\theta_n\}$, do not form complete sets. Secondly, only some subset of the set of propagating modes, $\{\varphi_n\}$, can be determined from experimental data. Consequently, some kind of *a priori* information must be taken into account in order to reconstruct the profile, $S(z)$ [12, 14]. In particular, it is convenient in many cases to seek a solution in the form:

$$S(z) = \sum \alpha_m f_m(z), \tag{3.27}$$

where α_m denotes unknown constants. and the functions, f_m, are chosen to be as close as possible to describing the expected structure of the inhomogeneity. Then, substituting Eq. (3.27) in Eqs. (3.25) and (3.26), we once again obtain the algebraic system of type Eq. (3.24), in which $y_n=\delta\kappa_n$, $a_m=\alpha_m$, and $b_{nm}=(\omega^2/2\kappa_n)\int dz\, f_m(z)\varphi_n^2(z)$ for modal-phase tomography, or $y_n=\delta v_n/v_n$, $a_n=\alpha_m$, $b_{nm}=\sum_{\mu} A_{n\mu}\int dz f_m(z)\varphi_\mu(z)\varphi_n(z)$ for modal-pulse tomography. Solving the resulting system by some regularization method, we obtain an expansion of the vertical structure in the selected basis of functions, $\{f_n(z)\}$.

The restrictions, formulated for the planar scheme of modal-phase tomography in [36], remain valid for the proposed three-dimensional, mode-tomography scheme. In addition, the accuracy of the delay-time measurements for modal-pulse tomography is subjected to the same requirements as for the ray-pulse scheme [12].

As a conclusion, it is important to note that the proposed scheme admits a natural factorization of the three-dimensional problem into a family of two-dimensional problems, so that the methods developed for estimation of the resolution of tomographic schemes in two-dimensional cases are applicable here [14, 45]. (Ray-based tomography would allow a factorization only by means of a special algorithm [45].)

3.11 DOPPLER ACOUSTIC TOMOGRAPHY OF BOTTOM STRUCTURE

The *Doppler Tomography Method* is based on combining the synthetic sonar aperture technique with Doppler effects. It was first used with radar to map lunar reflectivity and later in ultrasonic engineering and acoustics [74, 117]. It was demonstrated that a use of the technique in deep-ocean waveguides gives one an opportunity to separate the spatial dependencies of the Doppler shifts, corresponding to different-order-bottom-reflected signals, to signals scattered by the rough interfaces, and to signals propagating along "pure"-water rays. The spatial dependence of the intensities of the signals obtained by integration within rather narrow frequency bands and distance ranges along the appropriate trajectories in the Doppler-frequency-shift-versus-distance plane can be used for determining the reflecting and scattering properties of the ocean bottom. This method has been employed to find the angular dependence of the reflection and scattering coefficients of acoustic signals from smooth and rough bottoms, and to determine density and sound speed in the sediments. In the present section, the opportunities for the use of the Doppler tomography for determining the frequency and angular dependencies of the scattering strength for tonal acoustic signals are discussed. Theory and experiment using the technique are presented in [74, 117].

Figure 3.28 shows the results of the experiment conducted near a sharp coastal slope between shallow and deep-water regions of an ocean waveguide [117]. The sources, emitting tonal acoustic signals with the frequencies f_1=135 Hz and f_2=238 Hz, were towed with the velocity v = 2.1-2.6 m/s at a 50-m depth. Acoustic signals with frequencies, $f(r)$, dependent on source position were received by a single hydrophone of an autonomous recording station located at a height 100 m above the bottom in the shallow part of the waveguide at the range r=0.

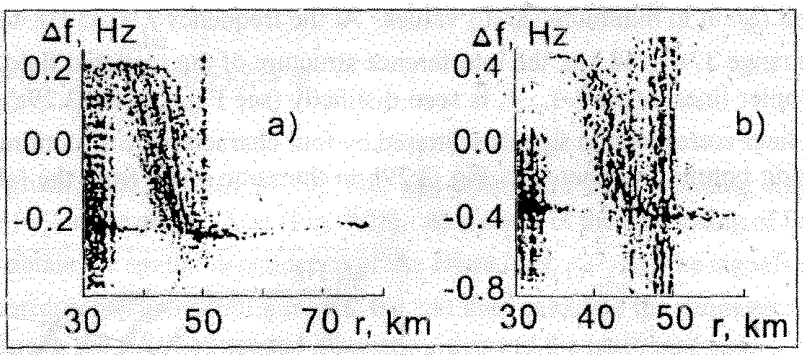

Figure 3.28. Dopplergrams for signals at (a) 135 Hz and (b) 238 Hz received on the shelf at r=0 from a source ship moving off the shelf beginning at 30 km (see Fig. 3.29b). (Adapted from [117].)

To obtain the Doppler-shift dependence on horizontal range, $\Delta f(r)=f(r)-f_0$, the received signal, $p(t)$, which was recorded simultaneously with a reference signal, was heterodyned at the intermediate frequency, f_n=1 Hz, and filtered in the band, Δf_q=2.3 Hz. The signal spectrum

$$S(t,f,\tau) = \frac{1}{\tau}\left|\int_{t}^{t+\tau} p_q(t')\exp(2\pi i f t')\,dt'\right|^2 \qquad (3.28)$$

was calculated for a duration, τ=340 s, of each sample and with a time step of $\Delta\tau$=100 s ($t=l\Delta\tau$, l=1,2...). The processing results are presented in Fig. 3.28 in the Doppler-shift-versus-distance plane, $(\Delta f,r)$, for the ranges, where the contribution of the signals scattered by the underwater slope is the most essential.

The following conclusions can be drawn from the Dopplerograms shown in Fig. 3.28. First, the bottom-reflected signals, which form the field in the shallow part of the waveguide, correspond to the almost horizontal Doppler trajectory, reliably observed when towing the source beyond the distance r> 40 km. The tow distance exceeds the ray-cycle length (10 km) for this region of the waveguide. The Doppler

shifts, corresponding to these signals, are not resolved, because of the small grazing angles, $\chi \le 10^{\circ}$, of the corresponding rays reaching the receiver.

Second, when the source leaves the shallow part of the waveguide ($r>30$ km), positive Doppler shifts appear at the Dopplerograms, which correspond to the signals transmitted from the source in the direction of its motion. After backscattering at the bottom slope, the signals reach the receiver by the rays that have grazing angles within the interval $5^{\circ} \le \chi \le 16^{\circ}$. As the source moves along the deep-water part of the waveguide, the Doppler shifts, corresponding to the scattered signals, vary from maximum ($\Delta f>0$) to minimum ($\Delta f<0$) values. At the frequency $f_1=135$ Hz within the distance range $37<r<48$ km, the interference structure of the scattered field, having four Doppler lines $\Delta f_j(r)$, $j=1,...,4$, is seen distinctly (see Figs. 3.28a, 3.29a). These separate lines correspond to signals scattered by four characteristic discontinuities of the sloping bottom, numbered in Fig. 3.29b in the same order from the left to the right.

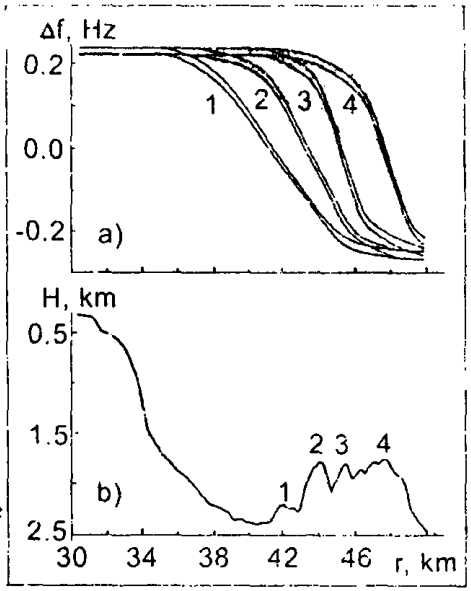

Figure 3.29. (a) Integration domains 1, 2, 3, 4 in the plane "Doppler shift vs. distance", corresponding to the scattering from appropriate bottom discontinuities; (b) Bottom profile (Adapted from [117].)

Third, at the higher radiation frequency, $f_2=238$ Hz, it is more difficult to single out the Doppler trajectories, $\Delta f_j(r)$, against the background of scattered signals produced by the interaction of primary waves with a rough bottom in the range of the incidence angles $0 \le \chi \le \pi/2$ (see Fig. 3.28b). That is, the fine interference structure of the scattered component of the acoustic field vanishes with an increase in radiation frequency. The latter means that the coherence of the scattered-field component decreases with an increase in radiation frequency. In fact, at $f_2=238$ Hz the interference structure of the scattered field is characterized by the only distinct

Doppler trajectory, $\Delta f_1(r)$, within the range $27<r<48$ km. This distinct line corresponds to signals scattered at the first discontinuity of the underwater slope. The Doppler trajectory, $\Delta f_2(r)$, can hardly be seen in the background, while the trajectories $\Delta f_3(r)$ and $\Delta f_4(r)$ are practically absent.

To obtain and compare the angular dependence of the scattering strength, $F_j(\theta)$, at different frequencies for the first, $j=1$, and second, $j=2$, discontinuities of the underwater slope, we first integrate $S(t,f,\tau)$ with respect to Doppler frequency

$$J_j(r) = \frac{1}{\delta f} \int_{f_j-\delta f/2}^{f_j+\delta f/2} S(t(r), f, \tau)\, df \tag{3.29}$$

in the given band, $\delta f = \delta(\Delta f) = 0.02$ Hz, and along the corresponding trajectories, $f_j = \Delta f_j(r) + f_n$, at the plane, $(\Delta f, r)$ (Fig. 3.28). As a result of the processing of Eq. (3.29), we can obtain the spatial dependence of the intensities, $J_j(r)$, of the signals scattered at the corresponding discontinuities. We can then calculate the propagation losses, $J_j'(r)$, due to the first and second discontinuities and the incidence angles of signals

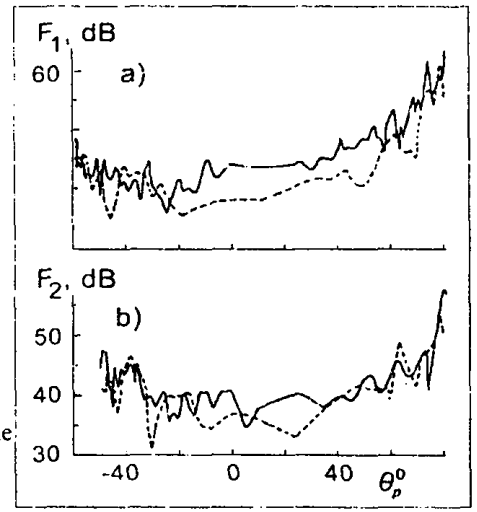

Figure 3.30. The dependence of scattering strength on the angle of incidence on the first (a) and second (b) bottom discontinuities for the frequencies of 238 Hz (solid line) and 135 Hz (dashed line). (Adapted from [117].)

on the discontinuities, $\theta(r)$, by using ray theory. It was assumed and experimentally proven that the bottom-reflection coefficients in the shallow part of the ocean waveguide was equal to unity for all presented incidence angles. After that we can use the experimental data for the acoustic-field intensity, $J_e(f_0)$, and find the necessary angular dependence for the scattering strength by employing the known relation:

$$F_j(\theta) = \log J_j(r(\theta)) - \log J_j^{I}(r(\theta)) - \log J_e(f_0). \qquad (3.30)$$

The results, obtained from the experimental data in accordance with Eq. (3.30), are given in Figs. 3.30. These results show that, if the radiation frequency increases by about 1.8 times, the scattering strength essentially increases by 5 to 10 dB only within the incidence angle range $-20° \le \theta \le 40°$, which is closer to the normal incidence of the primary waves on the slopes of the two discontinuities.

These results demonstrate the broad possibilities of the Doppler tomography method for the determination of seafloor characteristics.

Part II

DIFFRACTION TOMOGRAPHIC METHODS

Chapter 4:

DIFFRACTION TRANSMISSION TOMOGRAPHY FOR MESO- AND MICRO-SCALE OCEANIC INHOMOGENEITIES

Previously discussed tomographic methods were based on the adiabatic approximation, which neglects inter-mode and inter-ray energy exchange. Methods of diffraction tomography do not use the adiabatic approximation. As it is known [8], the applicability condition of the adiabatic approximation is define by the inequality $L > D_h$, where L is a characteristic scale of inhomogeneity, D_h is a maximum scale of the horizontal interference structure of the acoustic field (e.g., length of a ray cycle). If $L < D_h$, then the effects of scattering or diffraction of the acoustic field in the vertical plane become pronounced.

This section deals with the basic principles of acoustic reconstruction of the ocean volume and surface inhomogeneities for the case of $L < D_h$. More detailed mathematical aspects of the solution of the integral equations of diffraction tomography can be found in [5, 118].

4.1 INTEGRAL EQUATIONS OF DIFFRACTION TOMOGRAPHY

Diffraction tomography generally includes a variety of methods that utilize (in their theoretical basis) different physical approximations, such as Born's, Rytov's, Kirchhoff's, etc. [67, 119]. To outline some general problems of diffraction tomography, we shall consider an approach based on a single-scattering approximation [67]. To this end, we shall relate static ("frozen") inhomogeneities of the sound speed, δc, to the space-time structure of the acoustic pressure field, $p(\boldsymbol{R},t)$. The sound source will be monochromatic, i.e., $p(\boldsymbol{R},t)=p(\boldsymbol{R})\exp(i\omega t)$. Assuming the sound-speed perturbations, δc, to be small ($|\delta c| \ll c$) and applying Green's theorem to the Helmholtz equation, we arrive at the following integral equation for the scattered field [49, 67]:

$$p_S(\boldsymbol{R}) = p(\boldsymbol{R}) - p_0(\boldsymbol{R}) = \int_{-\infty}^{\infty} d^3\boldsymbol{R}'\, W(\boldsymbol{R},\boldsymbol{R}')\, g(\boldsymbol{R}'), \tag{4.1}$$

where $p_0(\boldsymbol{R})$ is the acoustic insonifying field ("illuminating" field) in the absence of inhomogeneities, i.e., $\delta c = 0$, $p_S(\boldsymbol{R})$ is the scattered (diffracted) field, $g(\boldsymbol{R}) = 2\delta c(\boldsymbol{R})/c(\boldsymbol{R})$ is a function describing an inhomogeneity, and

$$W(\boldsymbol{R},\boldsymbol{R}') = G_0(\boldsymbol{R},\boldsymbol{R}')\,k_0^2(\boldsymbol{R}')\,p(\boldsymbol{R}'), \quad k_0(\boldsymbol{R}) = \omega/c(\boldsymbol{R}),$$

where $G_0(\boldsymbol{R},\boldsymbol{R}')$ is the Green's function of an unperturbed medium. Therefore, in diffraction tomography, the problem of reconstruction of the inhomogeneity $g(\boldsymbol{R}')$ from measured data, $p_S(\boldsymbol{R})$, is generally reduced to the solution of the integral equation (4.1). However, the field $p(\boldsymbol{R})$ and, hence, the kernel of the integral equation, $W(\boldsymbol{R},\boldsymbol{R}')$, not only depend on the location of the sources and receivers but also on the sound-propagation conditions, which are described by the function $g(\boldsymbol{R}')$. Because of this, strictly speaking, the diffraction-tomographic problem is nonlinear.

A single-scattering approximation whose applicability condition is the smallness of the energy of the scattered field, $p_S(\boldsymbol{R})$, as compared with that of the non-diffracted field $p_0(\boldsymbol{R})$ allows the problem to be linearized. In this approximation, the total field, $p(\boldsymbol{R})$, is replaced by the non-diffracted field, $p_0(\boldsymbol{R})$, in the kernel of Eq. (4.1). As a result, Eq. (4.1) is reduced to a Fredholm integral equation of the second kind with the kernel

$$W \approx W_0(\boldsymbol{R},\boldsymbol{R}') = G_0(\boldsymbol{R},\boldsymbol{R}')\,k_0^2(\boldsymbol{R}')\,p_0(\boldsymbol{R}').$$

In general, the solution of this integral equation also involves certain difficulties. However, in a number of particular circumstances, the reconstruction algorithm for $g(\boldsymbol{R}')$ can be simplified considerably. Let us illustrate this for a plane illuminating wave, $p_0(\boldsymbol{R}) = \exp(i\boldsymbol{k}_i\cdot\boldsymbol{R})$. We assume that the unperturbed reference medium is homogeneous, i.e., $c(\boldsymbol{R}) = C = const$, and unbounded in space. If the measurements of $p_S(\boldsymbol{R})$ are performed in the far field with respect to the inhomogeneities, i.e., $|\boldsymbol{R}'| \ll |\boldsymbol{R}|$, then

$$R_0 = |\boldsymbol{R}-\boldsymbol{R}'| \approx R - \frac{\boldsymbol{R}\cdot\boldsymbol{R}'}{R} + \frac{1}{2R}\left[(R')^2 - \left(\frac{\boldsymbol{R}\cdot\boldsymbol{R}'}{R}\right)^2\right] + \ldots. \tag{4.2}$$

Substituting Eq. (4.2) into the exponent of the Green's function of the homogeneous unbounded space, $\Gamma_0(\boldsymbol{R},\boldsymbol{R}') = \exp(ik_0R_0)/R_0$, we can take into account only the first two expansion terms for the Fraunhofer diffraction zone: $k_0|\boldsymbol{R}'|^2 \ll |\boldsymbol{R}|$. Then, the integral transformation (4.1) with the kernel $W_0(\boldsymbol{R},\boldsymbol{R}')$ can be reduced to the Fourier transform of the desired function $g(\boldsymbol{R})$ [67]:

$$p_S(\boldsymbol{R}) = A_0\int_{V_g} d^3\boldsymbol{R}'\,g(\boldsymbol{R}')\,e^{-i\boldsymbol{q}(\boldsymbol{R})\cdot\boldsymbol{R}'} = A_0\,\hat{g}(\boldsymbol{q}(\boldsymbol{R})), \tag{4.3}$$

where $\hat{g}(\boldsymbol{q})$ is the spatial spectrum of $g(\boldsymbol{R})$,

$$\boldsymbol{q}(\boldsymbol{R}) = \boldsymbol{k}_S - \boldsymbol{k}_i, \quad \boldsymbol{k}_S = k_0\frac{\boldsymbol{R}}{R}, \quad A_0 = \frac{k_0^2}{R}e^{ik_0R},$$

and V_g is used to designate the inhomogeneity-occupied region.

Therefore, the reconstruction algorithm for $g(\boldsymbol{R})$, based on Eq. (4.3), consists of an inverse Fourier transform of the set of all the measured values of the spectrum $\hat{g}(\boldsymbol{q}) = p_s(\boldsymbol{R})$. An exhaustive examination of the values of the complex amplitude of diffracted field (projections) for all possible vectors $\boldsymbol{q}$ can be accomplished in two ways. The first method involves running through all scattered-wave observation angles and for all illuminating-wave incidence angles. It is apparent in this case that the measured values of the spectrum $\hat{g}(\boldsymbol{q})$ in the three-dimensional space of the wave vectors $\boldsymbol{q}$ fall within a sphere of radius $2k_0$. Consequently, spectrum values outside this sphere, for $|\boldsymbol{q}|>2k_0$, can only be determined from *a priori* assumptions.

The second method of an exhaustive search of projections involves running through all frequencies for fixed observation and incidence angles. Here, a measurement region in the space of vectors $\boldsymbol{q}$ is a straight line segment whose boundaries are determined by the range of frequencies used. In reality, even the two methods combined often do not allow the spectrum $\hat{g}(\boldsymbol{q})$ to be determined sufficiently. The limited number of projections make it necessary to interpolate or extrapolate (based on certain *a priori* assumptions) from the measured range of the values of $\boldsymbol{q}$ to the nodes of the lattice for which the integral-equation-solution algorithm is realized.

Let us consider another example of practical interest. Let the measurements be performed with an antenna of sufficient length, so that inhomogeneities for the antenna are located in the Fresnel diffraction zone. In this case, the receiving system allows measurement of not only the wavefront slope, as in the case of the Fraunhofer diffraction, Eq. (4.3), but also the wavefront curvature. This makes it possible to focus the antenna into a preselected region in space, as in optical systems [120]. The formal transition to the Fresnel diffraction is accomplished by taking the third (quadratic in $\boldsymbol{R}_1$) term of Eq. (4.2) into account. As a result, the reconstruction of inhomogeneities will be reduced to running through the focusing parameters (or space points into which the receiving system is focused) with subsequent integral transformation of the measured data.

4.2 SPECIFIC FEATURES OF DIFFRACTION OCEAN ACOUSTIC TOMOGRAPHY

Diffraction methods of tomography have been developed and used extensively in various fields of science and technology, such as ultrasonic diagnostics, non-destructive testing [51], etc. The medium, however, is assumed to be homogeneous in the above applications. The ocean environment is much more complicated. In the low acoustic-frequency range (10 Hz - 1 kHz), the ocean appears as a multi-mode waveguide, which can be inhomogeneous in the vertical and horizontal directions. Reconstruction objects are quite diverse in acoustic diffraction tomography of the ocean and include both spatially distributed random inhomogeneities (subsurface waves, turbulence, sound-speed fine structure , and sea

waves) and relatively compact deterministic formations (icebergs, fish shoals, and various types of acoustic lenses). Therefore, as reconstructable parameters characterizing the object under investigation, one can consider sound-speed and density perturbations, the characteristic function of the body (equal to one in an area occupied by inhomogeneities, and equal to zero outside it), and the correlation function (or its spectrum) of sound speed or waves.

Let us discuss the specific features of diffraction tomography in ocean acoustics. To this end, we shall consider the relationship of the measured field, $p_S(\boldsymbol{R})$, to the function $g(\boldsymbol{R}')$ for a horizontally stratified reference waveguide, $k_0^2(\boldsymbol{R}) = k_0^2(z)$. A mode description of an acoustic field will be used in this case.

Let the initial field, $p_0(\boldsymbol{R})$, be generated by a point source located at the point $\boldsymbol{R}_t = (\boldsymbol{r}_t, z_t)$, where $\boldsymbol{r}_t$ is the vector coordinate in the horizontal plane and z_t is the vertical coordinate. Assuming the inhomogeneity-occupied region, V_g, to be bounded and located far from the source and receiver, mode expansions of the Green's functions, $\Gamma_0(\boldsymbol{R},\boldsymbol{R}')$ and $p_0(\boldsymbol{R}') = G_0(\boldsymbol{R}',\boldsymbol{R}_t)$, in the wave region $k_0|\boldsymbol{R}-\boldsymbol{R}'| \gg 1$, $k_0|\boldsymbol{R}'-\boldsymbol{R}_t| \gg 1$ can be substituted into the formula for the kernel of Eq. (4.1) in a single-scattering approximation, W_0. Then

$$p_S(\boldsymbol{R},\boldsymbol{R}_t) = \sum_{n,m=1}^{N} A_{nm}(\boldsymbol{R},\boldsymbol{R}_t)\,\varphi_n(z)\,\varphi_m(z_t), \tag{4.4}$$

$$A_{nm}(\boldsymbol{R},\boldsymbol{R}_t) = \int\int d^2\boldsymbol{R}'\, L_{nm}(\boldsymbol{R},\boldsymbol{R}_t;\boldsymbol{R}')\, g_{nm}(\boldsymbol{R}'), \tag{4.5}$$

$$g_{nm}(\boldsymbol{R}') = \int dz'\, T_{nm}(z')\, g(\boldsymbol{R}',z'), \tag{4.6}$$

$$T_{nm}(z') = k_0^2(z')\,\varphi_n(z')\,\varphi_m(z'), \tag{4.7a}$$

and

$$L_{nm}(\boldsymbol{R},\boldsymbol{R}_t;\boldsymbol{R}') = \left(\kappa_n\kappa_m|\boldsymbol{R}-\boldsymbol{R}'||\boldsymbol{R}'-\boldsymbol{R}_t|\right)^{-1/2}\times$$

$$\times \exp\left(-i\kappa_m|\boldsymbol{R}-\boldsymbol{R}'| - i\kappa_m|\boldsymbol{R}'-\boldsymbol{R}_t| - i(\pi/2)\right), \tag{4.7b}$$

where N is the number of waveguide-trapped modes, $\varphi_n(z)$ are the vertical modal eigenfunctions of the reference waveguide, and κ_n are the horizontal modal wavenumbers. The complex amplitude of the scattered field, $p_S(\boldsymbol{R},\boldsymbol{R}_t)$, is entirely characterized by the matrix $\|A_{nm}\|$, whose elements are defined by the acoustic-path orientation (source-receiver couple $(\boldsymbol{R},\boldsymbol{R}_t)$) and the numbers of the emitted, n, and received, m, modes. Therefore, the maximum number of independent tomographic projections equals MN^2, where M is the number of acoustic paths. The elements of the matrix $\|A_{nm}\|$ are readily determined from the diffracted field values because of the

orthogonality of the vertical modal eigenfunctions. Considering the normalization of the vertical modal functions $\int_0^\infty \varphi_n^2(z)dz = 1$, Eq. (4.4) yields

$$A_{nm}(\boldsymbol{R},\boldsymbol{R}_1) = \int\int dz\,dz_1\, p_S(\boldsymbol{R},\boldsymbol{R}_1)\,\varphi_n(z)\,\varphi_m(z_1). \tag{4.8}$$

It is apparent from the above that Eq. (4.4) imposes no fundamental constraint on the possibility of determining $\|A_{nm}\|$. A more complicated situation arises when $g(\boldsymbol{R}')$ is reconstructed from the values of $A_{nm}(\boldsymbol{R},\boldsymbol{R}_1)$. The kernel of the integral transformation of $g(\boldsymbol{R}')$ to $A_{nm}(\boldsymbol{R},\boldsymbol{R}_1)$ is factorized in horizontal (kernel L_{nm}) and vertical (kernel T_{nm}) coordinates. Consequently, the initial integral equation is split into two Eqs. (4.5) and (4.6).

The reconstruction algorithm for the horizontal structure, based on Eq. (4.5), for fixed indices n and m is totally identical to the above case of a homogeneous unbounded space. The problems arising here are similar as well: restrictions in measuring the total spatial spectrum, $\hat{g}_{nm}(\boldsymbol{q})$, the need to interpolate or extrapolate to the nodes of the given lattice, the need to use *a priori* information, etc.

The possibility of reconstruction of the structure of inhomogeneities in a vertical plane, using Eq. (4.6), depends on the matrix $\|T_{nm}(z')\|$. *A priori* information is generally required due to the incompleteness of the set of N^2 functions $T_{nm}(z')$. This can be demonstrated using an example of an isovelocity waveguide, $k_0^2(z) = const$. Writing the waveguide eigenfunctions as the sum of two Brillouin waves, $\exp(\pm i\chi_n z)$, where $\chi_n = \sqrt{k_0^2 - \kappa_n^2}$, we obtain

$$g_{nm}(\boldsymbol{R}') = \sum_{\pm} \hat{g}(\boldsymbol{r}';\pm\chi_n \pm\chi_m).$$

Summation is performed over all combinations of "+" and "-" signs. Since the matrix $\|g_{nm}\|$ is only determined by spectrum components of the type $\hat{g}(\chi_n - \chi_m)$ and $\hat{g}(\chi_n + \chi_m)$, where $\hat{g}(-\chi) = \hat{g}(+\chi)$, information about the other spectral components is absent in the single scattering approximation. Moreover, g_{nm} is proportional to the sum of spectral components $\hat{g}(\chi_n - \chi_m)$ and $\hat{g}(\chi_n + \chi_m)$. It is, therefore, impossible in general to determine the vertical spectrum of inhomogeneities without some *a priori* assumptions about its structure.

The role of *a priori* information becomes much more important in the ocean than in the case of a homogeneous unbounded space. Firstly, the incidence and scattering angles are restricted to small values in the vertical plane. Secondly, measurements with a large number of receivers and transmitters are difficult to realize in the horizontal plane because of technical and cost reasons. Thirdly, a strong dependence of reconstruction accuracy on frequency restricts the range of the illuminating field frequencies. These factors make it necessary to choose an inhomogeneity model that can be described by the smallest number of parameters sufficient for solution of the reconstruction problem with the given considerable

incompleteness of the acoustic information measured.

Another important aspect of diffraction tomography of the ocean involves the acquisition of information on the diffracted (scattered) field structure. In addition to the above-mentioned requirements to get an accurate reconstruction, such as illuminating-angle variations, diffracted-field recording, or the illuminating-field frequency variation, one should use the methods to determine the matrix $\|A_{nm}\|$. This would be equivalent to singling out individual waveguide modes. Spatial filtering by vertical or horizontal antennae is used for this purpose. A selection of certain intervals of signal-arrival angles in this case can distinguish a certain mode or a mode package [2, 18, 48, 56]. The same aim can be accomplished through time sampling together with pulse excitation. Finally, the Doppler effect can be used in diagnostics of inhomogeneities when the observation time is much greater than the characteristic scale of the inhomogeneity temporal variation [18, 48] or when the illuminating source is in motion [3].

4.3 TRANSILLUMINATION PULSED DIFFRACTION TOMOGRAPHY OF RANDOM OCEANIC INHOMOGENEITIES

The conventional solution of the diffraction tomography problem involves the use of wideband illuminating signals. Temporal sampling of short pulses scattered by an inhomogeneity allows singling out individual regions, pulse spaces, of the ocean medium from which the scattered signal reaches a receiver at one and the same time [67], i.e., temporal sampling allows inhomogeneity localization in a corresponding pulse space. If the receiving antenna has a sufficiently narrow directional pattern in the horizontal plane, a scattering inhomogeneity can be fully localized. Its location is determined by the region where the corresponding pulse space and the direction pattern of the antenna intersect. Such a scheme works well if the horizontal inhomogeneity scale, L, is of the order of the illuminating wavelength, λ.

If $L \gg \lambda$ such that the scattering form factor λ/L is less than or of the order of the antenna directional pattern width in horizontal plane, the inhomogeneity scatters mostly in forward direction. Then the scattered signal concentrates near a straight line that connects the source and receiver. In this case, no conventional method permits inhomogeneity localization with respect to the horizontal coordinate. Moreover, a relatively weak scattered signal arrives at the receiver simultaneously with a relatively strong illuminating (direct) signal and is masked by it. There are a few different approaches for solving the problem in this case. Let us consider one of them -- a *differential method* [2, 50], which employs the multi-mode structure and dispersion properties of an ocean waveguide.

4.3.1 Modal Differential Ocean Acoustic Tomography

The backscattering phenomenon [67, 121, 122] or the influence of the inhomogeneity on the characteristics of signals transmitted through the investigated

region are used for the acoustic diagnostics of such inhomogeneities [8, 41]. Inhomogeneities can be localized, i.e., the spatial distribution of their parameters can be reconstructed, by pulse gating in combination with directional radiation and reception or by the application of acoustic tomography principles. These two approaches supplement each other. The first one is usually employed for obtaining information about inhomogeneities with the characteristic scale, L, of the order of the acoustic wavelength, λ. Then, one can adjust the algorithm to detect inhomogeneities with scales $L \gg \lambda$.

The tomographic principle of the localization of inhomogeneities is based on the simultaneous processing of a large number of arrived signals transmitted through the investigated region of the ocean along different acoustic paths. In fact, let us assume that a radiating system effectively generates only the nth mode of an ocean waveguide and that a receiving system detects the mth mode [50], and the group velocities of these modes, v_n and v_m, noticeably differ. Let an inhomogeneity be located at the horizontal distance x_Σ from the source. The inhomogeneity causes energy transformation from the nth to the mth mode (Fig. 4.1). The signal-propagation time along the path is $t = a/v_m + x_\Sigma(1/v_n - 1/v_m)$, where a is the length of the path. It can be easily seen that propagation times depend on the positions of the inhomogeneities, so the distribution of the inhomogeneities along the path can be reconstructed from the temporal structure of the received signal, as is done in the reconstruction of the scatterer distribution from backscattered signals [8]. This methodology also applies to the case when excited and received modal spectra are sufficiently narrow and distantly spaced. It will be shown below that the mode selection problem can be solved not only by using long vertical arrays, but also by the existence of natural "mode shadow" zones in the ocean.

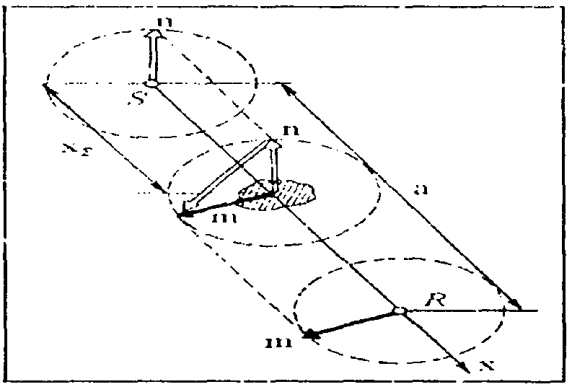

Figure 4.1. Energy transformation from mode n to mode m due to the inhomogeneity influence. (Adapted from [50].)

Here we consider a more detailed analysis of the reconstruction of the statistical parameters of the volume perturbations of the sound speed, $\delta c(x,y,z,t)$, and the relief, $\zeta(x,y,t)$, of the rough ocean surface along the specified acoustic path from the analysis of the intensity envelope function of the received pulsed signal. We

assume that a source generates the nth mode with the amplitude $A_S(n)$ in a waveguide with the vertical sound speed profile, $c(z)$, and that a receiving system identifies the mth mode with the amplitude $A_R(m)$. We consider the perturbations of the sound speed and the elevations of the rough surface to be stationary in time and quasi-homogeneous with respect to the horizontal coordinates, x and y. Assuming that the Rayleigh parameter $P=2k\sigma\sin\chi\ll 1$ [8], where k is the sound wave number, σ is the root-mean-square displacement of the rough surface, χ is the grazing angle of sound wave relative to the horizontal plane, and $\delta c \ll c$, we can represent the spectral component of complex sound pressure at an arbitrary point of the waveguide in the form of the modal sum [8, 50, 125, 126]

$$p(x,y,z,\omega) = \sum_{n=1}^{N} S_n(x,y,\omega)\varphi_n(z),$$

where $\varphi_n(z)$ denotes the eigenfunctions of the unperturbed waveguide, S_n denotes the complex modal amplitudes, which depend on the inhomogeneities, and N is the number of generated modes. Taking the quasi-static nature of the inhomogeneities into account, we may assume that $\varphi_n(z,\omega) = \varphi_n(z,\omega_*) = \varphi_n(z)$, where ω_* is the carrier frequency of the sensing signal. Applying Green's integral theorem for the first-order perturbation approximation, we obtain the complex amplitude of the backscattered component of the mth mode [119, 125, 126]:

$$S_m^{(1)}(x,y,\omega) = i\sum_{n=1}^{N}\iint_{\Sigma} dx'dy' \int_{-\infty}^{\infty} d\omega' b_n^m(x',y',\omega')$$

$$\times H_0^{(2)}[\kappa_m(\omega)\sqrt{(x-x')^2+(y-y')^2}\,]S_n^{(0)}(x',y',\omega-\omega'). \qquad (4.9)$$

In Eq. (4.9) $S_n^{(0)}(x,y,\omega) = A_S(n)F(\omega-\omega_*)H_0^{(2)}(\kappa_n(\omega+\omega_*)\sqrt{x^2+y^2})$ denotes the modal amplitudes of the radiated signal, $F(\omega)$ is the frequency spectrum of the radiated signal, and

$$b_n^m(x',y',\omega') = (1/8\pi)\varphi_n(0)\varphi_m(0)\zeta(x',y',\omega') + (1/4\pi)\times$$

$$\times(\omega_*+\omega-\omega')^2\int_0^z dz'\varphi_n(z')\varphi_m(z')\delta c(x',y',z',\omega')/c^3(z'). \qquad (4.10)$$

Eq. (4.10), which describes the scattering matrix, includes terms that characterize scattering by the rough surface and by volume inhomogeneities. Small-angle scattering occurs for large-scale inhomogeneities [8, 67, 119]. In this case, we may use the Taylor series expansion: $\sqrt{x'^2+y'^2}\approx x'+y'^2/2x'$, $\sqrt{(a-x')^2+y'^2}\approx a-x'+y'^2/2(a-x')$, and $\kappa_m(\omega)\approx\kappa_m(\omega_*)+(\omega-\omega_*)/v_m+\gamma_m(\omega-\omega_*)^2$, where $v_m=(d\kappa_m/d\omega)^{-1}|_{\omega=\omega_*}$ is the mode group velocity at the carrier frequency, and $\gamma_m=0.5(d^2\kappa_m/d\omega^2)|_{\omega=\omega_*}$. Using these expansions and

neglecting intra-modal dispersion (for the signal with narrow spectrum), we obtain from Eq. (4.9)

$$S_m^{(1)}(a,0,t) = -4\sum_{n=1}^{N} A_S(n)\int_0^a dx' \int_{-\infty}^{\infty} dy' b_n^m\left(x', y', t - \frac{a-x'}{v_m}\right) [\sqrt{\kappa_m \kappa_n}\sqrt{x'(a-x')}]^{-1} \times$$

$$\times F\left(t - \frac{a-x'}{v_m} - \frac{x'}{v_n}\right) \exp[-i\kappa_m(a-x'+y'^2/2(a-x')) - i\kappa_n(x'+y'^2/2x') - i\pi/2]. \tag{4.11}$$

On the basis of Eq. (4.11), the intensity of the single-scattered component of the field at the output of the receiving system has a form

$$\langle |p^{(1)}(a,0,t)|^2 \rangle = \sum_{n,m,\alpha,\mu} A_R(m) A_R^*(\mu) A_S(n) A_S^*(\alpha) I_{m\alpha}^{n\mu}, \tag{4.12}$$

where $I_{m\alpha}^{n\mu}$ depends on the spatial spectrum of the inhomogeneity, W, and is given by

$$I_{m\alpha}^{n\mu} = (32\pi/k^3 a)\int_0^a dx' F(t-(a-x')/v_m - x'/v_n) F^*(t-(a-x')/v_\mu - x'/v_\alpha) \times$$

$$\times \exp[i(\kappa_n - \kappa_\mu)x' + i(\kappa_\mu - \kappa_m)(a-x')] \int_{-\infty}^{\infty} dk_1 W_{mn}^{n\mu}[(\kappa_m + \kappa_\mu - \kappa_n - \kappa_\alpha)/2, k_1, x']. \tag{4.13}$$

The spectrum $W_{m\alpha}^{n\mu}(k_x, k_y, x')$ is the Fourier transform of the correlation function of the inhomogeneity:

$$B_{n\mu}^{m\alpha}(x, y, \tau, x') = \langle b_n^m(x'+x/2, y'+y/2, t+\tau/2) b_\mu^\alpha(x'-x/2, y'-y/2, t-\tau/2)\rangle$$

with respect to x and y at $\tau = 0$. It has been assumed in the derivation of Eqs. (4.11)-(4.13) that $L > \lambda\sqrt{a\Delta f}/c$, where Δf is the width of the frequency spectrum of the radiating signal, and $L/c \ll T_C, T_\xi$, where T_C and T_ξ are the temporal correlation radii of the sound speed perturbations and the surface roughness, respectively. Let $F(t)$ be a rectangular unit pulse of the duration T. Then, using Eq. (4.13), we can obtain from Eq. (4.12):

$$\langle |p^{(1)}(a,t)|^2 \rangle \approx (32\pi/k^3 a) |A_R(m)|^2 |A_S(n)|^2 \Delta x \int_{-\infty}^{\infty} dk\, W_{mn}^{nm}(\kappa_m - \kappa_n, k, x_\Sigma), \tag{4.14}$$

where $x_\Sigma = v_n v_m (t - a/v_m - T/2)/|v_n - v_m|$ and $\Delta x = v_n v_m T/|v_n - v_m|$. It has been assumed in Eq. (4.14) that the spatial resolution, Δx, is smaller than the horizontal fluctuation scale of the statistical characteristics of the inhomogeneities.

It is evident from Eq. (4.14) that the signal scattered by an inhomogeneous

layer of the thickness Δx at the distance $x_\Sigma(t_1)$ from the receiving system is recorded at $t = t_1$. Consequently, the distribution of the spatial inhomogeneity characteristics along the path can be reconstructed by scanning t.

The spatial resolution Δx is determined by the quantities T and $|v_n - v_m|$. A required spatial resolution can be achieved by using modes with distinctly different group velocities. This situation occurs for shallow-sea conditions and for the ocean waveguides with surface duct. For the depth dependence of the sound speed profile, $c(z)$, shown in Fig. 4.2a, Fig. 4.2b shows a typical curve of the group velocity, v_n, as a function of the mode number n. The resolution is $\Delta x \approx 20$ km for $|v_n - v_m| \approx 10$ m/s and $T \approx 0.1$ s. The estimate of Δx is obtained without taking intra-modal dispersion into account. Intra-modal dispersion causes Δx to increase, because T must be replaced by the duration T_{eff} of the spread pulse. This diminishes the sensitivity of the method. The spread of the pulse by intra-modal dispersion can be compensated for by special filtration. The form of the filter depends on x_Σ and the configuration of the overall signal-processing system. Thus, it is a fairly complex compensating procedure.

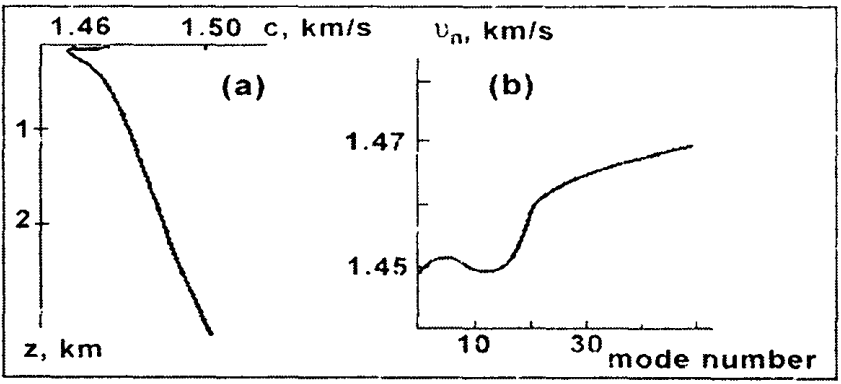

Figure 4.2. Surface-duct waveguide: (a) vertical sound speed profile; (b) mode group velocity dependence on mode number. (Adapted from [50].)

Individual modes cannot always be resolved in real situations. If the array is capable of distinguishing only groups of modes in the range $\Delta n \Delta m$, spatial resolution deteriorates, because the inter-modal dispersion within a particular group will now be a factor. If Δx is greater than the mode interference scale, the received signal has the form

$$\langle |p^{(1)}(a,t)|^2 \rangle \approx \sum_{n,m}^{n+\Delta n, m+\Delta m} |A_S(n)^2| \, |A_R(m)|^2 \, I_{nm}^{mn}(a,t).$$

Let us consider a surface-duct channel with a linear depth dependence of the sound speed: $C(z) = c + \alpha z$, where $\alpha = 0.017$ s^{-1} and $c = 1.47$ km/s. The emergence angle of the Brillouin wave, $\theta_n(z) = \cos^{-1}[\kappa_n / k(z)]$, at the depth z depends on the group velocity

v_n (see Fig. 4.3). A vertical radiating array situated near the surface (z_A=100 m) with the horizontally directed beampattern of the width θ_A generates a group of the low-order modes in this waveguide. A group of the higher-order modes can be distinguished by placing an analogous receiving array at the greater depth of 4 km for the inhomogeneity-loaded waveguide. The deviation of the group velocities within each group is about 2 m/s for θ_A=0.1 (in radian), and the difference in group velocities between groups is about 20 m/s (see Fig. 4.3). Then $\Delta x \sim 0.1a$. The curves of $\theta_n(v_n)$ show that the resolution can be substantially improved by varying the directivity of the array.

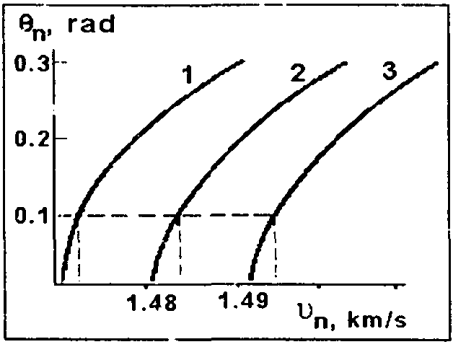

Figure 4.3. Angle of emergence of a Brillouin wave versus mode group velocity at various depths (channel with a linear profile): 1) z=0.1 km, 2) z=2 km, 3) z=4 km. (Adapted from [50].)

In many cases, a mode group can be separated by combining natural and artificial shadow zones. The natural shadow zone is created by depth-wise spacing of the arrays, and the artificial shadow zone depends on the directivity of arrays. It is more favorable from a practical point of view to use small arrays and to place them in "deep" mode shadow zones. At least three cases of the existence of well-developed natural mode shadow zones can be indicated: 1) when the radiator is situated on a shelf, and the receiver is in deep water near the bottom; 2) when the radiator and the receiver are situated in adjacent waveguides; 3) when the radiator and the receiver are situated near large bottom irregularities. In the first case only the lowest modes are excited efficiently, because the modes are cut off by the shelf wedge, and the receiver detects predominantly the higher modes, which are generated as the signal propagates in the range-dependent waveguide. In the second case the modal shadow zone is created by the generation of modes localized in one waveguide and the reception of modes localized in the other waveguide (the adjacent region of the waveguides can be diagnosed in this case). In the third case, spatial selection is induced by large underwater elevations through the same mechanism as in the shelf wedge zone.

If the analysis is carried out for the small perturbation approximation, the horizontal range under investigation is limited by: $a_{max} \ll d$, where d is the total characteristic scattering diameter [8, 67]. The above-described diagnostic technique is applicable not only in waveguides of various kinds, but also in any multimode media, in which inhomogeneities induce energy redistribution in the modal spectrum. The feasibility of the diagnostics of inhomogeneities by analyzing reverberation signals in the "transillumination" scheme has been investigated previously [127],

where it has been proposed that the angular dependence of the sound scattering coefficient for the rough ocean surface is determined from the measured values of the intensity before reverberation onsets.

It has been shown [46, 50] that the distribution of the parameters of oceanic inhomogeneities along an acoustic path can be reconstructed by the "strobing pulse method," if compact mode groups widely spaced in the modal spectrum are generated and received. The statistically averaged intensity of the recorded signal, $\langle |p(t)|^2 \rangle$, as a function of the time for the excitation of the nth mode and reception of the mth mode carries the information about the matrix $\|\sigma_{nm}(x_\Sigma)\|$ characterizing the inhomogeneities as a function of their positions, x_Σ, along the path:

$$\langle |p_{nm}(t)|^2 \rangle = \frac{2}{\pi k a} |A_S(n)|^2 |A_R(m)|^2 \sigma_{nm}(x_\Sigma) .$$

The value of the matrix element, σ_{nm}, indicates the amount by which the intensity of the recorded signal (scattered by the zone Δx from the nth into the mth mode) is smaller than the intensity of the "illuminating" signal for a receiving system with $|A_R(n)|^2 = |A_R(m)|^2$.

Let us analyze the expressions for σ_{nm} in order to consider the possibilities of identifying various types of inhomogeneities and determining their parameters. Since every horizontal element Δx contains different types of inhomogeneities, including volume fluctuations of the sound speed (e.g., thermohaline fine structure, random field of internal waves, turbulence, etc.) and fluctuations of the relief of the rough ocean surface (wind waves and swell), the matrix $\|\sigma_{nm}\|$ corresponding to the element Δx characterizes the total contribution of all types of inhomogeneities. The existence of disparities in the spatial and temporal characteristics of the inhomogeneities enables us to separate the contributions of the individual types of inhomogeneities by selecting the parameters of the radiating and receiving systems. Of course, it is necessary in this case to utilize *a priori* information about the structure of the correlation function of inhomogeneities. The actual reconstruction of the inhomogeneities along the propagation path includes the determination of the quantitative values of the parameters (or some of their combination) describing the inhomogeneity. As examples, we consider several typical models describing different types of inhomogeneities.

Volume Inhomogeneities. The following relation has been obtained in [46] for volume inhomogeneities:

$$\sigma_{nm}(x_\Sigma) = \omega_*^2 c^2 \Delta x \int_0^\infty \int dz_1 dz_2 \frac{\varphi_n(z_1)\varphi_m(z_1)\varphi_n(z_2)\varphi_m(z_2)}{c^3(z_1)c^3(z_2)} \times$$

$$\times \int_{-\infty}^{\infty} dx' B(x',0;z_1,z_2;x_\Sigma) \exp[ix'(\kappa_n - \kappa_m)], \qquad (4.15)$$

where $\varphi_n(z)$ denotes the vertical eigenfunctions of the waveguide, $c(z)$ is the sound speed at the depth z, and

$$B(x',y',z_1,z_2,x_\Sigma)=\langle\delta c(x_\Sigma+x'/2,y+y'/2,z_1,t)\delta c(x_\Sigma-x'/2,y-y'/2,z_2,t)\rangle$$

is the spatial correlation function of the sound speed fluctuations $\delta c(x,y,z,t)$. We can specify the spatial correlation function for different types of volume inhomogeneities.

Thermohaline Fine Structure of the Sound Speed. The correlation function for inhomogeneities of this type can be written approximately in the form

$$B(x',y',z_1,z_2,x_\Sigma)=\langle(\delta c)^2\rangle\Phi_1(x',y')\Phi_2(z_1-z_2)\Phi_3\left(\frac{z_1+z_2}{2}\right), \tag{4.16}$$

where d is the thickness of the waveguide subsurface layer in which the inhomogeneities are concentrated, $\langle(\delta c)^2\rangle$ is the variance of the sound speed fluctuations, and $\Phi_1(0,0)=1$, $\Phi_2(0)=1$, $\Phi_3(z)=1,0$ at $z\le d$ and $z>d$, respectively. It can be assumed that $\Phi_1(x',0)=\exp(-x'^2/l_x^2)$ and $\Phi_2(z)=\exp(-z^2/l_z^2)$, where l_x and l_z are correlation lengths. For $l_z\ll q_n^{-1}, q_m^{-2}=k^2-\kappa_m^2$,
we have

$$\sigma_{nm}=\pi k^2\Delta x\, l_x l_z\langle(\delta c/c)^2\rangle\exp\left[-\frac{l_x^2(\kappa_n-\kappa_m)^2}{4}\right]\int_0^d dz\,\varphi_n^2(z)\varphi_m^2(z). \tag{4.17}$$

Using the WKB approximation for the waveguide eigenfunctions in a channel with the linear sound speed profile $c(z)=c+\alpha z$, we obtain [8. 46, 49]:

$$\sigma_{nm}(x_\Sigma)=4\pi k^2\alpha^2\Delta x M_{nm}(x_\Sigma)/[c^2\theta_n^2(0)\theta_m^2(0)], \tag{4.18}$$

where $M_{nm}(x_\Sigma)=\langle(\delta c/c)^2\rangle l_x l_z d\exp[-l_x^2(\kappa_n-\kappa_m)^2/4]$ characterizes the "power" of fine-structure variations of the sound speed along the path, and $\theta_n(z)=\cos^{-1}[\kappa_n/(2\pi f/c(z))]$ is the emergence angle of the Brillouin wave at the depth z. Consequently, the diagnostics of the fine structure of the sound speed is reduced to determining $M_{nm}(x_\Sigma)$. According to Eqs.(4.17) and (4.18), the matrix element at the fixed angles θ_n and θ_m attains a maximum for the frequency $f_{\max}=2c/[\pi l_x(\theta_n^2-\theta_m^2)]$. We can therefore estimate the horizontal correlation radius l_x from the maximum of σ_{nm} by varying the radiation frequency, f. Additional *a priori* information is required to estimate the rest of parameters.

We estimate the value of σ_{nm} for $\theta_n^2(0)=0.03$, $\theta_m^2(0)=10^{-3}$, $T=0.2$ s, $\alpha=0.017$ s^{-1}, and $c=1.47$ km/s, which corresponds to the spatial resolution $\Delta x=50$ km. For the typical values $l_x=100$ m, $l_z=1$ m, $d=500$ m, $\langle(\delta c/c)^2\rangle=10^{-9}$ for the frequency $f=200$ Hz, we have $\sigma_{nm}\approx 10^{-5}$.

Turbulence. The spectrum of the correlation function has the form of a power law in this case [8]. The correlation function, Eq. (4.16), can also be used for anisotropic turbulence. We consider a generalized power-law spectrum of horizontally isotropic turbulence [46]:

$$\Phi_1(k_x,k_y)=R_1(k_x^2+k_y^2)^r(k_0^2+k_x^2+k_y^2)^{-p}\exp[-(k_x^2+k_y^2)/k_*^2]$$

and (4.19)

$$\Phi_2(k_z)=R_2k_z^{2\mu+1}(\kappa_0^2+k_z^2)^{-\nu}\exp[-k_z^2/\kappa_*^2],$$

where $k_0 \ll k_*$, $p>r+1$, $\kappa_0 \ll \kappa_*$, and $\nu>\mu+1$. The coefficients R_1 and R_2 are determined by the normalization conditions for Φ_1 and Φ_2. We obtain the following equation for the matrix element, σ_{nm}, from Eqs. (4.15), (4.16) and (4.19) for $k_0^2 \ll (\kappa_n-\kappa_m)^2$:

$$\sigma_{nm}\approx 2k^2\Delta x\langle(\delta c/c)^2\rangle|k_0/(\kappa_n-\kappa_m)|^{2p-2r-1}k_0^{-1}\exp[-(\kappa_n-\kappa_m)^2/k_*^2]\times$$

$$\times\{\Gamma(1/2)\Psi\left[\frac{1}{2},\frac{3}{2}+r-p,(\kappa_n-\kappa_m)^2/k_*^2\right]/\Gamma(r+1)\Psi[r+1,r+2-p,(k_0/k_*)^2]\}$$

$$\int_0^\infty\int dz_1dz_2\varphi_n(z_1)\,\varphi_m(z_1)\varphi_n(z_2)\varphi_m(z_2)\,\Phi_2(z_1-z_2)\Phi_3\left(\frac{z_1+z_2}{2}\right), \qquad (4.20)$$

where $\Gamma(\cdot)$ is the gamma function and $\Psi(\cdot)$ is a confluent hypergeometric function. We obtain Eq. (4.18) for σ_{nm} in a channel with the linear sound speed profile with M_{nm} in the form

$$M_{nm}=2\sqrt{\frac{2}{\pi}\left\langle\left(\frac{\delta c}{c}\right)^2\right\rangle\frac{d}{k_0\kappa_0}}\left\{\left|\frac{\kappa_0}{q_n-q_m}\right|^{2\nu-2\mu-1}\exp[-(q_n-q_m)^2/\kappa_*^2]\right.$$

$$\left.+\left|\frac{\kappa_0}{q_n+q_m}\right|^{2\nu-2\mu-1}\exp[-(q_n+q_m)^2/\kappa_*^2]\right\}R_{nm}, \qquad (4.21)$$

where

$$R_{nm}=(r+1)(p-r-1)(p-r)(\mu+1)(\nu-\mu-1)|k_0/(\kappa_n-\kappa_m)|^{2p-2r-1}/[p(2p-2r-1)],$$

when $k_* \gg |\kappa_n-\kappa_m| \gg k_0$ and

$$R_{nm}=(r+1)(p-r-1)(\mu+1)(\nu-\mu-1)/[(2r+1)(2p-2r-1)\nu],$$

when $k_0 \gg |\kappa_n - \kappa_m|$, $d \gg |q_n - q_m|^{-1}$, and $|q_n - q_m| \gg \kappa_0$. Thus, the turbulence diagnostics are also reducible to the determination of the power of the turbulent layer, M_{nm}, which, in turn, is determined by the set of parameters d, $\langle(\delta c/c)^2\rangle$, k_0, p, r, ν, μ, κ_0 (the dependence on κ_* is weak, because usually $\kappa_* \gg q_n + q_m$). It is virtually impossible to estimate the quantities d, $\langle(\delta c/c)^2\rangle$, k_0, and κ_0 themselves rather than some combination of them without drawing on additional information. It is readily discerned from Eqs.(4.18) and (4.21) that the parameters $(\nu - \mu)$ and $(\nu - \mu + p - r)$ can be determined in principle from measurements of the frequency dependence $\sigma_{nm}(f)$ at the fixed angles θ_n and θ_m.

A quantitative estimation of scattering matrix for the typical values $r=0$, $p=11/6$, $\nu=11/6$, $\mu=-1/2$ [46], $k_0=0.1\ m^{-1}$, $\kappa_0=0.1\ m^{-1}$, $d=500$ m, $\langle(\delta c/c)^2\rangle \approx 10^{-9}$, and the same parameters of the field and waveguide as above, yields $\sigma_{nm} \approx 4\cdot10^{-5}$. For $k_0=10^{-3}\ m^{-1}$ and $\langle(\delta c/c)^2\rangle \approx 10^{-8}$, we have $\sigma_{nm} \approx 6\cdot10^{-7}$.

Internal Waves. Using the Garrett-Munk model for the spatial spectrum of the sound speed correlation function [67], we obtain the matrix element σ_{nm} in the form [46]:

$$\sigma_{nm} = \frac{16 j_* k^2}{\pi b} \frac{\omega_i}{N_0} \langle\mu_0^2\rangle \Delta x \int_0^\infty\int dz_1 dz_2 \left[\frac{N\left(\frac{z_1+z_2}{2}\right)}{N_0}\right]^3 \varphi_n(z_1)\varphi_m(z_1)\varphi_n(z_2)\varphi_m(z_2) \times$$

$$\times \int_0^\infty\int \frac{\kappa\sqrt{k'^2+(\kappa_n-\kappa_m)^2}\cos\kappa(z_1-z_2)\,dk'\,d\kappa}{\left[k'^2+(\kappa_n-\kappa_m)^2+\frac{\omega_i^2}{N^2(\bar{z})}\kappa^2\right]^2\left[\kappa^2+j_*^2\frac{\pi^2N^2(\bar{z})}{b^2N_0^2}\right]}, \qquad (4.22)$$

where $N(z)$ is the Brunt-Väisälä frequency, $N_0=N(0)$, ω_i is the inertial frequency, $\langle\mu_0^2\rangle$ is the statistical mean-squared relative fluctuation of the sound speed near the ocean surface, and

$$b=\int_0^\infty dz\,[N(z)/N_0],\quad \bar{z}=(z_1+z_2)/2.$$

On the basis of experimental data, Munk and Zachariasen take $j_*=3$ [8]. It is evident from Eq. (4.22) that the diagnostic problem in this case is reduced to the determination of the parameter $\langle\mu_0^2\rangle$, from which the energy density of internal waves on unit area is determined uniquely.

Let us estimate the expected value of σ_{nm} quantitatively for a bilinear channel $c(z)=c+\alpha|z-b|$. In the WKB approximation for the waveguide eigenfunctions for

$\theta_n^2 \gg \theta_m^2$, (ω_t/N_0), we arrive at

$$\sigma_{nm} = 32\pi\sqrt{2\pi}\,\frac{\omega_t}{N_0}\,\frac{j_*\alpha^2\Delta x\,\langle\mu_0^2\rangle k}{c^2\theta_n^5\theta_m^2(k^2\theta_n^2+j_*^2\pi^2/b^2)}.$$

Using the same values of θ_n, θ_m, α, and T (and, accordingly, Δx) as above at a frequency f=200 Hz, along with $\langle\mu_0^2\rangle=10^{-7}$, $\omega_t/N_0=10^{-2}$ and b=100 m, we obtain $\sigma_{nm}=3\cdot10^{-4}$. If θ_n^2=0.1 and T=0.5 s (we have exactly the same spatial resolution Δx=50 km in this case), the information signal is attenuated considerably: $\sigma_{nm}=5.4\cdot10^{-6}$.

Ocean Waves. For this type of irregularities [46], we arrive at

$$\sigma_{nm}(x_\Sigma) = [\varphi'_n(0)]^2[\varphi'_m(0)]^2\,\frac{\Delta x}{8\pi k^2}\int_{-\infty}^{\infty} dk'\,W(\kappa_n-\kappa_m,k',x_\Sigma), \tag{4.23}$$

where W is the spatial spectrum of the waves.

Wind Waves. All the characteristics of fully developed wind waves are uniquely determined by the wind velocity V and wind direction Ψ_V (where Ψ_V is the angle between the direction of the wind and the horizontal axis) for a specified structure of the spatial spectrum. Assuming uniform angular distribution of the energy in the spectrum within the angular interval π and taking into account the relation $\sigma_{nm}(\Psi_V)=\sigma_{nm}(|\Psi_V|)=\sigma_{nm}(|\pi-\Psi_V|)$, we obtain the Pierson-Moskowitz (PM) sea-surface wind spectrum [121] for $f<0.27gc/(V^2|0_n^2-0_m^2|)$ in the form

$$\sigma_{nm}(x_\Sigma) = 0.174A_{PM}[\varphi'_n(0)\varphi'_m(0)]^2\Delta x V^6(x_\Sigma)k^{-2}g^{-3}, \tag{4.24}$$

where $A_{PM}=8.1\cdot10^{-3}$ and g=9.8 m/s^2 (the acceleration of gravity). Consequently, the wind velocity distribution $V(x_\Sigma)$ along the acoustic path can be reconstructed according to Eq. (4.24).

In a channel with a linear speed profile, $[\varphi'_n(0)]^2=[\frac{\partial\varphi_n(z)}{\partial z}]^2|_{z=0}=2\alpha k^2/c$, the quantitative estimate is $\sigma_{nm}=3\cdot10^{-4}$ at the frequency f=200 Hz for V=10 m/s and Δx=50 km.

Swell. We consider the spectrum of swell in the form of a narrowbeam wave [46]:

$$W(k_x,k_y) = \frac{2\pi^2H^2}{\Delta\psi\Delta\omega}\int_{\psi_S-\frac{\Delta\psi}{2}}^{\psi_S+\frac{\Delta\psi}{2}} d\psi\int_{\omega_S-\frac{\Delta\omega}{2}}^{\omega_S+\frac{\Delta\omega}{2}} d\Omega\left[\delta\left(k_x-\frac{\Omega^2}{g}\cos\psi\right)\times\right.$$

$$\times \delta\left(k_y - \frac{\Omega^2}{g}\sin\psi\right) + \delta\left(k_x + \frac{\Omega^2}{g}\cos\psi\right)\delta\left(k_y + \frac{\Omega^2}{g}\sin\psi\right)\Big], \tag{4.25}$$

where H is the rms height of the swell, ψ_S is the angle between the direction of propagation of the swell and the x axis, ω_S is the swell frequency, $\Delta\psi \ll 1$ rad is the width of the angular spectrum of the swell, and $\Delta\omega \ll \omega_S$ is the width of its frequency spectrum. We obtain the following equation for σ_{nm} from Eqs. (4.23) and (4.25):

$$\sigma_{nm} = \frac{\pi H^2 \Delta x}{4k^2 \Delta\psi \Delta\omega}[\varphi'_n(0)\varphi'_m(0)]^2 \int_{\psi_S - \frac{\Delta\psi}{2}}^{\psi_S + \frac{\Delta\psi}{2}} d\psi \int_{\omega_S - \frac{\Delta\omega}{2}}^{\omega_S + \frac{\Delta\omega}{2}} d\Omega \times$$

$$\times \Big[\delta\left(\kappa_n - \kappa_m - \frac{\Omega^2}{g}\cos\psi\right) + \delta\left(\kappa_n - \kappa_m + \frac{\Omega^2}{g}\cos\psi\right)\Big]. \tag{4.26}$$

According to Eq. (4.26), the matrix element $\sigma_{nm} \neq 0$ for $|\kappa_n - \kappa_m| = k_S \cos\psi_S$, where $k_S = \omega_S^2/g$ is the wavenumber. Consequently, efficient energy transfer between widely separated modes is possible only for certain angles ψ_S (closely spaced modes interact at $\psi_S = \pi/2$). In the case $|\kappa_n - \kappa_m| = k_S \cos\psi_S$:

$$\sigma_{nm} = [\varphi'_n(0)\varphi'_m(0)]^2 \frac{\pi H^2 \Delta x}{4k^2 k_S}\beta,$$

where

$$\beta = (\Delta\psi |\sin\psi_S|)^{-1} \text{ for } 2\Delta\omega/\omega_S\Delta\psi \le |\tan\psi_S| \le \cot\Delta\psi,$$

$$\beta = (2\Delta\omega \cos\psi_S/\omega_S)^{-1} \text{ for } \tan\Delta\psi \le |\tan\psi_S| \le [2\Delta\omega/\omega_S\Delta\psi],$$

$$\beta = (2\omega_S/\Delta\omega \cos\psi_S)^{\frac{1}{2}}/\Delta\psi \text{ for } \psi_S \sim 0, \sqrt{2\Delta\omega/\omega_S} \le \Delta\psi/2,$$

$$\beta = (2\Delta\omega \sqrt{\cos\psi_S}/\omega_S)^{-1} \text{ for } \psi_S \sim 0, \sqrt{2\Delta\omega/\omega_S} \ge \Delta\psi/2.$$

It is evident from these equations that the individual swell parameters cannot be determined by varying either the reception angle, θ_m, or the frequency, f, unless additional information is available. The entire diagnostic problem is reducible to the determination of the quantities $H^2\beta/k_S$ and $k_S\cos\psi_S$.

A numerical estimation of σ_{nm} for the same waveguide parameters and duration of the sensing pulse as in the preceding examples at a frequency of 200 Hz, k_S=0.04 m^{-1}, ψ_S=72°, $\Delta\psi$=0.1°, $\Delta\omega/\omega_S$=0.1, and H=0.5 m gives the value $\sigma_{nm}=10^{-3}$.

The number of elements of the matrix $\|\sigma_{nm}\|$ that must be measured in general for the reconstruction of oceanographic information about inhomogeneities is determined by the number of inhomogeneity parameters. If the inhomogeneities can be described by a model with a few parameters, it is sufficient to measure just one or two elements of σ_{nm}. An example of such a situation is sea wind, for which it suffices to estimate the wind velocity together with the background field of internal waves, whose characterization can be limited to the estimation of the energy density of internal waves on unit area of the ocean surface. If several parameters must be estimated, it is necessary to measure the maximum possible number of elements of σ_{nm}, to vary frequency, and to use *a priori* information about inhomogeneities.

It follows from estimates obtained at the frequency of 200 Hz that the most significant contribution to the resultant value, σ_{nm}, is from wind waves in the surface-duct sound channel and from the random field of internal waves in the deep-axis channel.

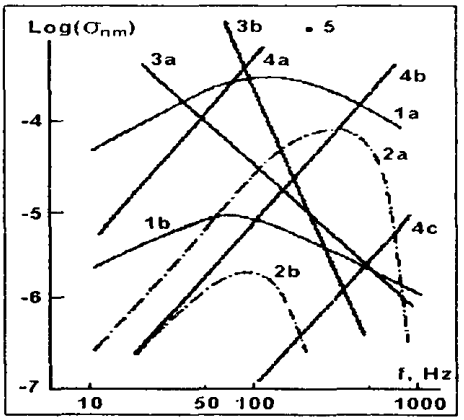

Figure 4.4. Matrix element σ_{nm} versus frequency at fixed angles θ_n^2 for $\theta_m^2 = 10^{-3}$, $\Delta x = 50$, and various types of inhomogeneities. 1) Background field of internal waves: (a) $\theta_n^2 \sim 0.03$; (b) $\theta_n^2 \sim 0.1$. 2) Thermohaline fine structure: (a) $\theta_n^2 \sim 0.03$; (b) $\theta_n^2 \sim 0.1$. 3) Turbulence: (a) $k_0 \sim 10^{-1} m^{-1}$, $\langle(\delta c/c)^2\rangle \sim 10^{-9}$, $\theta_n^2 \sim 0.03$; (b) $k_0 \sim 10^{-3} m^{-1}$, $\langle(\delta c/c)^2\rangle \sim 10^{-8}$, $\theta_n^2 \sim 0.03$. 4) Wind waves: (a) $V = 20$ *m/s*; (b) $V = 10$ *m/s*; (c) $V = 5$ *m/s*. 5) Swell. (Adapted from [46].)

These quantitative estimates have been calculated at a fixed frequency of the sensing pulse. A variation of the frequency can change the relative contributions of the individual types of inhomogeneities to the scattered signal. The latter result is essentially a consequence of differences in the forms of the spatial spectra of inhomogeneities. To confirm this fact, the frequency dependence of σ_{nm} for different types of inhomogeneities is plotted in Fig. 4.4. Eqs. (4.18), (4.21), (4.22), and (4.24) have been used for this purpose. The required functions for the above-indicated models of the inhomogeneity spectrum are shown in Fig. 4.4. It is evident from a comparison of the curves in the figure that the frequency range above 100 Hz can be discerned as the range, in which the predominant influence of internal waves in a mild wind (or in a deep-axis channel) is expected for $\theta_n^2 = 3 \cdot 10^{-2}$. Turbulence clearly provides the greatest contribution to σ_{nm} in the range below 100 Hz. The relative contribution of volume inhomogeneities is greatly suppressed for the larger spacing between the radiated and received modal spectra ($\theta_n^2 = 0.1$). In a strong wind ($V = 10$ m/s), wind waves mask other types of inhomogeneities in a channel with a linear sound speed profile.

The identification of individual types of inhomogeneities requires an optimization of the parameters of the radiating and receiving systems. Optimization mainly entails a search for the optimum angles of radiation θ_m and reception θ_n, and the optimum sensing frequency. The possibility of suppressing the influence of wind waves and swell for better estimation of volume inhomogeneity parameters is offered by the use of complex signals. Indeed, the coherence time is τ_t=1 s ($\tau_v \sim V/g$ for wind waves), whereas the coherence time for volume inhomogeneities is $\tau_{VO}=10^3 - 10^4$ s. For the complex sensing pulse of the duration T_p (the spatial resolution Δr is determined by the duration of the time-compressed signal after matched filtering, $T \ll T_p$) such that $\tau_t \ll T_p < \tau_{VO}$, the signal energy scattered from wind waves decreases by τ_t/T_p in comparison with the signal scattered from volume inhomogeneities. This means that information about volume inhomogeneities can still be extracted when strong wind waves are present in the investigated region. The sensing signal must be sufficiently narrowband, so that the pulse spreading due to intra-modal frequency dispersion can be neglected. Otherwise, it is necessary to use special filters to compensate intra-modal frequency dispersion.

4.3.2 Ray Differential Ocean Acoustic Tomography

The differential method, discussed in Section 4.3.1, is based on the modal approach [2, 50], which allows one to use the signal from a single acoustic path to find the spatial distribution along the path for the statistical parameters of inhomogeneities with horizontal scales smaller than synoptic ones. In this differential method, the reconstruction is performed from the intensity of the scattered sound field. To apply this technique, one needs to emit and receive normal waves substantially separated in the modal spectrum in order to separate the scattered signal from the more intense background direct field. Intermode dispersion causes a difference in the time delay of signals formed by scatterers situated in different parts of the acoustic path. This distinction allows one to localize the inhomogeneities by time gating.

Later we shall discuss the ray approach in the differential method, which may be more effective when intermode dispersion is not substantial, but the separation of short pulse signals into pulses corresponding to different rays is important [63, 128]. By analogy with the modal approach [2, 50], the emission and reception of rays with significantly different mean propagation velocities will permit one to localize inhomogeneities.

Let us consider an underwater acoustic waveguide with the sound speed field $c(r,t)=c(r)+\delta c(r,t)$, where $|\delta c| \ll c$, and $r=(x,y,z)$ in the Cartesian coordinates. A quasi-harmonic sound source located at the point $r_S=(x_S,y_S=0,z_S)=(R_S,y_S=0)$, where $R=(x,z)$, radiates a pulse $F(t)\exp[i\omega_0 t]$ of the duration T. The bandwidth of the signal is $\Delta f \ll \omega_0/2\pi$. The receiving system is at the point $r_r=(x_r,y_r=0,z_r)=(R_r,y_r=0)$. The received signal undergoes matched filtering, i.e., it is convolved with the reference signal, $F(t)\exp[i\omega_0 t]$.

We may assume that sound speed fluctuations, δc, are stationary and quasi-uniform over the space variables, and $\langle \delta c \rangle = 0$. We suppose that inhomogeneities of the sound speed are rather small, $L < \lambda$, $\lambda[a\Delta f/c]^{1/2}$, and vary sufficiently slowly over time, i.e., $L \ll c\tau_c$, where $a = |x_R - x_S|$ is the length of the acoustic path, λ is the wavelength of sound at the frequency ω_0, L is the horizontal correlation radius of δc, and τ_c is the temporal correlation radius of δc.

Let us derive a relationship between the intensity of the scattered pulse and the spectrum of the correlation function of sound speed fluctuations. The acoustic field will be treated in the ray approximation.

In determining the basic relations, we assume that the dependence of the sound speed $c(r)$ on x and y in the reference waveguide is sufficiently smooth, and the effects of horizontal refraction are negligible. It is known [67] that for large-scale inhomogeneities, the scattering angles are small. Thus, the region that mostly forms the scattered field in the horizontal plane is concentrated closely to the straight line connecting the source and the receiver. Therefore, we may assume $c(r) = c(R, y=0) = c(R)$.

The single-scattered component of sound field will be considered in the derivation. We denote the scattered field as $p_1(r,t)\exp[i\omega_0 t]$. Applying the perturbation theory to the wave equation, we obtain [67]

$$p_1(r,\omega) = -\frac{1}{2\pi}\int_{-\infty}^{\infty} h^2(r')d^3r' \int_{-\infty}^{\infty} d\omega' \varepsilon(r',\omega')\, p_0(r',\omega_0-\omega')G(r,r',\omega_0+\omega), \tag{4.27}$$

where

$$\begin{pmatrix} \varepsilon(r,\omega) \\ p_0(r,\omega) \end{pmatrix} = \int_{-\infty}^{\infty} \begin{pmatrix} \varepsilon(r,t) \\ p_0(r,t) \end{pmatrix} \exp(-i\omega t)dt, \quad h = \omega_0/c(r),$$

$$\varepsilon(r,t) = (c(r)/c(r,t))^2 - 1 \cong -2\delta c(r,t)/c(r),$$

$p_0(r,t)$ is the sound field without scatterers (illuminating field for $\delta c = 0$), and $G(r,r',\omega)$ is the Green's function in the reference waveguide at the particular frequency. The frequency spectrum of the complex amplitude of the received signal in the reference guide is $p_0(r,\omega) = P_0 F(\omega) G(r, r_S, \omega_0+\omega)$, where

$$F(\omega) = \int_{-\infty}^{\infty} F(t)\exp(-i\omega t)dt,$$

$$P_0 = \sqrt{8\pi\rho c E}$$

and

$$E = \int_{-\infty}^{\infty} |F(t)|^2 dt$$

is the total energy of the emitted pulse. To simplify the derivation, we shall assume $\int_{-\infty}^{\infty} |F(t)|^2 dt = 1$. After matched filtering, the single-scattered acoustic field takes the form:

$$P_1(r_R, r_S, \tau, \Omega) = \frac{1}{2\pi} \int_{-\infty}^{\infty} d\omega\, p_1(r_R, \omega) F^*(\omega - \Omega) e^{i\omega\tau}. \tag{4.28}$$

Substituting Eq. (4.27) into Eq. (4.28), we obtain the intensity of the single-scattered signal:

$$I(\tau,\Omega) = \langle |P_1(r_R, r_S, \tau, \Omega)|^2 \rangle = \frac{(P_0)^2}{(2\pi)^3} \int_{-\infty}^{\infty}\int d^3 r_1 d^3 r_2 \int_{-\infty}^{\infty} d\omega\, h^2(r_1) h^2(r_2) \times$$

$$\times B_\varepsilon(r_1, r_2, \tau) \exp(-i\omega\tau) \int_{-\infty}^{\infty} d\omega_1 F(\omega_1)\, F^*(\omega_1 + \omega - \Omega) \exp[i\omega_1 \tau] \times$$

$$\times G(r_1, r_S, \omega_0 + \omega_1) G^*(r_2, r_S, \omega_0 + \omega_2) \int_{-\infty}^{\infty} d\omega_2 F^*(\omega_2) F(\omega_2 + \omega - \Omega) \exp[-i\omega_2 \tau] \times$$

$$\times\, G(r_r, r_r, \omega_0 + \omega_1 - \omega) G^*(r_r, r_1, \omega_0 + \omega_2), \tag{4.29}$$

where $B_\varepsilon(r, r', \tau) = \langle \varepsilon(r, t' + \tau/2) \varepsilon(r', t' - \tau/2) \rangle$ is the correlation function of the sound speed inhomogeneities.

The Fourier transform of the Green's function with respect to the spatial variable y is

$$G(r, r_0, \omega) = \frac{1}{2\pi} \int_{-\infty}^{\infty} dk\, G(R, R_0, k, \omega) e^{-ik(y - y_0)},$$

where $h_0 = \omega_0 / c_0$, and c_0 is the sound speed on the channel axis. If $h(r) \approx h(R)$, then in the ray approximation G becomes

$$G(R, R_0, k, \omega) = \sum_j U(R, R_0, k, n_j) \exp[-i\psi(R, R_0, k, n_j)], \tag{4.30}$$

where

$$\psi(R,R_0,k,n_j) = \int_{R_j} \sqrt{(h^2(R') - k^2)}\, ds'$$

is the eikonal, n_j is a unit vector along the ray j, and R_j is the trajectory of the jth ray in the two-dimensional space (x,z). In Eq. (4.30) the summation is over all rays emerging from the point R_0 and incident in the point R.

For large-scale inhomogeneities, an acoustic pulse propagates from source to scatterer and from scatterer to receiver in essentially the same vertical plane that contains both the source and the receiver [2]. Therefore, the Green function in Eq. (4.29) is contributed to mostly by the components of G with rather small k, i.e., $|k| \ll h_0$. Then

$$\psi(R,R_0,k,n_j) \cong \omega t(R,R_0,n_j) - \frac{k^2}{2h_0}(x - x_0),$$

where

$$t(R,R_0,n_j) = \int_{R_j} ds'/c(R')$$

is the delay along the jth ray. As a result, the Green's function can be approximated by

$$G(r,r_0,\omega) \cong [i/2\pi h_0(x - x_0)]^{1/2} \times$$

$$\times \exp\left[-i\frac{h_0(y - y_0)^2}{2(x - x_0)}\right] \sum_j U(R,R_0,k \cong 0,n_j) \exp[-i\omega t(R,R_0,n_j)]. \tag{4.31}$$

Denoting the ray intensity by $\Gamma(R,R_0,n_j) = |U(R,R_0,k=0,n_j)|^2$, we obtain

$$G(r_1,r_0,\omega)G^*(r_2,r_0,\omega_2) \cong [4\pi^2 h_0^2 (x_1 - x_0)(x_2 - x_0)]^{-1/2} \times$$

$$\times \exp\left[-i\frac{h_0(y_1 - y_0)^2}{2(x_1 - x_0)} + i\frac{h_0(y_2 - y_0)^2}{2(x_2 - x_0)}\right] \sum_j \Gamma(R,R_0,n_j) \times$$

$$\times \exp\left[i(-\omega_1)t(R,R_0,n_j) - i\rho\frac{(\omega_1 + \omega_2)}{2}\frac{\partial t}{\partial R}\right], \tag{4.32}$$

where $R = (R_1 + R_2)/2$ and $\rho = R_1 - R_2$. Deriving (4.32), we have neglected the interference of different rays (plane waves) [129] and assumed that ρ is small. Substituting (4.32) into (4.29) and defining the uncertainty function of the emitted signal as

$$F_H(\tau,\Omega) = \frac{1}{2\pi}\int_{-\infty} d\omega F(\omega) F^*(\omega - \Omega) e^{i\omega\tau},$$

we readily obtain

$$I(\tau,\Omega) = \frac{P_0^2}{h_0^3 a}\sum_{j,l}\iint_{-\infty}^{\infty}\left(\frac{h(R)}{2\pi}\right)^4 d^2R\,\Gamma_S(R,n_j)\Gamma(R,n_l)\times$$

$$\times\int_{-\infty}^{\infty} d\omega W_\varepsilon(R;-\omega_0(\partial t_S/\partial R+\partial t/\partial R);\omega)\,|F_H(\tau-t_S-t;\omega-\Omega)|^2, \qquad (4.33)$$

where

$$W_\varepsilon(R;\kappa;\omega) = \iiint_{-\infty}^{\infty} d^2\rho d\tau B_\varepsilon(R+\rho/2,y_1=0;R-\rho/2,y_2=0;\tau)e^{-i\omega\tau+i\kappa\rho},$$

$$t_{S(r)}(R,n) = t(R,R_{S(r)};n),$$

and

$$\Gamma_{S(r)}(R,n) = \Gamma_{S(r)}(R,R,n).$$

Equation (4.33) relates the intensity $I(\tau,\Omega)$ to the local spectrum of the correlation function W_ε of sound speed inhomogeneities. The vectors $\omega_0(\partial t_S/\partial R)$ and $-\omega_0(\partial t/\partial R)$ are the wave vectors of the incident and scattered plane waves.

Thus, in the ray representation, the problem of reconstruction is reduced to solving the integral equation (4.33) and reconstructing the spatial distribution of the oceanic inhomogeneity characteristics (dependence of the local spectrum W_ε upon R). It is important to note that the reconstructed characteristics may be not only the spectrum W_ε, but also a certain combination of parameters describing the spectrum model (some examples of several standard models of oceanic inhomogeneities are discussed in [50]). Analyzing the frequency dependence of $I(\Omega)$, we can determine the frequency characteristics of the spectrum (temporal variability of inhomogeneities). The solution of this problem by using the ray approach does not differ noticeably from the modal approach [18].

A substantial peculiarity of the ray representation is revealed when localizing inhomogeneities in the spatial domain. We will examine this problem in more detail. Consider the ray representation in the case of static, frozen inhomogeneities when $W(r,\kappa,\omega) = 2\pi W(r,\kappa)\delta(\omega)$, where $W(r,\kappa)$ is the local spectrum of the spatial correlation function $B_\varepsilon(\bar{r}+\rho/2, y_1=0; \bar{r}-\rho/2, y_2=0; \tau=0)$. Then we have

$$I(\tau,\Omega) = \frac{2\pi\rho^2}{k_0^3 a_{ij}} \sum \iint_{S_0} |h(R)/2\pi|^4 d^2R\, \Gamma_S(R,n_i)\, \Gamma_r(R,n_i) \times$$

$$\times (F_H(\tau - t_S - t_r,\Omega))^2\, W_\varepsilon(R,\ \omega_0 \partial t_S/\partial R - \omega_0 \partial t_r/\partial R). \qquad (4.34)$$

It follows from Eq. (4.34) that for a fixed delay, τ, the intensity of the scattered field is controlled by the elements of the scattering volume, S_0, with satisfying the following two conditions: 1) $|\tau - t_S - t_r| \le \tau_0/2$, where τ_0 is the duration of the probing pulse after matched filtering and 2) the elements represent intersection regions for ray trajectories emerging from the receiver.

The first condition allows one to localize the scatterers from the variation in the temporal delays of short pulses traveling along different ray paths. The procedure is quite similar to the modal approach of the differential method [2]. Indeed, we assume a regular waveguide and introduce the mean pulse propagation speed along the ray $V(\chi) = D(\chi)/T(\chi)$, where χ is the ray grazing angle at the channel axis, $D(\chi)$ is the length of the ray cycle, and $T(\chi)$ is the delay over the cycle length. Inhomogeneities, located at a distance x_z, produce the scattered field at the receiver location in a time interval defined by $\tau_z = x_z/V_i + (a - x_z)/V_j \pm \tau_0/2$, where V_i and V_j are the mean velocities of rays i and j.

The relationship between I and τ can be determined by the dependence of the spectrum, W_ε, on the coordinate, x_z. The horizontal resolution for rays i and j is $\Delta x = \tau_0 V_i V_j / |V_i - V_j|$. The second condition gives us additional opportunities, compared to the modal approach, for localizing the scatterers both in the horizontal and the vertical planes. This fact substantially increases the efficiency of the reconstruction method.

The position and dimensions of the region that gives the main contribution to the integral (4.34), and the opportunity to extract a relatively weak scattered pulse from the intense illuminating background depend on the parameters of the underwater waveguide, on the positions of the source and the receiver, and on the influence of the ocean seafloor. A numerical simulation of the spatial-temporal structure of the illuminating and scattered signals and an analysis of the possibility of localizing the inhomogeneities along the path under different conditions will be discussed in the next section.

4.4 PARAMETERS OF DIFFRACTION OCEAN ACOUSTIC TOMOGRAPHY SYSTEMS

In homogeneous media the energy coupling between source and receiver and the signal propagation time can be easily predicted. In smoothly inhomogeneous environment, however, the acoustic energy propagates along more complex curved trajectories (rays), so that such prediction becomes more difficult. Rays form coupling channels with the complex structure in natural waveguides (such as the

ocean and the atmosphere) [8, 72, 129]. Complicated spatial structure of the propagation channels is displayed also in the temporal characteristics of received signals. An initially single radiated pulse splits into a series of pulses at the receiver location after propagating through an inhomogeneous medium due to different path lengths. Such pulses can be either overlapping or separately resolved, so that received signals form a complex temporal distribution.

This phenomenon plays an important role in a choice of the algorithm for the reconstruction of the parameters of oceanic inhomogeneities by tomographic monitoring systems in atmospheric and oceanic waveguides [76, 130]. Usually the locations of sources and receivers are determined by the goals and design of the particular monitoring system. The problem of choosing these locations becomes more complex in weakly inhomogeneous refracting media. The energetically coupling channels have more complicated structures in this case, and the locations of sources and receivers should be chosen taking this fact into account. The shadow zones (both for the source and for the receiver) existing in the ocean provides a good example confirming this conclusion. Localized inhomogeneities, situated in shadow zones, do not influence the structure of received signals. Thus, one can assume that the an observation area of imaging system is nonuniform. The knowledge of the propagation path losses, characterizing atmospheric or oceanic waveguides, allows for the estimation of the performance abilities of the imaging system for the given observation area [131, 132]. At the same time, the distribution of such loss, calculated for various source and receiver locations, must be combined to receive the detailed information about the observation area [133]. However, the complexity of such estimation depends on the complexity of the tomographic observation systems [35, 48, 75]. It is even more difficult to describe the connection between the spatial structure of the observation area and the temporal structure of received signals [73, 77]. The "differential" tomography, which does not consider the disturbances from random inhomogeneities, and the *Dark Field Method* for oceanic waveguides [2, 78] give estimations of the spatial structure in the observation area by processing responses from several receivers and sources.

The development of acoustic imaging systems requires the solution of the problem of the optimal choice of system parameters. The synthesis and the analysis of the acoustic field structure in a waveguide are necessary for designing optimal configurations of emitting and receiving systems, focusing the energy at the given region of the medium, and choosing the processing algorithm that will provide the high spatial resolution. If the size of the inhomogeneity in the refractive waveguide is large enough in comparison with the wavelength, then the optimal observation is along the direction of radiated signal. It is necessary to solve the internal diffraction problem for inhomogeneities in the inhomogeneous layered waveguide in order to estimate the performance abilities of tomographic systems [29]. The optimal disposition of sources and receivers is sought based on the results obtained.

Methods for the optimal choice of the parameters of acoustic imaging systems in refractive layered waveguides are discussed in the next sections. In particular, some optimization problems are considered and classified. The calculation of the field scattered by inhomogeneities in the refractive waveguides is presented also. The transferal characteristics of inhomogeneous media are defined and their computed

spatial distributions are analyzed. The method and results of optimizing the model of imaging system are presented. The limitations, the possible applications, and the development of proposed methods are discussed in the conclusion.

4.4.1 The Problem of Scattering in Smoothly Inhomogeneous Layered Waveguides

As noted above, the sensitivity of the structure of the coupling energy channel to variations of the location and parameters of the inhomogeneity should be estimated in order to analyze the efficiency of the acoustic imaging system. The spatial distribution of transferal characteristics can be studied in this case. Different regions of the observation area can be tested by using simulated objects appropriately describing the influence of inhomogeneity. The scattered field calculation can be based on the geometrical theory of diffraction (GTD) [8, 72, 129] implying the ray representation of acoustic field. The proposed methods can be generalized for the modal approximation [72].

Let the point source S, the point receiver R, and the firmly localized inhomogeneity P (its size is less than the scale of field variation) be placed in a smoothly inhomogeneous medium. The total received field can be expressed in the following way:

$$u = \sum_{n_1} A_{n_1} e^{ikS_{n_1}} + k^{-1} \sum_{n_2} \bar{A}_{n_2} e^{ikS_{n_2}} + (k^{-1})^2 \{...\} = u_0 + u_1 + ...,$$

where the first sum, corresponding to u_0, describes the field in the geometrical optics approximation (A_n is the amplitude, S_n is the phase, and k is the wave number). This group includes both the ordinary waves, propagating along the curved trajectories and the waves, reflected from the inhomogeneity. The second term u_1 describes diffraction effects of the order of k^{-1}. There are two subgroup in this group. The first one describes the diffraction effects on the ordinary wave (the transverse amplitude diffusion, the diffraction at the waveguide boundaries, etc.). The second one is associated with the diffraction on the localized inhomogeneity and includes the diffraction waves of different types [8, 72, 129].

4.4.2 The Problem of Ray Selection

It is necessary to trace curved trajectories (rays) to calculate the field at the receiver locations. Tracing all rays is often non-effective, because it requires the large amount of numerical calculations for small-scale inhomogeneities. Approximate estimations have shown that the number of rays grows proportionally to D/L, where D is the length of the propagation path and L is the scale of the inhomogeneity.

Special methods of focusing are more effective for small-size inhomogeneities. One of these methods is described below. Outside the inhomogeneity, the ray follows the rules of geometrical optics (Fermat's principle). Thus, the problem of ray aiming

consists of selecting pairs of rays that couple the source point S with the receiver point R with the point intermediate point on the surface of the scatterer. These pairs must satisfy the conjugation conditions at the given point of the surface. The conjugation conditions are determined by the ray type.

The conjugation condition for the wave of type I (see Fig. 4.5), reflected from the inhomogeneity surface, is [22]:

$$N = -\frac{t_S + t_R}{[2(1+\langle t_S, t_R\rangle)]^{1/2}}, \tag{4.35}$$

where $t_{S,R}$ are unit vectors along incident, S, and reflected, R, rays at the point of reflection, N is the external normal at the reflection point, and $\langle .,. \rangle$ is the scalar product of two vectors.

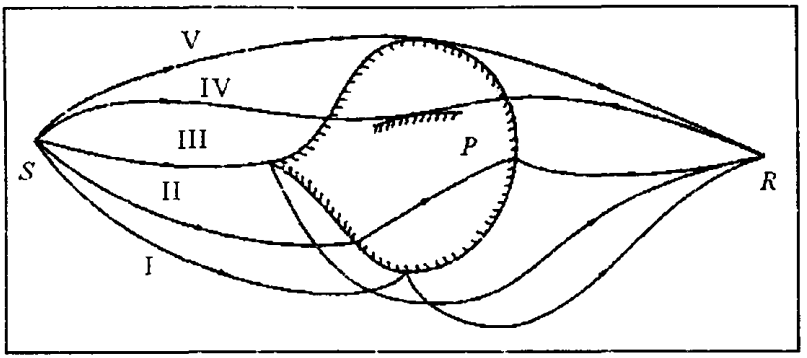

Figure 4.5. Positions of the source, S, receiver, R, and scatterer, P. Rays connecting S and R in scattering: *I* - reflected, *II* -refracted, *III* and *IV* - diffracted, and *V* - creeping. (Adapted from [22].)

The singly refracted wave, II in Fig. 4.5, is characterized by the following set of conditions [72, 133]:

$$N_1 = (\frac{1}{n_1}t_1 - q_1)/\|\frac{1}{n_1}t_1 - q_1\|, \quad N_2 = (\frac{1}{n_2}t_2 - q_2)/\|\frac{1}{n_2}t_2 - q_2\|, \tag{4.36}$$

where $N_{1,2}$ are the external normals of the surface at the incident and exit points, $n_{1,2}$ are ratios of refractive indexes, calculated at the ray incident and leaving points, $\|...\|$ is a norm of a vector, the vectors $q_{1,2}$ characterize an internal structure of the scattering object in the sense of an outward pointing unit vectors along the internal paths. The conditions for wave IV, originated in the process of scattering from the edge, are:

$$\langle e, t_S\rangle + \langle e, t_R\rangle = \langle e, t_S + t_R\rangle = 0, \tag{4.37}$$

where e is a unit vector tangential to the edge at the ray contact point.

The conditions for creeping wave, V, diffracted on the surface of smooth body,

are expressed as follows:

$$(\boldsymbol{N},\boldsymbol{t}_S) = 0, \quad (\boldsymbol{N},\boldsymbol{t}_R) \geq 0, \quad (\boldsymbol{N},\boldsymbol{t}_S,\boldsymbol{t}_R) = 0,$$

where $\boldsymbol{N}$ is the external normal to the surface at the contact point, $(.,.,.)$ is the scalar triple product. The normal at the creeping point can be easily found from this formula:

$$\boldsymbol{N} = (-\boldsymbol{t}_S(\boldsymbol{t}_S,\boldsymbol{t}_R)+\boldsymbol{t}_R)/\|[\boldsymbol{t}_S,\boldsymbol{t}_R]\|, \tag{4.38}$$

where $[.,.]$ denotes the vector product. One can draw the normal at the point of contact with the surface and limit the set of points of the surface, where the given type wave can appear. If the ray unit vectors $\boldsymbol{t}_{S,R}$ are known, then one can determine the normal direction in the ray incident point for the wave of type I or IV. In the case of the refracted wave II, the normals $\boldsymbol{N}_{1,2}$ can be found from Eqs. (4.36) after excluding the vectors $\boldsymbol{q}_{1,2}$. However, additional information about the internal inhomogeneity structure is required. Eq. (4.37) limits the set of permissible edge unit vectors, $\boldsymbol{e}$, and, therefore, the set of points, from which wave III can originate and reach a receiver. Analogously, the "sharp" points of the surface (type III), where the conjugation conditions are fulfilled, can be easily selected. The numerical solution of the problem can essentially be accelerated by restricting the set of points where the given types of waves can be originated. Then, it is enough to focus the imaging system at the suspicious points and check the conjugation conditions for the given pair of rays. However, there is no universal algorithm of *a priori* determination of the unit vectors $\boldsymbol{t}_{S,R}$ at the ray incident point for arbitrary inhomogeneous media and localized inhomogeneities. Nevertheless, these unit vectors can be approximated by the directions, $\boldsymbol{t}^*_{S,R}$, connecting the points S and R with an *a priori* fixed point P^* of the inhomogeneity. This approach is suitable if the size of the inhomogeneity is essentially less than the scale of field variations near the inhomogeneity. These conditions are realized for inhomogeneities, placed far from the ray caustic surfaces and waveguide boundaries. The details of the application of the mentioned approximation are analyzed in [129].

Thus, the focusing on the inhomogeneity can be implemented by the following iterative procedure: 1) tracing rays, coupling the points S,R with the given inhomogeneity point P^*; 2) determining the unit vectors $\boldsymbol{t}^*_{S,R}$ at this point; 3) searching the approximated normal (or the direction $\boldsymbol{e}^*$) at the contact point, based on $\boldsymbol{t}^*_{S,R}$; 4) selecting the points of the surface with the resulting normals; 5) aiming at the selected points and checking the required conditions for each pair of rays. The parameters of determined rays become the initial parameters for the next step of the iterative procedure.

As an example, let us consider aiming at points on the surface of a small ellipsoid. The interior of the ellipsoid is assumed to be acoustically homogeneous: $n_1 = n_2 = n$, $\boldsymbol{q}_1 = -\boldsymbol{q}_2$. The center of the ellipsoid, chosen as P^*, is the origin of the

Cartesian coordinate system. The radius vector of an arbitrary point of the ellipsoid can be expressed through the coordinates of the normal N at this point:

$$r = g(N) = (a^2N_x i + b^2N_y j + c^2N_z k)/(a^2N_x^2 + b^2N_y^2 + c^2N_z^2)^{1/2},$$

where i, j, k are the unit vectors of the Cartesian coordinate system, (a, b, c) are the lengths of the ellipsoid semi-axes defining the ellipsoid size. Let the unit vectors of rays reaching the point P^* be $t^*_{S,R}$. Then, one can find the point of the surface, corresponding to the reflected wave from formula (4.35):

$$r_0 = g(-(t^*_S + t^*_R)/[2(1 + (t^*_S, t^*_R))]^{1/2}).$$

The creeping point of the diffracted ray is obtained from Eq. (4.38):

$$r_S = g((t^*_R + t^*_S)(t^*_S, t^*_R)/\|[t^*_S, t^*_R]\|).$$

To obtain points, corresponding to the refracted ray, we should augment system (4.36) by the following relation:

$$r = \frac{g(N_2) - g(N_1)}{\|g(N_2) - g(N_1)\|} = F(N_1, N_2).$$

This expression relates the direction between two arbitrary points on the ellipsoid surface to the normals N_1, N_2. Finally, we get the system of equations:

$$N_1\|\frac{1}{n}t^*_S - F(N_1, N_2)\| = \frac{1}{n}t^*_S - F(N_1, N_2),$$

$$N_2\|\frac{1}{n}t^*_R - F(N_1, N_2)\| = \frac{1}{n}t^*_R - F(N_1, N_2)$$

to determine the incident and output points for the refracted rays: $r_{1,2} = g(N_{1,2})$.

The numerical simulation has been carried out for the bi-linear oceanic waveguide and localized inhomogeneity of the ellipsoid shape. It has shown that the iterative process converges to the solution with geometrical speed, if the searched ray exists. The algorithm becomes circular, if there is no solution. The computational time for the focusing procedure considerably decreases in comparison with a direct check of all surface mesh points when the ellipsoid size decreases.

4.4.3 Calculating Field Amplitude

The next step in calculating the diffracted field is the determinations of the amplitudes of waves propagating along rays [22]. In accordance with GTD [8, 129], these amplitudes are given by the following formula:

$$A_d = A_{inc} \cdot S(t_S, t_R) \frac{1}{\sqrt{|J|}},$$

where A_{inc} is the amplitude of the incident wave, J is the transformation Jacobian, which is proportional to the area of the cross-section of the ray tube, transforming the energy from the scattering point to the receiver point, $S(\cdot)$ is the diffraction coefficient. The amplitudes of the refracted and diffracted waves can be presented in similar manner.

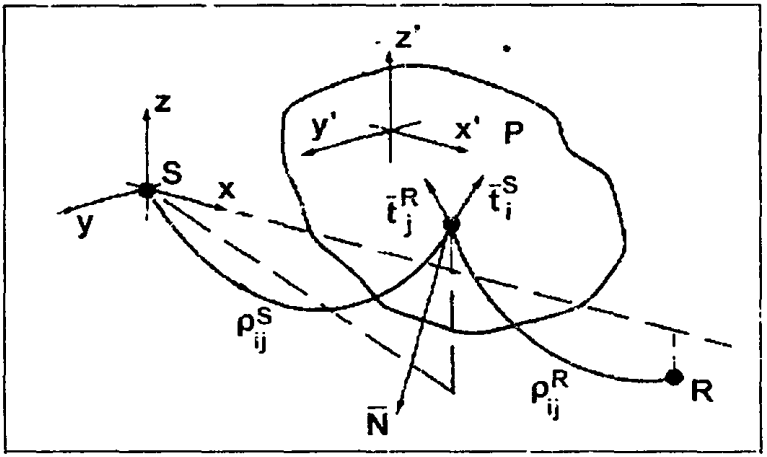

Figure 4.6. System of ray coordinates for the calculation of field diffracted by smooth curvilinear surface (Adapted from [22j.)

As an example, let us consider diffraction at a smooth curved surface in an horizontally stratified inhomogeneous waveguide (Fig. 4.6). We will assume that the source S is situated at the origin of the coordinate system. The ray coordinates are the azimuthal (φ) and polar (θ) angles of the ray unit vector and the parameter l, equal to the propagation length along the ray to the current point, $r(\theta,\varphi,l)$. This coordinate system fits the spatial form of the ray, but does not couple with the surface local curved coordinate system. The *ray function*, $R(M,q,l)=(X,Y,Z)$, describes the trajectory of the ray, originated at the point $M(x,y,z)$ along the direction $q=(\cos\beta\cos\gamma, \cos\beta\sin\gamma, \sin\beta)$. We should calculate the partial derivatives of the ray function to describe the ray tube

$$R'_l = t, \quad R'_z = (k - t_z t)\left(\frac{\partial z^{(p)}}{\partial z} - 1\right),$$

$$R'_\beta = (k - t_z t)\frac{\partial z^{(p)}}{\partial \beta}, \quad R'_\gamma = \rho e_\gamma, \tag{4.39}$$

where $\rho=\sqrt{X^2+Y^2}$, t is the ray direction at the current point, $e_\gamma=(-Y, X, 0)/\rho$ is the unit vector, orthogonal to the ray plane, $z^{(p)}$ is the vertical coordinate of the point of ray,

being on the surface $\rho=const$ (see Fig. 4.6). Then, the set of the reflected rays is given by the formula:

$$\boldsymbol{r}(\theta,\varphi,l) = \boldsymbol{O}(\theta,\varphi)+\boldsymbol{R}(P(\theta,\varphi), \boldsymbol{q}(\theta,\varphi), l-l(\theta,\varphi)), \tag{4.40}$$

where $\boldsymbol{O}(\theta,\varphi)=(O_\theta, O_\varphi)=\boldsymbol{R}(0, \boldsymbol{t}^0, l(\theta,\varphi))$ is the radius-vector of the ray reflection point $P(\theta,\varphi)$.

The intensity of the reflected wave reaching the receiver point is:

$$I = |\Gamma|^2 \frac{W}{4\pi} \frac{t_\perp^0}{|D|}, \quad D = \langle \boldsymbol{r}'_\theta, \boldsymbol{r}'_\varphi, \boldsymbol{r}'_l \rangle, \tag{4.41}$$

where W is the power of the omni-directional point source and Γ is the Fresnel coefficient at the reflection point. The expression for Jacobian follows from Eqs. (4.39) and (4.40) and has the form of the mixed vector product:

$$D = \langle f_1 \frac{\partial z^{(\rho_1)}}{\partial\theta} + \boldsymbol{k}\left[f_{1z} \frac{\partial z^{(\rho_1)}}{\partial\theta}\left(\frac{\partial z^{(\rho_2)}}{\partial z} - 1 \right) + \frac{\partial z^{(\rho_2)}}{\partial\beta} \frac{\langle \boldsymbol{q}'_\theta, \boldsymbol{k} \rangle}{q_\perp} \right] + \rho_2 \boldsymbol{e}_\gamma \frac{\langle \boldsymbol{q}'_\theta, \boldsymbol{e}_\gamma \rangle}{q_\perp},$$

$$\rho_1 f_2 + \boldsymbol{k}[f_{2z}\rho_1\left(\frac{\partial z^{(\rho_2)}}{\partial z} - 1 \right) + \frac{\partial z^{(\rho_2)}}{\partial\beta} \frac{\langle \boldsymbol{q}'_\varphi, \boldsymbol{k} \rangle}{q_\perp}] + \rho_2 \boldsymbol{e}_\gamma \frac{\langle \boldsymbol{q}'_\varphi, \boldsymbol{e}_\gamma \rangle}{q_\perp}, \boldsymbol{T} \rangle, \tag{4.42}$$

where $f_1=\boldsymbol{k}\times\frac{\boldsymbol{n}}{n_t}\boldsymbol{t}$ and $t_2=\boldsymbol{e}_\varphi-\frac{n_\varphi}{n_t}\boldsymbol{t}$ are the tangential unit vectors of the lines of the intersection of the coordinate planes $\varphi=C_1$ and $\theta=C_2$ and the scattering surface at the reflection point, and $\boldsymbol{t}$ and $\boldsymbol{q}=\boldsymbol{t}-2n_t\boldsymbol{n}$ are the unit vectors along the incident ray and the reflected ray, respectively. Based on Weingarten's derivative formulae, one arrives at:

$$\frac{\partial \boldsymbol{n}}{\partial\theta} = k_{11}^* \boldsymbol{O}'_\theta + k_{12}^* \boldsymbol{O}'_\varphi = k_{11} f_1 + k_{12} f_2, \quad k_{11}=k_{11}^* \frac{\partial z^{(\rho_1)}}{\partial\theta}, \quad k_{12}=k_{12}^* \rho_1,$$

and

$$\frac{\partial \boldsymbol{n}}{\partial\varphi} = k_{21}^* \boldsymbol{O}'_\theta + k_{22}^* \boldsymbol{O}'_\varphi = k_{21} f_1 + k_{22} f_2, \quad k_{21}=k_{21}^* \frac{\partial z^{(\rho_1)}}{\partial\theta}, \quad k_{22}=k_{22}^* \rho_1,$$

where the parameters $k_{11}^*,\ldots,k_{22}^*$ can be obtained from the first and second quadratic forms, describing the scattering surface. Thus, the derivatives in Eq. (4.42) are:

$$\boldsymbol{q}'_\theta = \left[\frac{1}{t_\perp} - f_{1t} \frac{d}{dz}(\ln c) \frac{\partial z^{(\rho_1)}}{\partial\theta} \right](f_1 - f_1 \boldsymbol{q}) - 2(k_{11}\boldsymbol{m}_1 + k_{12}\boldsymbol{m}_2),$$

and (4.43)

$$q'_{\varphi} = t_{\perp}(f_2 - f_{2t}q) + \rho_1 f_{2t}(f_{1t}q - f_1)\frac{d}{dz}(\ln c) - 2(k_{21}m_1 + k_{22}m_2),$$

where $m_1 = n_t f_1 + f_{1t} n$ and $m_2 = n_t f_2 + f_{2t} n$. Substituting Eqs. (4.43) into Eqs. (4.41) and (4.42), one can obtain the intensity at the receiver point. The general expressions are cumbersome, so we will consider several fairly simple examples.

Scattering by the azimuthally symmetrical surface (by a toroid). For the reflection from the surface, defined by the equation $F(\rho,z)=0$, the vectors n, t, q, and T are at the ray plane $\varphi = const$. Thus, the vectors f_1 and f_2 are directed along the principal directions of surface curvature: $k_{11}^* = -k_1$, $k_{12}^* = k_{21}^* = 0$, $k_{22}^* = -k_2 \equiv n_{\perp}\rho_1^{-1}$, where k_1 is the curvature of the normal intersection of the surface by the ray plane. Substituting the last expressions in Eq. (4.41), we arrive at:

$$I = |\Gamma|^2 \frac{W}{4\pi}\frac{t_{\perp}^0}{T_{\perp}} / \rho \left|\frac{\partial z^{(\rho)}}{\partial \theta}\right|, \quad \rho = \rho_1 + \rho_2 .$$

The expression confirms the symmetry existing in the problem. On the other hand, one can derive the asymptotical solution for the rays with small grazing angles, which corresponds to $k_1 \to \infty$, from Eqs. (4.41)-(4.43):

$$I \approx |\Gamma|^2 \frac{W}{8\pi}\left|\frac{q_n}{q_{\perp}}\right| F_1 F_2 \frac{1}{\rho_1\rho_2}\frac{1}{\rho|k_1|}, \tag{4.44}$$

where $F_1 = c_s\rho_1 / c\left|\frac{\partial z^{(\varphi_1)}}{\partial \theta}\right|$ and $F_2 = c\rho_2 / c_R\left|\frac{\partial z^{(\rho_2)}}{\partial \beta}\right|$ are factors of the vertical focusing of rays, reaching the reflection point from the points S and R, respectively. The intensity of the incident wave is equal to $(W/4\pi)F_1/\rho_1^2$. The Jacobian, J, of the transformation for the ray tube, connecting the points R and P, equals ρ_2^2/F_2. Taking the last two expressions into account, we can express the intensity in Eq. (4.44) as follows:

$$I = I_{inc} S^2 \frac{1}{|J|},$$

where

$$S^2 = \frac{1}{2}|\Gamma|^2 \left|\frac{q_n}{q_{\perp}}\right| \frac{1}{(\rho_1^{-1} + \rho_2^{-1})|k_1|} \tag{4.45}$$

is analogous to the diffraction coefficient for the reflected wave. Thus, the quantity S^2

can be called a coefficient of the reflection from the curved surface.

Scattering by an arbitrary surface in a homogeneous medium. In the homogeneous medium we have:

$$\frac{\partial z^{(\rho_2)}}{\partial z}=1,\ \frac{\partial z^{(\rho_1)}}{\partial \theta}=\frac{\rho_1}{t_\perp^2},\ \frac{\partial z^{(\rho_2)}}{\partial \beta}=\frac{\rho_2}{q_\perp^2}.$$

Then, Eq. (4.41) can be rewritten as:

$$I=|\Gamma|^2\frac{W}{4\pi}/\left|(l_1+l_2)^2+2l_1l_2(l_1+l_2)\left(\frac{k_1}{q_n}+k_2q_n\right)+4l_1^2l_2^2K\right|, \tag{4.46}$$

where k_1 is the curvature of the normal intersection of the scattering surface by the plane, containing the vectors t and q, k_2 is the curvature of the normal intersection of the scattering surface by the orthogonal plane, K is the Gaussian curvature of the surface calculated at the reflection point, and $l_{1,2}$ are the propagation lengths along the ray from the points S and R to the reflection point P, respectively. Taking into account that the intensity of the incident field equals $W/(4\pi l_1^2)$ and the Jacobian, J, equals l_2^2, we arrive at the following form of the reflection coefficient:

$$S^2=|\Gamma|^2\left|(l_1^{-1}+l_2^{-1})^2+2(l_1^{-1}+l_2^{-1})\left(\frac{k_1}{q_n}+k_2q_n\right)+4K\right|^{-1}. \tag{4.47}$$

Eq. (4.46) was first derived by Fock [129] for the intensity of the wave, reflected from the curvilinear interface between two homogeneous media.

Reflection from the surface with large Gaussian curvature. There is an asymptotical expression for the intensity of the wave reflected by a surface with large Gaussian curvature, i.e., $K\to\infty$, in an arbitrary stratified medium. The asymptotical form follows from Eqs. (4.41) - (4.43):

$$I\propto|\Gamma|^2\frac{W}{4\pi}\cdot\frac{F_1F_2}{4\rho_1^2\rho_2^2}\cdot\frac{1}{|K|}. \tag{4.48}$$

This shows that the asymptotical formula for the reflection coefficient is:

$$S^2=\frac{|\Gamma|^2}{4|K|}. \tag{4.49}$$

Similar expressions can be obtained for the refracted waves [31, 72].

As an example of using the derived expressions, Fig. 4.7 shows the dependence

of the intensity of the scattered field on the orientation of an ellipsoid placed in a bi-linear waveguide for the fixed locations of the source and the receiver.

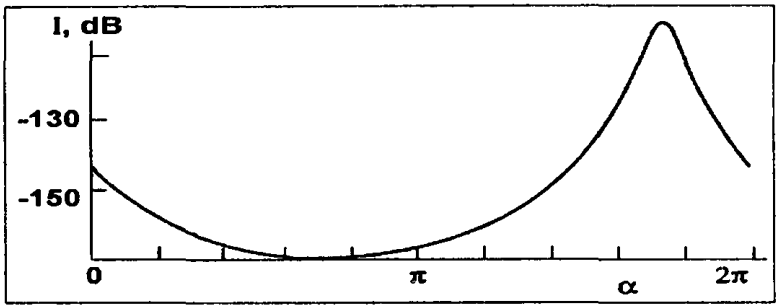

Figure 4.7. The diffracted signal intensity as a function of the ellipsoid orientation in a horizontal plane. (Adapted from [22].)

The procedure has been developed for layered waveguides of refractive type. However, some details have been omitted, because of the limited size of this paper. For example, we have not discussed multi-scattering effects for the inhomogeneities, located the waveguide boundaries, or the accurate calculation of the field near caustics, etc. These effects can be included on the basis of more precise theory. Nevertheless, the obtained estimations allows the effective optimization of imaging systems by using transferal maps, computed on the basis of the calculation of the field, scattered by probing (including isotropic scattering) model objects.

4.4.4 Tomographic System Parameter Optimization

Several optimization problems for acoustic imaging system are considered in this section. The discussed methodology is based on spatial maps of the medium transferal characteristics, such as a *Coefficient of Energetic Coupling* and *Anisotropic Coefficient*. It should be noted that the present review does not deal with the problems of the signal temporal characteristics optimization, which is based on the temporal medium transferal properties, such as a signal Mean Travel Time to a receiver, the probability of the separation of the direct and scattered signal, and so on [73, 133].

Total Intensity of the Reflected Wave. First of all, let us analyze the formula for the total intensity of the wave, reflected from the localized inhomogeneity, which can be readily derived from the consideration, presented in the previous section:

$$I = \frac{W}{4\pi} \sum_{ij} \frac{F_{ij}^{(1)} S_{ij} F_{ij}^{(2)}}{(\rho_{ij}^{(1)} \rho_{ij}^{(2)})^2}, \tag{4.50}$$

where the double sum corresponds to the incoherent summation over all rays, reaching the receiver after the reflection from the surface of the inhomogeneity. S_{ij}

is the coefficient of reflection, calculated at a given point on the surface of the inhomogeneity, $\rho_{ij}^{(1)}$ and $\rho_{ij}^{(2)}$ are the distances between source and surface inhomogeneity point and between surface inhomogeneity point and receiver, respectively (see Fig. 4.6).

If the inhomogeneity size is small, then we can assume that $\rho_{ij}^{(1)} \approx \rho_1$ and $\rho_{ij}^{(2)} \approx \rho_2$. Besides that, the set of all rays, coupling the source, S, with the inhomogeneity surface, can be divided into a few classes of ray bundles, not intersecting with each other. The individual class includes rays, differing insignificantly due to splitting the ray, connecting the point S with some central point P^* at the inhomogeneity surface corresponding to the incident point of the central ray of the particular bundle. The analogous separation can be carried out for the receiver rays. Then, we have for the focusing factors: $F_{ij}^{(1)} \approx F_i^{(1)}$ and $F_{ij}^{(2)} \approx F_j^{(2)}$, where $F_i^{(1)}$ and $F_j^{(2)}$ are the focusing parameters of the "central" rays. The prime coordinate system (x',y',z') will correspond to the local-body Cartesian-coordinate system. Any direction in this system can be characterized by a normal vector $\boldsymbol{n}'=(n_1',n_2',n_3')$. Then, the reflection coefficient, $S(\boldsymbol{n}')=S(n_1',n_2',n_3')$, can characterize the scattering surface at the particular point. If there are several points of the surface, corresponding to the same normal direction $\boldsymbol{n}'$, then this function results from summing the reflection coefficients over all these points.

Using Eq. (4.35) and the function $S(\boldsymbol{n}')$, let us derive the intensity of the field, reflected by the ideal reflector, $|\Gamma_{ij}|=1$. The reflection coefficient can be expressed in the medium coordinate system as:

$$S_{ij} = S\left(\overline{U}\boldsymbol{n}_{ij}\right), \quad \boldsymbol{n}_{ij} = \frac{-(\boldsymbol{t}_i^{(1)}+\boldsymbol{t}_j^{(2)})}{\sqrt{2\left(1+(\boldsymbol{t}_i^{(1)},\boldsymbol{t}_j^{(2)})\right)}},$$

where $\overline{U}$ is a unitary matrix of the transformation of the medium coordinate system (x,y,z) to the body coordinate system (x',y',z'), and $\boldsymbol{t}_i^{(1)}$ and $\boldsymbol{t}_j^{(2)}$ are the incident and reflected ray unit vectors at the point of reflection. Finally, the expression for the total intensity of the reflected wave is:

$$I = \frac{W}{4\pi\rho_1^2\rho_1^2}\sum_{\alpha} F_\alpha S\left(\overline{U}\boldsymbol{n}_\alpha\right), \tag{4.51}$$

where $\alpha=(ij)$, $F_\alpha=F_i^{(1)}F_j^{(2)}$. The intensity determined by Eq. (4.51) is a function of the parameters of the problem:

$$I = I(\boldsymbol{O}_S, \boldsymbol{O}_R, \boldsymbol{O}_P, S(\cdot), \overline{U}),$$

where $\boldsymbol{O}_{S,R,P}$ are the radius vectors of the source, the receiver, and the inhomogeneity

in the medium global coordinate system, respectively, $S(\cdot)$ is the function describing the reflection properties of the inhomogeneity, and the matrix $\overline{U}$ determines the spatial orientation of the reflector. Thus, the problem of the optimization of the mentioned parameters can be formulated to provide the maximum value of the received intensity. The greatest attention should be paid to the essential factors influencing on the solution.

4.4.5 Some Problems of Parameter Optimization

The Optimal Scatterer Form. Let us assume that all parameters, except the function $S(\cdot)$, are given and fixed:

$$I = I(S(\cdot)) - \underset{S(\cdot)}{extremum} .$$

Obviously, the determination of the optimal function, $S(\boldsymbol{n})$, can be easily replaced by seeking the optimal function $f(\boldsymbol{n}) = S(\overline{U}\boldsymbol{n})$. Thus, the initial problem is equivalent to the following one:

$$\sum_{\alpha} F_{\alpha} f(\boldsymbol{n}_{\alpha}) \to \underset{f(\cdot)\in F}{extremum},$$

where $\{F_{\alpha}, \boldsymbol{n}_{\alpha}\}$ is a given set of parameters, F is the functional class within which we are looking for the solution. This class should contain a large number of elements to provide the existence of the solution. On the other hand, it should follow some restrictions to provide the physical realization of the solution. It should be also in accordance with limits given by the problem statement.

As an example, let us consider the problem of satisfying the asymptotic formula, Eq. (4.49). This can be summarized as follows: A smooth, convex, closed surface $\boldsymbol{r} = \boldsymbol{r}(u,v)$, (u,v) are curvilinear coordinates at the scattering surface, is required that maximizes the sum $\sum_{\alpha} F_{\alpha} |K_{\alpha}|^{-1}$, where K_{α} is the total (Gaussian) curvature of the surface calculated at the point with the external normal $\boldsymbol{n}_{\alpha}$. It should be assumed that the surface area is given, the curvature at any arbitrary surface point is limited by the following inequalities: $0 < \delta_1 \le K_{\alpha} \le \delta_2$, where $\delta_{1,2}$ are the given values. This is a variational problem of the nonclassical type (the optimal control problem). Its specific feature is that there is no *a priori* information about the points of the surface where reflection takes place. A general mathematical formulation of the simpler two-dimensional problem can be expressed by the following set of equations:

$$\dot{\rho}_1 = \rho_2, \quad \dot{\rho}_2 = \rho_1 + 2\rho_1^{-1}\rho_2^2 - (\rho_1^2 + \rho_2^2)^{3/2}\rho_1^{-1}u, \quad 0 \le \varphi < 2\pi,$$

$$\int_0^{2\pi} \sqrt{\rho_1^2 + \rho_2^2}\, d\varphi = l, \quad 0 < \overline{\delta}_1 \le U \le \overline{\delta}_2,$$

$$\rho_1\cos\varphi-\rho_2\sin\varphi-(\rho_1^2+\rho_2^2)\cos\varphi n_\alpha^{(1)}|_{\varphi=\varphi_\alpha}=0,$$

$$\rho_2\cos\varphi-\rho_1\sin\varphi-(\rho_1^2+\rho_2^2)\sin\varphi n_\alpha^{(2)}|_{\varphi=\varphi_\alpha}=0,$$

$$\rho_1(0)=\rho_1(2\pi),\ \rho_2(0)=\rho_2(2\pi),$$

$$\sum F_\alpha u^{-1}(\varphi_\alpha)\to extremum,\quad 0\le\varphi_\alpha<2\pi,\quad \alpha=1,\ldots,\alpha_0,$$

where $\rho=\rho_1(\varphi)$ is the equation, giving the scatterer boundaries at the polar coordinates system, $\{n_\alpha^{(1)},n_\alpha^{(2)}\}$ is the set of normals, and l is the boundary length.

Optimal Scatterer Orientation. The problem of the scatterer orientation optimization consists of choosing the unitary matrix $\bar{U}$ that gives the maximum intensity at the receiver location. The orientation can be determined by two scalar parameters φ_1, φ_2 (for example, Euler's angles). Then, the following system of equations gives the necessity conditions of the extremum:

$$\frac{\partial I}{\partial\varphi_1}=\sum_\alpha\langle\overline{U_1^*}\nabla S,F_\alpha n_\alpha\rangle=0,$$

$$\frac{\partial I}{\partial\varphi_2}=\sum_\alpha\langle\overline{U_2^*}\nabla S,F_\alpha n_\alpha\rangle=0,$$

where $\overline{U_{1,2}}=\partial\bar{U}/\partial\varphi_{1,2}$, and (*) denotes the transposition operation. It is important to note that, if the absolute value of the vector $\sum_\alpha F_\alpha n_\alpha$ is small for the given scatterer location, then the gradient of the intensity function

$$(\nabla I)_i=\sum_\alpha\langle\overline{U_i^*}\nabla S,F_\alpha n_\alpha\rangle=\langle\overline{U_i^*}\,\overline{\nabla S},\sum_\alpha F_\alpha n_\alpha\rangle\approx 0,\ i=1,2$$

is also small. ($\overline{\nabla S}$ is the mean value of the gradient, calculated at some intermediate point). This fact means that the intensity, determined by Eq. (4.51), is weakly dependent on the scatterer orientation. In the opposite case, if the value of $\sum_\alpha F_\alpha n_\alpha$ is large, then the absolute value of the gradient depends essentially on the orientation. Therefore, the relative variations of the intensity are large with changing the scatterer orientation in space. Thus, the scalar parameter

$$\delta=\left|\frac{\sum_\alpha F_\alpha n_\alpha}{\sum_\alpha F_\alpha}\right|, \tag{4.52}$$

with its values in the interval [0,1] can be a measure of the dependence of the received intensity on the scatterer orientation. The larger δ is the stronger this

dependence will be. The parameter δ, called the "*Anisotropic Coefficient*" (AC) [72], is determined by medium properties and is not dependent on scatterer properties. It characterizes the non-uniformity of the reflector illumination from different directions.

Let us consider a concrete example of choosing the parameter defined above. Let the spherical surface be illuminated from the directions determined by the vectors $n_1, n_2, \ldots, n_k$. The intensity of the flow along the direction n_j is proportional to F_j. The illumination of the sphere point, defined by an external normal, N, is given by:

$$\Phi = \left| \sum_{\alpha} F_{\alpha} \chi((n_{\alpha}, N)) \right|,$$

where $\chi(x)$ $|\chi(x)| \le |x|$ is a given function. Thus, $\Phi \le \sum F_{\alpha}$, so we can define the relative illumination of the sphere point as:

$$\delta\Phi(N) = \frac{\Phi(N)}{\sum_{\alpha=1}^{L} F_{\alpha}} = \left| \frac{\sum_{\alpha} F_{\alpha} \chi((n_{\alpha}, N))}{\sum_{\alpha} F_{\alpha}} \right|.$$

The non-uniformity of the illumination can be defined analogously:

$$\delta = \max_{N} \delta\Phi(N) - \min_{N} \delta\Phi(N). \tag{4.53}$$

AC, defined by Eq. (4.52), follows from this expression for the functional form: $\chi(x) = -x$. However, the more physical assumption is that $\chi(x) = -x\,1(x)$, where $1(x)$ is a unit step-function. Equation (4.52) gives an AC value of 0, if the sphere is uniformly illuminated from all directions and the flow intensity is also uniform. However, Eq. (4.53) shows that δ decreases monotonically as $L \to \infty$. This expression is in agreement with an intuitive notion about the non-uniformity of illumination. Nevertheless, the parameter, determined by Eq. (4.52), generally describes the situation correctly, and it is the simpler one for calculation. Preliminary computation of the spatial maps of transferal characteristics (such as AC) can be carried out before solving practical optimization problems. First of all, the spatial maps of AC in inhomogeneous media provide a convenient visible representation of the properties of the particular waveguide. Secondly, the maps can be used as *a priori* information for future imaging system optimization.

Figure 4.8 shows the spatial distribution of AC in the vertical (Figs. 4.8a,c) and horizontal (Figs. 4.8b,d) planes for the bi-linear waveguide. The sound speed profile versus depth is (0, 1500), (-200, 1470), and (-3000, 1550), where (depth [m], c [m/sec]). The source is at a depth of -200 m for Figs. 4.8a,b, and the receiver is at the source depth in Fig. 4.8b. The distance between the source and receiver is 100 km. The greater the value AC, the darker point it is shown in the map. (A more detailed study of the transferal characteristics for different inhomogeneous waveguides can be found in [72, 73]).

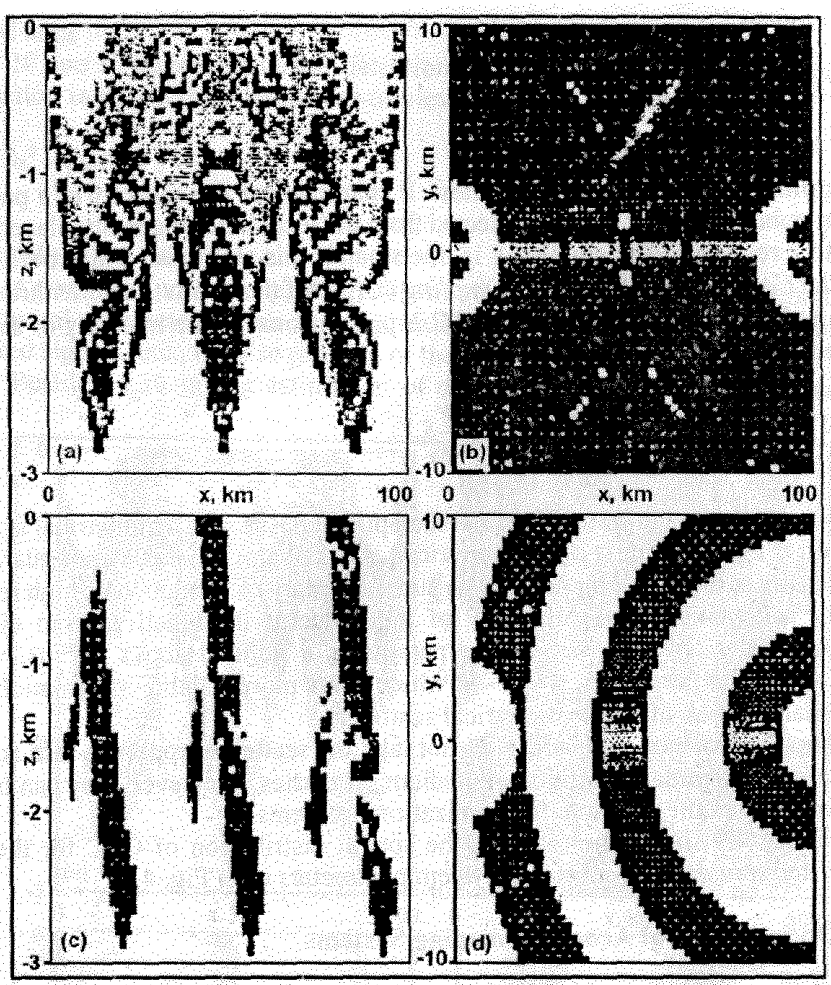

Figure 4.8. Spatial Distribution of the Anisotropy Coefficient at the vertical (a,c) and horizontal (b,d) planes for the bi-linear waveguide. (Adapted from [72].)

Optimal Scatterer Location. The problem consists of choosing the position of the scatterer (inhomogeneity) in the given region, Ω, using *a priori* information about the inhomogeneity and transmitting-receiving system parameters:

$$I = I(\boldsymbol{O}_\rho) \to \underset{P \in \Omega}{extremum}.$$

If the reflection coefficient is limited, that is, if $S \le S_0$, then the intensity is also limited:

$$I \le \frac{W}{4\pi} S_0 \frac{1}{\rho_1^2 \rho_2^2} \sum_\alpha F_\alpha.$$

The parameter

$$V(P) = \frac{1}{\rho_1^2 \rho_1^2} \sum_{\alpha} F_{\alpha} \tag{4.54}$$

is determined by the medium properties. It characterizes the capacity of a particular medium point to transfer energy, reflected from the local inhomogeneity placed at this point, to a receiver. The smaller V is, the smaller this ability is. This coefficient is called the *Coefficient of Energetic Coupling* (CEC) of the points S and R through the particular inhomogeneity point P. CEC is proportional to the intensity of the wave reflected by the probing sphere:

$$S = S_0, \quad I = \frac{W}{4\pi\rho_1^2\rho_2^2} \sum_{\alpha} F_{\alpha} S(\vec{U}\vec{n}_{\alpha}) = \frac{W}{4\pi} S_0 V.$$

Therefore, CEC gives information about the optimal position of symmetrical scatterer. However, if the scatterer is not symmetrical, a large value of V does not guarantee a high intensity at the receiving point. The supplementary confirmation of high received intensity is given by the uniformity of the reflector illumination from different directions. It is characterized by the parameter δ defined above. Thus, we can introduce a scalar parameter, $\gamma = V(1-\delta)$, which gives more reliable information about the optimal location of non-symmetrical scatterer.

The coefficients δ, V, and γ do not take the scatterer properties into account, so they provide a crude description of medium properties. However, they can be used as the first step in the solution of optimization problems.

Figure 4.9 shows the maps of the spatial distribution of CEC for the same medium and transmitting-receiving system parameters as in Fig. 4.8.

4.4.6. Optimization of Acoustic Imaging Systems

Let us consider a model of the imaging system consisting of the arrays of sources, S_i, $i=1,\ldots,n$, and receivers, R_j, $j=1,\ldots,m$, of acoustic waves observing a given region of an inhomogeneous medium.

The quality of viewing, carried out by the pair $P_{ij}=(S_i,R_j)$ can be characterized by the scalar parameter $\alpha_{ij} \geq 0$. The physical meaning of the parameter can vary depending on the goals of the particular viewing system. If the goal is a detection of inhomogeneities appearing in the given region, the measure of the quality of observing is the averaged energetic coupling of the points S_i and R_j through the points of viewed area:

$$\alpha_{ij}^{V} = \int_{\Omega} V(P)dP,$$

where $V(P)$ is the CEC calculated at the point P of the region and Ω defines the

viewed area.

If one is interested in the detection of the inhomogeneities changing their orientation in space, then the quality of viewing can be characterized by:

$$\alpha_{\eta} = \int_{\Omega} \delta(P) dP,$$

where $\delta(P)$ is the AC.

As we mentioned above, the quality of viewing can be also defined on the basis of temporal parameters, such as the probability of the separation of the direct and reflected signals, etc., if pulse probing of the medium is used.

Besides $\alpha_{\eta} > 0$ giving estimation of the quality of viewing, other parameters

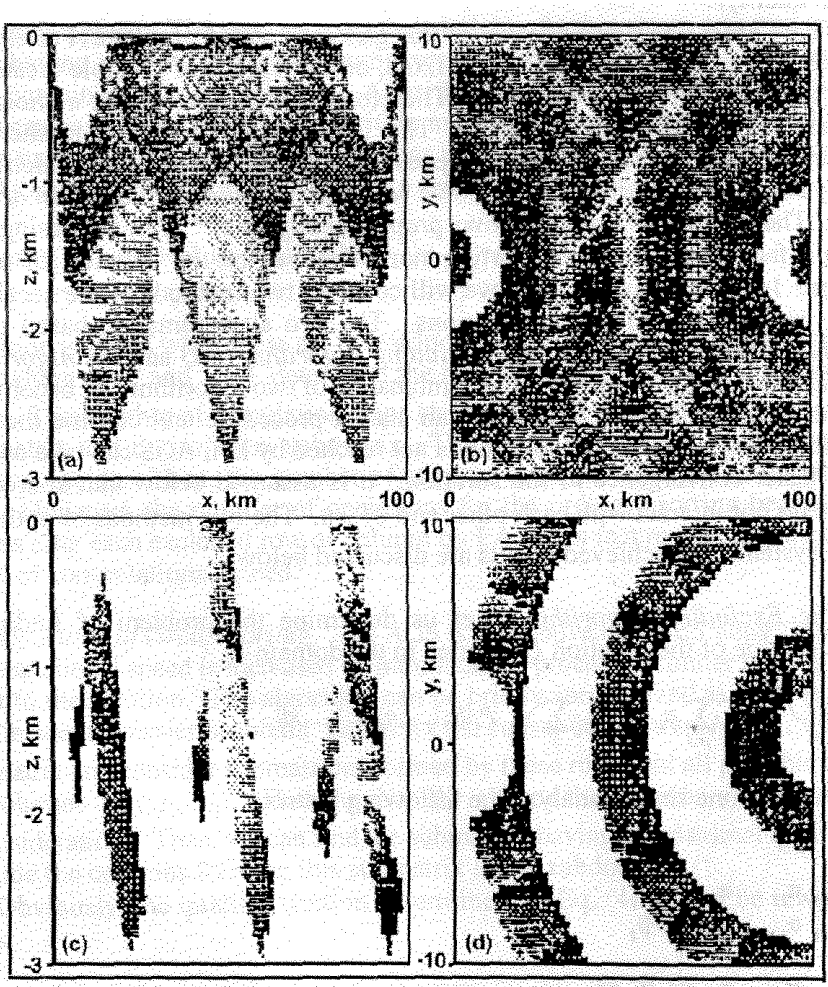

Figure 4.9. Spatial Distribution of the Coefficient of Energetic Coupling at the vertical (a,c) and horizontal (b,d) planes for the bi-linear waveguide. (Adapted from [72].)

characterizing the particular sets of sources and receivers should be introduced. Namely, let $\beta_i \geq 0$ characterize the quality deterioration resulting from placing the source S_i at a fixed position and let $\gamma_j \geq 0$ characterize the quality deterioration resulting from placing the receiver, R_j, at a fixed position. Let $\delta''_{i'j'}(|i'-i'|+|j'-j'|>0)$ be the quality deterioration because of the influence of the other connection pairs $P_{i'j'}$.

Then, the resulting quality of imaging system is determined by:

$$Q = \sum_{i,j=1}^{n,m} \alpha_{ij} - \sum_{i} \beta_i - \sum_{j} \gamma_j \quad \sum_{ij} \sum_{i'j'} \delta''_{i'j'}, \ (|i'-i| + |j'-j|>0).$$

Now the optimization problem can be formulated as forming the system, having the maximal quality.

There are a few simplification of this generally stated problem. For example, the number of pairs can be limited and fixed, or the regions of possible locations of sources and receivers can be known. Therefore, one can talk about a choice of a subsystem having the maximal quality. This is a problem of discrete mathematical programming. It always has a solution (possibly not unique, however), which can be found by sorting all possible variants. We will refer to this algorithm as an *ordinary sorting*. The number of variants grows proportionally to $2^{n \cdot m}$ with increasing n and m. This fact makes ordinary sorting non-effective for the solution of applied problems. In the next subsections we will consider two methods of the accelerated sorting, which require fewer calculations. The two algorithms are based on two alternative strategies. They are the *Excluding Algorithm (EA)* and the *Algorithm of Group Sorting (AGS)*. Sometimes the combination of two algorithm can become very effective. The Excluding Algorithm can start a procedure and confine the set of permissible subsystems. If the solution is not reached by EA, AGS can take over and provide faster convergence to the solution. It is assumed below that sources and receivers do not interact with each other and $\delta''_{i'j'}=0$. The two methods of optimizing imaging systems and achieved results are discussed below.

The Excluding Algorithm. Let us determine the problem of finding the maximum value of the function Q defined in the domain P:

$$Q(I,J) = \sum_{i \in I} \sum_{j \in J} \alpha_{ij} \quad \sum_{i} \beta_i - \sum_{j} \gamma_j, \ P:\{I \subset 1,\ldots,n;\ J \subset 1,\ldots,m\}. \tag{4.55}$$

In other words, one should analyze the following matrix:

$$\begin{array}{cccc|c} \alpha_{11} & \alpha_{12} & \cdots & \alpha_{1m} & -\beta_1 \\ \alpha_{21} & \alpha_{22} & \cdots & \alpha_{2m} & -\beta_2 \\ & \vdots & & & \\ \alpha_{n1} & \alpha_{n2} & \cdots & \alpha_{nm} & -\beta_n \\ \hline -\gamma_1 & -\gamma_2 & \cdots & -\gamma_m & * \end{array}$$

and select the subgroup of rows (from first n) and the subgroup of columns (from first m), so that the sum of the all submatrix elements would be maximal. Let I^* and J^* be optimal subdomains. The method discussed is based on the simple observation. The sum of the elements of the ith row should be positive for any $i \in I^*$, if I^* includes more than one row. Otherwise, it means non-optimal choice of the subdomain, and one can exclude the negative sum row and increase the quality function value. Obviously, the analogous observation is true for the subset of columns. Thus, the first stage of the algorithm can be summarized as follows: One should start from the input matrix of maximal size. All rows having a negative sum of elements should be excluded because they can not contribute to the solution. This step is called "step (1,0)" or just (1,0). Then, for step (01), all columns having a negative sum of elements are excluded. If the last operation produces negative sum rows, the algorithm should returns to the steps (1,0)-(0,1). This stage is repeated as long as negative sum rows and columns appear. The next step is labeled (1,1). At this stage, one row and one column, having a negative common sum are excluded simultaneously. The solution can not contain such combinations. After this stage, the negative sum rows and columns can appear again and the algorithm must return to the steps (1,0)-(0,1). The next step excludes one row and two columns with negative sum of the elements, and so on. As a result, the algorithm splits into the finite steps scheme:

$$start \to (1,0) \to (0,1) \to (1,1) \to (1,2) \to (2,1) \to (2,2) \to \ldots \to (n,m) \to end$$

The solution is found when there are no excluded rows and columns at any step up to (n_1,m_1), where n_1+1 and m_1+1 determine the dimension of the matrix that forms the solution. The number of calculation steps strongly depends on the difference of the initial matrix and the solution submatrix. The most unfavorable case is that both matrices coincide. Then, the number of steps of EA equals to that of the ordinary sorting. However, the number of operations for the ordinary sorting becomes two times less after each excluded row or column by EA. This fact results in the essential increase of computational speed.

Algorithm of Group Sorting. The AGS is alternative to the ES algorithm. Here the computational speed is increased by introducing a procedure similar to the gradient descent to the solution. The algorithm can be briefly summarized as follows: First, let us consider the easier problem. Let us fix the subset of the rows $I=\{i_1,i_2,\ldots,i_k\}$ of the initial matrix and consider submatrices formed by these rows and all possible subsets of the columns $J=\{j_1,j_2,\ldots,j_l\}$. (Here the row α_i, $i \in I$, and the column γ_j, $j \in J$, are taken into consideration.) Then, we can find the submatrix, having the maximal quality. Let us include the columns forming this submatrix in the subdomain J^*.

Obviously, the quality function determined by Eq. (4.55) can be rewritten as follows:

$$Q(I,J) = \sum_{i \in I} \sum_{j \in J} a_{ij} - \sum_{i \in I} \beta_i - \sum_{j \in J} \gamma_j = \sum_{i \in I} \left(\sum_{j \in J} a_{ij} - \gamma_j \right) - \sum_{i \in I} \beta_i = \sum_{i \in I} \delta_i(I) \cdot Q_{ii}(I),$$

where $\delta_j(I) = \left(\sum_{i \in I} \alpha_{ij} - \gamma_j \right)$, $Q_0(I) = \sum_{i \in I} \beta_i - const \geq 0$. The solution is based on the theorem, formulated below.

THEOREM. Let $I=\{i_1,i_2,...,i_k\}$, $k \in 1,...,n$, $I \subset I_0$, $I_0 \equiv 1,...,n$, be the fixed subset of rows, determining the class of submatrices. Then, the set of submatrix columns, J^*, having the maximal quality, contains:

(1) Either all columns having the positive value of $\delta_j(I)$ and only them, if such columns exist. That is, if $J_j \in J_0$, $J_0 \equiv 1,...,m$: $\delta_j(I) > 0$, then $J^* = \{j_1^*, j_2^*, ..., j_p^*\}$: $\delta_{j_p^*}(I) > 0$, and $\delta_j(I) \leq 0$ for any column not belonging to the subdomain J^*: $\forall j \in J_0 / J_p^*$.; or

(2) the single column, having the maximal value of $\delta_j(I)$, if the requirements of the first statement are not fulfilled. That is, if $\forall j \in J_0$: $\delta_j(I) \leq 0$.

Then $J^* = \{j^*\}$: $\delta_{j^*}(I) \geq \delta_j(I)$, $\forall j \subset J_0$.

Thus, the solution of the original problem can be found by analyzing all possible row subsets and finding a subsystem, having the maximal quality, for each row subset. In the final stage, the only one subsystem having the global maximum should be chosen. Estimates of computational speed have shown that only $n \cdot m \cdot 2^m$ computer operations are needed in this case. If one float-point-operation duration is about 20 μs (for INTEL-287) and $n=m=10$, then the computational time of AGS is about 2-4 seconds. On the other hand, ordinary sorting requires 3-4 minutes.

The combination of two algorithms can be desirable for some situations. The EA algorithm decreases the matrix size very effectively, if it operates on matrices, having the negative sums of row or column elements. However, AGS is more effective, if there are no such combinations in the matrix. Thus, one can start from EA. Let us assume that the negative sums become absent at the ith step. To decide what algorithm to use after this step, one may calculate the transition function $f(i,\tau_{next},T_{GS})$, where τ_{next} is the estimated time for a few next step of EA, T_{GS} is the estimated time of processing the matrix by AGS. The transition to AGS takes place, if the function f is positive or zero, i.e., $f \geq 0$. A form of the transition function may be, probably, defined as follows:

$$f(i,\tau_{next},T_{GS}) = (\tau_{next} - T_{GS}) + \sigma(i,i_0)((T_{GS} - \tau_{next}) + \varepsilon), \quad \varepsilon > 0,$$

where

$$\sigma(i,i_0) = \begin{cases} 1, i \geq i_0 \\ 0, i < i_0 \end{cases},$$

where i_0 is the final step number used for the comparison of two algorithms.

As a numerical example, let us determine the optimal disposition of five sources

and five receivers in the bi-linear waveguide with the parameters, defined above, for the given observed area (r_0,r_1,z_0,z_1)=(35, 38, -2.46, -2.67) km shown by shadowed rectangle in Fig. 4.10. Figure 4.10 shows the original positions of sources and receivers and the optimal set of three sources and one receiver (filled circles and triangles, respectively). The transferal coefficients are maximal in the given region for the optimal system configuration.

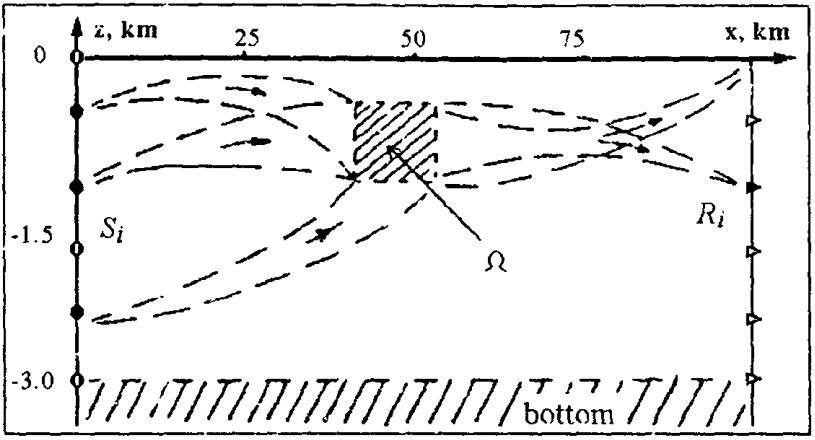

Figure 4.10. An optimization of hydroacoustical imaging system from 5 sources and 5 receivers for the given observation area Ω in the bi-linear ocean waveguide.(Adapted from [79])

4.4.7. Conclusions

The principles of the optimal choice of imaging-system parameters in a layered waveguide have been discussed. In particular, the transferal characteristics of the medium, such as CEC and AC, have been defined and analyzed. These characteristics were first defined in the papers [72, 73, 133] for designing the acoustic imaging systems in inhomogeneous media, including refractive type oceanic waveguides. In this paper the spatial maps of the coefficients have been used for optimizing the number and positions of the elements of imaging systems. That would provide the maximal sensitivity of the system.

It is important to mention some limitations implied in the discussed methods.

(1) The ray approach has been used for the calculation of the transferal characteristics. It limits the applications of the methods to the high-frequency range. However, both the mode and parabolic approximations can be also used for the characteristics calculations. Some preliminary results have shown that the spatial structures of CEC and AC are simpler for the low-frequency range [72].

(2) Besides the spatial transferal characteristics considered above, other

characteristics, related to the temporal signal structure, should sometimes be analyzed to optimize imaging systems in inhomogeneous media. Temporal characteristics have been analyzed in [73, 133]. First of all, the temporal characteristics are preferable for the monitoring of nonstationary objects or media. Secondly, the problem of the suppression of direct illumination signal fluctuations can be solved by using the temporal-transferal characteristics, for example, by using the Dark Field Method developed for inhomogeneous media [73, 75]. In this case we deal with more general optimization of acoustic imaging systems, taking the nonstationarity into account [18, 66]. It is important to note that geometrical dispersion has influence on temporal-transferal characteristics (unlike CEC and AC) for low frequencies that results in destroying the temporal pulse structure [134]. As a consequence, there are optimal frequency intervals for the observation of nonstationary inhomogeneities.

(3) The problem of acoustic imaging (similar to the problem of tomographic monitoring) is related to the inverse scattering problem. It is well-known that the regularization procedure based on *a priori* information is usually required to reject non-stable solutions. From this point of view, the optimization of the positions of the elements of imaging system, using *a priori* information about inhomogeneous media, provides an exclusion of non-stable solutions. The regularization issue requires more detailed future study.

(4) For the present consideration incoherent summation of rays has been used. It permits us to neglect fine-interference-field structure which is important in smoothly inhomogeneous media. The limitations on a use of this approximation depend on the properties of real inhomogeneous media, such as atmospheric and oceanic waveguides. If spatially distributed random inhomogeneities are present in such waveguides, then it should be assumed that the acoustic field has a partially coherent component. The importance of the coherent component is determined by both the space-time spectra of random medium variations and the scale of medium smooth variations [135]. The coherent or partially coherent summation of rays do not change the general methodology of optimization procedure.

(5) It is important to mention a problem, closely related to the discussed optimization examples. In optimizing the positions of sources and receivers, we have assumed a fixed observation area of medium. Thus, the optimal apertures for viewing a given, relatively small region of the medium have been estimated. If we assume a set of sources and receivers to be given, then in some sense, we can obtain a generalized aperture basis from the solution of the problem for every relatively small element of medium. Different working combinations of sources and receivers, allows us to carry out the spatial scanning of large regions of the inhomogeneous area. Each solution can be considered as a tomographic projection similar to one in the differential diagnostics [35].

Finally, we can suppose that the presented algorithms can be readily generalized for electromagnetic probing of atmosphere. Moreover, analogous approaches can be used in seismic exploration, in non-destructive control, and medicine.

4.5 FRESNEL DIFFRACTION TOMOGRAPHY IN THE OCEAN

The concept of visualizing primary and secondary sources of acoustic fields and objects in those fields has numerously and independently appeared in many applied areas, such as medicine and non-destructive testing and control and, more to the point here, in underwater engineering, environmental monitoring of extensive oceanic regions, navigation, and many others. To cite a single source, among many, we note the early paper on "acoustic vision" [7]. In acoustic vision the spatial distribution of some acoustic-field parameters is presented as patterns of varying intensities or colors, which can be referred to as an *acoustic image*.

Usually, the reconstruction of acoustic images is based on using some numerical technique. Such images provide informative interpretations of large quantities of measured data. However, one can not expect a direct analogy between acoustic and optic images because they deal with scatterer-wave interactions of different physical types. This fact makes acoustic images unusual in the sense of photographic perception. For example, internal structure of acoustically transparent objects can be visible, and, in that sense, be liken to an X-ray of the internal structure of the human body. Also, partially coherent interference structures of secondary source fields may lead to significant "highlights" in acoustic images, which can be referred to as speckle-noise. Finally, in optical vision we are usually thinking in terms of ray-theory propagation, whereas in acoustic vision we may be considering mode-theory propagation.

In this section we propose to generalize standard optical-vision methodology to acoustic vision in geophysical waveguides. Thus, it is assumed that the distances to the observation region from the radiating and receiving systems are great enough, so that the conditions of waveguide propagation are satisfied. First, it should be mentioned that the ocean medium is generally inhomogeneous. If rough and complex boundaries are not present, propagation in the water column can be described by using a smoothly inhomogeneous, layered waveguide model. Large-scale inhomogeneities complicate the process of local-inhomogeneity tomographic reconstruction from measured data, because such media are not iso-planar and do not "transmit" images [24].

Secondly, the ocean medium can be unsteady and randomly inhomogeneous. This produces illumination fluctuations that limit the use of the traditional vision methods developed for homogeneous media. Thirdly, observed objects usually have large dimensions in comparison with a wavelength, but weak gradients (for example, hydrolenses), so that the scattered-field energy is mostly concentrated in a small angular interval in the forward illumination direction. This is important because the quality of images depends on the useful signal to background noise ratio, and the "signal" is the weak forward-scattered part and the background is the strong forward propagating wave.

Summarizing the above-mentioned facts, we will assume that an imaging scheme, in which the investigated inhomogeneities are placed between the illumination source and receiving system, is designed for optimal hydroacoustic vision. This scheme is analogous to the optical one, but in the acoustic scheme, the spatially distributed radiating and receiving systems, in combination with numerical reconstruction algorithm, play the roles of the image-forming lenses.

The above described phenomena significantly complicate the process of acoustic-image reconstruction in comparison with free-space imaging. Thus, it is necessary to take into account waveguide propagation conditions in the reconstruction algorithm. Moreover, it is important that some means of reducing the forward-propagating field in comparison with the forward-scattered field be implemented. One such scheme providing filtration of the strong direct-illumination field that has been introduced is called the *Dark Field Method* [75].

In previous papers [75, 76], it has been shown, that under the above conditions of oceanic inhomogeneity, images can be reconstructed in a way similar to "shadow" images, which contain information about only one projection of the inhomogeneity. In the following subsections, we investigate possibilities of the simultaneous processing of a few inhomogeneity projections to obtain more complete information about the inhomogeneity's spatial distribution. We discuss some analytical and numerical results to complement data in the ultrasonic frequency range from physical laboratory model experiments.

4.5.1 The Analysis of the One-View Fresnel Image Reconstruction in the Ocean

The inhomogeneity-reconstruction algorithms, considered in many papers on tomography, are based on processing combinations of projections. The term *"projection"* is defined there as the field distribution along a receiving array for one fixed position of the radiating and receiving system. It is usually assumed that the illumination and scattered waves are planar, and that the scattering process consists of changing amplitude and phase (or propagation time) of the plane wave. This assumption can be satisfied if the inhomogeneity is large and weak [12, 50]. A different situation is considered in diffraction tomography, when we have a set of angles measuring diffracted signals for many fixed-illuminating source position [130]. Thus, we can define the received-field distribution, characterizing the scattered field for one fixed illumination angle, as one projection. The concept of projections is especially convenient for inhomogeneities of large-wave dimensions, when the scattered-signal spectrum is confined in a small interval of scattering angles, and the small array aperture is enough for measurements. In this case, we can assume that the array dimensions correspond to several Fresnel zones for the observed inhomogeneity. From a physical point of view, we deal with one projection, despite the fact that the aperture dimensions allow for reconstructing a two-dimensional inhomogeneity distribution by focusing the measured signal, but the longitudinal resolution is small. The obtained pseudo-image is the so-called "shadow" image. It is similar to a single projection in the tomographic method, but at the same time this image contains information on the longitudinal structure of inhomogeneity. Further we shall refer to

it as a *one-view image*. In previous papers (see, for example, [75]), the properties of such images were investigated and certain methods of spatial filtration of direct-illuminating signals were developed.

For more complete reconstruction of two-dimensional horizontal distributions of inhomogeneities, the simultaneous processing of projections or pseudo-images, measured at different illumination angles can be used. This allows for obtaining a more complete reconstruction of the shape of the inhomogeneity, even if only a few projections are available. It should be mentioned that this scheme is similar to the principle of human eyesight, i.e., to the binocular system, consisting of two lenses at a small angle from each other. The investigation of multi-view image characteristics will be considered in the next subsection. Here we analyze one-view images. In particular, we study the influence of waveguide propagation conditions on the formation of acoustic images in the ocean.

We can use the analogy between image formation by lenses and antennae in the Fresnel zone. In addition to that, we assume that the observed rigid inclusion of the horizontal and vertical dimensions, L and d, respectively, is situated in the waveguide between the source and the receiving system represented by horizontal and vertical arrays of hydrophones. The displacement velocity potential, $u(\boldsymbol{R})$, in the region of observation, $\boldsymbol{R}(x,y,z)$, is determined from the Helmholtz-Kirchhoff equation [8, 34]:

$$u_0(\boldsymbol{R}) + \frac{1}{4\pi}\oint_S \left[\frac{\partial u(\boldsymbol{R}_s)}{\partial n} G(\boldsymbol{R}_s,\boldsymbol{R}) + u(\boldsymbol{R}_s)\frac{\partial G(\boldsymbol{R}_s,\boldsymbol{R})}{\partial n}\right] dS = u(\boldsymbol{R}), \tag{4.56}$$

where $u_0(\boldsymbol{R})$ is the displacement velocity potential of the direct-illumination field, n is the outer normal on the inhomogeneity surface S, and $G(\boldsymbol{R}_s,\boldsymbol{R})$ is the Green's function of the unperturbed medium. The problem consists of the reconstruction of the inhomogeneity's location and shape by the reconstruction of the spatial distribution of secondary sources, $\partial u(\boldsymbol{R}_s)/\partial n$ and $u(\boldsymbol{R}_s)$, from the field, $u(\boldsymbol{R})$, measured on the array aperture, $M(y,z)$ (see Fig. 4.11). The measurements are carried out in the presence of noise.

As follows from Eq. (4.56), the problem of acoustic vision is the inverse scattering problem (ISP), because the integral equation with the known right-hand side should be solved with respect to the spatial distribution of secondary sources on the surface S of unknown shape. From this point of view, the problem of vision is a particular problem of ISP. ISP, itself, is the more general and complex problem of the reconstruction of both the internal structure and physical characteristics of inhomogeneities. On the other hand, the aim of vision is to create images of investigated objects convenient for visual observation.

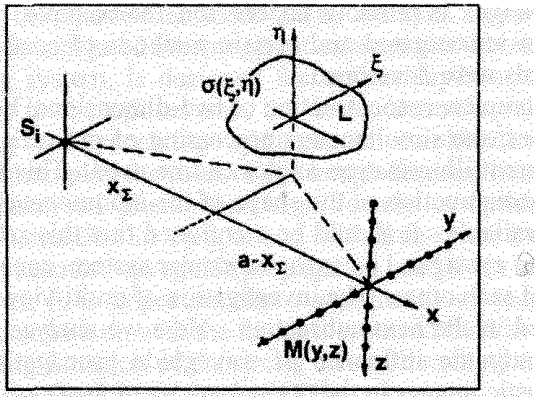

Figure 4.11. A scheme of one-view acoustical-vision system and measurement geometry. (Adapted from [34].)

For further analysis of imaging in oceanic waveguides, some approximations, which lead to problem simplification, are necessary. Let us assume that inhomogeneity is located far enough from waveguide surfaces, so that multiple scattering can be neglected. In addition to that, we assume that: 1) the horizontal dimension of the inhomogeneity is large compared to a wavelength (i.e., $L \gg \lambda$, where λ is the wavelength of the illuminating source); 2) narrow-angle scattering takes place; and 3) the distances between source, inhomogeneity, and receiver are large with respect to the waveguide thickness. In this case, Eq. (4.56) can be rewritten in the simplified form [34]:

$$u_0(\boldsymbol{R}) - \frac{1}{2\pi}\int\int_{\sigma} \sigma(\xi,\eta)\frac{\partial u_0(\xi,\eta)}{\partial n} G(\xi,\eta,0;\boldsymbol{R})\,d\xi\,d\eta = u(\boldsymbol{R}), \tag{4.57}$$

where $\sigma(\xi,\eta)$ is a part of plane limited by the line dividing the light and dark sides of the inhomogeneity situated at the point ($x_\Sigma, y_\Sigma, z_\Sigma$), where x_Σ is the distance from the source and $a - x_\Sigma$ - from the receiver (see Fig. 4.11). Further, we use the modal representation of the acoustic field in an oceanic waveguide [8]. Thus, we get the expression for the incident field and the Green's function:

$$u_0(x,y,z) = \sum_{n=1}^{N} A_0 \varphi_n(z)\varphi_n(z_i)\frac{\exp\left[i\left(a\kappa_n - \frac{\pi}{4}\right)\right]}{\sqrt{(a\kappa_n)}}\exp\left[i\frac{y^2}{2a}\kappa_n\right], \tag{4.58}$$

$$G(\xi,\eta,0,x,y,z) = \sum_{m=1}^{N} \varphi_m(y)\varphi_m(\eta)\frac{1}{\sqrt{\kappa_n(a-x_\Sigma)}} \times$$

$$\times \exp\left[i(a-x_\Sigma)\kappa_m + i\frac{\eta^2+y^2}{2(a-x_\Sigma)}\kappa_m - i\frac{y\eta\kappa_m}{a-x_\Sigma} - i\frac{\pi}{4}\right], \qquad (4.59)$$

where N is a number of propagating waveguide modes and κ_n and φ_n are the horizontal modal wavenumbers and the vertical modal eigenfunctions, respectively. The distances included in the exponential terms are represented by a Taylor expansion, including the second-order components; so that we take into account the sphericity of the incident and scattered fields, and A_0 is a constant determined by the power of the source.

Combining Eqs. (4.58), (4.59), and (4.57), we obtain the integral equation with respect to the unknown location and shape of inhomogeneity. For an arbitrary inhomogeneity shape, determined by σ, the vertical and horizontal coordinates, (ξ,η), in Eq. (4.57) are interrelated, complicating the analysis. Because these dependencies contain different physical information, it is convenient to investigate them separately. In the vertical direction only, trapped waveguide modes take part in the scattering at large distances and that causes a transformation of the modal spectrum [28]. In the horizontal direction, the diffraction of each mode on the inhomogeneity is analogous to diffraction in free space. For simplification of the analysis, we assume that a separation of coordinates is possible for the given inhomogeneity shape, $\sigma(\xi,\eta)=L(\eta)\cdot T(\xi)$. Then, taking Eqs. (4.58) and (4.59) into account, we can arrive at the following form of integral equation (4.57):

$$u(a,y,z_a) = A_0\sum_{n=1}^{N}\frac{\varphi_n(z_a)\varphi_n(z_\Sigma)}{\sqrt{r_0\kappa_n}}\exp\left[i\left(r_0\kappa_n-\frac{\pi}{4}\right)\right] - \frac{A_0}{2\pi}\sum_{m=1}^{N}\varphi_m(z_a)\sum_{n=1}^{N}\frac{\varphi_m(z_\Sigma)(-i\kappa_n)T_{nm}}{\sqrt{\kappa_n\kappa_m r' s'}}\times$$
$$\times \exp\left[i(\kappa_n x_\Sigma - \kappa_m(a-x_\Sigma)+\kappa_m\frac{y^2}{2(a-x_\Sigma)}-\frac{\pi}{2})\right]\int_{-\infty}^{\infty}L(\eta)\exp\left[-i\left(\frac{y}{s'}\kappa_n+\frac{y}{r'}\kappa_m\right)\eta\right]d\eta\,, \qquad (4.60)$$

where

$$r_0 = a+\frac{y^2}{2a}\,, \quad r' = a-x_\Sigma+\frac{y^2}{2(a-x_\Sigma)}\,, \quad s' = x_\Sigma+\frac{y^2}{2x_\Sigma}\,,$$

and

$$T_{nm}=\int_{-\infty}^{\infty}T(\xi)\varphi_n(\xi+z_\Sigma)\varphi_m^*(\xi+z_\Sigma)d\xi. \qquad (4.61)$$

The first term on the right-hand side of Eq. (4.60) represents the incident field in the observed region in the modal representation. The second term corresponds to the scattered field. Let us consider Eq. (4.60) from the point of view of the image reconstruction from the field distribution measured on the aperture, $M(y,z)$. First, we examine the possibilities of the inhomogeneity's vertical distribution. As follows from

Eq (4.60), the scattering in the vertical direction consists in the modal spectrum transformation, which is defined by the matrix component in Eq. (4.61). If the vertical inhomogeneity dimension, d, is small, then the characteristic scale of the waveguide-field fluctuations is much larger than d. Then, the modal vertical functions for the isovelocity waveguide can be written as:

$$\varphi_n(z) = \sin(q_n z) = \frac{1}{2i}(e^{iq_n z} - e^{-iq_n z}).$$

Defining the function

$$T_{n\pm m} = \frac{1}{2\pi}\int_{-\infty}^{\infty} T(\xi) e^{i\xi(q_n \pm q_m)} d\xi,$$

we obtain the expression for the matrix T_{nm}:

$$T_{nm} = \mp\frac{\pi}{2}[T_{n+m} - T_{n-m}]. \tag{4.62}$$

The spatial filtration of waveguide modes in the scattering process can be described (as in free space) by the convolution of the "input" discrete-mode spectrum and the modal filter T_{nm}, determined by Eq. (4.61):

$$\varphi_m(z) = -\sum_{n=0}^{N} \frac{\pi}{2}\varphi_n (T_{n+m} - T_{n-m}) L_{nm}, \tag{4.63}$$

where

$$L_{nm} = i\kappa_n \int_{-\infty}^{\infty} L(\eta) \exp\left[-i\left(\frac{y_t}{s'}\kappa_n + \frac{y}{r'}\kappa_m\right)\eta\right] d\eta .$$

If the waveguide surfaces are removed to infinity, Eq. (4.63) transforms into the convolution integral, corresponding to the spatial filtration in the free space. As seen from Eq. (4.63), estimating the vertical structure of the inhomogeneity is possible, if we solve Eq. (4.63) by the deconvolution method. However, *a priori* information about the incident-field modal spectrum and the measured modal spectrum of the scattered field is required. As an example, let us consider the situation when the inhomogeneity is illuminated by a single mode and the scattered field consists of many modes, which can be resolved by a measuring system. In this case, the envelope function of the modal spectrum represents the scattering directional pattern, which permits estimating the vertical dimension of the inhomogeneity by the inverse Fourier transform. However, it should be mentioned that such a way of reconstruction generally requires a waveguide-mode selection. This could be done by the use of vertical arrays, time strobing or other methods. These methods are associated with

both technical difficulties and complex processing algorithms [50, 66].

Here, we only details the reconstruction of images based on information on horizontal distributions of inhomogeneities. As follows from Eq. (4.60), for the given indices, (n,m), the field distribution along the receiving aperture is the Fresnel transform of an unknown function, which determines the inhomogeneity shape in the horizontal plane, in the transfer direction. The multi-mode structure reveals itself in additional interference modulation within the observed region, because of the mode summation. In Refs. [28, 29], the conditions for which the interference-modulation spatial spectrum and the spatial spectrum corresponding to the inhomogeneity influence differ substantially are obtained; that is,

$$\left(\frac{4\pi r_0}{\Delta\kappa_{ij}}\right)^{\frac{1}{2}} \approx \frac{r_0\pi}{\langle\kappa_{ij}\rangle L}, \qquad \Delta\kappa_{ij}=|\kappa_i-\kappa_j|, \tag{4.64}$$

where $r_0=a-x_\Sigma$ and $\langle\kappa_{ij}\rangle$ denotes the average value of the modal wavenumber. For fixed parameters of the waveguide and the inhomogeneities, the distance of observation, r_0, plays an important role. Thus, for $r_0\gg\tilde{r}_0$, where $\tilde{r}_0$ is the distance at which the condition imposed by Eq. (4.64) is satisfied, the frequency of the interference modulation is higher than the frequency of the modulation caused by the inhomogeneity; and, for $r_0\ll\tilde{r}_0$, it is less than the "useful" variations. This provides easy filtration of two effects. However, when Eq. (4.64) is satisfied, the interference modulation may be filtered only by using *a priori* information about waveguide and inhomogeneity parameters. Thus, the image of the inhomogeneity, reconstructed without taking the modal structure into account, may be significantly altered. At the distances satisfying condition (4.64), the images corresponding to different modes superpose making the resulting image interpretation rather difficult. At large distances, inhomogeneity images are multiplied.

Let us consider an example of the case when only one mode is present and $n=m$. To this end, we may assume that mode selection is carried out, or one mode is differentiated as a result of dissipation loss in waveguide propagation, or the mode interference component is filtered within the imaging process [76]. In the one-mode approximation, Eq. (4.60) is equivalent to:

$$u(a,y,z_a) \approx S_n^0 e^{i\frac{y^2}{2a}\kappa_n} - S_n e^{i\frac{y^2}{2(a-x_\Sigma)}\kappa_n}\int_{-\infty}^{\infty} I_\Sigma(\eta) e^{-i\left(\frac{y_0}{s'}+\frac{y}{r'}\right)\kappa_n\eta}\,d\eta, \tag{4.65}$$

where

$$S_n^0 = A_0\varphi_n(z_a)\varphi_n(z_1)(r_0\kappa_n)^{-1/2}\exp\left[i\left(a\kappa_n-\frac{\pi}{4}\right)\right],$$

$$S_n = \frac{A_0}{2\pi}\varphi_n(z_a)\varphi_n(z_1)(-i\kappa_n)T_{nn}(\kappa_n^2 r's')^{-1/2}\exp\left[i\left(\kappa_n x_\Sigma+\kappa_n(a-x_\Sigma)-\frac{\pi}{2}\right)\right].$$

Assuming that $y_0 = 0$, we obtain the expression for the second term in Eq. (4.65):

$$second\ term = S_n \int_{-\infty}^{\infty} L(\eta) \exp\left[i\left(-\kappa_n \frac{\eta}{r'} y + \kappa_n \frac{y^2}{2(a - x_\Sigma)} \right) \right] d\eta .$$

This is the Fresnel integral where the exponential functions represent the complete orthonormal basis [133]. This fact helps in obtaining the solution of integral equation (4.65) with respect to $L(\eta)$, using the property of the Fresnel-basis orthonormality. To do this, it is necessary to multiply both sides of the equation by the factor $\exp[i(\kappa_n y \sin\alpha - \kappa_n y^2/R)]$, where $[\alpha, R]$ are the polar coordinates of the point (x,y), and to integrate the expression over the whole region where the Fresnel functions are defined. Then, on the left-hand side of Eq. (4.65), we obtain the Fresnel transform of the field measured by an infinite aperture. The right-hand side contains two images: the point-illuminating source image for $\alpha' = 0$ and $R' = 2a$ (the first term) and the image $L(\alpha, r')$, determined for $R = 2(a - x_\Sigma)$. However, it is a formal solution, because, in reality, we deal with finite apertures in experiments. Defining this aperture by the function $M(y_A)$, we multiply both sides of Eq. (4.65) by $M(y_A)\exp[i(\kappa_n y_A \sin\alpha - \kappa_n y_A^2/R)]$ and integrate it within infinite limits. Then, on the left-hand side, we obtain the function $\Phi_n(\alpha, R)$, which determines the algorithm for image reconstruction using the measured data. Two terms on the right-hand side of Eq. (4.65) can be written as:

$$right\text{-}hand\ side = S_n' F_n\left(\alpha, \left(\frac{1}{2a} - \frac{1}{R} \right)^{-1} \right) - S_n \int_{-\infty}^{\infty} L(\eta) F_n\left(\alpha - \frac{\eta}{r'}, \varepsilon^{-1} \right) d\eta , \qquad (4.66)$$

where $\varepsilon = \dfrac{1}{2(a - x_\Sigma)} - \dfrac{1}{R}$ is a parameter of vision-system focusing, $\sin\alpha \approx \alpha$, and F_n is the pulse-transient characteristic of reconstruction system, i.e., the image of a primary or secondary point source:

$$F_n(\alpha, R) = \int_{-\infty}^{\infty} M(y_A) \exp\left\{ i\kappa_n \left[\left(\frac{\eta}{r'} - \alpha \right) y_A + \varepsilon y_A^2 \right] \right\} dy_A . \qquad (4.67)$$

It is known from the theory of image-reconstruction systems (for example, for optical systems) that the quality of imaging is characterized by the pulse-transient function. For some cases, this function appears to be independent of the point-source position within a vision area. However, in acoustical applications this does not occur because the image of a discrete, point-scattering object essentially depends on point location within the vision area. As seen from Eq. (4.67), this dependence is very pronounced, when the observation point moves out of the possible measurement area. For the rectangular aperture, when

$$M_n(y_A) = \begin{cases} 1, |y_A| \le D/2 \\ 0, |y_A| > D/2 \end{cases},$$

and, for $\varepsilon=0$ (for a focused image), $F_n(\alpha, a-x_\Sigma) = D\,sinc(\kappa_n \alpha D)$, and the transverse resolution (along the y-axis) can be characterized by $\Delta y = \lambda(a-x_\Sigma)/2D$. The point-source image is much wider in the longitudinal direction: Δx is approximately 5 to 10 times Δy. Better estimates can be obtained directly from the Fresnel integral. As an observed object moves away, the separate resolution elements extend along the x-axis. As follows from Eq. (4.66), the structure of the point-source image determines the number of independent resolution elements in the final object image.

In Fig. 4.12, the images of two point sources at different angles and distances, $a-x_\Sigma = D$, $D = 30\lambda$, relative to receiving array are shown. It can be seen that the image of the distant source is displayed in the observation area as a quasi-uniform background. This is caused by the finite dimensions of the antenna aperture and, therefore, by weak focusing of the field from distant sources. It should be noted that the number of independent image elements is determined not only by the size of the point-source image, but also by the limited area of vision. This circumstance is stipulated by an inapplicability of the Fresnel approximation near the antenna and the resolution decrease at large distances and large displacements along the x-axis. As follows from Eq. (4.56), the receiving system registers both the scattered field, characterizing the observed inhomogeneities, and the direct-illumination field. The first term in Eq. (4.56) defines the source image. Once again, if the source is far enough from the receiver, then its image occupies the whole vision area. As mentioned before, the strong direct signal fluctuations mask inhomogeneity images. In addition to that, the presence of a strong direct signal leads to a decrease of dynamic range in signal registration. To overcome these difficulties and suppress the direct-illumination field, the Dark Field Method has been developed by an analogy with the optic case [75 76]. This method is based on the essential separation of scattered and direct-signal spatial spectra, which arises from the differences in distances from receiving system. There are two different ways to accomplish the Dark Field Method. In the first case, the focused signals of two adjacent receivers are subtracted and multiplied by a certain mask. Then, the resulting spatial components are filtered [76]. The second way is based on the spatial filtration of the Fresnel images by

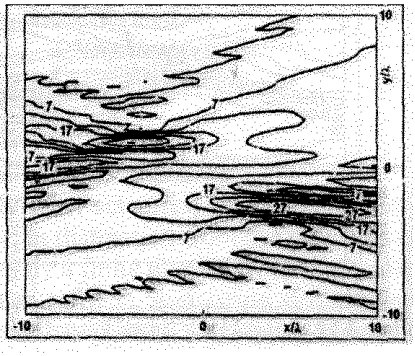

Figure 4.12. Fresnel images of two point sources distributed in a horizontal plane from one projection with sources situated at different angle and distances. (Adapted from [34].)

two-dimensional filters, adjusted to the illumination-source image [76]. Both methods require *a priori* information about the illumination-source location. However, the second way may be more effective in complex, non-stationary media because the filter can be constructed by using the empirical data in the absence of inhomogeneities.

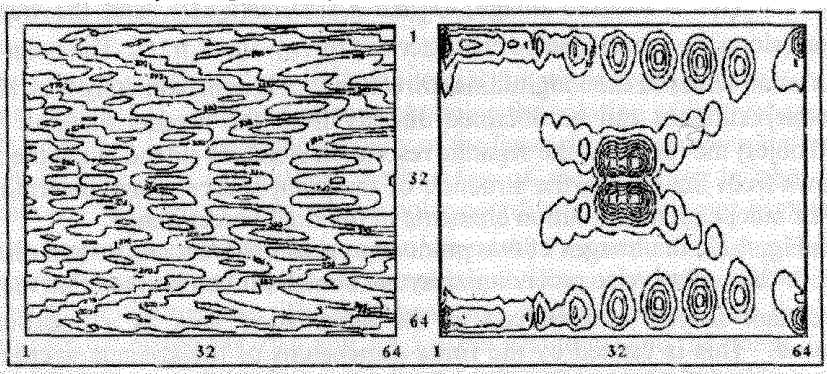

Figure 4.13. Image of an illumination source and scatterer: (a) without filtering; (b) after filtering. (Adapted from [79].)

An example of the diffracted signal filtering from the high-level illumination background, when the illumination signal is about 15 dB higher than the diffracted one, is given in Fig. 4.13 [79]. Figure 4.13b shows the scatterer image, obtained by using the two-dimensional spatial spectrum filter, $\theta(\xi_x,\xi_y) = |F^0(\xi_x,\xi_y)|^{-1}$, where $F^0(\xi_x,\xi_y)$ is the source spectrum, and ξ_x and ξ_y are spatial frequencies. In the presented example, the dimensions of the aperture are about ten Fresnel zones of the illumination source.

Reference [76] describes the application of this method to the image reconstruction of a vertical steel rod in a water layer. The interference of waveguide modes in these experiments resulted in a strong distortion of the source image in the observation area. This led to the almost complete masking of the steel rod image. The

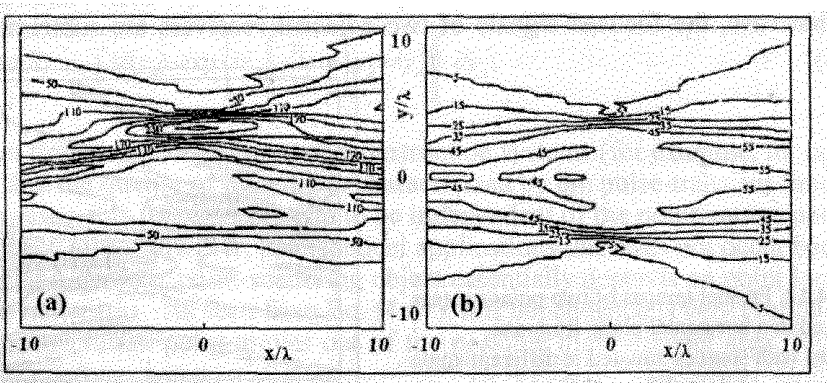

Figure 4.14. Images of a Greek letter Π (a) and the transverse rectangle (b) reconstructed from one projection with the direct illumination field suppressed. Figure illustrates problems with one-view image reconstruction. (Adapted from [34].)

spatial filter, designed by an inversion of the illumination source-amplitude spectrum, taking modal interference into account, was used to localize the rod. As seen from the analysis of different kinds of one-view images, a significant portion of information may be lost for complex spatial distributions that leads to some uncertainty in the estimation of the observed objects shape and location. To illustrate this fact, images of a Greek letter, Π, and a rectangle, extended in the transverse direction, y, of the same dimensions along the y-axis are given in Fig. 4.14 [34].

Numerical simulations show that an adequate interpretation of various objects from one-view images is difficult. Recently, tomographic methods providing the most complete reconstruction of spatial distributions of inhomogeneities by the simultaneous processing of projections at different angles have been developed. However, the consequent measurements of signals in the ocean at many angles is a long-termed process, which is not effective for non-stationary inhomogeneity observations. On the other hand, the design of schemes of simultaneous measurements at different angles is very expensive. Apparently, a possible solution is an application of scanty-view schemes, which allow for the partial resolution of this problem. Additionally, when waveguide influences become significant, it is important to maintain illumination sources and receiving arrays in the most effective aspects with respect to natural ocean-waveguide conditions. However, it is necessary to take into account technical and other difficulties arising in the design of remote acoustic-vision systems. The use of long horizontal antennas of continuous aperture, measuring many Fresnel zones, appears to be less effective than the use of arrays of sparse acoustic receivers.

Some vision schemes, based on sparse transducer arrays and used in the scheme of reconstruction from two projections (i.e., a "binocular scheme") are discussed in the next subsections. It is also necessary to pay attention to the influence of waveguide conditions on vertical receiver locations. In papers [46, 130] differential diagnostics methods have been proposed for the reconstruction of inhomogeneity spatial structures by vertical radiating and receiving arrays. In this way, an optimal receiving-system disposition provides for matched radiation and reception of waveguide modes significantly separated in the modal spectrum. The general problem of the optimization of source and receiver locations in the acoustic-vision scheme is considered in [133], where the translation characteristics of inhomogeneous media are introduced and special optimization algorithms are discussed.

4.5.2 Binocular Scheme of Acoustic Vision

Returning to the consideration of scanty-view schemes, we shall assume that one-mode propagation can take place. However, in distinction from the previous case, we will consider the imaging of inhomogeneities by a finite number of sparsely located receivers. Before the analysis of the binocular scheme, consisting of two remote arrays, we consider briefly the one-view reconstruction by a discrete array. The aperture function $M(y_A)$ for a finite number, N, of receivers can be written as:

$$M(y_A) = \sum_{n=1}^{N} A_0 \delta(nd - y_A) \Pi_{y_A}, \tag{4.68}$$

where

$$A_0 = const, \qquad \Pi_{y_A} = \begin{cases} 1, |y_A| \le D/2 \\ 0, |y_A| > D/2 \end{cases}, \qquad d = D/N,$$

and D is the array length.

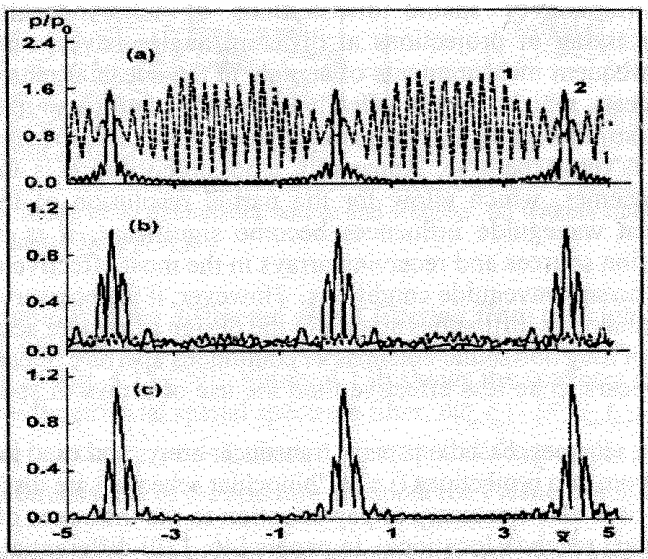

Figure 4.15. Images of an illumination source (dashed line) and a scatterer in the plane of the scatterer: (a) before filtering; (b) and (c) after filtering. (Adapted from [76]).

It is well-known that the use of finite-size arrays results in the multiplication of images [76]. Figure 4.15a shows the resulting multiplied images of the point scatterer and the point-illumination source in the area of scatterer localization. The received signal was processed by focusing the source image and leaving the scatterer image unfocused. Substituting Eq. (4.68) into Eq. (4.67), we obtain the focused-multiplied image of the illuminating source in the focusing plane of the illumination source:

$$P(x,y) \sim \sin\left(N\frac{kxd}{2a}\right) \sin^{-1}\left(\frac{kxd}{2a}\right),$$

where a is the distance between the source and receiver, and $k=2\pi/\lambda$.

For direct-signal suppression, a filter enclosing the main and two adjacent maxima of each source image was used. Then, the obtained signal was focused into each point of the vision area (Fig. 4.15 b). Besides that, more effective filtration can be achieved, when the matched-filter multiplier is $\theta \sin(kvd'2a)$. Suppressing the spectral harmonics, $\pm N$, we obtain a pure scattered signal (Fig. 4.15c). The vision area of such a system is limited by the number of receiving elements. In the considered case, the number of individual elements of the image in the transverse direction (along

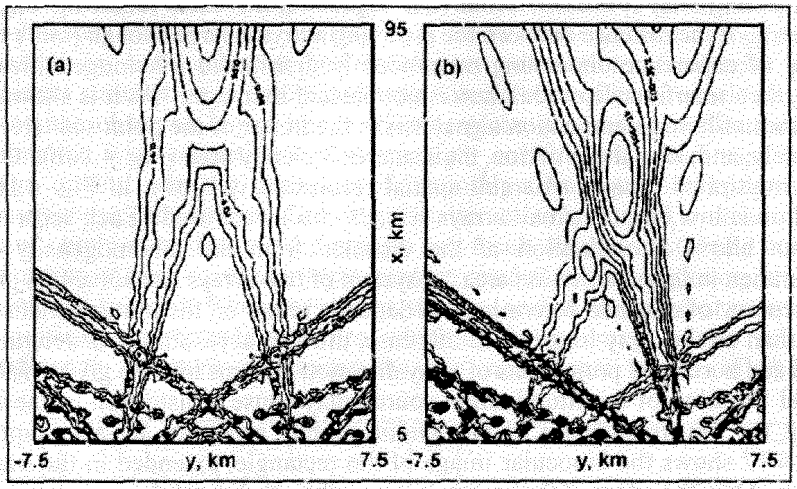

Figure 4.16. Image reconstruction by two 8-element arrays of length equal to 10λ separated by 800λ before (a) and after (b) filtering. Binocular tomographic reconstruction scheme. (Adapted from [79]).

the y-axis) is of order $N \cdot D/d$. Apparently, these simplified schemes are useful for the observations of small objects. To determine the true location of observed object by using the same receiving system, one may get a set of images for different illumination frequencies. The true image in obtained patterns keeps the same location. By summing the received images from different frequencies, we can get the true object location. The resolution in the longitudinal direction is limited both by the dimensions of the region of measurements, as for the continuous aperture, and by the multiplication effect. As it was mentioned before, it is necessary to increase the receiving aperture dimensions to increase the spatial resolution in the longitudinal direction (along the x-axis). This is difficult to design for practical purposes. However, one can avoid these difficulties by using a receiving system consisting of two remote antennas. Then, the vision is carried out from two directions that can provide some advantages, for example, an increase of longitudinal resolution. According to Eqs. (4.66)-(4.68), images, reconstructed by each array, are similar to those shown in Fig. 4.15, and the resulting image may be obtained by coherent or incoherent summation of these images. As a result of coherent summation, the obtained signal is modulated by the interference component, characterized by different

spatial periods for different distances from the antennas. In particular, the spatial frequency of modulation decreases as the distance from observation area to receiving arrays increases. Moreover, the modulation frequency increases with the angular displacement augmentation. In certain cases such spatial modulation allows for the determination of the distance from the scattering inhomogeneity, but this requires either observations at several frequencies or the presence of moving inhomogeneities.

Let us examine closely the incoherent summation of images [34, 79]. This type of processing may be used, when the signals from each receiving region are incoherent. If the distance between the receiving arrays is large enough (more than the interval of coherence depending on randomly distributed inhomogeneities in the ocean), then interference modulation is not present in images. As it is shown in Fig. 4.16a, the unfiltered-illumination signal masks the image of the point scatterer almost completely, and, after the filtration, the scatterer is clearly seen (Fig. 4.16b). Only one of the multiplied images of small spatial resolution is shown in Fig. 4.16. The resolution is low because small arrays (i.e., $D \sim 10\lambda$) were used. Each separate array does not allow determination of the distance from the inhomogeneity and its configuration in the given vision area. A system of two arrays can solve this problem. The accuracy of distance determination depends rather on the mutual orientation of arrays than on the array lengths. In this case, the spatial resolution is determined by vertical and horizontal projections of array direction patterns into the given vision area. Spectral filtration of the illumination source may cause a distortion of the images, because the low frequencies in the inhomogeneity spectrum are also suppressed. Figure 4.17 shows the binocular image of the rectangle, extended in the transverse direction. Only the edges of the rectangle are visible, because these regions are formed by the high-frequency component of the spatial spectrum, which was not suppressed by the filtration.

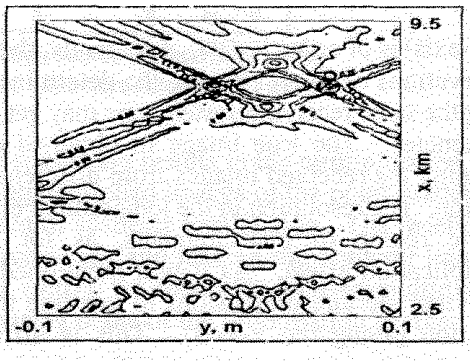

Figure 4.17. Filtered image of the transverse rectangle reconstructed from two projections. (Adapted from [79].)

The presented consideration has shown that the reconstruction of the spatial distribution of inhomogeneities by using sparse-element arrays and a few angles of observations may be carried out effectively only in certain situations. Apparently, it is possible to observe spatially localized inhomogeneities moving in the vision area. The reconstruction of complex-shaped objects or the spatial distribution of several objects requires a registration of a large amount of data. To this end, in the next subsection we shall consider the possibilities of acoustic imaging by a common processing of a few images at various observation angles, i.e., *multi-view images*.

4.5.3 Multi-View Images

Contrary to the binocular scheme, in which the images were formed for only one illuminating source, we now consider schemes where the illumination and receiving angles will be changed simultaneously with the same step-size in opposite directions, and the receiving-array, bearing-angle shift at the same pitch in opposite directions. For observation of stationary distributions, the subsequent measurements of partial images at each angular view may be carried out [34]. In the opposite case, simultaneous measurements are required. As mentioned, the resulting image may be obtained by both coherent and incoherent summation of separate projections. Coherent summation is associated with interference effects, which can essentially distort the observed object image. Furthermore, processing in this manner allows summation with correcting complex weight coefficients, which may improve the image quality. In the presence of randomly distributed inhomogeneities, it is convenient to carry out incoherent summation to reduce speckle-noise. Figure 4.18 shows a multi-view image of a rectangle as a result of coherent (a) and incoherent (b) summation of twelve partial images, reconstructed at various angles equidistant within the interval from 0 to 90 degrees. First, we can see that the coherent summation gives a significant interference structure, which masks the image of the rectangle. The interference structure is caused by the anisotropic shape of the scatterer.

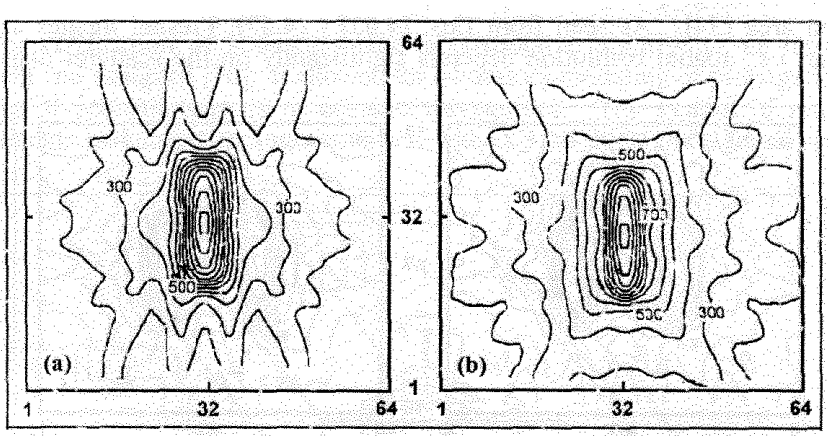

Figure 4.18. Filtered multi-view image of the horizontal rectangle as a result of coherent (a) and incoherent (b) summation of 12 projections. (Adapted from [79].)

Consequently, the two images, corresponding to observations from the longer sides of the rectangle, interfere as in the binocular scheme. Secondly, spatial interference of the resulting image is caused by a complex structure of each separate projection. And, finally, the interference from numerous separate image details of approximately equal brightness produces the speckle-noise [8]. This is well known not only in acoustics but also in optical reconstruction by the laser light. These phenomena can be taken into account in the development of the special methods of acoustic vision, in particular, in ultrasonic medical diagnostics. However, in certain cases, when an estimate of the average distribution of inhomogeneities is required or when partial

images are incoherent due to the influence of random inhomogeneities. incoherent summation should be carried out (as in Fig. 4.18b). In this case, there are no interference structures in the resulting image, so the image looks smoother. However, one loses the opportunity for coherent processing of signals.

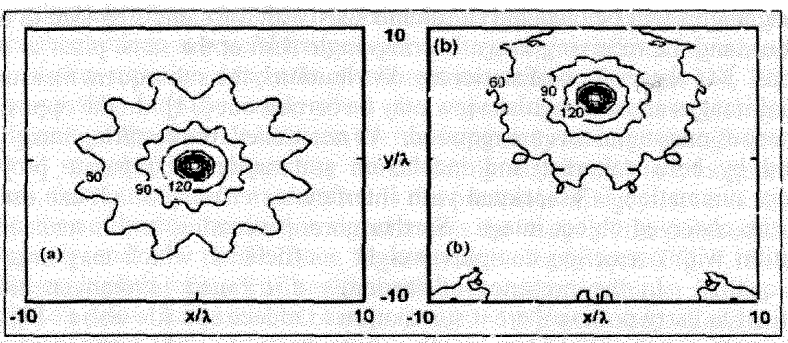

Figure 4.19. Multi-view image of the point source reconstructed from 12 projections when the source is situated at the center (a) and near the edge (b) of the vision area. (Adapted from [34].)

It is also important to examine the characteristics usually used for the description of image quality, namely, the spatial resolution and the array-formed shape of vision area [34]. As seen from Eqs. (4.65) - (4.67), Fresnel images are non-isoplanar, i.e., spatial resolution depends significantly on the scatterer disposition

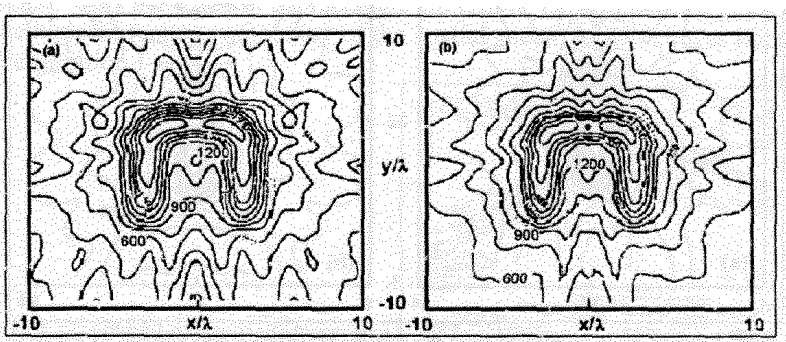

Figure 4.20. Coherent (a) and incoherent (b) multi-view images of the Greek letter Π reconstructed from 32 projections. (Adapted from [34].)

within the vision area. In multi-view imaging, the best resolution appears in the area center (Fig. 4.19a) because all partial images of the point source are identical. An individual element of resolution becomes spread out and decreases in its amplitude as it is displaced from the center of formed vision area (Fig. 4.19b). This occurs because, for several angles, the observation point is located at greater distances, so that its image is elongated in the direction of the corresponding array. Thus, the resulting image becomes spread out in space. Numerical simulation has shown that, for the multi-view system of reconstruction in the Fresnel zone, the optimal vision area is a

circle of the radius $0.75a$ with the center in the point $(0.5a,0)$. The multi-view images of the Greek letter Π are given in Fig. 4.20 for coherent (a) and incoherent (b) summation of images at 32 observation angles, equidistantly distributed within the interval from 0 to 180 degrees.

In the considered example, the image of the self-illuminating object is calculated. This allows the possibility to investigate Fresnel image reconstruction without reference to the problem of the direct-illumination field suppression. It can be seen that information about the source spatial distribution is augmented by incoherent summation. In coherent summation, one of the lines forming the letter is barely visible. This effect is evidently caused by the interference because it disappears with a shift of the letter with respect to the center of observation area. A comparison of two images shows that, in the case of incoherent summation, the noise appears in the form of some averaged "halo", which may be removed by low-frequency filter. For the other case, when partial images are summed coherently, the interference speckle-noise appears. This noise has wide a spatial spectrum that makes the filtration difficult.

4.5.4 Experimental Reconstruction of Scanty-View Images by Physical Modeling

For verification of acoustic-image-reconstruction algorithms, an ultrasonic experiment was designed [76]. It allowed for laboratory modeling of propagation and scattering of acoustic signals in oceanic waveguides. The system of modeling measurements includes a homogeneous water layer 3 cm thick and a sound speed of

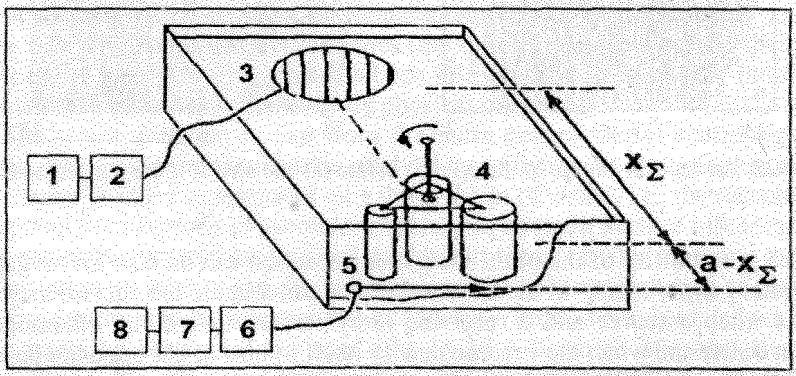

Figure 4.21. A scheme of the modeling experiment: 1 - pulse generator, 2 - power amplifier, 3 - pulse source, 4 - an observation object, 5 - a moving receiver, 6 - an amplifier, 7 - a filter, 8 - a computer. (Adapted from [79].)

1485 m/s overlaying a rubber bottom. A piezoceramic source having a horizontal directional pattern allowed for the avoidance of reflection from the basin walls. Quasi-harmonic pulsed signals of the duration of 300 micro-seconds at the frequencies of 140 kHz and 512 kHz were used. Because of strong losses in the rubber bottom, only a

few modes were propagated. The received signals were recorded by two quadrature channels for later processing and image reconstruction by a computer system (see Fig. 4.21). An inhomogeneity in the form of a vertically positioned steel cylinder of diameter 0.25 cm was placed at a distance of 20 cm from the source. The field was measured at a distance of 44.6 cm from the source by scanning with the receiving system. The length of the synthetic aperture was 28.6 cm. A distinctive feature of the experimental set was the appreciable length of both the scattering inhomogeneity and the illumination source (with the horizontal dimensions of 7 cm).

Figure 4.22a shows the image of the cylinder, reconstructed from one projection. Evidently, the image mainly represents the illuminating source. Here the waveguide modal interference is clearly depicted as vertical strips fully masking the image of the cylinder. The scatterer image after the spatial filtration is given in Fig. 4.22b. The filter was inversely proportional to the amplitude spectrum of the illumination and took the source geometry and modal interference into account. The filter was formed from the experimental data in the absence of the cylinder. The image after filtration allowed determination of the cylinder position. The cylinder dimensions were less than a wavelength, so the reconstruction of the inhomogeneity shape was practically impossible.

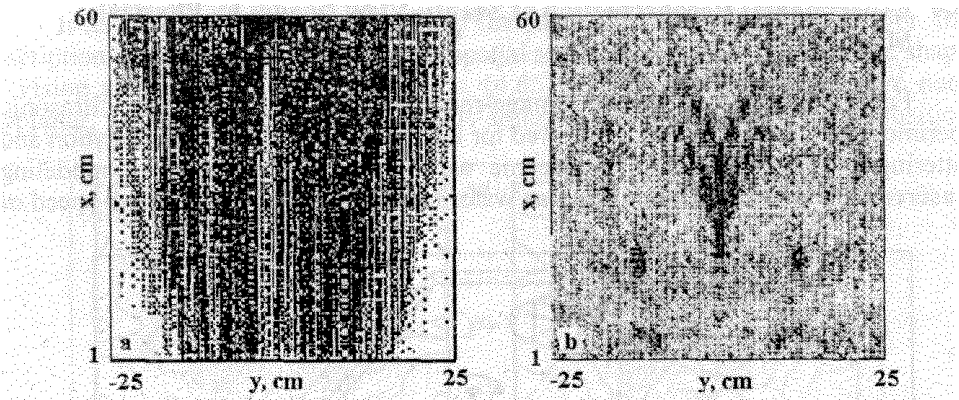

Figure 4.22. An one-view image of the cylinder before (a) and after (b) filtering. (Adapted from [76].)

The possibilities of the multi-view reconstruction can be also investigated by this laboratory experiment. In the experiment, we can assume the equivalency of the situations when a source and a receiving array rotates around the inhomogeneity situated in center and when the inhomogeneity itself rotates in the opposite direction. Three scattering vertical cylinders with the diameters of 1, 2, and 3 cm can be mounted on the mechanically rotatable frame. The distances between them were 9, 5, and 6 cm. The length of the array in this part of the experiment, synthesized by moving a receiver at the depth z_A = 0.3 cm, was 36.5 cm. The depth of the source was 1.7 cm. The results of reconstruction of the inhomogeneity spatial distribution from 32 projections are presented in Fig. 4.23. In the experiments, the inhomogeneity was located off the center of the acoustic path, where $x_\Sigma = a/2$, but closer to the antenna at $a - x_\Sigma$ = 25 cm,

a=152 cm. These parameters were taken into account in summation of partial images. As shown in the images, significant interference distortions appear in the reconstruction process, including the spatial-frequency range, where the useful signal is present. This does not allow the suppression of the interference by simple methods.

In this section, the possibilities of the image reconstruction of large-scale oceanic inhomogeneities by scanty-view systems, when the illumination and reception have been carried out in the limited range of angles, have been investigated. The

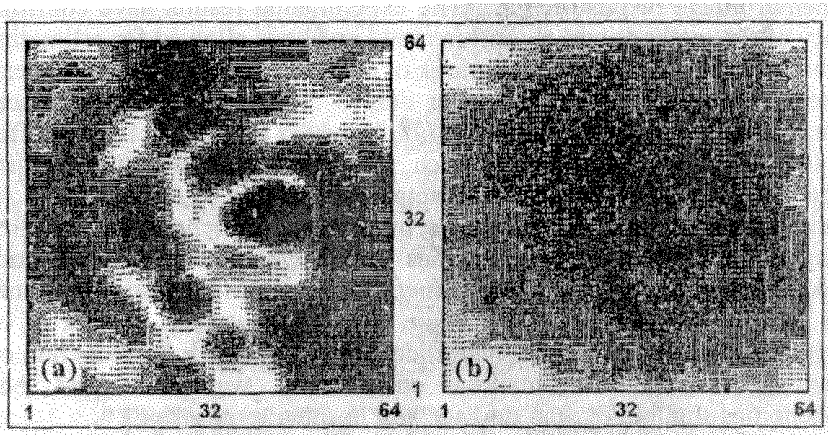

Figure 4.23. Coherent (a) and incoherent (b) multi-view images of three cylinders, reconstructed from 32 projections. (Adapted from [79].)

features of the acoustic imaging in the Fresnel zone for multi-mode oceanic waveguides have been analyzed. From the point of view of practical difficulties in the design of acoustic-vision systems, particular attention was paid to systems consisting of a few sparsely positioned hydrophones (the binocular system among them). The analysis of the multi-view systems has been fulfilled both theoretically (analytically and numerically) and experimentally by physical modeling.

The vision problem is one from the more general set of scattering inverse problems. The vision problem can be resolved by applying the tomographic methods. In this chapter we have investigated only the problem of vision, i.e., the reconstruction of the spatial distributions of secondary sources in terms of surface inhomogeneities without reconstruction of their physical internal structures. In this case, one can obtain the information on inhomogeneity localization in the observation area and its shape.

The results can be summarized as follows. First, it has been shown that for measurements by horizontal antennas (the lengths of which are more than a few Fresnel zones for observed inclusions), the reconstruction of inhomogeneity distributions are possible by consecutive angle scanning and focusing into each point of the vision area. The spatial-resolution and vision-area bounds have been estimated.

Secondly, it has been shown that the Dark Field Method (in particular, in the form of *a posterior* two-dimensional spatial filtration of the resulting image) is required to improve image characteristics.

Thirdly, it has been found that the application of the binocular observation scheme (consisting of two receiving arrays) leads to the improvement of image spatial

resolution in the longitudinal direction.

Fourthly, the limitations on the spatial resolution and vision area dimensions have been estimated for receiving arrays, consisting of a few scanty hydrophones.

Fifthly, the dependence of spatial resolution on coherent and incoherent summation of projections with possible use of Dark Field Method has been studied for multi-view schemes.

The efficiency of image reconstruction methods has been examined by the experimental image reconstruction. The experimental results have confirmed the efficiency of the methods and algorithms used and have allowed for estimating their applicability limits. Thus, the distortions of complex scatterer image (for example, three steel cylinders) apparently appear due to diffraction on "strong" scatterers (according to the classification used in [41]), for which multiple scattering effects are significant. The reconstruction of such inhomogeneities becomes substantially complicated and requires the use, for example, of iterative algorithms [41]. Another important causes of distortions are the interference structures, arising from the scattering from random inhomogeneities and waveguide boundaries and from waveguide modal interference. The reduction of random-inhomogeneity influence may be attained by averaging of random data, if the spatial spectra of random inhomogeneities and the signals of interest do not intersect. For the reduction of other disturbances, *a priori* information on oceanic waveguide and observed inhomogeneities should be taken into account in signal processing.

The analysis of possibilities for the reconstruction of vertical spatial-inhomogeneity distribution reconstruction is of specific scientific interest. For the illumination by low frequency sources (when propagation of only a few-modes occurs), the reconstruction in the vertical direction is practically impossible. In the case of high-frequency illumination (when the number of propagating waveguide modes is high), vertical-distribution reconstruction is possible, but it requires the special methods of matched filtration using both vertical arrays and vertical illuminating systems. Examples of these methods, based on angular selection and weight sorting by vertical radiating and receiving arrays, have been considered in [50].

Part III

OTHER NOVEL TOMOGRAPHIC METHODS

Chapter 5:

EMISSION OCEAN ACOUSTIC TOMOGRAPHY

The reconstruction of spatial distributions of ocean noise sources is a subject of *Emission Ocean Acoustic Tomography*. Three typical methods of Emission Tomography are described in this chapter. These methods have been developed for reconstruction of natural ambient noise (for example, noise of wind-driven surface waves) and man-made noise.

5.1 EMISSION OAT FOR LOW-FREQUENCY SOURCES

A method of acoustic diagnostics of the ocean using the low-frequency noise fields is discussed in this section. The integral equations that relate the intensity of the sound field to the spatial distribution of noise sources are obtained. A spectral tomography scheme is considered, and its effectiveness is estimated. As an example, the spatial distribution of ship noise is reconstructed on the basis of experimental data.

5.1.1 The Basic Idea of Emission Tomography

Various modifications of transmission tomography have been proposed for remote acoustic diagnostics of the ocean (see, for example, [117, 12]). The need to use a large number of active radiation systems situated at the boundaries of the investigated region complicates the engineering of the such systems. Thus, the development of tomographic methods using the characteristics of "ambient" noise fields generated by processes of interaction between wind and the water surface (dynamic noise), human engineering activity, and biological and seismic activities may be very useful.

As a rule, the sources of ambient noise are distributed over the entire test range of the ocean. Two types of tomography can be based on using the noise field: the reconstruction of the spatial distribution of the parameters of noise sources themselves (emission scheme) and a determination of the parameters of ocean medium, based on a use of *a priori* information about the noise sources. We discuss here only the first type of problems. The second type is a special case of methods previously discussed. The effectiveness is estimated, and the feasibility of emission tomography is demonstrated by using experimental data.

As an example, let us to consider a horizontally homogeneous layered ocean with an arbitrary SSP. We assume that the field of noise-acoustic surface or volume sources is stationary and quasi-homogeneous with respect to the horizontal

coordinates; that is, $l \ll R_s$, where l and R_s are the spatial scales of coherence and horizontal synoptic fluctuations of the sources. We consider the sources as a certain set of the effective secondary sources obtained by spatial averaging over an area of radius $R (l \ll R \ll R_s)$. We assume that in the azimuthal direction the radiation patterns of the primary (non-averaged) noise sources are isotropic. Thus, each secondary source has a locally isotropic radiation pattern in the horizontal plane. Ignoring the specific physical mechanism of noise generation, which is not important for later discussions, we characterize the spatial distribution of the effective secondary sources over the ocean region by the excitation coefficients $P_n(r,f)$ of the normal modes of the underwater waveguide, where n is the mode number, $r=(x,y)$, x and y are the horizontal coordinates, and f is the sound frequency.

Processes of sound scattering by inhomogeneities along the propagation path in the ocean change the energy spectrum of the modes $|P_n|^2$, i.e., information about the initial source may be lost. The intensity of noise at frequency f is created mainly by sources situated at distances smaller than or equal to $R_m(f) \cdot \gamma(f)^{-1}$ from the reception point, where $\gamma(f)$ is the sound attenuation coefficient [104, 105]. The effective radius, R_m, of the "noisy" region of the ocean from the particular source diminishes with increasing frequency. Calculations [106, 107] have shown that the intensities, $|P_n|^2$, remain practically unchanged under the influence of volume inhomogeneities (e.g., internal waves) at distances of the order of R_m for frequencies above 100 Hz. Thus, and the influence of volume inhomogeneities on the noise field can be neglected. If the noise is generated near the surface, the energy of the noise field is mainly concentrated in modes that interact strongly with the surface. Accordingly, the attenuation associated with sound scattering by a rough surface must be taken into account together with the attenuation $\gamma(f)$ [8, 106]. We assume that the ocean waves are also quasi-homogeneous in this case. We consider the fluctuation of the SSP under the influence of synoptic inhomogeneities to be insignificant, so we can neglect its influence on the variation of the energy spectrum of noise-field modes.

Let us derive a relation between the noise intensity at frequency f and the spatial distribution of the effective source power, $\langle |P_n|^2 \rangle$, where $\langle \cdot \rangle$ denotes statistical averaging over the source ensemble. For the condition $R_m \gg l$ the result of a Fourier transform of the complex amplitude of the sound pressure of the noise field at an arbitrary point of the ocean waveguide can be represented in an approximate form as:

$$p(r,z,f) \approx \iint d^2 r' \sum_{n=1}^{N(f)} \varphi_n(z,f) \frac{P_n(r',f)}{|r-r'|^{\frac{1}{2}}} \times$$

$$\times \exp\left[-(-i\kappa_n + \frac{1}{2}\gamma)|r-r'| - \frac{1}{2} \int_{S(r,r')} dS \cdot \gamma_n(r'',f) \right], \qquad (5.1)$$

where z is the vertical coordinate, $\varphi_n(z,f)$ is the nth mode vertical eigenfunction at frequency f, $N(f)$ is the number of propagating modes, $\kappa_n(f)$ is the modal horizontal wavenumber, $\gamma_n(r,f)$ is the attenuation coefficient of mode n due to sound scattering by the rough surface, $\mathfrak{L}(r,r')$ is the ray joining points r and r' in the horizontal plane, r'' is a current point on the ray $\mathfrak{L}$. The attenuation coefficients, $\gamma_n(r,f)$, in Eq. (5.1) are assumed to be independent on the orientation of the ray $\mathfrak{L}$ passing through the point r''. This requirement is valid, for example, for an isotropic sea state. (Other conditions that would lead to the same situation are discussed in [91].) From Eq. (5 1) we obtain the following expressions for the noise sound pressure and intensity at the output of the ith receiving element, which is characterized by the mode-excitation coefficients $A_n(i,f)$ and the directivity function $G_i(r,f)$ in the horizontal plane:

$$p_i(r_i,f) = \int_{-\infty}^{\infty}\int d^2r' G_i(r',f)\sum_{n=1}^{N(f)} A_n(i,f)P_n(r',f)|r_i-r'|^{-1/2}\times$$

$$\times \exp\left[-\left(-i\kappa_n+\frac{1}{2}\gamma\right)|r_i-r'|-\frac{1}{2}\int_{\mathfrak{L}(r',r_i)} dS\,\gamma_n(r'',f)\right], \qquad (5.2)$$

and

$$I_i(r_i,f) = \langle|p_i(r_i,f)|^2\rangle = \int_{-\infty}^{\infty}\int\int\int d^2r'\,d^2r''\sum_{n,m=1}^{N} A_n(i,f)A_m(i,f)\times$$

$$\times\langle P_n(r',f)P_m(r'',f)\rangle|r_i-r'|^{-\frac{1}{2}}|r_i-r''|^{-\frac{1}{2}}G_i(r',f)G_i^*(r'',f)\times$$

$$\times\exp[-i(\kappa_m|r_i-r''|-\kappa_n|r_i-r'|)-\frac{1}{2}\gamma(|r_i-r'|+|r_i-r''|)-$$

$$-\frac{1}{2}\int_{\mathfrak{L}(r_i,r')} dS\,\gamma_n(r',f)-\frac{1}{2}\int_{\mathfrak{L}(r_i,r'')} dS\,\gamma_m(r'',f)]. \qquad (5.3)$$

Representing the effective sources in the horizontal plane by a set of uncorrelated point sources with a vertical radiation pattern corresponding to the mode-excitation coefficients, P_n [104], we can make the approximate substitution into Eq. (5.3):

$$\langle P_n(r',f)P_m^*(r'',f)\rangle \approx I^2(f)\delta^2(r'-r'')\langle P_n(r',f)P_m^*(r',f)\rangle.$$

In the ocean, as a rule, the horizontal scales of mode interference satisfy the inequality $l_{nm} = 2\pi/|\kappa_n - \kappa_m| \ll R_i$, so that the interference terms $\langle P_n P_m^* \rangle \exp[-i(\kappa_n - \kappa_m)|r_i - r'|]$ with $n \neq m$ do not contribute to the total noise-field intensity $I_i(r_i, f)$ in Eq. (5.3). We, therefore, obtain instead of Eq. (5.3):

$$I_i(r_i, f) = \int_{-\infty}^{\infty}\int d^2r' |G_i(r', f)|^2 \frac{Q_i(r', f)}{|r_i - r'|} e^{-\gamma(f)|r_i - r'|} \tag{5.4}$$

and

$$Q_i(r', f) = I^2(f) \sum_{n=1}^{N} |A_n(i, f)|^2 \langle |P_n(r', f)|^2 \rangle \exp\left[-\int_{\mathcal{G}(r_i, r')} dS \gamma_n(r', f)\right]. \tag{5.5}$$

The integral equation (5.4) is a consequence of the Van Cittert-Zernike theorem. An unknown spatial-frequency distribution of the power of the noise sources and the modal-excitation coefficients, $|P_n|^2$, of the generated noise field can be determined on the basis of Eqs. (5.4) and (5.5) from measurements of the noise intensity. In general, the implementation of emission tomography scheme requires a set of receiving systems with different positions, r, and differently oriented horizontal and vertical radiation patterns, $|G_i(r', f)|^2$ and $|A_n(i, f)|^2$. The solution of Eqs. (5.4) and (5.5) for $\langle |P_n|^2 \rangle$ can be obtained on the basis of algorithms using standard regularization schemes [108, 110]. In particular, the exponential Radon transform (by analogy with Eq. (5.4)) has been inverted in [110] with allowance for *a priori* information on the spatial distribution of the excitation coefficients. Censor, et al., [111] have analyzed a reconstruction algorithm that can be used to determined not only the sources, but also the spatial distribution of the excitation coefficients. Such an algorithm makes it possible, in principle, to determine the frequency dependence of $\gamma(f)$ and $\gamma_n(r, f)$ which can be then used to diagnose the rough surface of the ocean from the values of the coefficients γ_n [86].

5.1.2 Features of Emission Tomography

Let us now discuss an important consequence of integral equation (5.4) We assume that sound-attenuation effects associated with scattering by ocean waves are insignificant. We consider a receiving system situated at the point $(x, y) = (0,0)$. We drop the subscript i for this system. We also assume that $\langle |P_n(r, f)|^2 \rangle = R_n(f) Q_n(r)$, so that the function, $Q(r, f)$, describing the power distribution of the noise sources in the two-dimensional space of horizontal coordinates and frequency, is factorable:

$$Q(r, f) = Q_0(f) Q_1(r), \tag{5.6}$$

where

$$Q_0(f) = I^2(f)\sum_{n=1}^{N} |A_n(f)|^2 R_n(f).$$

Using Eq. (5.6), we obtain from Eq. (5.4)

$$J(f) = \frac{I(f)}{Q_0(f)} = \int_0^{\infty} dr' q(r') e^{-\gamma(f)r'}, \tag{5.7}$$

where

$$q(r') = \int_0^{2\pi} d\varphi |G(r',\varphi)|^2 Q_1(r',\varphi),$$

where $x = r'\cos\varphi$ and $y = r'\sin\varphi$. It is evident from this result that, when the spectral functions, $Q_0(f)$ and $\gamma(f)$, are known, the problem of reconstructing the noise sources, $q(r)$, is reducible to the spectral tomography scheme [108, 109]. The function $Q_0(f)$ is determined from experimental data or from the theory of noise generation. If the receiving system has a sufficiently narrow radiation pattern, $|G(r,\varphi)|^2$, then the spatial distribution of the sources subtended by the radiation pattern can approximately be assumed to be dependent only on the distance from receiver. We can set $|G(r,\varphi)|^2 \sim \theta\delta(\varphi-\psi)$, where ψ is the angle, at which the axis of the radiation pattern of receiving system $\mathfrak{L}(\psi)$ is oriented relative to the x-axis. Whereupon, we arrive at $q(r) = \theta\, Q_1(r,\psi)$. Consequently, the reconstruction of the two-dimensional field $Q_1(r)$ does not generally require a set of receiving systems with different horizontal coordinates r_i. An analysis of the noise spectrum at one receiver makes it possible to reconstruct the spatial distribution, $Q_1(r,\psi)$, along each ray, $\mathfrak{L}(\psi)$, on the basis of the solution of integral equation (5.7). The set of all one-dimensional distributions obtained for the family of rays $\mathfrak{L}(\psi)$ $(0 \le \psi \le \pi)$ then gives the required field $Q_1(r)$.

Experimental data used in solving such problems are always approximate, so that the values of the parameters reconstructed by emission tomography are also approximate. The range of admissible deviations of the reconstructed values of the parameters from their true values characterizes an effectiveness of the particular method. For the spectral tomography scheme we estimate the spatial-resolution scale, which is used to determine the possible error in the source localization. Let us use a spatial distribution model of the form $q(r) = q\delta(r-a)$. We obtain the following expression for it from Eq. (5.7):

$$J(f) = a\exp(-\gamma(f)a),$$
$$K(f) = 10\log I(f) = 10\log Q_0(f) + 10\log q - \beta(f)a, \tag{5.8}$$

where $K(f)$ is the level of the noise field, $\beta(f) = \gamma(f)10\log(e)$ is the attenuation coefficient in dB/km. Let us denote (q_1,a_1) as the true values of the source parameters of the source and (q_2,a_2) as the reconstructed values. Let $\beta_1(f)$ describe the true sound attenuation, and let $\beta_2(f)$ describe the estimated attenuation. In a certain frequency interval, $f_1 \le f \le f_2$, $\Delta f = f_2 - f_1$, we investigate the levels of the sound field, $K_1(f)$ and $K_2(f)$, corresponding to the quantities (q_1,a_1,β_1) and (q_2,a_2,β_2). We introduce the average value of noise-level measurement error δ in the interval $[f_1,f_2]$. The random error of the measurement of the noise level at an individual frequency can be much greater than δ. Consequently, the entire interval $[f_1,f_2]$ should be used in estimating the source parameters in the general case when no *a priori* information is available. In this case, obviously, the difference between the exact value, $K_1(f)$, and the measured value, $K_2(f)$, of the noise level satisfies the condition

$$\int_{f_1}^{f_2} df(K_1(f) - K_2(f))^2 < \Delta f \delta^2. \tag{5.9}$$

If the attenuation is known exactly, $\beta_2(f) \equiv \beta_1(f)$ and $q_1 = q_2$, we obtain the spatial-deviation scale on the basis of Eq. (5.9) and the calculations in Eq. (5.8):

$$\Delta a = |a_1 - a_2| = \delta\left(\frac{1}{\Delta f}\int_{f_1}^{f_2} df\,\beta_1^2(f)\right)^{-\frac{1}{2}}. \tag{5.10}$$

It is evident from this equation that the scale Δa is determined by the frequency dependence of the attenuation coefficient $\beta(f)$. There are several well-known dependencies for $\beta(f)$ [112] which are used to approximate diverse experimental data on sound attenuation in the ocean. The scale Δa is plotted as a function of f_2 in Fig. 5.1 for Vadov's and Toetz's dependencies, which are encountered quite often. It follows from calculations using the actual error value $\delta = 0.5$ dB that the spatial-deviation scale, Δa, is greater than 100 km in the low-frequency range. The scale Δa increases as the frequency f_2 decreases. Acoustic spectral tomography becomes ineffective for $f_2 < 200$ Hz, when the attenuation is determined by Toetz's equation. The scale Δa does not change significantly, when the width of the frequency interval, Δf, is varied.

Equation (5.10) does not allow for the source localization error that results of the error, $\pm\Delta\beta$, in the determination of the coefficient $\beta(f)$. If $q_1 = q_2$, we infer from Eq. (5.9) that the domain of possible values of the source position, a_1, for a

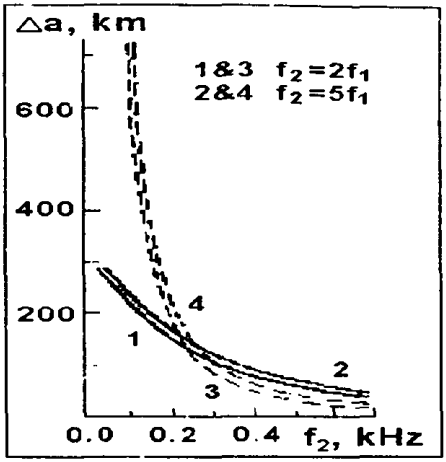

Figure 5.1. Deviation of the estimated source location from its true value as a function of the upper frequency limit for Vadov's (1,2) and Toetz's (3,4) dependencies for the attenuation coefficient. (Adapted from [58].)

reconstructed value, a_2, is determined by the condition $\max[0,(1+B-F)a_2] \le a_1 \le (1+B+F)a_2$, if $\beta_2=\beta_1+\Delta\beta$, or by the condition $\max[0,(1-B-F)a_2] \le a_1 \le \max[0,(1-B+F)a_2]$, if $\beta_2=\beta_1-\Delta\beta$, where

$$B=(\Delta a)^2(\Delta\beta/\delta\Delta f)\int_{f_1}^{f_2} df\,\beta_1(f),$$

$$F=[B^2+(\Delta\beta\Delta a/\delta)^2+(\Delta a/a_2)^2]^{1/2}.$$

The boundaries of the domain of possible values of a_1 as a function of the frequency f_2 for an octave frequency band, $f_2=2f_1$, are plotted in Fig. 5.2. An analysis of the plots shows that the error of the determination of source position increases considerably

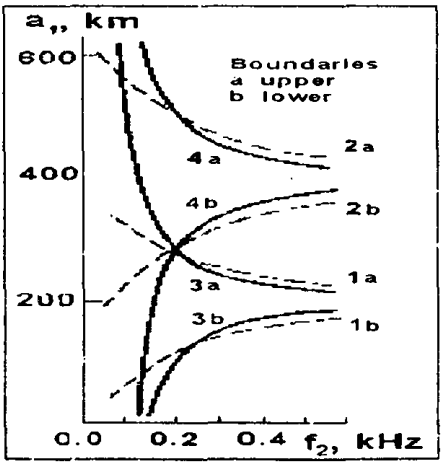

Figure 5.2. The boundaries of possible estimated source location as a function of upper frequency limit for Vadov's (1,2) and Toetz's (3,4) dependencies for the attenuation coefficient for $\Delta\beta=5\cdot10^{-4}$ dB/km and $\delta=0.5$ dB and for (1 & 3) $a_2=500$ km, (2 & 4) $a_2=1000$ km. (Adapted from [58].)

with increasing distance between the source and the receiver. Moreover, the effectiveness of spectral tomography is also lowered for frequencies f_2<100 Hz, when the attenuation is described by Vadov's equation.

Another parameter characterizing the effectiveness of spectral tomography is the sensitivity of the method to the variations of source power. We infer from condition Eq. (5.9) for $a_2=a_1$ and $\beta_2(f)=\beta_1(f)$ that $10|\log(q_1/q_2)|\le\delta$, i.e., the error of reconstruction of the level of the sound field radiated by source cannot be smaller than the average error of measurement of the noise level over the entire frequency interval.

Our estimates show that the scheme for acoustic spectral tomography of the ocean is efficiently applicable for the frequencies f_2>100-200 Hz. To illustrate its practical feasibility, we consider reconstruction of the spatial distribution of noise sources on the basis of published experimental data of the measurements of the low-frequency noise spectra [145]. Figure 5.3 shows the hydrological conditions of the experiment. The sound channel made a smooth transition from a deep-ocean-type channel (in the range interval $x<a=1100$ km) to a surface-duct channel. Hydrophones A and C were located at two stations in the horizontal plane on the axis of the sound channel (i.e., $(x=0,y=0)$ and $(x=a,y=0)$, respectively). The spectral intensities $I_A(f)$ and $I_C(f)$ of the noise were measured at these two stations, and the results were averaged over a long period of time (of the order of 24 hours).

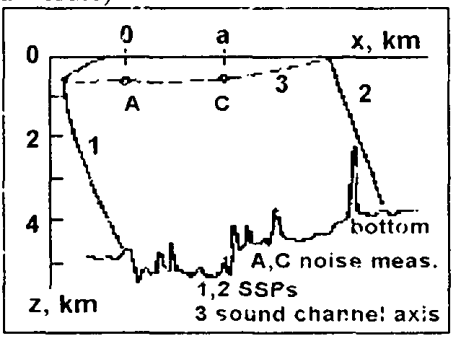

Figure 5.3. The bathymetry and range-dependent sound-speed profile for an experiment on the measurements of low-frequency noise spectra. (Adapted from [58].)

The region $x>a$ was characterized by heavy ship traffic. The noise was clearly decisive in the frequency interval 10<f<240 [145]. We shall assume below that the noise fields at the measurement stations, A and C, were produced entirely by ship noise. It can be readily estimated that the variation of the sound-speed profile (see Fig. 5.3) has an insignificant influence on the noise intensity at the points on the axis of the sound channel [145]. We introduce the average spectrum, $Q_0(f)$, of noise radiated by ocean vessels within a large ocean region and within a long period of time. We can then make an assumption that the spatially averaged source function, $Q(r,f)$, is approximately factorable (see Eq. (5.6)). For station A we determine the spatial distribution of the source power, $q(r)$ (r is the distance from station A to the noise source in the horizontal plane), on the basis of the spectral tomography equation, Eq. (5.7), using the spectra $I_A(f)$ and $I_C(f)$ given in [145]. To find $Q_0(f)$ and test the validity of the solution, it is necessary to know *a priori* the spatial distribution of noise sources, $Q_1(x,y)$. We choose a simple model in accordance with data in [145]:

$Q_2(x,y) = 0$ for $x < a$ and $Q_2(x,y) = 1$ for $x > a$. Then we assume the model for the spatial noise distribution: $q(r) = 0$ for $r < a$ and $q(r) = 2\arccos(a/r)$ for $r > a$. The measured spectral intensity at station C is: $I_C = \kappa Q_0(f)/\gamma(f)$. We determine the spectrum $Q_0(f)$ from the last relation, whereupon we can then reconstruct the spatial distribution $q(r)$ from the measured spectrum $I_4(f)$. The reconstruction results are shown in Fig. 5.4. The calculations are carried out in the interval $40 \le f \le 200$ Hz for the attenuation described by Vadov's equation [144]. A program developed in [144] on the basis of Tikhonov's regularization method [86] for the solution of the Fredholm equations of the first kind for a set of non-negative numbers was used to solve Eq. (5.7) numerically. A regularization parameter, α, was selected in the program in correspondence with the generalized residual theorem [86]. A comparison of the postulated and reconstructed distributions indicates fairly good agreement between them within allowance for the deviation scale (see, for example, Figs. 5.1 and 5.2).

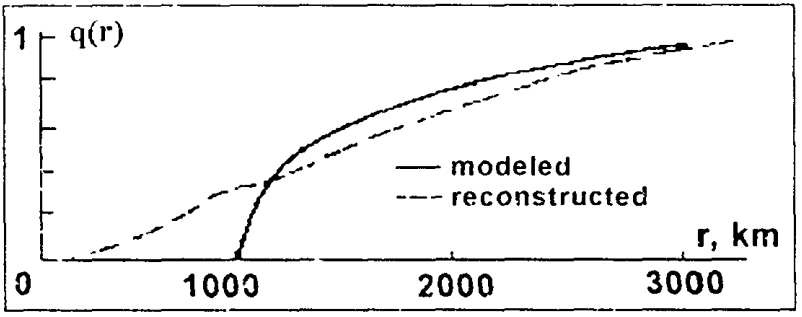

Figure 5.4. The model and reconstructed spatial distribution of noise sources for r_0=4000 km and $\alpha = 6 \cdot 10^{-5}$. (Adapted from [58].)

The presented spectral tomography scheme can be used to reconstruct the spatial distribution of not only ship noise, but also dynamic (ambient) noise. In fact, at low frequencies ambient noise admits the factorization of Eq. (5.6) with the function $Q_1(r) \sim (V(r)/V_0)^{\nu}$, where $V(r)$ is the velocity vector in the surface layer of the atmosphere, V_0 is a certain fixed value of the wind velocity, and ν is a power that depends slightly on the frequency and wind velocity ($1 \le \nu \le 3$) [138]. Thus, the wind-velocity field $V(r)$ can be reconstructed on the basis of Eq. (5.7).

5.2 MAXIMUM LIKELIHOOD ESTIMATION OF TOMOGRAPHIC SIGNAL POWER IN THE PRESENCE OF AN UNKNOWN NOISE FIELD

The maximum likelihood estimation (MLE) of the parameters of noise signal, emitted by an underwater noise source, from sensor-array data has received considerable attention in tomographic investigations. As a rule, MLE solutions are computationally expensive. Generally, when *a priori* information about the covariance matrix structure or about covariance components is available, the MLE performance can be greatly improved by allowing the simpler implementations of the

MLE scheme. This and closely related problems were investigated in [147,149, 151].

Problems of structured-covariance-MLE have been studied intensively. Problems of tomographic signal and noise power estimations have been considered for different cases of structured covariance. The simple MLE of signal and noise powers has also been derived for the case of low-rank signal and noise covariance matrices, which have been known *a priori* except for scaling. The MLE of signal and noise powers has also been obtained for cases of full-rank noise-covariance matrices and arbitrary-rank signal-covariance matrices, which have been assumed to be known, except for scaling.

However, in many practical situations an assumption of known, except for scaling, noise-covariance matrix is unrealistic. Actually, in these situations sensor-noise powers may be different and unknown, because of non-ideal antenna channels and problems related to antenna calibration. Another reason of the presence of unknown noise is the influence of acoustic reverberation. Reverberation generates the external noise, which is usually uncorrelated between array sensors and has different powers in each sensor due to medium inhomogeneities.

In many references the problem of signal-power estimation is discussed on the basis of an assumption that the spatial-covariance matrix of the received signal is a rank-one matrix and is known *a priori* except for scaling. Such an assumption corresponds to the situation when the received signal has an *a priori* known wavefront and is fully coherent within the array aperture. However, unlike earlier works, the noise covariance matrix is assumed to be an unknown diagonal matrix. In other words, the noise is assumed to be uncorrelated and to have different unknown variances in each array sensor. We have derived the simple Approximate MLE (AMLE) of the signal power assuming that the signal is weak and that the number of recorded signal samples is large.

The variance of the derived estimator has been compared analytically with the exact Cramer-Rao Limit (CRL) of this problem [139]. Such a comparison allows us to prove that the AMLE asymptotically converges to the CRL for the majority of practically important cases (not only in a weak-signal case). Furthermore, in the case of non-identical noise powers, the statistical performance of the AMLE has been compared with the statistical performance of the well-known Exact MLE, which is based on matched-filter processing and is usually referred to as a conventional beamformer. The significantly better performance of the AMLE has been demonstrated. The analogy between these two estimators has also been considered. This analogy enables one to generalize the AMLE for the case of well-separated, weak, multiple sources with unknown locations and to consider this estimator as a type of conventional beamformer for arbitrary and unknown noise powers. The estimation errors of the AMLE have been compared with the CRL by numerical simulations [139, 140]. Simulation results show that the root-mean-square estimation errors of the AMLE are very close to the CRL for a wide range of signal power and for arbitrary difference between unknown sensor noise variances.

5.3 TOMOGRAPHIC RECONSTRUCTION OF MOVING ACOUSTIC NOISE SOURCES

Another type of tomographic investigation is related the connection of the spatial distribution of noise sources and far-field reconstruction using the near-field measurements [151-153].

At present so-called near-field methods are broadly used for the determination of the antenna radiation patterns. Since the 1970's, a reliable technology based on near-field methods has been developed for the measurement of microwave-antenna characteristics. Both the radiator far field and the amplitude and phase distribution of elementary sources along a radiator can be reconstructed with high accuracy by processing the near-field data. Proceeding from the fact that the measurements are made near a radiator, the main merits of near-field methods are the possibility using decreased radiation power and the reduction of error components caused by medium propagation and reverberation effects.

NF methods in acoustics have been developed for the measurements of extended sound sources with *a priori* unknown spectrum (e.g., for diagnostics of noise radiation of cars, ships and so on). The final aim here are the reconstruction of angular-averaged, intensity distributions in the far field and the identification of the equivalent distribution of acoustic elementary sources along a radiator from measured data. Such near-field methods should be generalized as follows: Firstly, reconstruction methods should be generalized for broadband-spectrum signals having random nature. In this case the second-order statistical moments of acoustic field depending on spatial coordinates and frequency should be estimated. Secondly, an algorithm's robustness against external noise should be investigated, because, in many cases, the acoustic signals of interest do not exceed the background level. Thirdly, radiator motion and signal propagation (at least, boundary reflections) should be taken into account.

For low frequencies the most accessible measuring system is a linear array. On the other hand, there is a broad class of acoustic radiators essentially oblong along one of coordinate axes that can be studied by using linear arrays. (Radiation from such geometry sources may be described by a set of elementary sources on a segment of straight line.) Investigation reveals that, in these cases, noise-source reconstruction can be carried out correctly.

All the above mentioned conditions must be taken into account for the use of near-field methods for the determination of acoustic-radiator characteristics. The theoretical part of the near-field method consists in a design of algorithms of measured data transformation and in a substantiation of their correction, whence the requirements on receiving system can be formulated.

Proceeding from the random nature of the radiation field, we propose that the signal processing procedure should be divided into four main steps. The first step is the narrowband filtering of received signals. The second one is the execution of the algorithm of the spatial processing: the transformation of the array signal vector, p_i, having passed through the narrowband filter into a vector of the momentary direction pattern, d_i, or into a vector of the momentary distribution of discrete equivalent

sources along radiator, m_j, for every time point j, and for every narrow frequency band. Then,

$$d_j = \hat{\Gamma}_j p_j. \tag{5.11}$$

The matrix, $\hat{\Gamma}_j$, has been derived on the basis of two approximations: the high-frequency approximation for solving appropriate integral equations (HFA algorithm) and the MLE with regularization (MLER algorithm).

The HFA algorithm had been originally developed for the measurement of electromagnetic antenna characteristics, and then it has been modified for acoustic applications [151]. The HFA algorithm is notable for simplicity of realization and physical interpretation. It permits easy estimation of the influence of measuring system parameters on the final result. For the HFA algorithm, the matrix $\hat{\Gamma}_j$ does not depend on time and is determined as

$$\Gamma_{kn}^{(HFA)} = d_a \sqrt{\frac{f}{c}\rho(x_n,\theta_k)}\, e^{-2\pi i \frac{f}{c} l(x_n,\theta_k)}, \tag{5.12}$$

where d_a is the array spacing, c is the average sound speed. The functions $\rho(x_n,\theta_k)$ and $l(x_n,\vartheta_k)$ are determined only by the angle θ_k, characterizing the directional pattern in the far field and by the geometry of the mutual disposition of the receiving array and the trajectory of the source motion.

This algorithm is not optimum relative to the background noise and is basically oriented for free-space propagation. These facts may lead to an increase in the total reconstruction error for measurements in inhomogeneous noisy media. As a result, an optimum algorithm based on maximum likelihood principle for the estimation of acoustic-radiator characteristics from near-field measurements was considered. For the realization of the MLER algorithm the linearization of maximum likelihood equations for certain models of the signal and external noise covariance matrices is used. For the MLER algorithm, the matrix has a form:

$$\hat{\Gamma}_j = \hat{U}(\hat{G}_j^{+}\hat{G}_j + \varepsilon\hat{I})^{-1}\hat{G}_j^{+}, \tag{5.13}$$

where the superscript + denotes conjugate transpose, $\hat{G}_j$ is the matrix of mapping the equivalent sources into measured samples, when the propagation conditions can be taken into account. The matrix $\hat{U}$ is the standard Fourier transform of the estimated m_j into the momentary direction pattern. The regularization procedure for the inversion of the matrix $\hat{G}_j^{+}\hat{G}_j$ indicates the presence of small eigenvalues in spectrum of this matrix. This allows for the impossibility of unbiased estimation of source characteristics by numerical methods. The optimum value of the parameter can be found from *a priori* known signal-noise ratio.

The third and fourth steps consist of the estimation of the second-order statistical moments (averaged intensity structure) by time averaging with weighting coefficients and the compensation of external noise:

$$D_{kk} = D(\theta_k) - \sum_j \gamma_{k,j} |\hat{d}_{k,j}|^2 \cdot D_{kk}^{comp}. \qquad (5.14)$$

The introduction of the weighting coefficients follows from the existence of angular sectors of trustworthy reconstruction (Trustworthy Reconstruction Sector - TRS) of direction pattern for the current source location relative to the array [151]. The estimation error is much smaller in the TRS than outside of it. The $\gamma_{k,j}$ calculation for this procedure of the so-called "projection synthesis" is based on the determination of the TRS for model sources.

Some components of the total error of radiator-characteristic reconstruction have been investigated. As the main components of total error, the following factors have been chosen and analyzed [152]:

a) The errors associated with different approximations for designing reconstruction algorithms (e.g., an approximate solution of the integral equation, radiator identification by a finite number of elementary sources, finite dimensions of receiving system);
b) The error caused by external noise;
c) The error associated with a non-ideal receiving array transmission channel;
d) The error caused by the inaccurate estimation of the mutual disposition of radiator and receiving array; and
e) The error associated with inaccurate information about propagation channel and its fluctuations.

The results of extensive numerical simulation and source-characteristic reconstruction in natural experiments have shown that the estimates based on the above-mentioned algorithms have a high degree of accuracy. Furthermore, the MLER algorithm allows for adapting the signal processing to complex source structure and propagation conditions. Besides being used for the investigation of noise acoustic objects, the MLER algorithm can be developed for a broad range of applied problems (for example, for estimation of hydrological and other ocean parameters, for acoustic monitoring, in medicine diagnostics, etc.).

Chapter 6:

TOMOGRAPHIC RECONSTRUCTION OF OCEANIC INHOMOGENEITIES BY USING PARTIALLY COHERENT ACOUSTIC WAVES

6.1 COHERENT FIELD STRUCTURES OF NOISE SOURCES IN OCEANIC WAVEGUIDES

Coherent acoustic signals in the ocean fluctuate strongly in the space-time domain due to the interference between sources, multiple propagation paths and scattering from random boundary and volume inhomogeneities. These fluctuations in space and time, which we may call spatial distortion and interference noise, decrease the sensitivity and accuracy of measuring and imaging systems for tomographic reconstruction. Similar problems are well-known in optics and ultrasonic imaging [83, 120, 123]. The interference of partial waves, for example, normal modes or rays, has high-frequency spatial and temporal variations. Taking into account the complex multipaths of noise signals in inhomogeneous media for spatial and temporal domains, the high-frequency interference structures can be described statistically, if the number of partial waves is large enough.

To reduce interference noise and spatial distortions for the purpose of improving high-accuracy tomographic measurements, different methods of averaging and filtering can be used [104, 105]. Possibilities for accomplishing this task in optical and ultrasonic imaging are provided by the use of partially coherent (PC) sources [80, 161]. The use of PC acoustic waves for tomographic reconstruction of inhomogeneities in oceanic waveguides has previously been introduced in the literature [39, 80-82, 155, 161]. The optimal elimination of illuminating-acoustic-wave coherence consists of increasing the sizes and frequency bandwidths of noise sources. This leads to the elimination of the interference noise and diffractive distortions by allowing the possibility for space-time filtering.

In this chapter the investigation of space-time structures of PC acoustic waves in oceanic waveguides is discussed from the point of view of recommendations for the use of PC sources for tomographic reconstruction of oceanic inhomogeneities.

6.1.1 Partially Coherent Space-Time Waves in Oceanic Waveguides

Formulation of the basic concept. The physical problem formulated in the chapter introduction can be presented as a stochastic problem for the excitation of PC space-time waves by spatially localized noise sources, $q(\boldsymbol{\rho},\omega)$, where $\boldsymbol{\rho} = [\xi,\eta,\zeta] = [e,\zeta]$ is a given point in the spatial distribution of the noise source in a layered refractive waveguide with the SSP, $c(z)$, and an angular frequency, ω. (The geometry of the problem is

shown in Fig. 6.1.) To formulate and solve the problem, physical models of spatially localized noise sources, as well as models of layered waveguide, must be introduced.

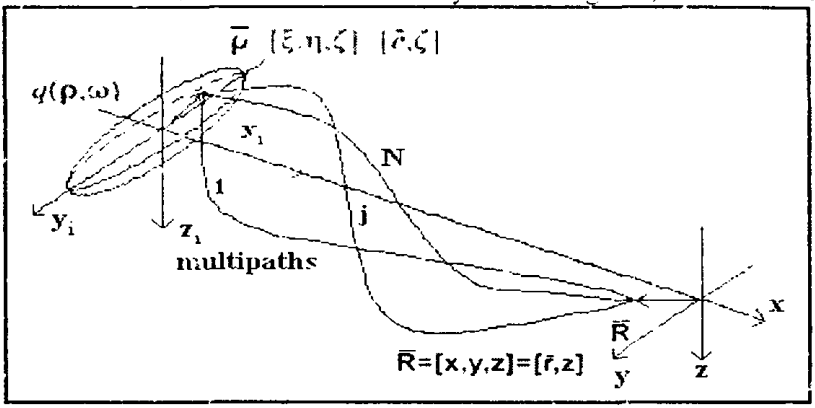

Figure 6.1. Geometry of the problem. (Adapted from [161].)

The particle velocity potential, $\varphi(\boldsymbol{R},t)$, where $\boldsymbol{R}=[x,y,z]=[\bar{r},z]$ is a given point in a waveguide, can be expressed as a sum of partial waves from each point element of the noise source with the complex amplitude $q(\boldsymbol{\rho},\omega)$:

$$\varphi(\boldsymbol{R},t) = \int\int\int\int q(\boldsymbol{\rho},\omega)e^{-i\omega t}G(\boldsymbol{\rho},\boldsymbol{R},\omega)d\boldsymbol{\rho}d\omega, \tag{6.1}$$

where $G(\boldsymbol{\rho},\boldsymbol{R},\omega)$ is the Green's function for the inhomogeneous propagation medium.

Correlation analysis will be used for the description of stochastic waves under the assumption that parameters of our problem allow the use of the ergodic theorem. We assume that the noise sources satisfy the hypothesis of statistical uniformness and spectral purity. This means that the space-time dependencies of the source function are factorized. We also assume that source coherence can be separated from medium coherence because of the scale differences. The coherence function of the received signal can be defined as:

$$\Gamma_{12}(t_1,t_2)=\Gamma_{21}(t_2,t_1)=<\varphi(\boldsymbol{R}_1,t_1)\varphi^*(\boldsymbol{R}_2,t_2)>.$$

Then, using Eq. (6.1) and above-mentioned assumptions, we arrive at:

$$\Gamma_{12}(t_1,t_2)=\int\int\int\int<q(\boldsymbol{\rho}_1,\omega_1)q^*(\boldsymbol{\rho}_2,\omega_2)>e^{-i(\omega_1 t_1-\omega_2 t_2)}<G(\boldsymbol{\rho}_1,\boldsymbol{R}_1,\omega_1)G^*(\boldsymbol{\rho}_2,\boldsymbol{R}_2,\omega_2)>$$

$$\times d\boldsymbol{\rho}_1 d\boldsymbol{\rho}_2 d\omega_1 d\omega_2, \tag{6.2}$$

where <..> denotes an ensemble averaging for either the source or the medium. Further, we may also assume stationarity of the coherence function when it depends only on a time difference $\tau=t_2-t_1$.

Noise Source Models. To continue a more detailed analysis of PC waves in the ocean, we should specify source-function models, $\langle q(\boldsymbol{\rho}_1,\omega_1)q^*(\boldsymbol{\rho}_2,\omega_2)\rangle$. Appropriately chosen source models can simplify considerably the coherence function in Eq. (6.2). It is important that these models should be related to real noise sources, since such sources may prove useful for acoustic probing of oceanic inhomogeneities. In some cases narrowband spectral components, present in ship noise, can be singled out as quasi-harmonic signals by a receiver [40, 138, 139].

Model A - Broadband Point Source. For model A, we use the noise-source function given by $q(\boldsymbol{\rho},\omega) = A_0(\boldsymbol{\rho})\sqrt{g(\omega)}\delta(\boldsymbol{\rho}-\boldsymbol{\rho}_0)$, where $g(\omega)$ is the energy spectrum of uncorrelated spectral components and $\boldsymbol{\rho}_0$ determines a location point of the source. The source coherence function for this model becomes:

$$\langle q(\boldsymbol{\rho}_1,\omega_1)q^*(\boldsymbol{\rho}_2,\omega_2)\rangle = A_0^2(\boldsymbol{\rho})\delta(\boldsymbol{\rho}_1-\boldsymbol{\rho}_2)g(\omega_1)\delta(\omega_1-\omega_2), \tag{6.3}$$

where δ denotes the Dirac delta-function. Using Eq. (6.3), the coherence function at the receivers (Eq. (6.2)) can be represented by the following expression:

$$\Gamma_{12}(\tau)=A_0^2(\boldsymbol{\rho}_0)\int g(\omega)\langle G(\boldsymbol{\rho}_0,\boldsymbol{R}_1,\omega)G^*(\boldsymbol{\rho}_0,\boldsymbol{R}_2,\omega)\rangle e^{i\omega\tau}d\omega. \tag{6.4}$$

Model B - Narrowband Extended Source. The source-coherence function for Model B can be expressed as

$$\langle q(\boldsymbol{\rho}_1,\omega_1)q^*(\boldsymbol{\rho}_2,\omega_2)\rangle = A^2(\boldsymbol{\rho}_1)sinc(\boldsymbol{\rho}_1-\boldsymbol{\rho}_2)g_0(\omega_0)e^{-\frac{(\omega_1-\omega_0)^2}{\Lambda\omega}}\delta(\omega_1-\omega_2), \tag{6.5}$$

where $A^2(\boldsymbol{\rho})$ determines the spatial form of the noise source, $g_0(\omega_0)$ specifies a narrowband spectrum centered at the frequency ω_0, and *sinc* $x=\sin x/x$. Substituting Eq. (6.5) into Eq. (6.2) and assuming that the spatial-coherence scale is small, we obtain the coherence function for the stationary case:

$$\Gamma_{12}(\tau) \propto g_0(\omega_0)e^{i\omega_0\tau}\int A^2(\boldsymbol{\rho})\langle G(\boldsymbol{\rho},\boldsymbol{R}_1,\omega_0)G^*(\boldsymbol{\rho},\boldsymbol{R}_2,\omega_0)\rangle d\boldsymbol{\rho}. \tag{6.6}$$

Model C - Horizontally Moving Narrowband Point Source. Let model C be a noncoherent, narrowband point source, which moves for a distance L along the η-axis at a depth ζ_0, and the receiver is a vertical array on the line $\boldsymbol{R}=[a,0,z]$ with hydrophones at depths between z_1 and z_2 (see Fig. 6.1). If the averaging time of the receiver is more than the characteristic time of motion, then the source function is:

$$\langle q(\rho_1,\omega_1)q^*(\rho_2,\omega_2)\rangle = A^2(\eta)\delta(\xi-0)\delta(\zeta-\zeta_0)g_0(\omega_0)e^{\frac{(\omega_1-\omega_0)^2}{\Delta\omega^2}}\delta(\omega_1-\omega_2), \tag{6.7}$$

where $A^2(\eta)=(1,\eta\le L;\ 0,\eta>L)$. The coherence function is

$$\Gamma_{12}(\tau) \propto g_0(\omega_0)e^{i\omega_0\tau}\int A^2(\eta)\langle G(\eta,\zeta_0,a,z_1,\omega_0)G^*(\eta,\zeta_0,a,z_2,\omega_0)\rangle d\eta. \tag{6.8}$$

Let us note that we have chosen the noise-source models, so that in one case (model A) the source is localized in space (point source), and in another case (model B) it is localized in frequency domain (narrowband source). The final case (model C) is a combination of models A and B, where the narrowband point source also moves. The resulting coherence functions (Eqs. (6.4), (6.6), and (6.8)) have similar forms. They indicate the smoothing of the space-time interference structure of $\Gamma_{12}(\tau)$ due to the influence of the source size, $A^2(\rho)$, and bandwidth, $g(\omega)$.

Propagation in a Waveguide. Propagating signal in an inhomogeneous waveguide can take various paths (see Fig. 6.1). Such propagation can be represented as a sum of the waveguide partial waves:

$$G(\boldsymbol{\rho},\boldsymbol{R},\omega)=\sum_{n=1}^{N}G_n(\boldsymbol{\rho},\boldsymbol{R},\omega). \tag{6.9}$$

For example, such partial waves can be described by using the modal approximation [8]:

$$G_n(\boldsymbol{\rho},\boldsymbol{R},\omega)=\varphi_n(\zeta)\varphi_n(z)e^{i(|\boldsymbol{e}-\boldsymbol{r}|\kappa_n-\pi/4)}/(|\boldsymbol{e}-\boldsymbol{r}|\kappa_n)^{1/2}, \tag{6.10a}$$

where φ_n and h_n denote vertical eigenfunctions and horizontal modal wavenumbers of the unperturbed waveguide, respectively. We can also rewrite Eq. (6.9) by using the ray approximation:

$$G_n(\boldsymbol{\rho},\boldsymbol{R},\omega)=a_n e^{ikS_n}, \tag{6.10b}$$

where a_n and kS_n are the amplitude and phase of a partial ray, and k is the wavenumber. It should be noted that both representations describe the real wave field, so they can be transformed one into another [8].

6.1.2 Partially Coherent Structures of Acoustic Waves in a Waveguide

The substitution of Eq. (6.9) in either of its two forms (Eq. (6.10a) or (6.10b)) into Eq. (6.2) (or into the subsequent forms, Eqs. (6.4), (6.6), or (6.8)) would lead to the possibility of splitting the coherence function into two terms:

$$\Gamma_{12}(\tau)=\Gamma_{12}^{E}(\tau)+\Gamma_{12}^{I}(\tau). \tag{6.11}$$

The first term represents the energy sum for the ray paths or modes with the same number (i.e., $m=n$) in the expansion of $\langle G(\cdot)G^*(\cdot)\rangle$, and the second term is the interference between ray paths or modes (i.e., $m\neq n$).

The analysis of these equations shows that, for the scales associated with the interaction of partial waves with large differences in indices, the increases of source size or frequency bandwidth of the noise source smooths the space-time variations of the acoustic field. For the limiting case, when all variations are eliminated, the size of the source and the noise frequency bandwidth must be larger than all scales of variations of $\langle G(\cdot)G^*(\cdot)\rangle$ in the space and frequency domains. Such fields can be considered as noncoherent acoustic fields. The more exact definitions for coherent and noncoherent acoustic fields in the ocean require taking into account the properties of oceanic waveguides as spatial and frequency domain filters.

To illustrate some of the concepts and provide a basis for further development, let us examine two cases:

Case I - An Application of the Ray Representation to Model A: The substitution of Eq. (6.10b) into Eq. (6.9) and then into Eq. (6.4) gives

$$\Gamma_{12}(\tau)=A_1^2(\mathbf{p})\sum_{mn}\int g(\omega)a_m a_n^* e^{i[k(S_m-S_n)-\omega\tau]}d\omega. \tag{6.12}$$

Case II - An Application of the Modal Representation to Model C. Assuming the small-angle approach, we can obtain the coherence function by the substitution of Eq. (6.10a) in Eq. (6.8):

$$\Gamma_{12}(\tau)=g_0(\omega_0)e^{i\omega_0\tau}\sum_{mn}\varphi_m(z_1)\varphi_n^*(z_2)\int A^2(\eta)\exp[i|\eta-\sqrt{a^2+z_1^2}|\kappa_m-i|\eta-\sqrt{a^2+z_2^2}|\kappa_n]\times$$
$$\times[|\eta-\sqrt{a^2+z_1^2}|\kappa_m|^{-1/2}][|\eta-\sqrt{a^2+z_2^2}|\kappa_n|^{-1/2}]d\eta. \tag{6.13}$$

The integral in Eq. (6.13) determines the interference noise elimination for different spatial scales. If $L\ll a$, then Eq. (6.13) can be simplified further. For the examples considered later, we shall use a bi-linear SSP in the (x,z)-plane defined as $[z_i(m),c_i(m/s)]=[0,1500]$, $[200,1470]$, $[3000,1550]$.

According to the analytical results of preceding sections, acoustic waves in oceanic waveguides can have significant interference noise due to the interaction among partial waves in a waveguide, as well as due to their interaction with waveguide inhomogeneities. This distinguishes the acoustic ocean imaging from optical and ultrasonic imaging, where waveguide interference is not a problem. For short scales, the interference structure in the space-time domain can be imaged like random patterns and can be described statistically.

6.1.3 Coherence Transfer Properties

In this section we analyze the interference structures suggested by the separation in Eq. (6.11) into two terms. Let us introduce the term *Coherence Transfer Properties* (CTP) that describes a change of the space-time function as a signal propagates from a source to a waveguide point. This change is associated with Eq. (6.2).

Vision Coefficients for Interference Structures. The high-frequency space-time interference structure, which is produced by many partial waves characterized by very different parameters, can be defined as an interference noise. Coherence can not be maintained for long distances due to high dispersion of the parameters among those partial waves. To describe the space-time interference structure, we introduce a quantity, $\beta(\boldsymbol{R}) = \overline{\Gamma_{11}^{E}}/\overline{\Gamma_{11}^{I}}$, that is the time-averaged, single-receiver energy part of the coherence function divided by the interference part. This quantity is a special ratio of CTP that we call the *Vision Coefficient* (VC) of the interference structure. Figure 6.2 shows VC maps of $\beta(x,z)$ in the (x,z)-plane for Case I. The waveguide is bi-linear with randomly distributed inhomogeneities in phase with different standard deviations (in radians per meter of ray-path length). The noise signals have a bandwidth of 1 Hz.

Analysis of the energy and interference terms, leading to the spatial

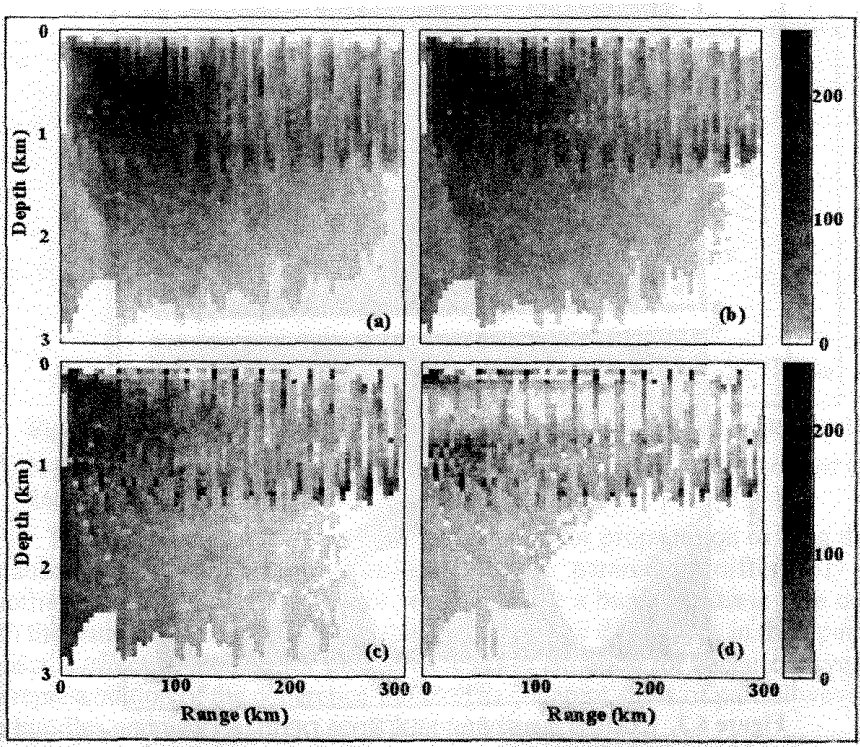

Figure 6.2. Vision Coefficient maps of the interference structure $\beta(x,z)$ in the (x,z)-plane for Case I for different bandwidths (a) 1, (b) 10, (c) 100, and (d) 1000. (Adapted from [161].)

distributions of VC in Fig. 6.2, suggests that a diversity in paths, coupled with strong random phase dispersions among these paths, leads to a strong interference and rapid decorrelation with increasing distance. On the other hand, in regions where the energy terms dominate, coherence is maintained for greater distances. These results suggest a method for the analysis of the wave structures corresponding to the interference of rays (i.e., $I:(m \neq n)$) in Eq. (6.11). The energy part of Eq. (6.11) (i.e., $E:(m=n)$) has a broadband spatial spectrum, including large-scale interference, that can be smoothed by using large-scale-noise sources.

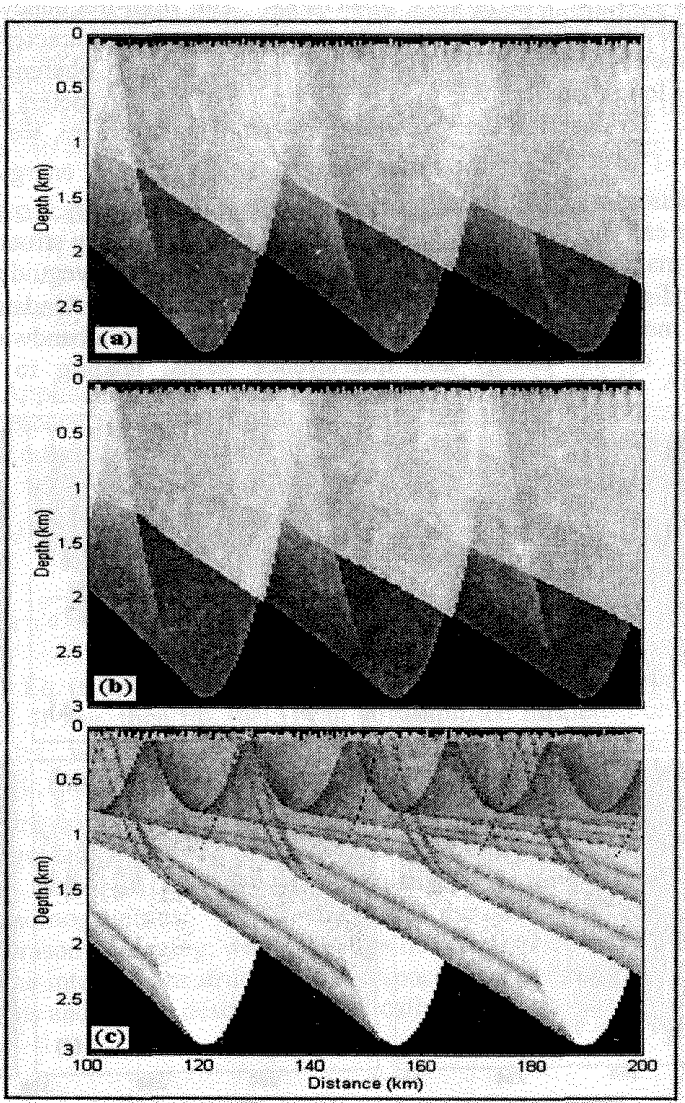

Figure 6.3. Example maps of (a) MDTT, (b) DDTT, (c) MinTT for a source depth of 100m. (Adapted from [161].)

Inhomogeneous structures lead to complex space-time variations of acoustic noise signals in oceanic waveguides. CTP, defined in terms of time delays, can provide a tool for the interpretation of the space-time variations of noise signals. For example, the Mean Difference in Travel Times (MDTT) for different rays at different receivers, $\overline{\Delta\tau_{mn}}$, as well as their Dispersion Difference in Travel Times (DDTT) can be used for such an interpretation. The Minimal Difference in Travel Times (MinDTT) is also useful for the analysis of the noise coherence structures in waveguides. Figure 6.3 shows examples maps of MDTT, DDTT, and MinDTT calculated for a bi-linear oceanic waveguide.

Double Scaleness of Coherence and the Coherence Window. Interference noise can be isolated relatively simply in optical and ultrasonic imaging as short-scale, space-time variations. Similar operation for acoustic noise signals in oceanic waveguides can be performed more effectively by using another method. This method uses the natural space-time filtering properties of oceanic waveguides that image signal structures localized in the space-time domain [112].

Other characteristics may also be imaged in analyzing PC structures in oceanic waveguides. For example, Fig. 6.4 shows the dependencies of ray-cycle lengths, $L(\alpha_i)$, on initial path angles, α_i, for a bi-linear waveguide. As analysis shows, these dependencies have relatively smooth local extrema, which determine the formation of ray bundles (or more generally, partial-wave bundles).

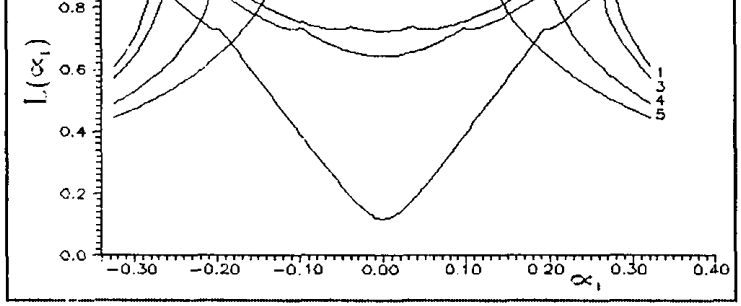

Figure 6.4. Dependencies of ray-cycle lengths, $L(\alpha_i)$, on initial path angles, α_i, for the bi-linear waveguide for depths (1) 50 m, (2) 190 m, (3) 1260 m, (4) 2000 m, and (5) 2600 m. (Adapted from [161].)

The coherence in the bundle is maintained for propagation to long distances, because within a bundle or beam, partial-wave parameters differ only slightly. Another situation exists for rays or waves outside a bundle. These lose coherence with the bundle partial waves very rapidly due to large differences in their parameters. Thus, the effective method for interference noise isolation for oceanic waveguides is the representation of the coherence function as coherent sums of partial waves within the bundles and as incoherent sums between them:

$$\Gamma_{12}(\tau)=\sum_{k=1}^{s}\sum_{m,n\in\Delta_k}\Gamma_{12}^{mnk}(\tau)+\sum_{m,n\notin\Delta_k}\Gamma_{12}^{mnk}(\tau), \qquad (6.14)$$

where Δ_k, $(k=1,...,s)$ denotes the localized bundles. Each bundle is formed by a set of PC waves. On this basis, we can introduce two different scales of coherence and interference variations for oceanic waveguides: the first scale is associated with a smooth interference structure within partial-wave bundles, while the second scale is associated with diffuse interference of partial-wave components outside the bundles.

To simplify the physical meaning, we can interpret this two-scale structure as the existence of space-time coherence "windows" in oceanic waveguides. As numerical simulation has shown, the space-time properties of these windows are determined by waveguide characteristics. They also depend on the source depth. Random oceanic inhomogeneities can distort an image by their influence on both scales. But very strong perturbations of the ocean environment are necessary to eliminate the coherence window (see Figs. 6.2 and 6.3).

Investigations of PC space-time structures of acoustic waves in waveguides produced by spatially localized noise sources reveal interesting phenomena associated with the influence of constructive and destructive interference of partial waves. The existence of partial-wave bundles (i.e., waves having close parameters and maintaining the coherence along ray paths or modes for long distances) or coherence windows have been found. Such coherence structures appear as beams of complex form in space and pulses in time. Another part of the interference structure in waveguides is relatively uniform distributions of random or diffuse terms. The diffuse component of the acoustic field can be effectively smoothed by using PC noise sources.

6.2 POSSIBILITIES FOR THE USE OF PARTIALLY COHERENT ACOUSTIC WAVES FOR TOMOGRAPHIC RECONSTRUCTION

The method of tomographic reconstruction of SSP perturbations in the ocean using low-frequency acoustic waves has been successfully developed [12, 23, 62].

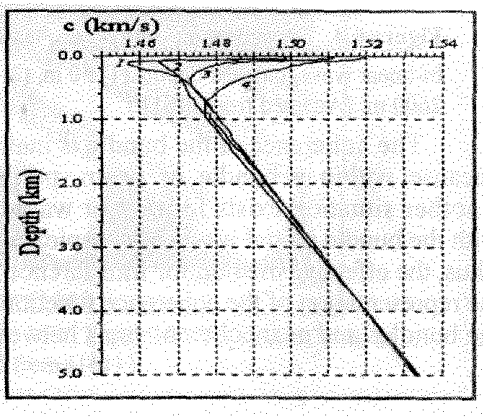

Figure 6.5. SSPs for transition across a front. (Adapted from [155].)

using low-frequency acoustic waves has been successfully developed [12, 23, 62]. Current methods are based on the analysis of ray or mode travel times or other characteristics, such as phase, amplitude and intensity measurements. A goal of this section is to describe the possibilities of using PC acoustic noise sources for tomographic reconstruction of the spatial forms of inhomogeneities.

A good quality of tomographically reconstructed images of oceanic inhomogeneities can be provided by highly accurate acoustic measurements.

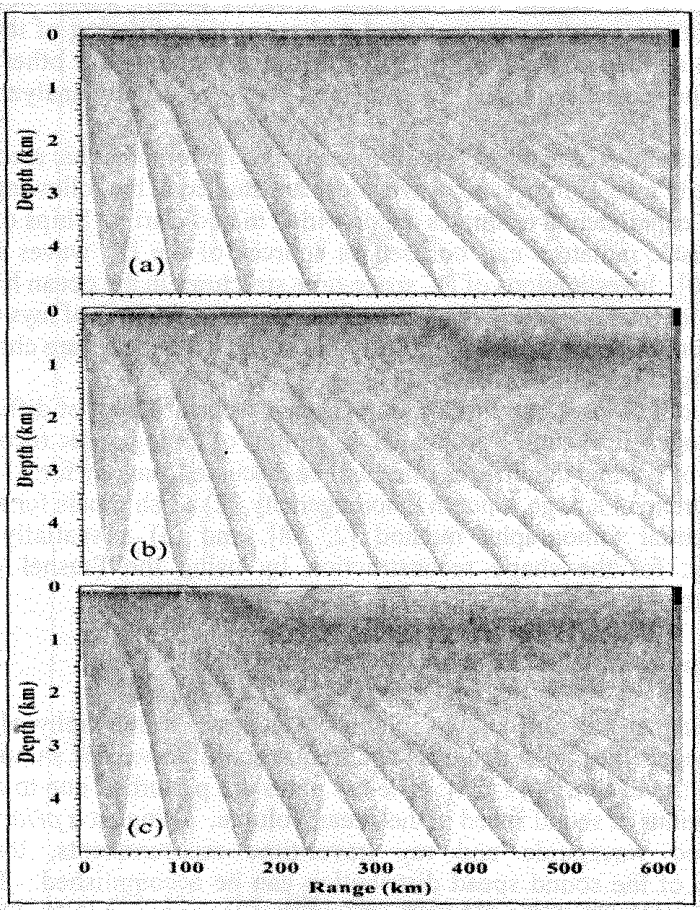

Figure 6.6. Shows the modeled propagated-signal level for the specific placements of the front: (a) no SSP transition, (b) transition begins at 350 km, and (c) transition begins at 150 km. (Adapted from [155].)

However, technical and physical factors can limit such accuracy. First, there are difficulties related to the accurate positioning of the receiving array, synchronization, optimal filtering, and so on. Second, measured signals are also influenced by unresolved nonuniformities and nonstationarities in the ocean environment that produce undesired space-time variability. And third, additive background noise lowers the precision of estimates. If the influence of the background noise can be

remaining interference noise can be reduced by optimal space-time filtering that requires only the use of *a priori* information about an observed object and the random variability of ocean environment [12].

Motion of oceanic inhomogeneities limits observation times, and the finite spatial dimensions of measuring systems sets the resolution limits. To extend these limits, one can apply spatial or frequency diversity by using large partially coherent, broadband noise sources with following appropriate filtering [40]. Similar techniques have been applied in optical and ultrasonic imaging [154]. According to these methods, PC noise signals are transmitted and space-time filtering of the received signals is then applied. The intensity and coherence functions (or other statistical moments) of the received signals, referred to as CTP, are usually analyzed in these situations [40, 154].

The possibilities of using PC space-time signals for tomographic reconstruction of inhomogeneity images in oceanic waveguides are studied in the following sections. Numerical and experimental examples are provided to add clarity. Ships or specially designed acoustic radiators can be used as sources of the PC waves in oceanic waveguides [40]. Investigations of PC space-time structures in the ocean have shown the conditions for the formation of bundles of partial waves (groups of rays or modes). If the parameters of partial waves are nearly the same, the bundles are characterized by relatively high internal coherence [161].

The use of PC-wave bundles for tomographic reconstruction of different types oceanic inhomogeneities can be proposed. Examples of tomographic reconstruction for three types of oceanic inhomogeneities will be discussed, namely for: (1) an ocean front as an example of a large, smooth inhomogeneity, (2) a fish shoals for application of the differential tomography method [2, 68], and (3) a spatially localized inhomogeneity, for the shape reconstruction by using the Fresnel diffraction tomography method [154].

6.2.1 PC Tomographic Monitoring of Oceanic Fronts

According to the well-known method of acoustic tomography of relatively smooth inhomogeneities, such as eddies and frontal zones flows, one should measure delays for ray travel times [12, 23]. The ray paths are perturbed due to changes of spatial distributions of sound speed in the ocean volume. Using an *a priori* model of an unperturbed waveguide and ray travel-time measurements, tomographic reconstruction of the sound speed distribution can be accomplished. To achieve relatively good results, highly accurate measurements are required [12]. Fluctuations in the received signals due to randomly distributed inhomogeneities and nonstationarities of the ocean environment under natural conditions can prevent one from achieving accurate reconstruction. Partially coherent signals are often used in optical and ultrasonic imaging to overcome these difficulties [154]. The measurements and filtering of space-time parameters (CTP) of PC acoustic noise signals can form the basis for the application of similar methods to oceanic waveguides [161]. The aim of such methods is the elimination of interference noise and diffraction distortions by the reduction of coherence structures of partial waves in the waveguide through increasing the source size and bandwidth.

and diffraction distortions by the reduction of coherence structures of partial waves in the waveguide through increasing the source size and bandwidth.

Let us now discuss the possibility of using this method for tomographic reconstruction of large and relatively smooth inhomogeneities. Figure 6.5 shows the SSP for the ocean-front simulation. An acoustic source with a horizontal length of 100 m and bandwidth of 500 Hz is placed near the surface duct axis (type 1 in Fig.

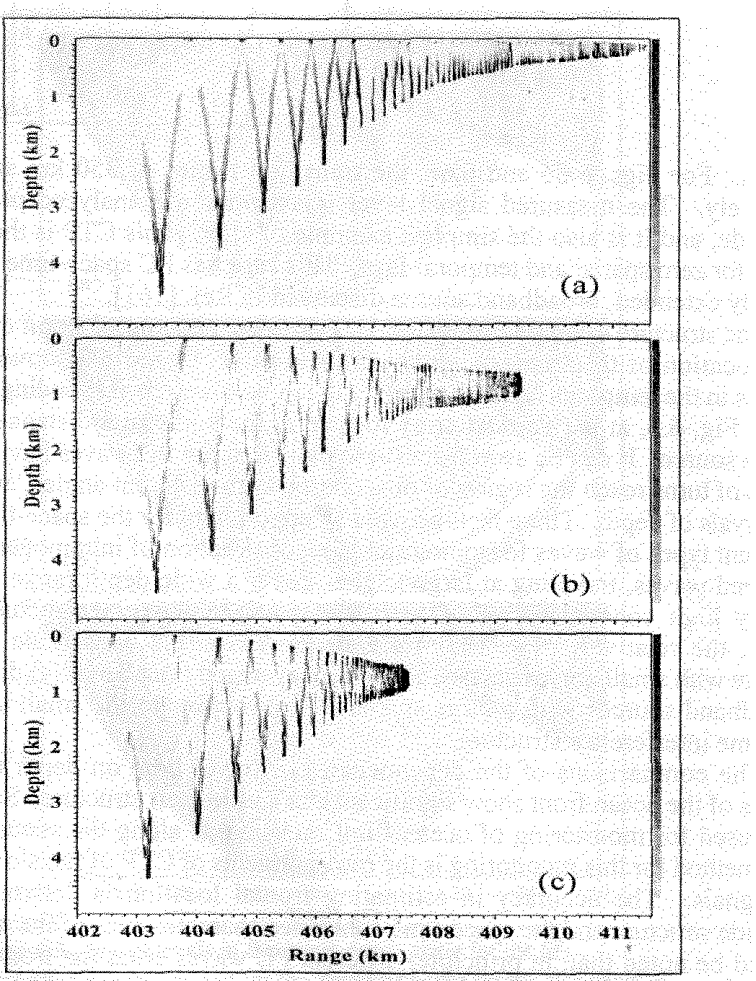

Figure 6.7. Shows the arrival structures in the temporal-depth domain for the three cases, corresponding to cases (a), (b), and (c) in Fig. 6.6 for the vertical array located at the horizontal distance of 600 km from the source. (Adapted from [155].)

6.5). The front is simulated by the SSP transitions from type 1 to type 4 along the 50-km distance. This ocean front is typical for the northeast region of the Pacific Ocean.

Figure 6.6 shows the modeled propagated-signal level for the specific placements of the front and propagation out to 600 km. There is no SSP transition in

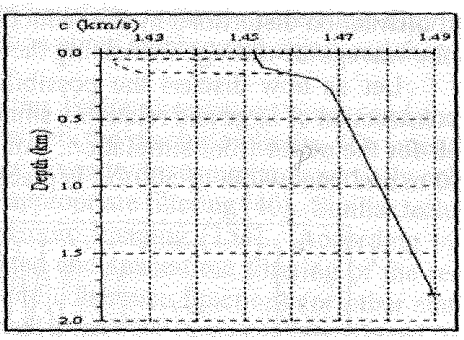

Figure 6.8. Simulated inhomogeneity (dashed curve) in the surface-duct waveguide with the SSP (solid curve). (Adapted from [155].)

Fig. 6.6a. For Figs. 6.6b and 6.6c, the transition begins at 350 km and 150 km, respectively. The measured signal level is a commonly analyzed property of a waveguide, and it is also the simplest example of CTP. This CTP is the coherence function for zero spatial and temporal lags. This case has PC space-time features for a spatially extended, broadband source discussed in Ref. [161].

The structure of propagated-noise signals in the temporal domain depends also on the location of the front along the acoustic path. Figure 6.7 shows the arrival structures in the temporal-depth domain for the three cases, corresponding to the three cases in Fig. 6.6, at the vertical array located at the horizontal distance of 600 km from the source. It can be seen from these plots that the PC waves having different numbers of turns reach the region of observation with different angles, arrival times, and intervals of depth. These facts provide an opportunity for the space-time filtering of different types of waves for tomographic reconstruction of inhomogeneities. The high-speed waves, traveling at large angles, cover a wide depth range. They have relatively high coherence due to their low spatial-frequency structure. On the contrary, the relatively slow waves are focused near the waveguide axis. They propagate with small angles and are effectively averaged (incoherently) due to the use of broadband sources with a large spatial extent relative to the small scales of the space-time interference structure.

The comparisons of the dependencies of travel time on depth for different locations of the ocean front show significant changes in their structure. Such changes can be used for monitoring of ocean front movements along the acoustic path. A simple method for this monitoring is the measurements of CTP of the slow PC space-time signals. The accuracy in estimating frontal location is determined by the waveguide structure and the space-time coherence characteristics of the noise source. It should be noted that, in principle, different PC waves cross the front at different angles. Accordingly, additional information about the frontal structure can be extracted by analyzing the changes of these parameters.

To solve similar reconstruction problems involving the horizontal structure of a frontal zone, one should use a moving noise source, such as a ship, and then PC methods can be applied. Such a scheme can consist of a stationary receiving vertical array and a noise source moving along a direction parallel to frontal zone. For the case discussed above, the number of elements of the vertical array may be about thirty. Such a system of observation can be used for tomographic reconstruction of the frontal structure in the vertical domain also.

6.2.2 Partially Coherent Differential Tomography

As has been described above, the idea of differential tomography is based on the possibility of reconstruction of localized inhomogeneities by analyzing the differences in ray structures with and without the presence of inhomogeneities [2, 68].

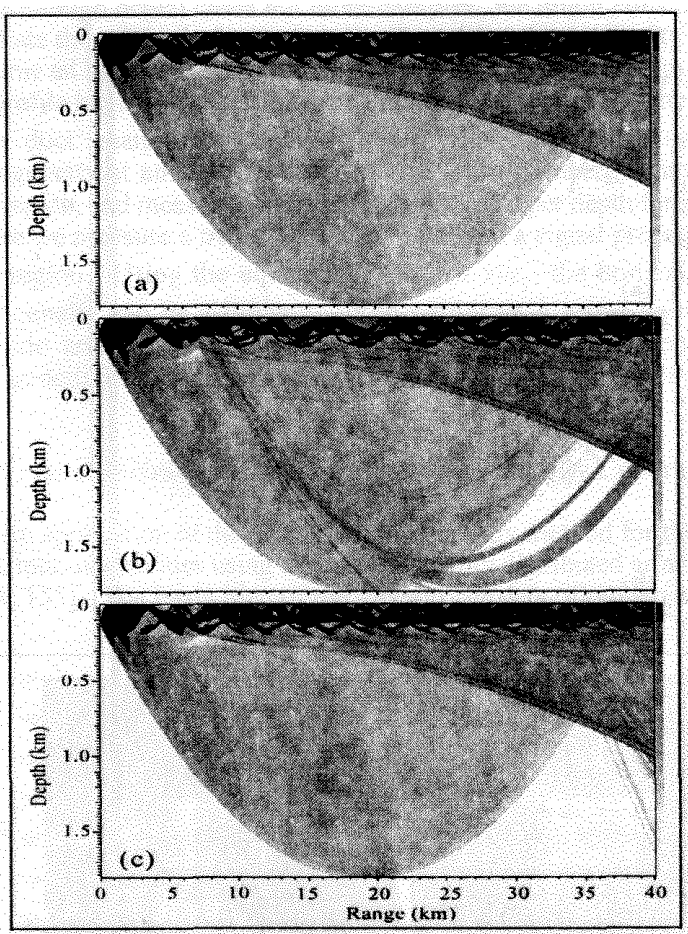

Figure 6.9. Signal levels in the range-depth plane for the (a) unperturbed waveguide and for the perturbed case for the fish shoal at the range of (b) 7 km and(c) 33 km. (Adapted from [155].)

According to this method of tomographic reconstruction, the spatial distribution of inhomogeneities along acoustic paths is determined by scanning the intensity of the scattered waves for different travel times and different depths of reception. A similar principle can be developed for PC waves.

To demonstrate this possibility, we discuss the scenario where an acoustic noise source (similar to the previous case) is placed in the surface-duct waveguide with the SSP shown in Fig. 6.8. The solid curve in Fig. 6.8 is the SSP for the unperturbed case, and the dashed curve represents a sound speed modification due to localized inhomogeneities at a given points along the range. We may consider this inhomogeneity to be a shoal of fish 100 m long and 10 m high. The sound speed

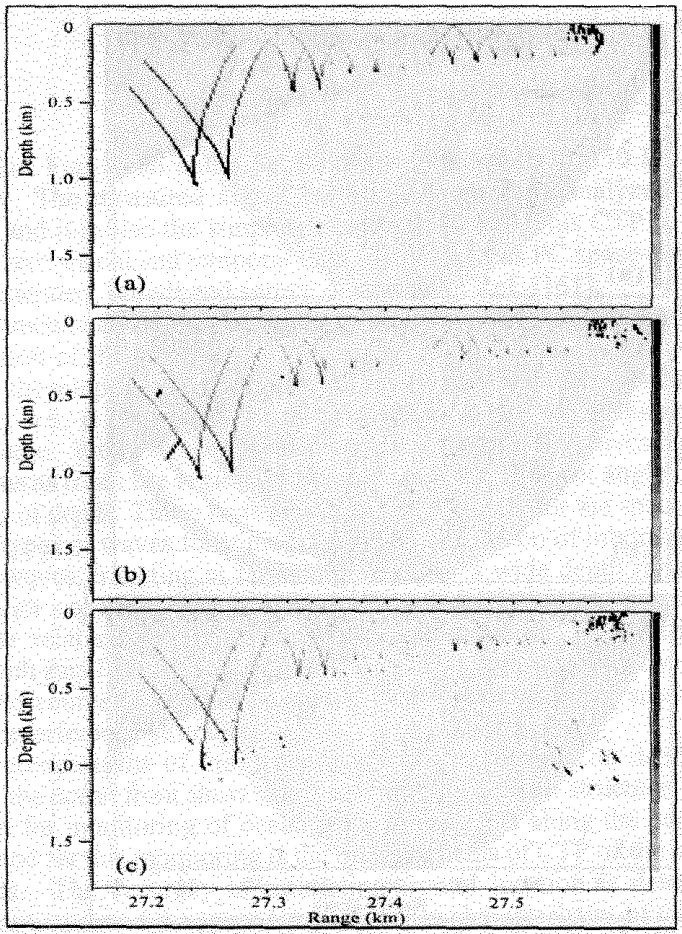

Figure 6.10. Signal levels at the range of 40 km in the time-depth plane for the (a) unperturbed waveguide and for the perturbed case for the fish shoal at the range of (b) 7 km and(c) 33 km. (Adapted from [155].)

perturbation is presumed to be due to a compact collection of fish swim bladders and can be described by known simple models [160].

Figures 6.9a and 6.10a show the signal levels in the range-depth plane and at the range of 40 km in the time-depth plane, respectively, for the unperturbed waveguide. Figures 6.9b,c and 6.10b,c show the equivalent parameters for the

perturbed case for the fish shoal at the range of 7 km and 33 km, respectively. These plots show that inhomogeneities can be considered as secondary sources, producing scattering waves which produce significant changes in the structure of PC waves. In particular, new waves arise in regions of the time-depth domain that were originally devoid of energy. The existence of significant energy in these previously non-insonified regions can form a basis for tomographic reconstruction.

Although actual cases are more complex, we might consider a simple model to illustrate the principle for the localization of an inhomogeneity. For this purpose, we assume an idealization of the SSP in Fig. 6.8, for which the upper and lower parts of the profile have constant values of c_1 and c_2, respectively. Then, the signal in the surface duct channel propagates mostly near the surface until it reaches an inhomogeneity at an unknown range, x. After that energy starts leaking into the deeper region, and measurements are made at the deeper depth for some greater range, a, where we measure a travel time delay, τ_x, from a signal propagating solely in the deeper region. Using the equation, $\tau_x = x/c_1 + (a-x)/c_2$, the horizontal location of the inhomogeneity can be estimated. With sufficient *a priori* knowledge of the real waveguide and a sufficiently complex measuring system, one can reconstruct inhomogeneities in natural waveguides using a similar approach.

6.2.3 Fresnel Diffraction Tomography with Partially Coherent Waves

An application of the diffraction tomography method for the reconstruction of oceanic inhomogeneities using a long horizontally distributed array has been proposed in [154, 155]. The basic idea of the method consists of numerical inverse focusing

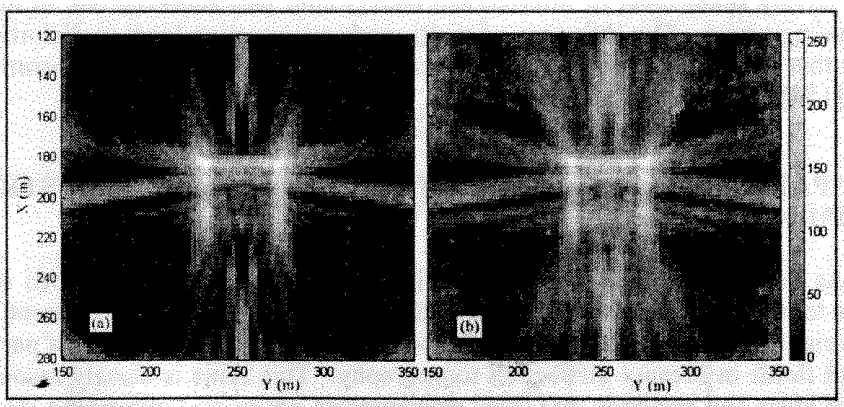

Figure 6.11. CTP maps showing the influence of the multiplicative effect due to large distances between the receivers: (a) one mode and (b) two modes. (Adapted from [155].)

of measured data into each point of the observation region. To increase the spatial resolution of reconstructed pseudo-images, a multi-view tomographic method was developed [154]. It is based on the use of the dark-field method to eliminate the

direct illuminating field. This is equivalent to placing an object at the focal point of the illuminating plane wave in physical optics. The results of numerical simulation and ultrasonic model experiments have shown that interference noise and diffraction distortions of images can be effectively minimized and reliable reconstruction results can be achieved. The effective way of smoothing out the influence of both these phenomena is the use of the PC illuminating sources. It is important to note that the use of such sources allows for the following space-time filtering. The filtering can be used for isolating waves that interact with the inhomogeneities from the background of interference and additive ocean noise [154].

The analysis of contrast CTP (i.e., CTP improved by the method described above) associated with the use of various horizontal arrays and bandwidths of PC sources has shown the existence of the optimal illuminating field space-time coherence that allows the effective elimination of interference noise and diffractive distortion. The results of numerical modeling of tomographic image reconstruction based on the PC illumination are presented in Fig. 6.11. These images were computed for the following scenario. An object of complex form, representing the Greek letter *pi* of the sizes of 40 by 40 m, was placed at the bottom of homogeneous isovelocity waveguide of the depth of 50 m. It was illuminated by a quasi-harmonic acoustic-noise source having a central frequency of 360 Hz and the horizontal size of 100 m. A horizontal receiving array 7.5 km long and consisting of 32 receivers was placed near the bottom. It was located at a distance of 7.5 km from the center of rotation between the source and receiving arrays about the observation region, which was 0.5 by 0.5 km. Thirty-two partial images of the observation region were obtained. Then they were incoherently summed, after the dark-field method was applied for the elimination of the direct-field background. Figure 6.11 shows the influence of the multiplicative effect due to the large distances between the receivers. The relatively small level of interference background was achieved due to the PC illuminating waves. The influence of multi-mode propagation leads to distortion of images that can be reduced by further decreasing the coherence of the insonifying waves [154].

6.3 SPATIAL FILTERING OF PARTIALLY COHERENT ACOUSTIC IMAGES

As noted in the previous sections in different practical applications of the acoustic tomographic systems, the illumination fields can be partially coherent. It is interesting to investigate in more details the problems related to the use of partially coherent fields in Fresnel diffraction tomography. This issue is closely associated with the ideas and methods that were developed in optics and ultrasound imaging systems [82]. The results of many research works have illustrated the following: On one hand, random inhomogeneities of the medium and motion of the elements of the vision system destroy of the sound coherence. On the other hand, special methods have been developed for the reconstruction of imaged objects using noncoherent illumination to suppress speckle-noise in images [123]. In any case we should investigate the scattering of partially coherent sound by objects to understand the

details of partially coherent imaging. A technique of acoustic image reconstruction in natural media can also be build on this basis. Theoretical estimation and experimental data have shown [123, 154, 155] that the effectiveness of the spatial filtering of the images diminishes for incoherent illumination systems. It is interesting to investigate, for example, the cases of the ocean tomographic reconstruction when the observed inhomogeneities are smooth and forward-scattering. The application of PC sound for the construction of the acoustic images provides the possibilities of decreasing the coherent noise and spatial filtering of images.

6.3.1 Diffraction of PC Fields in Layered Waveguides

In this section we investigate the problem of spatial filtering of partially coherent acoustic images by using a horizontal array in layered waveguides. The theoretical analysis of low-frequency acoustic images is accompanied by laboratory experiments.

Partially Coherent Fields. For simplicity, we assume that the field of the source S illuminates a large (in wavelength scales) absolutely ridged scatterer σ (see Fig. 6.12). The diffracted fields in the far zone of the scatterer can be represented by using of the Green's function of the unperturbed waveguide,

$$G(x,y,z;x_s,y_s,z_s) = \sum_{n=1}^{N} \varphi_n(z_s)\varphi_n(z)\exp[i(\kappa_n|\boldsymbol{r}_s - \boldsymbol{r}| - \frac{\pi}{4})](\kappa_n|\boldsymbol{r}_s - \boldsymbol{r}|)^{-1/2}, \qquad (6.15)$$

where $\boldsymbol{R} = (\boldsymbol{r},z) = (x,y,z)$ defines the receiving point, φ_n and κ_n are the eigenfunctions and horizontal modal wavenumbers, respectively, and N is the entire number of the

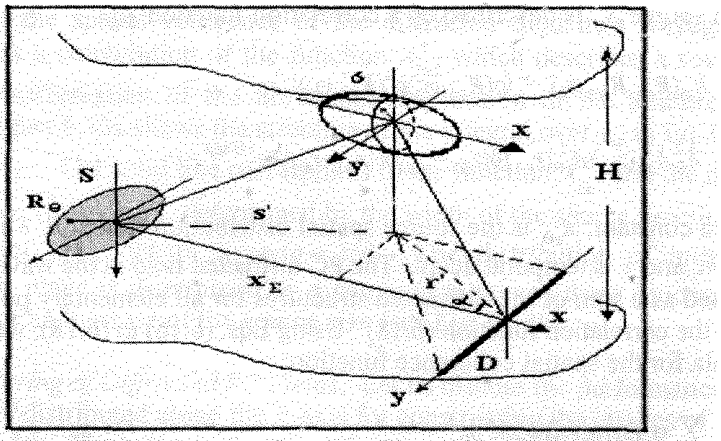

Figure 6.12. Geometry the study of the PC field diffracted into the far zone by a ridged scatterer. (Adapted from [28].)

propagating waveguide modes. Let us assume that the conditions of the small-angle approximation are satisfied. In this case, the diffracted field from the Green's

theorem using the Kirchhoff approximation can be deduced. For the potential of displacement velocity of the scattered field, $\Psi_s = \Psi - \Psi_0$, we have:

$$\Psi_s = \sum_{n=1}^{N} \varphi_n(z) \exp[i(\kappa_n s' - \frac{\pi}{4})](\kappa_n s')^{-1/2} \sum_{m=1}^{M} \varphi_m(z_s) \exp[i(\kappa_m r' - \frac{\pi}{4})](\kappa_m r')^{-1/2} S_{nm}, \quad (6.16)$$

where Ψ_0 is the potential of illumination field, $s' = (x_\Sigma^2 + y_s^2)^{1/2}$, $r' = ((a - x_\Sigma)^2 + y^2)^{1/2}$ (see Fig. 6.12), x_Σ is the displacement of the scatterer, a is the distance between the source and the observation region, and M is the number of the diffracted waveguide modes. The scattering matrix of the waveguide modes, S_{nm}, is determined by the form of the scatterer, σ, and waveguide characteristics:

$$S_{nm} = T_{nm} L_{nm} = i\kappa_n \int_\zeta T(\zeta) \varphi_m(\zeta + z_\Sigma) \varphi_n(\zeta + z_\Sigma) d\zeta \int_\eta L(\eta) e^{i(\frac{\kappa_n x_\Sigma}{s'} + \frac{\kappa_m y}{r'})\eta} d\eta, \quad (6.17)$$

where the form of the shadow-generated line, $\sigma(\zeta,\eta)$, can be approximately represented as a product of two functions: $\sigma(\zeta,\eta) = T(\zeta) L(\eta)$.

As follows from Eqs. (6.16) and (6.17), the short-wave diffraction in waveguides contains a transformation of the waveguide modes in vertical direction (described by the matrix elements T_{nm}) and in horizontal plane (described by matrix L_{nm}). The resulting field is constructed as a sum of all diffracted waveguide modes, each of which is formed by the transformation of all illuminating modes [28].

Diffraction of PC Fields in Waveguides. Let us assume that a quasi-monochromatic illumination source S_Θ is described by a correlation function K_Θ:

$$\begin{aligned} K_\Theta &= K_\Theta(\boldsymbol{R}_{\Theta 1}, \boldsymbol{R}_{\Theta 2}, \omega_0) = \langle \rho(\boldsymbol{R}_{\Theta 1}, \omega_0) \rho^*(\boldsymbol{R}_{\Theta 2}, \omega_0) \rangle = \\ &= A_0^2 A_{z\Theta}^2(z_{\Theta 1}) A_{r\Theta}^2(\boldsymbol{r}_{\Theta 1}) \delta(z_{\Theta 1} - z_{\Theta 2}) \delta(|\boldsymbol{r}_{\Theta 1} - \boldsymbol{r}_{\Theta 2}|) e^{-i2\pi f_0 \tau}, \end{aligned} \quad (6.18)$$

where A_0 is a constant, $A_{z\Theta}$ is the source spatial distribution function, δ is the Dirac delta function, and τ is temporal delay. The PC diffracted field in the waveguides can be represented as a sum of the diffracted structures for all elementary point-sources weighted by the correlation function (6.18). Using Eqs. (6.16) to (6.18), we can arrive at the formula for the spatial coherence function:

$$K_{12}^g = \sum_{m\mu} \varphi_m(z_1) \varphi_\mu^*(z_2) \langle b_m^g b_\mu^{g*} \rangle,$$

where b_m^g are the coefficients of the modes. Then

$$K_{12}^{g} = \sum_{nm\nu\mu} A_0^2 \varphi_\nu \varphi_\mu^* \int_{z_\Theta} A_z^2(z_\Theta)\, T_{nm} T_{\nu\mu}^* \kappa_n \kappa_\nu \varphi_n(z_0) \varphi_\nu^*(z_\Theta) dz_\Theta \times$$

$$\times \int_{r_\Theta} A_r^2(r_\Theta) L_{nm} L_{\nu\mu}^* [\kappa_m \kappa_\mu | r_\Theta - r_1 | - | r_\Theta - r_2 |]^{-1/2} e^{i(|\kappa_m| r_\Theta - r_1| - \kappa_\mu | r_\Theta - r_2|)} dr_\Theta . \qquad (6.19)$$

This expression connects the spatial coherence function of the diffracted field with the form and displacement of the scatterer. Contrary to the formula for the infinite medium, Eq. (6.19) describes the effects of the interference of the waveguide modes (n,m,ν,μ-indexes). It can be shown that multimode propagation complicates the diffraction patterns when scatterer sizes and spatial delays considerably exceed the scales of the mode interference.

If $A_{z\Theta} \ll \Delta_z$, where Δ_z is a scale of the variability of the waveguide field for vertical direction, and if $\eta^2/x_\Sigma \ll 1$, $y^2/x_\Sigma \ll 1$, we have from Eq. (6.19):

$$K_{12}^{g} = \sum_{nm\nu\mu} L_{nm}^{\nu\mu} \Phi_{nm}^{\nu\mu} \int_{y_\Theta} A_{y_\Theta}^2 \, sinc([p\kappa_n + qy_1\kappa_m]\eta_0) sinc^*([p\kappa_\nu + qy_2\kappa_\mu]\eta_0) dy_\Theta , \qquad (6.20)$$

where $p = (y_\Theta - y')/x_\Sigma$, $q = 1/(a - x_\Sigma)$, and

$$L_{nm}^{\nu\mu} = -A_0^2 \varphi_n(z_\Theta) \varphi_\nu^*(z_\Theta) \varphi_m(z) \varphi_\mu^*(z) \kappa_n \kappa_\nu T_{nm}^{\nu\mu} \eta_0^2 ,$$

$$\Phi_{nm}^{\nu\mu} = [x_\Sigma (a - x_\Sigma) \kappa_n \kappa_m \kappa_\nu \kappa_\mu]^{-1/2} \exp[i(x_\Sigma(\kappa_n - \kappa_\nu) + (a - x_\Sigma)(\kappa_m - \kappa_\mu))] ,$$

$sinc(x) = \sin x/x$, and η_0 is the scatterer size in the horizontal direction. Equation (6.20) shows that the spatial coherence of the diffracted field in a waveguide can be presented as a convolution of the function $A_{y_\Theta}^2$, which describes a source, and the Fourier transformation of the horizontal distribution of the scatterer secondary sources. Figure 6.13a shows the structure of the integral over y_Θ in Eq. (6.20), when $y = y'$, $n = \nu$, $m = \mu$. The solid line corresponds to the function $A_{y_\Theta}^2$, and the dash line is a function $sinc^2([p+qy]\eta_0\kappa_n)$, determined by the width of the source function Δ_η and its displacement y/x_{eq}, where $x_{eq} = x_\Sigma(a - x_\Sigma)/a$. The distribution of intensity in the observation plane is determined by a common region of these functions, and it is averaged for an increase of the source size (see Fig. 6.13b).

Spatial Filtering of Diffracted PC Fields. Let us discuss the performance of an array horizontally distributed along the y-axis for constructing the images of the scatterer in waveguides. The aperture function of the array is determined by the expression: $M_m^\Sigma(z,y) = M_m(y)\, M'_m(z) \exp[i(\kappa_m y \sin\alpha - \kappa_m y^2/\rho)]$, where $M_m(y)$ and $M'_m(z)$ describe the array construction, and α and ρ determine the wavefront slope angle and the focus

distance of array, respectively. In this case, the image constructed by the array can be presented as a convolution of the diffracted field (Eq. (6.20)) and the aperture

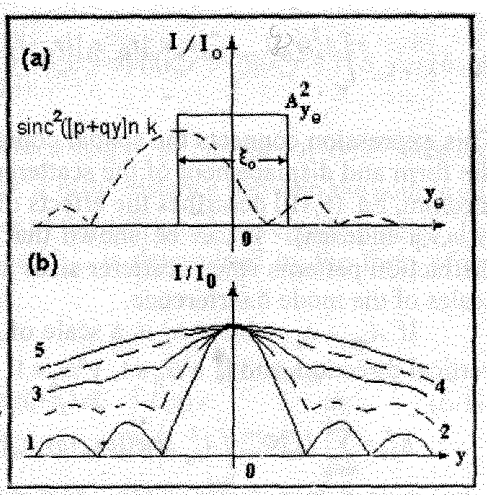

Figure 6.13. (a) Compares $A^2_{y_\Theta}$ with $sinc^2([p+qy]\eta_0\kappa_n)$ and (b) the distribution of intensity in the observation plane determined by its average for an increase of the source size (Adapted from [154].)

function $M^{\Sigma}_m(z,y)$ [76]. For simplification let us assume that the mode selection (for example, by the array focusing angle or by the arrival time of the propagating gated pulse) has been fulfilled. Thus, we have for the image constructed by the array:

$$\langle |P_\Sigma(\alpha,\rho)|^2 \rangle = \int_{y_\Theta} A^2_{y_\Theta} S'^2_{mm} \times$$

$$\times \Big| \int_\eta L(\eta) \int_D \exp(-i[p+qy]\kappa_m\eta + \kappa_m y^2[\tfrac{q}{2}-\tfrac{1}{\rho}]\cdot\kappa_m y\alpha) M_m(y)\,dy\,d\eta \Big|^2 \, dy_\Theta \,, \tag{6.21}$$

where $S'^2_{mm} = A_0^2\kappa_m^2\psi_m^2(z_\Sigma)\varphi_m^2(z_\Theta)\kappa_m^2 x_\Sigma(a-x_\Sigma)(d/H)^2$, and H is the depth of the waveguide. The procedure for the image reconstruction can be accomplished by focusing into all points of the observation region and summing the signals from all array sensors. The performance of this imaging system is characterized by the contrast transfer function (CTF) $K(\alpha,\rho,u)$, where u is a spatial frequency for y direction. To obtain the function K, we substitute the observed object model in the form $L(\eta) = \exp(i\eta u) + \exp(-i\eta u)$ in Eq. (6.21). In this case we arrive at the following expression for the CTF:

$$K(\alpha,\rho,u) = \int_{y_\Theta} A^2_{y_\Theta} M_m[l(p\kappa_m - u)]\, M_m^*[l(p\kappa_m + u)]\, \exp(i[\varepsilon\kappa_m l^2 2\kappa_m p + 2\alpha\kappa_m l]u)\,dy_\Theta \,, \tag{6.22}$$

where $l = (a-x_\Sigma)/\kappa_m$ and $\varepsilon = 1/(2(a-x_\Sigma)) - 1/\rho$ is a focusing parameter of imaging system. The deduced expression for the CTF describes the image reconstruction in the waveguide (for the single-mode approximation) for the partially coherent illumination. For the asymptotical cases, when $\xi_0 \ll l/D$ and $\xi_0 \gg l/\Delta_{min}$ (Δ_{min} is the

distance between sensors), Eq. (6.22) describes the asymptotical cases of coherent and noncoherent imaging systems, well-known in optics [123].

Figure 6.14a shows the results of the calculation of the CTF structure transformation for different spatial frequencies and for different source sizes, when the low-frequency filter (dark-field filtration) is used. The calculation has shown, that, when $\xi_0 < D$, one can effectively eliminate the direct illumination background that is important for the reconstruction of the weak oceanic inhomogeneities. The results of the background elimination for the computer simulated images are presented in Fig. 6.14b.

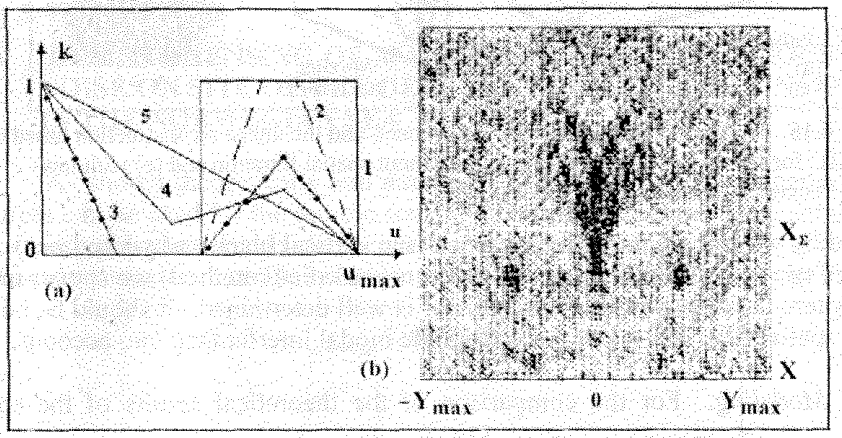

Figure 6.14. (a) The results of the calculation of the CTF structure transformation for different spatial frequencies and for different source sizes and (b) the results of the background elimination for the computer simulated images. (Adapted from [3].)

6.3.2 Some Experimental Results

For the justification of the theoretical results, experiments in the high-frequency region (about 140 kHz) and in the optical region (as the simple model from the point of view of the modeling of the partially coherent illumination) have been carried out.

High-Frequency Imaging. A receiving array with a synthetic aperture of 28 cm, formed by the motion of the point receiver, was used for the imaging of the scatterer spatial distribution (see Fig. 6.15a) in the tank experiment. The quasi-monochromatic pulse with the time-duration of 300 μs was used with the reverberation reduction by time-gating. The isovelocity water layer of the depth of 3 cm was used as a simple model of the layered oceanic waveguide. The distance between the source and observation region was 44.6 cm.

A vertical steel cylinder of the diameter of 0.25 cm was situated at the mid-point between source and receiving array. Figures 6.15b,c show the image reconstruction based on Eq. (6.21) for the case of coherent source. Figure 6.15b presents the image without spatial filtration. We can only see the image of the source

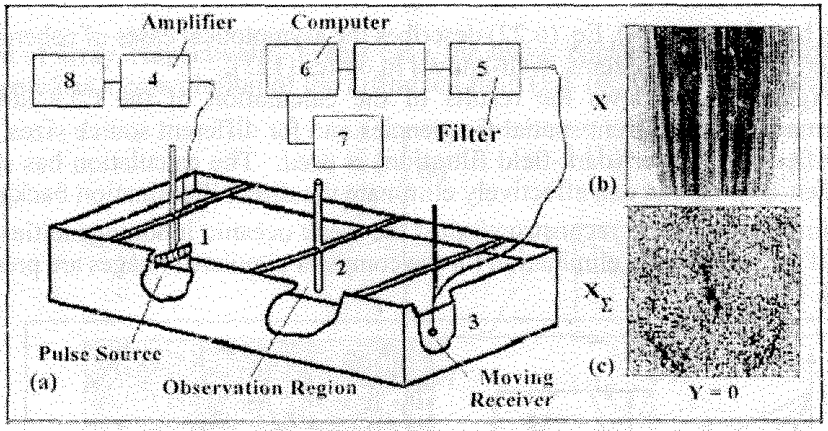

Figure 6.15. (a) A schematic of the tank experiment, and the image reconstruction based on Eq. (6.21) for the case of coherent source (b) without spatial filtration and (c) with low-spatial-frequency-filtration. (Adapted from [3].)

distorted by waveguide mode interference (see vertical black and white lines). The results of the low-spatial-frequency-filtration (dark-field method) are shown in Fig. 6.15c, where the disposition of the cylinder is well determined. It should be noted that the spatial filter has taken the waveguide modal interference into account.

Optical Modeling. For the comparison of the theoretical results of the spatial

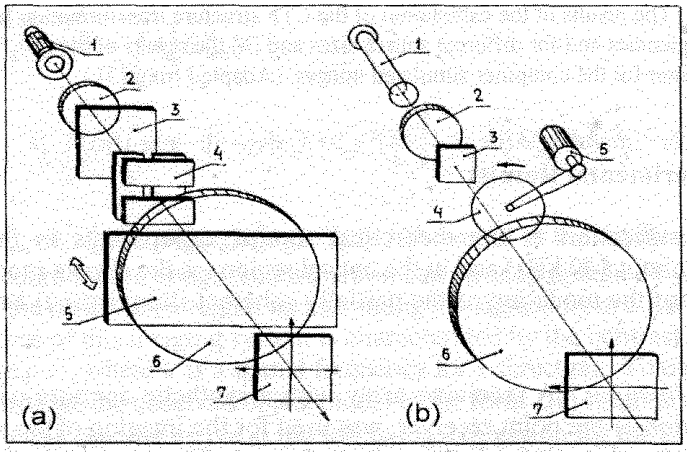

Figure 6.16. Schematic of systems for PC image reconstruction in optical fields for (a) spatially incoherent and (b) spatially coherent. (Adapted from [82].)

filtration of the PC images with experimental data for the optical case, the special laboratory facilities were built. These facilities have allowed for constructing PC images in optical fields [82]. An important aspect of the experimental systems is a light source that can be switched from spatially incoherent to coherent (element 1 in

Figs. 6.16a and 6.16b, respectively). The use of these facilities provides an opportunity for high-frequency imaging-system modeling. But this approach can not be used for the analysis of imaging systems for the case of multi-mode propagation. The block scheme of the experiment mounting includes optical lenses (element 2 in Fig. 6.16) that is an analogy of the array of acoustic sources with variable coherence.

Figure 6.17a shows the results of the CTF measurement for different sizes of the source. This allows us to estimate the efficiency of partially coherent image filtration. An example of the filtration is shown in Figs. 6.17b and 6.17c, where images of letters after low-frequency filtration are presented for different source sizes.

6.4 REMOTE SENSING OF MARINE SEDIMENTS BY ACOUSTIC NOISE ON SITE OF THE DEEP SEA DRILLING HOLE N643 IN THE NORWEGIAN SEA

As shown theoretically and empirically, noise or partially coherent acoustic sources can be used for the remote sensing of bottom structure. In general, bottom-structure reconstruction can also be viewed as a tomographic procedure, because the bottom-layer structure can be reconstructed as tomographic projections by monitoring

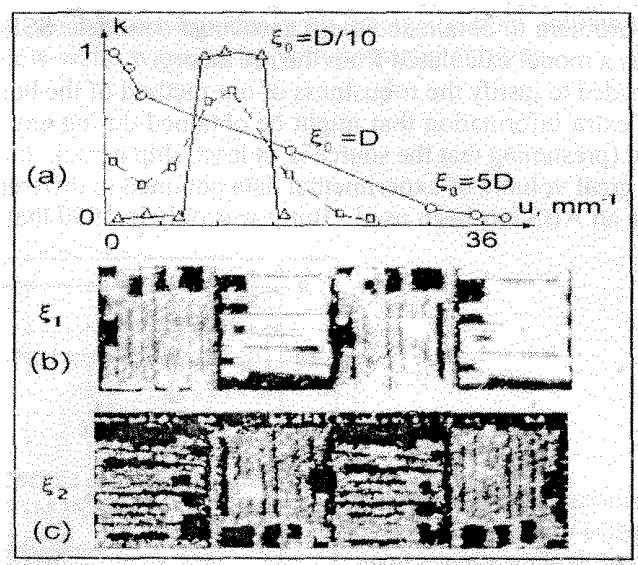

Figure 6.17. (a) The results of the CTF measurement for different sizes of the source and the resulting image reconstructions for the source sizes (b) -- and (c) --. (Adapted from [82].)

in the spatial domain. Although not yet fully developed, prospects for the future are very promising. We explore these ideas in the current section and briefly discuss the results from the point of view of the investigations associated with the use of noise partially coherent acoustic sources for remote sensing of the bottom structure in the ocean.

For the bottom monitoring one needs to have the high-resolution seismic surveys providing the information about the acoustic parameters of marine sediments. In principle, these parameters can be obtain from in-situ measurements in drilling holes or wide-aperture seismic reflection data. However, this approach is ineffective for deep-sea regions, because of measurement difficulties and high costs. To overcome this problem, we proposed more efficient and cheaper method for the estimation of sound speed profile, attenuation and the reflection coefficients in sediment layers [162].

Our approach consists of remote sensing of sediment layers of the seafloor in the following manner. Continuous low-frequency acoustic noise is emitted from sea surface by a moving ship. The sound source may represent the ship own noise or a more powerful source. But the use of a ship's own noise can provide satisfactory results. The receiver is a vertical array mount at an Automatic Bottom Station (ABS). ABS is a pressure resistant container with a recorder and microcomputer. Unlike the traditional seismic method where travel times are determined, we have suggested the measurements of delay times between direct and bottom-layers-reflected-signals arrivals. Delay times can be determined from the locations of autocorrelation maxima of received signal. Using data from the array, we can determine the direction to the source and obtain basic dependence of delay times on arrival angles. Then we can solve the inverse problem to obtain sediment geoacoustic model. SSP in sediment layers is defined as a model calculated from the ray theory.

The data needed to justify the robustness of our method of the bottom sensing can be viewed as extra information that might be obtained during any experiments where ABS is used (presuming that the source is, at least, ship noise). For this reason we already have a great volume of experimental data obtained in different regions of the oceanic where an ABS has been used. But it was only in 1990 that this method

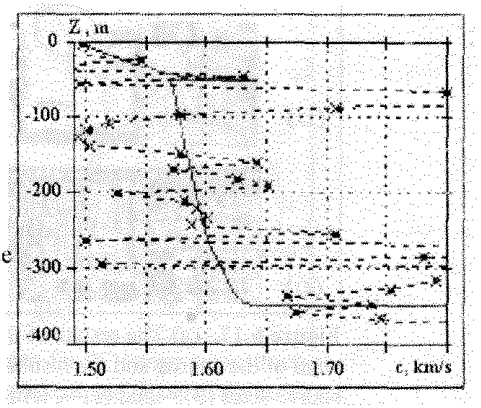

Figure 6.18. Reconstructed SSP using ship noise data (solid line) compared with a laboratory determination of the speeds of the samples from the drilling hole (dashed line) (Adapted from [162])

was checked directly when two ABSs were launched to the bottom at the depth of 2780 m directly on site of a deep-sea drilling hole N643 (ODP LEG 104) in the Norwegian Sea close to the Voring Plateau.

The bottom SSP was reconstructed by the processing of data of ship noise produced by the moving vessels, *Akademik Ioffe* and *Akademik Sergey Vavilov*, near the site of the drilling hole. As shown in Fig. 6.18, the reconstructed SSP (solid line)

is in a good agreement with laboratory determination of speeds of the samples of the drilling hole (dashed line) [162].

In this experiment a special source of low-frequency noise from the *Akademik Ioffe* was also used. The continuous noise signal was emitted at the depth of 300 m when the vessel was drifting away from the site of N643 and ABS. The results of the bottom sensing were not significantly improved when the special source of acoustic noise was used.

Partially coherent space-time acoustic noise sources used as an insonifying field form the basis for the discussion of three different types tomographic reconstruction of the oceanic inhomogeneitics. Some simple procedures for the extraction of the parameters of inhomogeneities, namely, their spatial distributions, were proposed for: (1) an oceanic front representing a relatively smooth inhomogeneity, (2) a shoal of fish representing a spatially localized inhomogeneity, and (3) an object of complex form. It was shown that statistically averaged characteristics of noise waves can be measured for reconstruction. Partially coherent space-time structures of partial-wave bundles, which improve the tomographic reconstruction quality, have arisen for all cases. It is interesting to note that the bundles of PC waves that preserve high internal coherence are useful for tomographic monitoring in oceanic waveguides with strong random inhomogeneities as, for example, shallow-water waveguides with powerful currents.

Chapter 7:

SUMMARY AND CONCLUSIONS

Recent accomplishments in ocean acoustic tomography were discussed in the previous sections. In particular, topics on the adiabatic approach in tomographic reconstruction and the methods of Diffraction and Emission Tomography have been addressed in some details. In this final chapter, the major ideas will be summarized to indicate concisely the modern status of tomographic investigations, particularly, as it exists in Russia.

7.1 ACOUSTIC TOMOGRAPHY IN THE OCEAN ENVIRONMENT

It seems that no method for reconstructing the volumetric structure of large regions of the ocean is more effective than the acoustic remote sensing. It is important to keep in mind that complex methods of processing large amounts of data should be employed to produce three-dimensional ocean images. Ocean acoustic tomography can lead to the solution of this problem.

It is known from our everyday experience that our two eyes create special images of real world. We might refer to this as binocular vision. For large ocean regions that are practically non-transparent for the optical vision systems, one can effectively use acoustic-vision systems. For such acoustic-vision systems, a role similar to the binocular vision may be played by spatially distributed arrays of receivers with images of acoustic scatterers or sources created by computer.

The peculiarity of acoustic-vision systems, in contrast to the case of optical vision, is the small size of acoustic receiving apertures in comparison with the acoustic wavelength. Consequently, we frequently observe only pseudo-vision images from one projection. However, such pseudo-images do provide some possibilities for making decisions about the presence of objects and for estimating their locations, sizes, and properties. On the other hand, certain tomographic methods offer the reconstruction of full three-dimensional distributions of inhomogeneities by the combined processing of many projections.

Problems in OAT arise because of the inhomogeneity scales and the complex variability of the ocean medium. These problems lead to a complexity in form, scale, and distributions of acoustic systems and their resulting tomographic projections, as well as to the loss of part of the information about observed scatterers due to specific propagation conditions in ocean waveguides and due to distortions of reconstructed images given the interference of partial waveguide waves [2, 3, 7, 8, 23, 34, 44, 49, 65, 72, 83, 118].

7.1.1 Schemes for Ocean Acoustic Tomography

Ocean acoustic tomography schemes can be separated into three major and distinct groups, as follows:

a) The first group includes *transmission schemes* for observing nearly transparent objects or weakly interacting inhomogeneities. The measured characteristics of the acoustic waves interacting with such objects are propagation times and amplitudes and phases of received signals.
b) The second group units *diffraction schemes* for observing more strongly interacting inhomogeneities. Here one needs to measure complex amplitudes of diffracted and scattered waves for large observation regions over wide interval of arrival angles, as well as signal propagation times.
c) Finally, the third group includes *emission schemes* for observing spatial, temporal and frequency distributions of noise sources in the ocean.

An additional scheme, which might combine some or all of the above schemes, is based on the use of partially coherent acoustic waves.

Another name associated with the weak interaction case is *adiabatic tomography* that can be synonymous with the transmission scheme. It implies that non-interacting mode-propagation or the ray-acoustic methods can be applied. This is in contrast with diffraction schemes where modal spectrum transformation takes place.

This leads us to a final comment about the classification of tomographic schemes. We may need to distinguish between the application of ray and modal approaches for the solutions of tomographic problems. Both approaches have their own distinct realm of optimum application with some overlap. As in other branches of ocean acoustics, the ray method works the best at higher frequencies for environments with less boundary influence (e.g., the deep-water case). Modal methods are most suitable at lower frequencies in the boundary limited cases.

Adiabatic tomographic methods were developed first. Numerical simulation and experiments, based on these methods, have been carried out successfully. The impetus for the fast development of these methods was a need to solve certain large-scale oceanographic problems and problems related to global climate changes. Appropriate algorithms and experimental schemes have been developed sufficiently to solve these problems on a routine basis.

The situation for diffraction tomography methods is completely different. The basis of this direction of OAT are methods that were developed in ultrasound and other branches of acoustics. Pulse gating by vertical and horizontal arrays, the Doppler technique, and dark-field filtering method are combined in diffraction tomography, because the signature of diffraction effects is very weak. For these reasons the evolution of diffraction tomography has been much slower.

7.1.2 Fundamental Problems of Ocean Acoustic Tomography

Mathematically, the problem of tomographic reconstruction can be reduced to the solution of the Fredholm integral equations of two kinds. Transmission and diffraction tomography for the reconstruction of spatially distributed inhomogeneities are related to the Fredholm integral equation of the second kind. Emission tomography for reconstruction of self-illuminating objects can be described by the Fredholm integral equation of the first kind. The problems accompanying the solution of such equations are well-known in the theory of inverse problems. The three most pervasive issues are:

a) Incorrectness (due to attenuation of the radiated and scattered waves and the presence of noise);
b) Sub-definiteness (due to difficulties associated with measurements in natural conditions and necessity of processing large volumes of information);
c) Nonlinearities (for example, due to the multi-scattering effects).

All three issues add mathematical and numerical complexities in the solution of tomographic problem very often requiring one to establish a unique solution procedure for every particular tomographic problem. In addition, every natural ocean waveguide is characterized by the influence of randomly distributed inhomogeneities and bottom of complex structure (especially, for shallow-water regions of the ocean) that, on the other hand, can often be a subject for the reconstruction by OAT.

The most important method for overcoming these difficulties is an effective use of *a priori* information about observation objects, as well as about the surrounding medium to optimize the measurement schemes and to choose the optimal basis functions for the description of the medium and observation objects. It is necessary to take into account the fact that often all information necessary for the solution of an inverse problem is not available *a priori*. This is often the basis for non-stable solutions, which then requires appropriate regularization schemes [1, 3, 5, 6, 8, 11, 14, 44, 83, 118].

7.1.3 Types of Oceanic Inhomogeneities

A successful solution of a particular tomographic problem is mostly determined by an efficient use of available information about the observation object and the surrounding ocean medium. From this point of view, it is important to have theoretical and numerical basis models of oceanic inhomogeneities. Spatial and temporal scales used for the classification of the oceanic inhomogeneities range over very broad limits. The following simplified classification can be proposed for the description of oceanic inhomogeneities. According to this scheme, oceanic inhomogeneities can be divided into three main groups:

a) Micro-scale inhomogeneities: particles, bubbles, plankton, turbulence, etc.;
b) Meso-scale inhomogeneities: internal waves, hydrolenses, wind waves, fish

shoals, ice floe, ships. engineering construction, bottom inhomogeneities, etc.;

c) Synoptic and gyro-scales inhomogeneities: eddies, hydro fronts and season variabilities.

Measurement schemes and parameters of sensing acoustic signals must be chosen in accordance with the scales of oceanic inhomogeneities and the peculiarities of the acoustic-wave propagation in specific ocean waveguides. For example, one would use one of the transmission schemes to reconstruct smooth and weak changes in the distribution of sound speed in the deep ocean, but would use one of diffraction schemes to determine the location and shape of underwater spatially localized object [8, 9, 10, 13, 23, 28, 33, 46, 55, 156, 157].

It is interesting to note that randomly distributed oceanic inhomogeneities can play a different role depending on whether the scheme employed is adiabatic or diffraction. In the first case, they play the role of noise, while in the second case, they can be objects for reconstruction.

7.2 METHODS OF OCEAN ACOUSTIC TOMOGRAPHY

In this section we shall summarize the methods discussed above.

7.2.1 Adiabatic Tomography Methods

The idea of reconstruction of weak or gradual changes in the distribution of sound speed in the ocean using multiple acoustic sources and receivers surrounding large observation regions and measuring the shifts of the travel times of acoustic pulses propagating along different ray paths was proposed by Munk and Wunsch in 1979. Several experimental tests of the adiabatic methods by Russian and American groups individually and jointly have been carried out recently. Here we recall some of those discussed in earlier chapters:

a) An experiment with six acoustic sources (frequencies of 250 Hz and 400 Hz) and a vertical receiving array by Russian-American-French international team;

b) An experiment on propagation of low-frequency waves (about 20 Hz) along a 2500-km-long, Arctic-acoustic-path between a Russian ice camp near Spitsbergen, where an acoustic source was set, and an American ice camp in Beaufort Sea, where horizontally and vertically distributed receiving arrays were mounted;

c) An experiment in the Norwegian Sea with a 105-Hz source and a path length of 105 km, conducted by Russian scientists.

In the processing of experimental data, the ray approach was applied. However, the modal approach can be associated with the adiabatic methods as well. Matched-field processing can be applied as a part of that approach. In adiabatic cases,

the reconstruction problem can usually be reduced to the solution of a system of algebraic equations by using appropriate discretizations of functions and choosing the acceptable basis conditions of the unperturbed ocean to linearize the problem.

New phenomena associated with the formation of coherent bundles of acoustic waves in ocean can also be utilized by OAT. The existence of such structures in the real ocean has been predicted theoretically and have been tentatively confirmed by experiments. The properties of wave bundles, including their coherence, have been investigated, and ideas of their application to OAT have been discussed in the literature on OAT [3, 11, 12, 23, 36, 44, 45, 56, 57, 59, 63, 111, 113, 114, 115].

7.2.2 Diffraction Tomography Methods

Diffraction can play an important role, if the wavelength of sensing waves is of the sizes of observed inhomogeneities and the inhomogeneity boundaries are sharp enough. Diffraction of acoustic waves in the ocean manifests itself as horizontal diffraction patterns (similar to free space) for each waveguide mode and as a transformation of the modal spectrum in the vertical plane.

In this case, the use of pulse signals, vertical arrays, and frequency filtering allows one to separate different waveguide modes. Using horizontally distributed or synthetic aperture antennas, for example horizontally distributed inhomogeneities can be reconstructed by inverse focusing of the measurement data in the regions of interest. When the integral equation allows linearization, the Born and Kirchhoff approximations can offer simple and effective methods for diffraction tomography problem. Also, as in ultrasonic acoustics, analytical inversion can be used when the appropriate conditions for the application of the Fourier and Fresnel transforms are satisfied.

Generally, such tomographic reconstruction procedures can be described as follows: The initial step of reconstruction is the collection of *a priori* information about the environment (ocean waveguide) and the objects to be observed. Using this information, basis functions can be chosen as the second step to calculate the spectrum of measured and filtered data in the space of the appropriate basis functions. At the third step, the inhomogeneity images can be numerically produced. Finally, decisions about the presence of objects, their parameters, and variability can be made. Information on basis functions, measuring scheme, and some threshold values are combined to make a decision in tomographic vision [2, 3, 18, 19, 26, 27, 28, 30, 32, 34, 35, 46, 48, 49, 68, 79, 80, 83].

It may be readily shown that a full reconstruction of the vertical structure of inhomogeneities in the ocean is impossible, because of a limited number of waveguide propagating modes. Additionally, the multiplicity of acoustic images is a practical problem in diffraction tomography, which can be easily demonstrated by the modal decomposition of the Green's function and the incident field in the Born approach.

This approach also allows obtaining the limitations on the sizes of objects and arrays for investigation of the situations when multi-mode propagation destroys the final image. The Fresnel Tomography algorithm, including the focusing of scattered waves into each point of the observation region and filtering by the Dark-Field

Method to reduce the direct illumination can be used for the reconstruction of the distribution of scatterers in horizontal plane. As calculations have shown, multi-mode interference leads to image distortion, especially for the cases when only a few modes propagate.

Differential Tomography. The peculiarities of propagation and diffraction of acoustic waves in ocean waveguides allows for possibilities of constructing different tomographic vision systems for the remote sensing of oceanic inhomogeneities. The differential method is one of them. It uses vertical radiating and receiving arrays and time gating of illuminating acoustic pulses. If the mode with number, n, is radiated and the mode with number, m, is received, we can isolate the signals scattered by the inhomogeneities that are situated within the vertical layer with definite width that is located at the fixed distance from the receiving system. Accordingly, we can reconstruct the distribution of inhomogeneities that are situated along the path between the source and receiving system by gating the intensity of scattered pulses in the temporal domain. In order to separate signals from different types of oceanic inhomogeneities (such as wind waves, swell, turbulence, internal waves and others) and to estimate their parameters, differences in the spatial spectra can be used. Such spectral differences arise due to the nature of these inhomogeneities manifested in the frequency domain. According to this method, the tomographic reconstruction of randomly distributed inhomogeneities requires the joint processing of sets of projections in the spatial, temporal, and frequency domains to separate different types of inhomogeneities and to obtain their spatial distributions. It may be noted that the differential method can be developed for the ray approach as well [2, 18, 30, 35, 46, 48, 49, 50, 68, 69, 72, 73].

Fresnel Tomography. Acoustic vision systems using horizontally distributed or synthetic aperture arrays provide an opportunity to develop a tomographic method of reconstructing images similar to optical vision systems (e.g., lenses). Algorithms for such methods are based on analytical inversions of the integral equation in the Born or Kirchhoff approaches and on the presentation of the image as the spectrum of the received signals in Fresnel basis-function decomposition. This tomographic algorithm consists of the processing of array data to single out the scattered signals from the area of interest and the reduction of the direct illuminating signal that fluctuates due to random inhomogeneities and nonstationarities of the ocean medium. To suppress the strongly fluctuating background, the Dark Field Method can be used. It consists of filtering the low-frequency region of the spatial spectrum. The scheme, using one horizontally distributed array of a length acceptable to satisfy the Fresnel approach, produces a pseudo-image (single-view projections). Such a vision scheme cannot produce good spatial resolution, especially along the axis connected the source and receiving arrays. To improve the spatial resolution, a set of projections (pseudo-images) can be used for the reconstruction of two-dimensional tomographic images [28, 29, 34, 75-79, 132].

7.2.3 Emission Tomography Methods

In emission tomography an observation object is self-illuminating, so this type of OAT can be considered to be passive. For this method, which requires the reconstruction of the spatial, temporal, and frequency distributions of the sources, the problem consists of overcoming the incorrectness due to the influence of non-propagating waves in the ocean waveguide [23, 34, 39, 44, 45, 49, 57-59, 62, 88, 154].

7.3 PARTIALLY COHERENT IMAGING IN THE OCEAN

As experiments and theoretical investigations have shown, interference noise, arising due to randomly distributed inhomogeneities and multi-ray and multi-mode propagation in the ocean, can destroy the results of the tomographic reconstruction. Partially Coherent (PC) illumination can be used to reduce the interference noise influence in a waveguide.

The use of PC waves for tomographic reconstruction in the ocean is based on the peculiarities of forming partially coherent waves structures and interacting PC waves with oceanic inhomogeneities. As preliminary analysis has shown, weakly divergent bundles (WDBs) of partial waves with similar parameters exist for the various different types of oceanic waveguides. These bundles are characterized by a high degree coherence that diminishes relatively slowly despite the influence of randomly distributed oceanic inhomogeneities. Thus, WDBs can be used for tomographic reconstruction in the regions of the ocean where strong random inhomogeneities, (e.g., intense ocean currents) are present. Some tomographic schemes, with PC illumination, have been discussed for the reconstruction of large, smooth oceanic inhomogeneities, such as ocean fronts, and of spatially localized inhomogeneities, such as fish shoals.

Another approach, closely connected with previous case, is the investigation of the use of PC waves for diffraction or Fresnel tomography schemes. The tomographic image in this case can be described by coherence functions. To analyze the structure of the pseudo-image, the Transferal Contrast Function can be used. It determines the spatial resolution and characterizes the spatial filtering of the images, for example, for decreasing the direct-illuminating field.

As can be shown, the Transferal Contrast Function is connected with the coherence function of the illuminating field, which is determined by the sizes and frequency bands of the noise-acoustic source and the parameters of waveguide modes [39, 40, 80, 81, 82, 87, 136, 138, 154, 155, 161].

7.4 EQUIPMENT FOR OAT EXPERIMENTS

The major part of our discussion on OAT was related to the methods of OAT and the results of computer simulations. But the experimental testing in this field is

a very important issue. In great brevity, the major elements of experimental schemes are introduced in this book only to outline the problem.

In OAT there are many practical problems associated with the development of the principles of designing and manufacturing of the elements of measuring tomographic schemes. The design of low-frequency sources with a high level of radiated acoustic energy and long linear arrays with position, navigation, and synchronization control are among the problems. We have discussed some examples of low-frequency experimental facilities, which were manufactured in the Institute of Applied Physics (IAP) of Russian Academy of Sciences [17]. A low-frequency electromagnetic monopole sources radiation system was built and tested successfully in Arctic experiments. The system includes a large source operating between approximately 50 and 90 Hz and a smaller one operating around 200 Hz. The sources level of these projectors is in excess of 200 dB ref. 1 μPa. IAP also produced a low-frequency mobile linear antenna for mounting either vertically or horizontally.

REFERENCES

1. J. Radon, "Ueber die bestimmung von funktionen durch ihre integralwerte langs gewisser mannigfaltigkeiten," Ber. Saechs. Akademie der Wissenschaften, Leipzig, Mathematisch-Physikalische Klasse, **69**, 262-277 (1917).

2. A.G. Nechaev and A.I. Khil'ko, "Differential acoustic probing of ocean statistically distributed inhomogeneities," Akust. Zh. **34**(1), 65-71 (1988). [English transl.: Sov. Phys. Acoust. **34**(1), (1988)]

3. V.V. Goncharov, V.Yu. Zaitsev, V.M. Kurtepov, A.G. Nechaev, and A.I. Khil'ko, *Acoustical Tomography of Ocean*, IAP RAS, Nizhny Novgorod (1997). [in Russian]

4. Yu.A. Chepurin, V.V. Goncharov, and A.G. Voronovich, "Modal analysis of sound field in deep sea," *Acoustical Imaging*, ed. By H. Ermert and Hans-Peter Harjes, **19**, 897-901 (1991).

5. A.N. Tikhonov and V.Ya. Arsenin, *Methods of Solving Ill-Posed Problems*, Nauka, Moscow, (1979). [in Russian]

6. V.V. Pikalov and N.G. Preobrgensky, "Computer tomography and physical experiment," Uspekhi Fizicheskikh Nauk **141**(3), 469-498 (1983). [in Russian]

7. P. Gregush, *Soundvision*, Mir, Moscow (1982). [in Russian]

8. L. Brekhovskikh and Yu. Lysanov, *Fundamentals of Ocean Acoustics*, Springer-Verlag, Berlin-Heidelberg-New York (1982).

9. V.M. Kurtepov, "Influence of the internal waves, Rossby waves, mesoscale eddies and flows on sound propagation in the ocean," *Ocean Acoustics. Modern Conditions*, ed. by L.M. Brekhovskikh and I.B. Andreeva, Nauka, Moscow (1982), 36-52. [in Russian]

10. V.M. Kurtepov, "Acoustic effects due to the mesoscale variability of the ocean," *Problems of Ocean Acoustics*, Nauka, Moscow (1984). [in Russian]

11. L.M. Brekhovskikh, "Contemporary strategy in exploration and development of the ocean," *Problems of Exploration and Development of the World Ocean*, Sudostroyeniye, Leningrad (1979), 5-17. [in Russian]

12. W. Munk and C. Wunsch, "Ocean acoustic tomography: a scheme for large scale monitoring," Deep-Sea Res., **26**, 123-161 (1979).

13. R.F. Shvachko, "Sound fluctuation due to volume inhomogeneities in the Ocean," *Ocean Acoustics. Modern Conditions*, ed. by L.M. Brekhovskikh and I.B. Andreeva, Nauka, Moscow (1982), 132-141. [in Russian]

14. V.M. Bukhshtaber, V.K. Maslov, and A.M. Trokhan, "Acoustic tomosynthesis of hydrophysical inhomogeneities in the ocean and algebraic methods of image reconstruction," *Methods of Hydrophysical Research*, IAP, AS USSR, Gorky (1984), 209-224. [in Russian]

15. V.M. Bukhshtaber, V.K. Maslov, and A.M. Trokhan, "On an ocean acoustic tomography method," Izv. Akad. Nauk SSSR Fiz. Atmos. Okeana **20**(7), 630-639 (1984). [English transl.: Bull. Acad. Sci. USSR Atmos. Oceanic Phys. **20**(7), 571-577 (1984)]

16. W. Munk, P. Worcester, and C. Wunsch, *Ocean Acoustic Tomography*,

Cambridge University Press, Cambridge (1995).

17. P. Mikhalevsky, A. Baggeroer, A. Gavrilov, M. Slavinsky, "Continuous wave and M-sequence transmissions across the Arctic," J. Acoust. Soc. Am. **96**(5), 3233-3235 (1994).

18. I.R. Karetnikova, A.G. Nechaev, and A.I. Khil'ko, "Features in the diagnosis of random time-varying nonuniformities in a waveguide using complex pulse signals," Izvestiya Vysshikh Uchebnykh Zavedenii, Radiofizika, **33**(12), 1370-1379 (1990). [English transl.: Radiophysics and Quantum Electronics, **33**(12), 1009-1017 (1990)]

19. V.M. Bukhshtaber and V.K. Maslov, "Tomosynthesis of wave fields and inhomogeneous media (the theory of diffractional tomography)," *Tomographical Methods in Physical and Technical Measurements*, VNIIFTRI, Moscow, 7-34, (1985). [in Russian]

20. V.A. Burov and O.D. Rumyantseva, "Solution of the two-dimensional acoustical inverse scattering problem on the basis of functional-analytic methods," Akust. Zh. **38**(3), 413-420 (1992). [English transl.: Sov. Phys. Acoust. **38**(3), 226-230 (1992)]

21. V.A. Burov and O.D. Rumyantseva, "Solution of the two-dimensional acoustical inverse scattering problem on the basis of functional-analytic methods: II. Range of effective application," Akust. Zh. **39**(5), 793-803 (1993). [English transl.: Sov. Phys. Acoust. **39**(5), 419-424 (1993)]

22. I.P. Smirnov and A.I. Khil'ko, "Ray approximation in wave scattering by curvilinear surface in inhomogeneous medium," Akust. Zh. **41**(1), 139-145 (1995). [English transl.: Acoustical Physics **41**(1), 118-123 (1995)]

23. V.V. Goncharov and V.M. Kurtepov, "Successes and problems of acoustic tomography of the ocean," *Acoustic Waves in the Ocean*, ed. by L.M. Brekhovskikh and I.B. Andreeva, Nauka, Moscow (1987), 15-23. [in Russian]

24. Yu. A. Kravtsov, V.M. Kuz'kin, and V.G. Petnikov, "A method for the solution of wave diffraction problem in a waveguide with weakly changing parameters," Izvestiya Vysshikh Uchebnykh Zavedenii, Radiofizika, **26**(4), 400-446 (1983). [English transl.: Radiophysics and Quantum Electronics, **26**(4), (1983)]

25. S.O. Kviatkovsky, "Sound wave diffraction by scattering in a waveguide," Akust. Zh. **34**(4), 730-734 (1988). [English transl.: Sov. Phys. Acoust. **34**(4), 430-431 (1988)]

26. A.I. Khil'ko, V.E. Belov, S.M. Gorsky, and A. Yu. Zinov'iev, "Diffraction of the acoustical fields by the elastic bodies in oceanic waveguides: solution by the combined integral method," *Proceedings of the 2nd European Conference on Underwater Acoustics,* Copenhagen, Denmark, 165-170, 4-8 July 1994.

27. A.I. Khil'ko and I.P. Smirnov, "Ray-formed field scattering on the smooth localized surface in inhomogeneous media," Journal de Physique IV **4**, Colloque C5, Supplement au Journal de Physique III, C5-1117 - C5-1120, May 1994.

28. N.V. Gorskaya, S.M. Gorsky, A.I. Khil'ko, V.A. Zverev, et al., "Features of short-wave sound diffraction in multimode layered waveguides", *Ocean Acoustics*, ed. by L.M. Brekhovskikh and I.B. Andreeva (Nauka, Moscow (1991), 175-189. [in Russian]

29. N.V. Gorskaya, S.M. Gorsky, V.A. Zverev, et.al., "Short-wave diffraction

in a multimode layered waveguide," Akust. Zh. **34**(1), 55-59 (1988). [English transl.: Sov. Phys. Acoust. **34**(1), 29-32 (1988)]

30. I.P. Smirnov and A.I. Khil'ko, "On a 'targeting' in the problem of sound field calculation in inhomogeneous medium with localized inhomogeneities," Vesti KPI, Electroacoustics and Sound Techniques **16**, 9-12 (1992). [in Russian]

31. I.P. Smirnov and A.I. Khil'ko, "Structure of high-frequency acoustic fields in stratified inhomogeneous medium with curvilinear surfaces," Vesti KPI, Electroacoustics and Sound Techniques **16**, 5-9, (1992). [in Russian]

32. I.L. Oboznenko and S.V. Pasechnyi, "Scattering of a sound by a localized inhomogeneity in a waveguide," *The Formation of Acoustic Fields in Oceanic Waveguides*, ed. by V.A. Zverev, IAP, RAS, Nizhny Novgorod (1991), 115-129. [in Russian]

33. K.D. Sabinin, "Internal waves in the ocean," *Ocean Acoustics. Modern Conditions*, ed. by L.M. Brekhovskikh and I.B. Andreeva, Nauka, Moscow (1982), 209-226. [in Russian]

34. E.L.Borodina, N.V.Gorskaya, S.M.Gorsky, V.A. Zverev, G.N. Nikolaev, A.I.Khil'ko, and V.N.Shirokov "Multiaspect Imaging Systems in a Plane Layered Medium," Acoustical Physics, **41**, 157-164, 1995.

35. A.G. Nechaev and A.I.Khil'ko, "Reconstruction of ocean inhomogeneities along acoustic paths by differential probing method," Preprint **178**, IAP, RAS, Nizhny Novgorod (1987). [in Russian]

36. Yu. A. Kravtsov and V.G. Petnikov, "On the possibilities of phase tomography of the ocean using normal waves," Izv. Akad. Nauk SSSR Fiz. Atmos. Okeana **22**(9), 992-994 (1986). [English transl.: Bull. Acad. Sci. USSR Atmos. Oceanic Phys. **22**(9), 769-771 (1986)]

37. V.A. Zverev, "An aperture synthesis in layered inhomogeneous media," *Proceedings of the 7th School-Seminar on Statistical Hydrophysics*, Novosibirsk (1977). [in Russian]

38. V.A. Zverev, et al., "Source image reconstruction in a model waveguide using holography method with optical noncoherent systems," *Proceedings of the 8th Acoustic Meeting*, Moscow (1973). [in Russian]

39. V.A. Zverev, "Holography in ocean acoustics," *Ocean Acoustics. Modern Conditions*, ed. by L.M. Brekhovskikh and I.B. Andreeva, Nauka, Moscow (1982). [in Russian]

40. *Interference of Broad-Band Sound in the Ocean* , ed. by V.A. Zverev and E.F. Orlov, IAP, AN USSR, Gorky, (1984). [in Russian]

41. V.A. Burov, A.A. Goryunov, A.V. Saskovets, and T.A. Tikhonova, "Inverse scattering problems in acoustics (a review)," Akust. Zh. **32**(4), 433-449 (1986). [English transl.: Sov. Phys. Acoust. **32**(4), 273-282 (1986)]

42. V.Yu. Zaitsev, A.G. Nechaev, and L.A. Ostrovskii, "An algorithm for three-dimensional mode tomography of the ocean," Akust. Zh. **33**(6), 1124-1125 (1987). [English transl.: Sov. Phys. Acoust. **33**(6), 657-658 (1987)]

43. I.B. Burlakova, V.N. Golubev, at el., " Doppler tomography in ocean acoustics," Akust. Zh. **34**(4), 756-758 (1988). [English transl.: Sov. Phys. Acoust. **34**(4), 439-440 (1988)]

44. A.G. Nechaev, "Tomography in ocean acoustics," *Ocean Acoustics*, ed.

by L.M. Brekhovskikh and I.B Andreeva, Nauka, Moscow (1991), 175-189. [in Russian]

45. V.M. Bukhshtaber, V.K. Maslov, "A method for the solution of inverse problems in remote sensing of the ocean," *Methods of Hydrophysical Investigations*, IAP, Nizhny Novgorod (1987). [in Russian]

46. A.G. Nechaev and A.I. Khil'ko, "Determination of the local characteristics of ocean inhomogeneities distributed along the acoustical range," Akust. Zh. **34**(4), 694-699 (1988). [English transl.: Sov. Phys. Acoust. **34**(4), 399-402 (1988)]

47. V.M. Bukhshtaber, V.K. Maslov, and A.M. Trokhan, "A procedure for reconstructing the spatial structure of inhomogeneous media," Dokl. Akad. Nauk SSSR **272**(2), 331-334 (1983). [English transl.: Trans. USSR Acad. Sci. **272**(2), (1983)]

48. A.G. Nechaev and A.I. Khil'ko, "Diagnostics of waveguide nonuniformities based on the intensity envelope of a pulsed signal," Izvestiya Vysshikh Uchebnykh Zavedenii, Radiofizika, **33**(1), 65-71 (1990). [English transl.: Radiophysics and Quantum Electronics, **33**(1), 54-59 (1990)]

49. A.G. Nechaev and A.I. Khil'ko, "Acoustic diffraction tomography of the ocean," Izvestiya Vysshikh Uchebnykh Zavedenii, Radiofizika, **36**(8), 738-751 (1993). [English transl.: Radiophysics and Quantum Electronics, **36**(8), 493-503 (1993)]

50. A.G. Nechaev and A.I. Khil'ko, "Differential acoustic diagnostics of random inhomogeneities in the ocean," Akust. Zh. **34**(2), 285-289 (1988). [English transl.: Sov. Phys. Acoust. **34**(2), 167-170 (1988)]

51. V.A. Burov, A.V. Glazkov, I.P. Prudnikova, O.D. Rumyantseva, M.I. Rychagov, and E. Ya. Tagunov, "Reconstruction of acoustic inhomogeneities in a plane waveguide by the analysis of diffracted scattering of sound waves," *The Formation of Acoustic Fields in Oceanic Waveguides*, ed. by V.A. Zverev, IAP, AS USSR, Nizhny Novgorod 1991), 200-213. [in Russian]

52. I.B. Burlakova, Yu. A. Dubovoi, A.L. Zeigman, A.G. Nechaev, M.M. Slavinskii, and N.M. Smirnov, "Feasibility of acoustic tomography of the rough ocean surface," Akust. Zh. **34**(3), 423-430 (1988). [English transl.: Sov. Phys. Acoust. **34**(3), 246-250 (1988)]

53. A.L. Virovlyanskii, A.I. Saichev A.L., and M.M. Slavinsky, "Signal spectrum from moved receiver in underwater sound channel," Akust. Zh. **31**(1), 22-26 (1985). [English transl.: Sov. Phys. Acoust. **31**(1), 13-15 (1985)]

54. V.S. Averbakh, et al., "Remote surface reverberation of sound in the ocean," Akust. Zh. **36**(1), 29-33 (1990). [English transl.: Sov. Phys. Acoust. **36**(1) (1990)]

55. N.E. Mal'tsev, K.D. Sabinin, and A.V. Furduev, "Acoustical and oceanologic experiment at the lens of Mediterranean water in the Atlantic Ocean," Akust. Zh. 36(1), 86-93 (1990). [English transl.: Sov. Phys. Acoust. **36**(1), 46-50 (1990)]

56. A.G. Voronovich, et al., "Comparative analysis of methods for the normal mode decomposition of a sound field in a waveguide: numerical simulation and full-scale experiment," Akust. Zh. **38**(4), 661-670 (1992). [English transl.: Sov. Phys. Acoust. **38**(4), 365-370 (1992)]

57. V.V. Goncharov and A.G. Voronovich, "An experiment on matched-field acoustic tomography with continuous wave signals in the Norway Sea," J. Acoust. Soc. Am. **93**(4), Pt. 1, 1873-1881 (1993).

58. I.N. Didenkulov and A.G. Nechaev, "Acoustic emission tomography of the ocean," Akust. Zh. **35**(3), 461-467 (1989). [English transl.: Sov. Phys. Acoust. **35**(3), 270-273 (1989)]

59. L. Ya. Lubavin and A.G. Nechaev, "Acoustic interference tomography of the ocean," Akust. Zh. **35**(4), 703-709 (1989). [English transl.: Sov. Phys. Acoust. **35**(4), 406-409 (1989)]

60. P.N. Mikhalevsky, R.D. Muench, and F.R. DiNapoli, "Acoustic measurements of Arctic ocean warming," SAIC's project (1991).

61. V.Yu. Zaitsev and V.V. Kurin. "Laboratory modeling of tomographical reconstruction of ocean waveguide structure using the perturbation of normal mode characteristics of probing acoustic signals," *Proceedings of the 4th All-Union Symposium on Computer Tomography, Pt. 2*, Tashkent (1989), p. 35. [in Russian]

62. V.Yu. Zaitsev, A.G. Nechaev, and L.A. Ostrovskii, "Aspects of acoustic tomography of the ocean," Akust. Zh. **34**(1), 193 (1988). [English transl.: Sov. Phys. Acoust. **34**(1), 113 (1988)]

63. V.Yu. Zaitsev, A.G. Nechaev, and L.A. Ostrovskii, "An algorithm for three-dimensional mode tomography of the ocean," Akust. Zh. **33**(6), 1124-1125 (1987). [English transl.: Sov. Phys. Acoust. **33**(6), 657-658 (1987)]

64. V.Yu. Zaitsev and M.A. Raevskii, "On a transformation of wave field space-time spectrum in a waveguide with rough surface," Izvestiya Vysshikh Uchebnykh Zavedenii, Radiofizika, **28**(1), 65-74 (1985). [English transl.: Radiophysics and Quantum Electronics, **28**(1), (1985)]

65. A.G. Nechaev, "A priori information in acoustic interference tomography of the ocean," *Proceedings of the 3rd Meeting on Geotomography*, Sverdlovsk Institute of Geophysics, Ural Branch of Science Academy of USSR (1991), 60-61.[in Russian]

66. N.V. Gorskaya, S.M. Gorskii, S.N. Gurbatov, et al., "Applicability of frequency-modulated waves for the investigation of scattering in irregular waveguides," Akust. Zh. **37**(5), 914-921 (1991). [English transl.: Sov. Phys. Acoust. **37**(5), 475-478 (1991)]

67. S.M. Rytov, Yu.A. Kravtsov, and V.I. Tatarskii, *Introduction to Statistical Radiophysics. Part II: Random Fields*, Nauka, Moscow (1978). [in Russian]

68. A.Yu. Kazarova, L. Ya. Lybavin and A.G. Nechaev, "Interference tomography of the synoptic inhomogeneities and ocean bottom," *Journ. De Physique IV Coll. C5, Jurnal de Physique III,* **4**, C5-1099-C5-1103, (1994).

69. A.G. Nechaev, V.N. Fokin, and M.S. Fokina, "Temporal structure of acoustic signals scattered by ocean inhomgeneities," Akust. Zh. **40**(2), 284-289 (1994). [English transl.: Acoustical Physics **40**(2), 258-263 (1994)]

70. A.I. Khil'ko, I.P. Smirnov, and A.Yu. Zorin, "Spatial and temporal characteristics of noise propagation paths in inhomogeneous media", *Proceedings of Int. Conference on Noise and Vibration Control*, Interpublish LTD, St. Petersburg (1993), **5**, 145-148.

71. A.I. Khil'ko, I.P. Smirnov, and A.Yu. Zorin, "The space-time

characteristics of connecting channels in the inhomogeneous refractive waveguides," *Proceedings of SPIE Symposium*, Orlando, FL, USA (1994), SPIE **2223**, 245-249.

72. A.I. Khil'ko, I.P. Smirnov, and A.Yu. Zorin, "Energetic characteristics of coupling channels between inhomogeneous medium points," Izvestiya Vysshikh Uchebnykh Zavedenii, Radiofizika, **36**(8), 443-455 (1993). [English transl.: Radiophysics and Quantum Electronics, **36**(8), 767-771 (1993)]

73. A.I. Khil'ko, I.P. Smirnov, and A.Yu. Zorin, "Temporal characteristics of communication connecting channels between source and receiver in inhomogeneous medium," Izvestiya Vysshikh Uchebnykh Zavedenii, Radiofizika, **37**(11), 1373-1387 (1994). [English transl.: Radiophysics and Quantum Electronics, **37**(11), (1994)]

74. I.B. Burlakova, Yu.V. Petukhov, and M.M. Slavinskii, "Determination of the acoustical characteristics of the bottom of ocean waveguides by Doppler tomography," Akust. Zh. **35**(6), 1015-1020 (1989). [English transl.: Sov. Phys. Acoust. **35**(6), 591-594 (1989)]

75. E.L. Borodina, N.V. Gorskaya, S.M. Gorskii, et al., "The possibilities of shadow methods for studying diffracted sound fields in waveguides," *The Formation of Acoustic Fields in Oceanic Waveguides*, ed. by V.A. Zverev, IAP, RAS, Nizhny Novgorod (1991), 174-200.

76. E.L. Borodina, N.V. Gorskaya, S.M. Gorskii, et al., "Spatial filtering of images in the ultrasonic imaging of large inhomogeneities," Akust. Zh. **38**(6), 1004-1012 (1992). [English transl.: Sov. Phys. Acoust. **38**(6), 551-555 (1992)]

77. E.L. Borodina, N.V. Gorskaya, et al., "Reconstruction of the noise "soiling" of inhomogeneous media by dark field methods," *Proceedings of the 1st Symposium of RAS*, Moscow, AKIN (1992), 19-22.

78. N.V. Gorskaya, V.A. Zverev, G.N. Nikolaev, et al., "On a reconstruction of the spatial localization of secondary hydroacoustic sources," *Proceedings of 11th All-Union Acoustic Conference*, VNIIFTRI, Moscow (1991), Section T, 16-18. [in Russian]

79. E.L. Borodina, N.V. Gorskaya, S.M. Gorskii, V.A. Zverev, G.N. Nikolaev, A.I. Khil'ko, and V.N. Shirokov, "The formation of multi-view images in ocean waveguides by the Dark-Field Method." *The Formation of Acoustic Fields in Oceanic Waveguides: The Reconstruction of Inhomogeneities*, IAP, RAS, Nizhny Novgorod, 102-130, (1995).

80. A.I. Khil'ko, "Spatial filtering of partially coherent acoustical images," *Acoustical Imaging*, ed. by J.P. Jones, **21**, 357-363 (1994).

81. A.I. Khil'ko, "Spatial filtering of partially coherent images," *Proceedings of Quatorzieme Colloque GRETSI*, Juan-Les-Pins, France, 13-16 Sept. 1993.

82. A.I. Khil'ko, "Partially coherent image reconstruction," *Proceedings of SPIE Symposium*, Orlando, FL, USA, **1967**, 381-411, 10-15 April 1993.

83. A.A. Gorunov and A.V. Saskovets, *Inverse Scattering Problems in Acoustics*, MGU, Moscow, (1989). [in Russian]

84. I.Sh. Fiks, N.A Sidorovskaia, and V.I. Turchin, "Measurements of complex moving broadband acoustic radiators using near-field technique," *Proceedings of the 2nd European Conference on Underwater Acoustics*, Copenhagen, Denmark, 4-8 July 1994, **2**, 745-750.

85. N.A. Sidorovskaya and V.I. Turchin, "Time-spatial processing of near-

field measurements," *Proceedings of Quatorzieme Colloque GRETSI*, Juan-Les-Pins, France, 13-16 Sept. 1993, 301-304.

86. A.N. Tikhonov, V.Ya. Arsenin, and A.A. Timonov, *Mathematical Problems of Computer Tomography*, Nauka, Moscow (1987). [in Russian]

87. V.K. Maslov and U.F. Fezkhanov, "Passive long-wave tomography of radiating systems," *Proceedings of the 4th All-Union Symposium on Computer Tomography, Pt. 1*, Tashkent (1989), 210. [in Russian]

88. A.I. Knafel, Matveev A.L., Khil'ko A.I. et al., "On a interference method isolating of quasi-stationary signal from noise background," Izvestiya Vysshikh Uchebnykh Zavedenii, Radiofizika, **32**(10), 1250-1257 (1989). [English transl.: Radiophysics and Quantum Electronics, **32**(10) (1989)]

89. V.K. Maslov, V.M. Bukhshtaber, A.M. Trokhan, "Frequency-time representation of non-stationary signals in hydroacoustic investigations," *Metrological Problems in Geophysical and Geoacoustical Measurements*, VNIIFTRI, Moscow (1990), 106-122. [in Russian]

90. Walter H. Munk, Robert C. Spindel, Arthur Baggeroer, and Theodore G. Birdsall, "The Heard Island Feasibility Test," J. Acoust. Soc. Am. **96**(4), 2330-2342 (1994).

91. S.V. Burenkov, A.N. Gavrilov, A.Y. Uporin, and A.V. Furduev, Heard Island Feasibility Test: Long-range sound transmission from Heard Island to the Krylov underwater mountain," J. Acoust. Soc. Am. **96**(4), 2458-2463 (1994).

92. Yu. P. Lysanov, A.M. Plotkin, and G.I. Shapiro, "Effect of intra-thermocline lenses on acoustic fields in the ocean," Izv. Akad. Nauk SSSR Fiz. Atmos. Okeana **25**(12), 1272-1280 (1989). [English transl.: Bull. Acad. Sci. USSR Atmos. Oceanic Phys. **25**(12), 939-945 (1989)]

93. V.V. Goncharov, S.A. Dremuchev, V.M. Kurtepov, V.G. Selivanov, Yu.A. Chepurin, and S.M. Shapovalov, "Acoustic experiments on a "lens" of Mediterranean water," Dokl. Akad. Nauk SSSR **315**(2), 481-483 (1990). [English transl.: Trans. USSR Acad. Sci. **315**(2), 304-306 (1990)]

94. L.M. Brekhovskikh, V.V. Goncharov, S.A. Dremuchev, V.M. Kurtepov, V.G. Selivanov, and Yu.A. Chepurin, "Experiments on long-range sound propagation in the Canary Basin of the Atlantic Ocean," Akust. Zh. **36**(5), 824-831 (1990). [English transl.: Sov. Phys. Acoust. **36**(5), 461-465 (1990)]

95. B. Cornuelle, C. Wunsch, D. Behringer, et al., "Tomographic maps of the ocean mesoscale. Part : Pure acoustics," J. Phys. Oceanogr. **15**, 133-152 (1985).

96. Bruce M. Howe, Peter F. Worcester, and Robert C. Spindel, "Ocean acoustic tomography: mesoscale velocity," J. Geophys. Res. **92**(c4), 3785-3805 (1987).

97. O.A. Godin, D.Yu. Mikhin, S.Ya. Molchanov, "Inverse problem of geometric acoustics of a moving medium," Izv. Akad. Nauk SSSR Fiz. Atmos. Okeana **27**(2), 139-150 (1991). [English transl.: Bull. Acad. Sci. USSR Atmos. Oceanic Phys. **27**(2), 92-99 (1991)]

98. T. Rossby, "An oceanic vorticity meter," J. Marine Res. **33**, 213-222 (1975).

99. W. Munk and C. Wunsch, "Biases and caustics in long-range acoustic tomography," Deep-Sea Res. **32**, 1317-1346 (1985).

100. V.V. Goncharov and V.M. Kurtepov, "Numerical experiments on ocean tomography," Dokl. Akad. Nauk SSSR **297**(6), 1461-1465 (1987). [English transl.: Trans. USSR Acad. Sci. **297**(6), 239-242 (1987)]

101. V.V. Goncharov and V.M. Kurtepov, "Numerical experiments on ocean tomography," *Acoustics of Ocean Medium*, ed. by L.M. Brekhovskikh and I.B. Andreeva (Nauka, Moscow (1989), 107-115. [in Russian]

102. V.Ya. Arsenin and A.A. Timonov, "Local regularization of mathematical problems in computerized tomography," *Proceedings of the Second All-Union Symposium on Computerized Tomography*, Kuibyshev Aviatz. Inst., Kuibyshev (1985), 14-15. [in Russian]

103. W.H. Munk and A.M.G. Forbes, "Global ocean warming: an acoustic measure?" J. Phys. Oceanogr. **19**, 1765 1778 (1989).

104. W.H. Munk, "The Heard Island Experiment," Naval Res. Rev. **42**, 2-22 (1990)

105. B. E. McDonald, W. A. Kuperman, M. D. Collins, and K. D. Heaney, "Trans-oceanic acoustic propagation and global warming," 1993 NRL Review, 83-93.

106. En-Cen Lo, Ji-Xun Zhow, Er-Chang Shang, "Normal mode filtering in shallow water," J. Acoust. Soc. Am. **74**, 1833-1841 (1983).

107. C. Fueillade, W.A. Kinney, and D.R. DelBalzo, " Shallow-water matched-field localization off Panama City, Florida," J. Acoust. Soc. Am. **88**(1), 423-433 (1990).

108. T.C. Yang. "A method of range and depth estimation by modal decomposition," J. Acoust. Soc. Am. **82**(5), 1736-1745 (1987).

109. Jean-Marie Q.D. Tran and Williams S. Hodgkiss, "Matched-field processing of 200 Hz continuous wave (cw) signals," J. Acoust. Soc. Am. **89**(2), 745-755 (1991)

110. S.A. Dremuchev , V.G. Selivanov, and Yu.A. Chepurin, "Measurement of acoustic-field structure with a vertical array," Oceanology **30**(5), 641-646 (1990).

111. L.M. Brekhovskikh, et al., "Acoustical tomography of the ocean and related problems," *Proceedings of the 14th Intern. Congress on Acoustics*, Beijing, China (1992), **P**, P4.

112. V. Goncharov and V. Kurtepov, "Formation and propagation of weakly divergent bundles of rays in a horizontally inhomogeneous ocean," Akust. Zh. **40**(5), 773-781 (1994). [English transl.: Acoust. Phys. **40**(5), 685-692 (1994)]

113. Yu.V. Petukhov, "Sound beam with minimal wavefront divergence in stratified ocean waveguide," Akust. Zh. **40**(1), 97-105 (1994) [English transl.: Acoustical Physics **40**(1), 97-105 (1994)]

114. S.D. Chuprov, "Selection of modes and rays in underwater sound channel," *Acoustics of Ocean Medium*, ed. by L. Brekhovskikh and I. Andreeva, Nauka, Moscow (1989), 56-64.

115. L. Brekhovskikh, V. Goncharov, V.Kurtepov, "Weakly divergent bundles of sound rays in Arctic," *Proceedings of Russian Acoustical Society*, Moscow (1995).

116. W. Munk and F. Zachariasen, "Sound propagation through a fluctuating stratified ocean: theory and observation," J. Acoust. Soc. Am. **59**, 818-838 (1976).

117. I. B. Burlakova, A. L. Zeigman, Ya. V. Petukhov, and M. M. Slavinsky, "The method of Doppler tomography for the study of the acoustic characteristics of

the bottom of deep-water ocean waveguides," *The Formation of Acoustic Fields in Oceanic Waveguides: The Reconstruction of Inhomogeneities*, ed. by V.A. Zverev, IAP, RAS, Nizhny Novgorod, 91-121, (1994). [in Russian]

118. V. V. Picalov and N. G. Preobrazhenskii, *Reconstructive Tomography in Gas Dynamics and Plasma Physics*, Nauka, Novosibirsk (1987).

119. F.G. Bass and I.M. Fuks, *Wave Scattering by Statistically Rough Surface*. Nauka, Moscow (1972).

120. V.A. Zverev, *Radio-optics*, Sov. Radio, Moscow (1975).

121. I.B. Andreeva and V.I. Goncharov, "Methods for the calculation of multipath reverberations and controlling comparison with experiments," *Problems of Ocean Acoustics*, Nauka, Moscow (1984), 69-77.

122. D.I. Abrosimov and L.S. Dolin, "Surface reverberation in the waveguide propagation of sound in the ocean," Akust. Zh. **27**(6), 808-816 (1981). [English transl.: Sov. Phys. Acoust. **27**(6), 448-452 (1981)]

123. V.A. Zverev, A.V. Shisharin, and A.I. Khil'ko, "On using white light in optical filtering systems," Avtometria, **2**, 108-118, (1978). [in Russian]

124. M.I. Karnovsky, V.P Pugach, and A.I. Toropov, "Extruction of modes by arrays in waveguides," *Acoustical Ultrasound Technique*, **19**, 104-106 (1984). [in Russian]

125. R.I. Kriazev and V.M. Kudriashov, "Influence of boundary scattering on the sound field in waveguide,"*Problems of Ocean Acoustics*, Nauka, Moscow (1984), 57-69.

126. A.G. Sazontov and V.A. Farfel', "Single scattering of an acoustic signal by internal waves in an underwater sound channel," Akust. Zh. **32**(5), 635-641 (1986). [English transl.: Sov. Phys. Acoust. **32**(5), 393-396 (1986)]

127. L.M. Brekhovskhikh, Yu.P. Lysanov, and N.V. Studenichnik, "A contribution to the theory of pre-reverberation of sound in the sea." Dokl. Akad. Nauk SSSR **239**(1) 211-213 (1978). [English transl.: Trans. (Doklady) USSR Acad. Sci. **239**(1) 194-196 (1978)]

128. W. Munk and C. Wunch, "Ocean acoustic tomography: rays and modes," Rev. Geophys. Space Phys. **21**, 777-793 (1983).

129. Yu.A. Kravtsov and Yu.I. Orlov, *Geometrical Optics of Inhomogeous Medium*, Nauka, Moscow, (1980).

130. A.G. Nechaev and A.I. Khil'ko, "Acoustic diffraction tomography of the ocean," *"Proceedings of the Int. Scientific School-Seminar on Dynamic and Stochastic Wave Phenomena."* Nizhny Novgorod University, Nizhny Novgorod, (1992), 177-181.

131. E.L. Borodina, A.I. Khil'ko, and V.N. Shirokov, "Structure of sound field in a water layer excited by a source located in air," Akust. Zh. **38**(4), 609-615 (1992). [English transl.: Sov. Phys. Acoust. **38**(4), 336-340 (1992)]

132. E.L. Borodina, A.I. Khil'ko, and V.N. Shirokov, "Formation of acoustical field by modes as well as by shear and side waves in a few mode stratified inhomogeneous ocean waveguides," *Formation of Acoustical Fields in Ocean Waveguide*, IAP, RAS, Nizhny Novgorod (1991), 66-82.

133. A.I. Khil'ko, I.P. Smirnov, and A.Yu. Zorin, "The characteristics of energetic coupling of inhomogeneous medium points," *Proceedings of the Int.*

Scientific School-Seminar on "Dynamic and Stochastic Wave Phenomena," Nizhny Novgorod University, Nizhny Novgorod (1992), 194-200.

134. Yu.V. Petukhov and A.I. Khil'ko, "An estimation of seismic-acoustical source sizes in layered inhomogeneous waveguides," Preprint **352**, NIRFI, Nizhny Novgorod (1992). [in Russian]

135. S.M. Flatte, R. Dashen, W. Munk, K. Watson, and F. Zachariasen, *Sound Transmission through a Fluctuating Ocean*, Cambridge University Press (1979).

136. A.I. Khil'ko, "Overview of applied physics institute (RAS) activities in the field of acoustical probing of oceanic waveguides," *Proceedings of the 20 Workshop "Exploring the Opportunities for Cooperative Research"*, ARL, Orlando, Florida, (185-205), 8-9 April 1994.

137. A. V. Furduev, "Ocean noise," *Ocean Acoustics*, Nauka, Moscow (1974), 615-631. [in Russian]

138. B. F. Kur'yanov, "Underwater ocean noise," *Ocean acoustics: Current Status*, ed. by L. M. Brekhovskikh and I. B. Andreeva, Nauka, Moscow (1982), 164-174. [in Russian]

139. B. F. Kur'yanov and B. I. Klyachin, "An application of radiation transport theory to the problems of noise transmission in the ocean," *Problems of Ocean Acoustics*, ed. by L. M. Brekhovskikh and I. B. Andreeva, Nauka, Moscow (1984), 16-30. [in Russian]

140. A. A. Moiseev , "Ambient noise field of a randomly inhomogeneous ocean," Akust. Zh. **33**(6), 1105-1111 (1987). [English transl.: Sov. Phys. Acoust. **33**(6), 642 (1987)]

141. A. N. Tikhonov and V. Ya. Arsenin, *Solution of Ill-Posed Problems*, Halsted Press, New York, (1977).

142. N. G. Preobrazhensky and V. V. Picalov, *Unstable Problems in Plasma Diagnostics*, Nauka, Novosibirsk (1982), 237

143. Y. Censor, D. E. Gustafson, A. Lent, H. Tuy, "A new approach to the emission computerized tomography problem: simultaneous calculation of attenuation and activity coefficients," IEEE Trans. Nucl. Sci. **NS-26**, 2775-1779, (1979).

144. R. A. Vadov, "An attenuation of low-frequency sound in the ocean," *Problems of Ocean Acoustics*, ed. by L. M. Brekhovskikh and I. B. Andreeva, Nauka, Moscow (1984), 31-42. [in Russian]

145. A.C. Kibblewhite, J.A. Shooter, and S.L. Watkins, "Examination of attenuation a very low frequencies using the deep-water ambient noise field", J. Acoust. Soc. Am. **60**, 1040-1047, (1976).

146. A. N. Tikhonov, A. V. Goncharsky, V. V. Stepanov, and A. G. Yagola, *Regularization Algorithms and a priori Information*, Nauka, Moscow (1983), 200

147. A.B. Gershman, A.L. Matveev, and J.F. Boehme, "ML-estimation of signal power in the presence of unknown noise field -- simple approximate estimator and explicit Cramer--Rao limit," *Proceedings of ICASSP'95*, May 1995, 1824-1827.

148. A.F. Erkin, Kazarova A.Ju., Kapustin P.A. at all, "Identification of the ray pulses in the ocean acoustic tomography with moving", Akust. Zh., **41**(4), 632-635, (1995).

149. A.L. Matveev and S.M. Gorsky, "An estimation of signals by filtering

correlation functions," *Tomographic Methods in Physical-Technical Measurements*. VNIIFTRI, Moscow (1990), 181-190. [in Russian]

150. Yu. V. Petukhov and A.I. Khil'ko, "The possibilities for tsunami source sizes estimation using the space coherence seismic and hydroacoustic waves", *Theoretical and experimental investigations of low wave processes*, Vladivostok, DVNC AN USSR, 37-51, (1985).

151. V.I. Turchin, I.S. Fiks, et al., "Distant Measurements of Characteristics of Moving Radiators with Complex Spatial-Time Structure," *Tomographic Methods in Physical-Technical Measurements*, VNIIFTRI, Moscow (1990), 159-180.

152. Yu.K. Postoenko, N.A. Sidorovskaia, V.I. Turchin, R.A. Ugrinovsky, G.E. Fiks, I.Sh. Fiks. "Reconstruction of the structure of moving acoustic sources with complex spectrum," *The Formation of Acoustic Fields in Oceanic Waveguides: The Reconstruction of Inhomogeneities*, ed. by V.A. Zverev, IAP, RAS, Nizhny Novgorod, 247-281, (1994). [in Russian]

153. I.Sh. Fiks, N.A. Sidorovskaia, and V.I. Turchin, "Measurements of complex moving broadband acoustic radiators using near-field technique," *Proceedings of the 2nd European Conference on Underwater Acoustics*, Copenhagen, Denmark, 4-8 July 1994, **2**, 745-750.

154. N.A. Sidorovskaia and A.I. Khil'ko, "Partially coherent acoustic images in layered refractive waveguides." Izvestiva Vysshikh Uchebnykh Zavedenii, Radiofizika, **38**(1-2), 127-133 (1995). [English transl.: Radiophysics and Quantum Electronics, **38**(1-2), 85-88 (1995)]

155. D.I. Abrosimov, A.I. Khil'ko, and J.W. Caruthers, "Tomograhpical reconstruction of oceanic inhomogeneities: Part 2- Application of partially coherent acoustic waves structures to the Fresnel Diffraction and differential tomography," *Proceedings of OCEANS'95*, 1476-1482, San Diego (1995).

156. V.M. Kamenkovich, M.N. Koshliakov, and A.S. Monin, *Synoptical Eddies in the Ocean*, Gidrometeoizdat, Leningrad (1982).

157. I.B. Andreeva, "Sound scattering by surface and pre-surface ocean layer." *Ocean acoustics: Current Status*, ed. by L. M. Brekhovskikh and I. B. Andreeva. Nauka, Moscow (1982), 118-132.

158. V.I. Tatarsky, *Wave Propagation in Turbulent Atmosphere*, Nauka, Moscow (1967). [in Russian]

159. A.S. Monin and R.V. Ozmidov, *Ocean Turbulence*, Gidrometeoizdat, Leningrad (1981).

160. I.B. Andreeva, A.V. Belousov, G.F. L'vovskaya, and L.L. Tarasov, " Acoustic properties of dense oceanic Pelagian Clusters." Akust. Zh. **40**(1), 9-16 (1994). [English transl.: Acoustical Physics **40**(1), 5-11 (1994)]

161. I.P. Smirnov, A.I. Khil'ko, and J.W. Caruthers, "Tomographical reconstruction of oceanic inhomogeneities using partially coherent space-time acoustic fields: Part 1- Formation and analysis of space-time acoustic fields in an oceanic waveguide," *Proceedings of OCEANS'95*, 1469-1475, San Diego (1995).

162. B.F. Kur'anov and A.I. Vedenev, "Remote sensing of marine sediments by acoustical noise on site of the deep sea drilling hole n 643 in the Norvegian sea", *Okeanologia*, **34**(4), 345-349, (1994).

CONTENTS

PART II: DIFFRACTION TOMOGRAPHIC METHODS

PART III: OTHER NOVEL TOMOGRAPHIC METHODS